Interplay of Dynamics and Network Topology in Systems of Excitable Elements

DISSERTATION

zur Erlangung des akademischen Grades
doctor rerum naturalium
(Dr. rer. nat.)

im Fach Physik

eingereicht an der
Mathematisch-Naturwissenschaftlichen Fakultät
der Humboldt-Universität zu Berlin

von

Dipl.-Phys. Petar Georgiev Tomov

Präsident der Humboldt-Universität zu Berlin:
Prof. Dr. Jan-Hendrik Olbertz

Dekan der Mathematisch-Naturwissenschaftlichen Fakultät:
Prof. Elmar Kulke

Gutachter:
1. PD Dr. Michael A. Zaks
2. Prof. Dr. Antonio C. Roque
3. PD Dr. Jan A. Freund

Tag der mündlichen Prüfung: 11.02.2016

Abstract

In this work we study global dynamical phenomena which emerge as a result of the interplay between network topology and single-node dynamics in systems of excitable elements.

We first focus on relatively small structured networks with comprehensible complexity in terms of graph-symmetries. We discuss the constraints posed by the network topology on the dynamical flow in the phase space of the system and on the admissible synchronized states. In particular, we are interested in the stability properties of flow invariant polydiagonals and in the evolutions of attractors in the parameter spaces of such systems. As a suitable theoretical framework describing excitable elements we use the Kuramoto and Shinomoto model of sinusoidally coupled "active rotators". We investigate plane hexagonal lattices of different size with periodic boundary conditions. We study general conditions posed on the adjacency matrix of the networks, enabling the Watanabe-Strogatz reduction, and discuss different examples. Finally, we present a generic analysis of bifurcations taking place on the submanifold associated with the Watanabe-Strogatz reduced system.

In the second part of the work we investigate a global dynamical phenomenon in neuronal networks known as self-sustained activity (SSA). We consider networks of hierarchical and modular topology, comprising neurons of different cortical electrophysiological cell classes. In the investigated neural networks we show that SSA states with spiking characteristics, similar to the ones observed experimentally, can exist. By analyzing the dynamics of single neurons, as well as the phase space of the whole system, we explain the importance of inhibition for sustaining the global oscillatory activity of the network. Furthermore, we show that both network architecture, in terms of modularity level, as well as mixture of excitatory-inhibitory neurons, in terms of different cell classes, have influence on the lifetime of SSA.

Keywords: clustering, stability, active rotators, hexagonal lattice, neuronal network models, self-sustained activity, cortical oscillations, intrinsic neuronal diversity, chaotic neural dynamics.

Zusammenfassung

Wir untersuchen globale dynamische Phänomene, die sich von dem Zusammenspiel zwischen Netzwerktopologie und Dynamik der einzelnen Elementen ergeben.

Im ersten Teil untersuchen wir relativ kleine strukturierte Netzwerke mit überschaubarer Komplexität. Als geeigneter theoretischer Rahmen für erregbare Systeme verwenden wir das Kuramoto und Shinomoto Modell der sinusförmig-gekoppelten "aktiven Rotatoren" und studieren das Kollektivverhalten des Systems in Bezug auf Synchronisation. Wir besprechen die Einschränkungen, die durch die Netzwerktopologie auf dem Fluss im Phasenraum des Systems gestellt werden. Insbesondere interessieren wir uns für die Stabilitätseigenschaften von Fluss-invarianten Polydiagonalen und die Entwicklungen von Attraktoren in den Parameterräume solcher Systeme. Wir untersuchen zweidimensionale hexagonale Gitter mit periodischen Randbedingungen. Wir untersuchen allgemeine Bedingungen auf der Adjazenzmatrix von Netzwerken, die die Watanabe-Strogatz Reduktion ermöglichen, und diskutieren verschiedene Beispiele. Schließlich präsentieren wir eine generische Analyse der Bifurkationen, die auf der Untermannigfaltigkeit des Watanabe-Strogatz reduzierten Systems stattfinden.

Im zweiten Teil der Arbeit untersuchen wir das globale dynamische Phänomen selbstanhaltender Aktivität (self-sustained activity / SSA) in neuronalen Netzwerken. Wir betrachten Netzwerke mit hierarchischer und modularer Topologie , umfassend Neuronen von verschiedenen kortikalen elektrophysiologischen Zellklassen. Wir zeigen, dass SSA Zustände mit ähnlich zu den experimentell beobachteten Eigenschaften existieren. Durch Analyse der Dynamik einzelner Neuronen sowie des Phasenraums des gesamten Systems erläutern wir die Rolle der Inhibierung. Darüber hinaus zeigen wir, dass beide Netzwerkarchitektur, in Bezug auf Modularität, sowie Mischung aus verschiedenen Neuronen, in Bezug auf die unterschiedlichen Zellklassen, einen Einfluss auf die Lebensdauer der SSA haben.

Schlagwörter: Clusterbildung, Stabilität, aktive Rotatoren, hexagonale Gitter, neuronale Netzwerkmodelle, selbstanhaltende Aktivität, kortikale Oszillationen, intrinsische neuronale Diversität, chaotische neuronale Dynamik.

Contents

Introduction

According to Encyclopædia Britannica [83], "In the broadest sense, physics (from the Greek *physikos*) is concerned with all aspects of nature on both the macroscopic and submicroscopic levels." Some of the greatest achievements in modern physics are, on the one hand, the development of the Standard Model of Physics [113] describing the forces responsible for the interaction of the known subatomic particles and, on the other hand, the General Theory of Relativity [114] describing the gravitational force. Although both theories have their issues and are subject to further development [94] they are, thus far, the two best tested theoretical models describing the laws governing matter. The implementation of those theories exceeds by far a purely theoretical understanding about the behavior of an exotic particle or a galaxy, by finding application in various technologies; and yet, it is highly nontrivial and usually impractical to apply the fundamental physical laws to "*all* aspects of nature". Furthermore, finding the corresponding exact solutions of the underlying mathematical equations is in most cases impossible. In the late 19th century, in an attempt to promote the mathematical journal *Acta Mathematica,* a competition sponsored by the Swedish King Oscar II took place. One of the questions asked was on the application of Newton's Laws on a system of mass particles and on finding the corresponding exact solution. The aim was to understand the planetary motions within the solar system better and in particular– its stability; a question which has engaged scientists like Newton, Euler, Lagrange, Poisson and many others. It was Poincaré who won the prize. Although he did not provide exact solutions to the problem, his manuscript created the foundation of what is now known as Dynamical Systems or Chaos Theory [28, 34, 13]: a theory which, next to quantum mechanics and relativity, is believed to have revolutionized not only physics but all sciences. Its implementation in the field of "Interdisciplinary Physics" (a categorization given by academic publishers such as Frontiers Media S.A or Elsevier B.V.) range from Nuclear Materials and Energy, Geography and Climatology, to Medicine and Biology, making it applicable to "*various* aspects of nature".

In the broadest sense, a dynamical system is a rule describing the time evolution of a system. In most applications the systems of interest consist of interacting entities and the dynamical system describes changes in the state of each entity by means of first order coupled Ordinary Differential Equations (ODE's) [17, 100]. Depending on the nature of the problem, it is often the case that the involved entities have distinct internal properties and are subject to different interactions among each other. For example, if we consider a group of neurons in the brain coupled to each other via dendrites and synapses, in general, there will be various types of neurons, some of them being excitatory and others inhibitory, which will deffer not only in their internal dynamics but also in the way they influence each other. For instance, as their names suggest, the excitatory neurons will tend to excite (activate) the neurons they are directly coupled to and the inhibitory neurons will tend to inhibit (suppress) the activity of their postsynaptic neighbors. In cases when distinct entities comprise the system, this differentiation enables the division of these entities within the system as well as their interactions into particular groups. From this point of view it seems quite natural to consider the dynamical system not solely as a coupled system of

ODE's but as complex dynamical network, where the (different types of) entities correspond to (different types of) nodes and the (different types of) interactions to (different types of) edges connecting the nodes. This perspective emphasizes not only the dynamical differences between the involved entities and their interactions but much more the underlying coupling structure which is captured by the topology of the network. Regarding our example, it is intuitive to speak of neural networks. Networks are prevailing in biological systems and have given rise to the branch of "network biology", researching the network of molecular interactions within a cell, gene regulatory networks, metabolic networks, food webs and many others. Complex Network Theory is as universal as Dynamical Systems or Chaos Theory and has found various applications not only in biology but in all scientific disciplines reaching from pure physics and mathematics to climatology and sociology [81, 18]. It is, therefore, not surprising that both theories overlap in most of the applications and that their joint theoretical study is of increasing interest. In this work we focus on the dynamical aspects of complex networks. We study global dynamical phenomena which emerge as a result of the interplay between network topology and single-node dynamics in systems of excitable elements.

In part I we consider theoretical settings of relatively small networks and investigate the effects of the network topology on the dynamical states of the system. We focus on the collective behavior of the nodes comprising the network, which is a global phenomena in contrast to the local coupling structure determined by the network topology. A suitable theoretical framework, emphasizing collective behavior in terms of synchronization, is a system of coupled phase oscillators. In section 1 we introduce the paradigm of phase oscillators and the concept of synchronization. In subsection 1.2 we discuss general constraints posed by the network topology on synchronous dynamical states and introduce the resulting flow-invariant submanifolds. Those constraints affect the dynamics of the system and lead to non-generic bifurcation scenarios reflecting the symmetry of the underlying graph. In particular, little is known about the evolution of attractors in the parameter spaces of such systems. To advance in this direction, we restrict our study to identical phase oscillators and focus on the repulsive coupling. The first condition ensures the emphasis of the network symmetry in the dynamics and the second one is motivated by the fact that the traditionally considered opposite, positive coupling, commonly favors the onset of global synchronization [8], while repulsive coupling is known to result in less trivial effects like clustering and hysteresis [104]. For this investigation, a convenient choice for the single-node dynamics is the Kuramoto and Shinomoto model of sinusoidally coupled "active rotators" [91]. In general, dynamical phenomena, such as transition from globally synchronous state to chaos or cluster synchronization, depend on the eigenvalues of the underlying adjacency matrix whose degeneracy determine the dimension of the center manifold at the bifurcation points. Plane hexagonal lattices with periodic boundary conditions provide a suitable theoretical framework for such investigations since the degeneracy of the eigenvalues of the adjacency matrix strongly depends on the size of the lattice while keeping the local, hexagonal, symmetries of the system fixed. In section 2 we study the dynamics of coupled "active rotators" on small hexagonal lattices with periodic boundary conditions. Besides, we are interested in determining generic conditions on the network

topology allowing the onset of collective dynamical phenomena. In such states, the dimensionality of the problem can be strongly reduced, in the sense of synchronous clustering, to the number of clusters, or even to a 3-dimensional submanifold according to the Watanabe-Strogatz reduction [111, 112, 78]. In sections 3 and 3.3 we investigate the constraints on the adjacency matrix of the underlying graphs enabling such phenomena. The systems of interest range from various ring topologies to k- partite graphs, represented in sections 4 and 5. Finally, in section 6 we present a generic analysis of bifurcations taking place on the submanifold associated with the reduced system.

In part II we tackle similar questions about the interplay between network topology and single-node dynamics, in more realistic, neuronal networks. There we investigate a global dynamical phenomenon, known as self-sustained activity, characterized by irregular firing of individual neurons and population oscillations with a broad frequency range in the absence of external stimulus [54]. The architecture of the cortical connections presents different features when viewed from different spatial scales. At microscopic scale cortical circuitry is highly recurrent with both excitatory and inhibitory neurons involved in many superposed positive and negative feedback loops, while at macroscopic, or systems level scale, the organization of cortical connections seems to be hierarchical and modular, with dense excitatory and inhibitory connectivity within modules and sparse excitatory connectivity between modules [15, 119, 80]. A number of studies, just to mention a few [108, 74, 110], consider effects of the structure of cortical connections on the existence of self-sustained cortical activity and on variability of the single-cell and population firing rates in that regime. Emphasizing the role of the topological structure of the cortical networks, most of these models do not take into account the possible joint role of the multiple firing patterns of the different types of neurons that comprise the cortex and do not capture the diversity of firing patterns of cortical neurons [63]. Given the variability of cortical firing patterns, the natural questions are: (i) how does the inclusion of neurons with varying intrinsic dynamics in a hierarchical and modular cortical network model affect the occurrence of SSA in the network? (ii) how does a combination of hierarchical and modular network topology with individual node dynamics influence the properties of the SSA patterns in the network? To address these questions, we use hierarchical and modular network model which combines excitatory and inhibitory neurons from the five cortical cell types described by the Izhikevich neuron models [62]. At the beginning of part II we show the connection between the Izhikevich neuron model and the phase oscillator model discussed in part I. In section 8 we introduce the models and methods underlying the numerical investigation and in section 9 we present the results from the numerical simulations. In sections 10 and 11 we analyze the system from dynamical point of view and discuss the results thereof in section 12.

Part I
Phase Dynamics on Small Networks with Nontrivial Local Topology

1 Phase Oscillators on Complex Networks

In the first part of this section we introduce briefly the paradigm of phase oscillator and the concept of synchronization. For more details we refer to [84]. In the second part of the section we consider synchronization on complex networks and based on [97, 50, 51, 35] we discuss general constraints posed by the network topology on synchronous dynamical states and introduce the resulting flow-invariant submanifolds.

1.1 Phase Oscillators

Repetitive phenomena are not uncommon in nature. The list of scientific articles studying repetitive phenomena in various disciplines is countless. They are observed in mechanical, optical and chemical systems as well as in astronomy, biology, climatology, geology and even economics and sociology.

In all those cases the system returns repeatedly to an earlier state after some time T. As dynamical systems with the appropriate state variables (say $(x_1, ..., x_N) = x$)

$$\frac{d}{dt}x(t) = f(x(t)) \tag{1}$$

such phenomena evolve through periodic trajectories in their state space: i.e. if $\bar{x}(t)$ denotes the periodic trajectory then, after a period T, $\bar{x}(t) = \bar{x}(t+T)$. Choosing an arbitrary initial point $\bar{x}_0$ on the periodic orbit any other point along the orbit can be characterized by the time φ since the last passing through $\bar{x}_0$. The variable φ is called the phase of the oscillation and after normalization by T or $T/2\pi$ it is bounded by 1 or 2π, respectively. The introduction of the phase variable enables the reduction of the N-dimensional system to a 1-dimensional system along the periodic trajectory rendering a much simpler dynamical model

$$\frac{d}{dt}\varphi = 1\,. \tag{2}$$

By that, there is a one-to-one correspondence between points on the periodic orbit $\bar{x}$ and the introduced phase variable φ: i.e. both $\bar{x} = \bar{x}\,(\varphi)$ and $\varphi = \varphi(\bar{x})$ are well defined. The intensity of oscillation is characterized by its amplitude.

Consider a small perturbation $p(x)$ of the original system (1) representing, for example, an interaction with the environment

$$\frac{d}{dt}x = f(x) + \epsilon p(x)\,. \tag{3}$$

Because of the perturbation the system will no longer evolve along the initial periodic orbit $\bar{x}(t)$. Nevertheless, if the perturbation is small ($\epsilon \ll 1$) and the periodic orbit

is stable (a limit cycle), the new trajectories of the perturbed system will remain in the vicinity of $\bar{x}$.[1] In the vicinity of $\bar{x}$ the amplitude of the perturbed periodic orbit remains approximately unchanged. This suggests that the dynamics of the perturbed system can still be described via a phase variable: all points along a trajectory, which starts at x_0, can be characterized by the time φ spent along that trajectory. Consider once again the unperturbed system (1). In the vicinity of the periodic orbit it defines a map

$$\Phi : \, x(t) \mapsto x(t+T) \tag{4}$$

such that all points along the periodic orbit $\bar{x}(t)$ are fixed points under the action of Φ: $\Phi(\bar{x}(t)) = \bar{x}(t+T) = \bar{x}(t)$. Since the limit cycle is attracting, under the action of Φ, each point $\bar{x}(t_0)$ on the limit cycle is also attracting and we can consider the set $I(\bar{x}(t_0))$ of all points in the vicinity of the limit cycle that are attracted to $\bar{x}(t_0)$. This set forms an $(N-1)$ dimensional hypersurface called an isochrone. Accordingly, the family of isochrones at different points $\bar{x}$ along the limit cycle can be parametrized by the phase: $I(\varphi)$. This allows us to define the phase not only for points along the limit cycle ($\varphi(\bar{x})$) but also in its vicinity $\varphi(x)$, whereby points belonging to the same isochrone have the same phase. The changes in the amplitude caused by the perturbation are changes along the isochrones. Observe that the isochrones are well defined, in the vicinity of the periodic orbit, also for unstable periodic orbits. In the case, instead of considering $\bar{x}(t_0)$ as a sink it is considered as a source for the set $I(\bar{x}(t_0))$.

The equation of motion (2) can be written for the extended phase $\varphi(x)$ as

$$\begin{aligned} \frac{d}{dt}\varphi(x) &= \sum_i \frac{\partial \varphi}{\partial x_i}\frac{dx_i}{dt} \\ &\overset{(1)}{=} \sum_i \frac{\partial \varphi}{\partial x_i} f_i(x) \\ &\overset{(2)}{=} 1 \end{aligned}$$

and for the perturbed system (3) this becomes

$$\begin{aligned} \frac{d}{dt}\varphi(x) &= \sum_i \frac{\partial \varphi(x)}{\partial x_i}\left(f_i(x) + \epsilon p_i(x)\right) \\ &= 1 + \epsilon \sum_i \frac{\partial \varphi(x)}{\partial x_i} p_i(x)\,. \end{aligned}$$

Assuming that the perturbation in (3) is small ($\epsilon \ll 1$), the deviations of the perturbed trajectory from the periodic orbit are also small

$$x = \bar{x} + \mathcal{O}(\epsilon)$$

[1] In the case of unstable periodic orbits, the trajectory still remains in the vicinity of $\bar{x}$ (because of continuity) for some time. This time interval depends on the magnitude of the perturbation and the instabilities.

and up to the first order in ϵ we have

$$\begin{aligned}\frac{d}{dt}\varphi(x) &= 1+\epsilon\sum_i \frac{\partial\varphi\left(\bar{x}(\varphi)\right)}{\partial x_i}p_i\left(\bar{x}(\varphi)\right)\\ &\equiv 1+\epsilon\Gamma(\varphi)\,. \end{aligned} \tag{5}$$

The last equation represents the (perturbed) original system as a phase oscillator.

In many cases the external force acting on the phase oscillator is caused by a mutual interaction with one or many other phase oscillators. Hence, we speak of (weakly) coupled phase oscillators. Each one of those phase oscillators might have its own frequency (this would be the case when the original systems (1) have different periods) and it is therefore mandatory to write (2) as

$$\frac{d}{dt}\varphi_i = \omega_i\,.$$

Furthermore, we can weaken the condition that the phase is a monotonically increasing function along the periodic orbit and write instead

$$\frac{d}{dt}\varphi_i = g_i(\varphi_i)\,.$$

In this case, equation (5) describing the dynamics of a system of N weakly coupled phase oscillators becomes

$$\frac{d}{dt}\varphi_i = g_i(\varphi_i)+\kappa\sum_{j=1}^{N}\Gamma_{ij}(\varphi_i,\varphi_j)\,. \tag{6}$$

Here, κ denotes the coupling strength. It is assumed to be small ("weakly coupled"), just as ϵ, in order to justify the approximations from above. Therefore, it is also usually normalized by the total number of oscillators to avoid inconveniences in the case $N\to\infty$. Γ_{ij} denotes the coupling function between oscillators i and j taking into account that different oscillators might couple differently. It is a periodic function and because of weak coupling and resonance conditions [84] it can be further approximated to its general form $\Gamma_{ij}(\varphi_j-\varphi_i)$.

1.2 Synchronization and Clustering on Networks

One of the main interests when investigating systems of coupled phase oscillators is the question of synchronization.

In a system of coupled phase oscillators (6) we say that oscillator k is *synchronized* with oscillator l iff

$$\varphi_k(t)=\varphi_l(t)\ \text{ for }\forall t\,. \tag{7}$$

Equivalently, we say that oscillators k and l belong to the same *cluster*. From this definition follows that a clustered (or synchronous) state should be flow-invariant: once in this state, always in this state. This means also that oscillators belonging to the same cluster have identical dynamical evolutions, hence, the clustered system

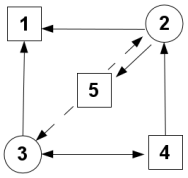

Figure 1: Five coupled phase oscillators. Nodes with the same internal dynamics are displayed by the identical shape and identical edges represent the same coupling functions.

evolves on a lower dimensional subspace, which according to (7) geometrically corresponds to a *polydiagonal* in the phase space. Even though every clustered state corresponds to a polydiagonal, the opposite is not necessarily true. If we choose the initial conditions at t_0 to lie, for example, on the polydiagonal $\varphi_m(t_0) = \varphi_n(t_0)$ it does not follow automatically from (6) that $\dot{\varphi}_m(t_0) = \dot{\varphi}_n(t_0)$; therefore, it might well be that $\varphi_m(t) \neq \varphi_n(t)$ at some later time $t > t_0$.

In a series of papers [97, 50, 51, 35] Golubitsky, Stewart and coauthors develop a powerful mathematical formalism, based on groupoid theory, which is applicable to generic "coupled cell systems" and enables the identification of flow-invariant polydiagonals corresponding to clustered states. In some parts of this work we apply the goupoid formalism directly or indirectly. In the rest of this section, without going into mathematical details, we outline some of the concepts, in a form suitable for networks of phase oscillators. We remark that, for the sake of simplification, some of those concepts, as presented here, might slightly differ from their original definitions. For detailed discussions, examples and generic proofs, see the original works [97, 50, 51, 35].

Let $\mathcal{C} = \{1, ..., N\}$ denote the set of all N oscillators. Let $I(k)$ be the *input set* of $k \in \mathcal{C}$: i.e. the set of all oscillators with nontrivial coupling towards k

$$I(k) = \{m \in \mathcal{C} \,|\, \exists \varphi_m : \Gamma_{km}(\varphi_k, \varphi_m) \neq 0\} \ .$$

We say that two oscillators k, $l \in \mathcal{C}$ are *input equivalent* $k \sim_I l$ if and only if there exists a bijection

$$\begin{aligned} \beta : I(k) &\rightarrow I(l) \\ m &\mapsto \beta(m) \end{aligned}$$

such that $g_k(x) = g_l(x)$ and, $\Gamma_{k,m}(x, y) = \Gamma_{l,\beta(m)}(x, y)$ and $g_m(x) = g_{\beta(m)}(x)$ $\forall m \in I(k)$. I.e., two oscillators are input equivalent if they have the same internal dynamics and receive input via the same set of coupling functions from the same type of oscillators. Figure 1 gives an example of five coupled phase oscillators where identical nodes (displayed by the same shape) represent identical internal dynamics and identical edges represent identical coupling functions. Here, the input set of oscillator 4 is $I(4) = \{3\}$ and of oscillator 5 is $I(5) = \{2\}$. Because oscillators 2 and 3 have the same internal dynamics and couple, respectively, via the same coupling coupling functions towards oscillators 5 and 4, there is a bijection β such that $3 = \beta(2)$; therefore, oscillators 4 and 5 are input equivalent. The same is true for oscillators 3 and 2: $2 \sim_I 3$.

Let us denote the set of all input isomorphisms between oscillators k and l in $\mathcal{C}$ by

$$B(k,l) = \{(\beta, k, l,)|\beta \text{ is an input isomorphism from } k\text{to } l\} \ .$$

In particular $B(k,l) \neq \emptyset \Leftrightarrow k \sim_I l$. Observe that the sets $B(k,l)$, for all k, $l \in \mathcal{C}$ together, have a group similar structure: for example, if $\beta : I(k) \to I(l)$ and $\beta^{'} : I(l) \to I(m)$, then $\beta \circ \beta^{'} : I(k) \to I(m)$. However, they do not form a group acting on $\mathcal{C}$ because, in general, not all elements in $\mathcal{C}$ are input equivalent, i.e. there would be elements for which the "group action" would not be defined. The set

$$\mathcal{B} = \underset{c,d \in \mathcal{C}}{\cup} B(c,d) \tag{8}$$

is called the *(symmetry) groupoid of the network*. A groupoid is an algebraic structure similar to a group, except that the product of two groupoid elements might not be defined [56].

If we consider $k \sim_I l$ and choose the initial conditions at t_0 to lie, for example, on the polydiagonal $\varphi_k(t_0) = \varphi_l(t_0)$ and $\varphi_m(t_0) = \varphi_{\beta(n)}(t_0)$ $\forall m \in I(k)$ it does follow from (6) that $\dot{\varphi}_k(t_0) = \dot{\varphi}_l(t_0)$. Nevertheless, this is still not sufficient to assure $\varphi_k(t) = \varphi_l(t)$, at some later time t, since the equivalence relation $k \sim_I l$ does not guarantee that $\dot{\varphi}_m(t_0) = \dot{\varphi}_{\beta(n)}(t_0)$ $\forall m \in I(k)$. Therefore, we need an equivalence relation stronger than $\sim_I$. Let $\bowtie$ be an equivalence relation on the set $\mathcal{C}$ and let $\Delta_{\bowtie}$ represent the corresponding polydiagonal

$$\Delta_{\bowtie} = \{\overrightarrow{\varphi} \mid k \bowtie l \Rightarrow \varphi_k = \varphi_l\} \ . \tag{9}$$

We call $\bowtie$ a *balanced equivalence relation* if for every k, $l \in \mathcal{C}$ with $k \bowtie l$ and $k \neq l$

$$k \bowtie l \Longrightarrow k \sim_I l \ \wedge \ \exists \beta_{kl} \in B(k,l) : \ m \bowtie \beta_{kl}(m) \, \forall m \in I(k) \ . \tag{10}$$

From the main theorem of the groupoid formalism (Theorem 7.2. [51]) follows that a polydiagonal is flow-invariant if it corresponds to a balanced equivalent relation. Here, we present an equivalent proof of this statement.

Theorem 1 In a system of coupled phase oscillators (6) a synchronous state $\vec{\varphi}(t_0) \in \Delta_{\bowtie}$ is flow-invariant if the polydiagonal $\Delta_{\bowtie}$ (9) corresponds to balanced equivalence relation (10).

Proof: The temporal evolution of (6), for the i^{th} component of the vector field, is given by the Taylor series

$$\varphi_i(t) \ = \ \varphi_i(0) + t\dot{\varphi}_i(0) + \frac{t^2}{2}\ddot{\varphi}_i(0) + \frac{t^3}{3!}\dddot{\varphi}_i(0) + ...$$

Let $\Delta_{\bowtie}$ correspond to an equivalence relation $\bowtie$ (9). Consider $k \bowtie l$. The polydiagonal $\Delta_{\bowtie}$ is flow-invariant if the Taylor series for $\varphi_k(t)$ and $\varphi_l(t)$ are (component wise) equal for any t. The first term ($\mathcal{O}(t^0)$) in the Taylor series corresponds to the initial condition $\varphi_k(0) = \varphi_l(0)$ and is guaranteed. The second term ($\mathcal{O}(t)$) requires that $\dot{\varphi}_k(0) = \dot{\varphi}_l(0)$ which is guaranteed for $k \sim_I l$ and $m \bowtie \beta_{kl}(m) = n$, $\forall m \in I(k)$. The third term ($\mathcal{O}(t^2)$) requires additionally that $\dot{\varphi}_m(0) = \dot{\varphi}_n(0)$ is guaranteed for $m \sim_I n$ and $i \bowtie \beta_{mn}(i)$ $\forall i \in I(m)$ a.s.o. By induction follows that $\Delta_{\bowtie}$ is flow-invariant if $\bowtie$ is a balanced equivalence relation (10). $\square$

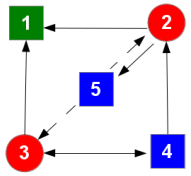

Figure 2: Synchrony state of the five coupled phase oscillators from figure 1.

The represented equivalence relations can be visualized by introducing a *color*. Let $\vec{\varphi}(t^{'})$ be the state of a network of coupled phase oscillators (6) at time $t^{'}$. We say, that two oscillators k and l have the same *color* if $k \sim_I l$ and $\varphi_k(t^{'}) = \varphi_l(t^{'})$. With the concept of color, the theorem states that a synchronized state is flow-invariant if any two oscillators of the same color receive input from the same set of colors. In figure 1 oscillators 2 and 3, as well as, 4 and 5 are input equivalent, hence, only they can have the same color. From figure 2 we see that the polydiagonal

$$\Delta = \{\varphi_1, \varphi_2 = \varphi_3, \varphi_4 = \varphi_5\} \ .$$

is flow-invariant because both 2 and 3 receive the same input from a blue oscillator and both 4 and 5 receive input from a red one. Observe also that the dimension of the polydiagonal corresponds to the number of clusters. For further simple examples see section 3.3.

Throughout this work we consider finite networks of identical coupled phase oscillators (6) with identical coupling functions and nontrivial coupling topology:

$$\omega_i = \omega_j \ \text{ for } \forall i, j$$

or in the more general case

$$g_i(\varphi) = g_j(\varphi) \ \text{ for } \forall i, j$$

and

$$\Gamma_{ij}(\varphi_j - \varphi_i) = C_{ij}\Gamma(\varphi_j - \varphi_i) \, .$$

The $N \times N$ matrix C denotes the coupling topology and is defined as

$$C_{ij} = \begin{cases} 1 & \text{if } j \in I(i) \\ 0 & \text{otherwise} \end{cases} \ . \tag{11}$$

The equations of motion (6), describing the system of coupled phase oscillators, become

$$\frac{d}{dt}\varphi_i = g(\varphi_i) + \kappa \sum_{j=1}^{N} C_{ij}\Gamma(\varphi_j - \varphi_i) \, . \tag{12}$$

Observe that for a regular network C any two oscillators k, $l \in \mathcal{C}$ are input equivalent $k \sim_I l$ and the groupoid (8) becomes a group. Note also that the adjacency matrix C of the network is not unambiguous because of isomorphisms. We can choose any other adjacency matrix A connected to C via a permutation $P \in S_N$

$$A = PCP^{-1}.$$

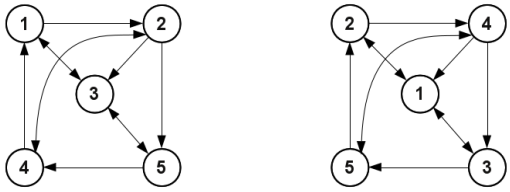

Figure 3: Isomorphic adjacency matrices. On the left the adjacency matrix C and on the right $A = PCP^{-1}$ (see text; equation (14)).

Remark that this corresponds to a trivial transformation: a reordering of the coupling matrix, or equivalently, to a renumbering of the cells. The dynamics of the system with respect to the new, reordered, adjacency matrix is given by

$$\frac{d}{dt}\widetilde{\varphi}_i = g(\widetilde{\varphi}_i) + \kappa \sum_{j=1}^{N} A_{ij}\Gamma(\widetilde{\varphi}_j - \widetilde{\varphi}_i) \tag{13}$$

and is identical to (12), with different numeration of the cells: $\vec{\widetilde{\varphi}} = P\vec{\varphi}$. Although at this point it might be convenient to think of the permutation transformation as a mere renumbering of the cells, it is important for later considerations to point out that it might be considered as a map from the phase space of (12) to the phase space of (13). In the latter case, all trajectories of (12) are trivially mapped by index permutation to the trajectories of (13).

The permutation invariance allows us to choose any possible numeration of the cells. Figure 3 gives an example of a 5-cell network with two isomorphic adjacency matrices: C (on the left), A (on the right)

$$C = \begin{pmatrix} 0 & 0 & 1 & 1 & 0 \\ 1 & 0 & 0 & 1 & 0 \\ 1 & 1 & 0 & 0 & 1 \\ 0 & 1 & 0 & 0 & 1 \\ 0 & 1 & 1 & 0 & 0 \end{pmatrix}, \; A = \begin{pmatrix} 0 & 1 & 1 & 1 & 0 \\ 1 & 0 & 0 & 0 & 1 \\ 1 & 0 & 0 & 1 & 0 \\ 0 & 1 & 0 & 0 & 1 \\ 0 & 0 & 1 & 1 & 0 \end{pmatrix} \tag{14}$$

and the corresponding permutation matrix P

$$P = \begin{pmatrix} 0 & 0 & 1 & 0 & 0 \\ 1 & 0 & 0 & 0 & 0 \\ 0 & 0 & 0 & 0 & 1 \\ 0 & 1 & 0 & 0 & 0 \\ 0 & 0 & 0 & 1 & 0 \end{pmatrix}.$$

Let $\vec{\varphi}^*(t)$ be a solution corresponding to a balanced pattern of synchrony $\bowtie$ with $\dim\Delta_{\bowtie} = c$ clusters. In this state the indices of the cells can be ordered, according to the cluster they belong to, into c equivalence classes $\chi_\delta = [i]$ ($\delta = 1, ..., c$) with $[i] = \{j \in \mathcal{C} \,|\, i \bowtie j \Leftrightarrow \varphi_i(t) = \varphi_j(t)\, \forall t\}$. Let $n_\alpha = |\chi_\alpha|$ denote the number of elements belonging to the same cluster and let the clusters be numerated such that $n_1 \leq n_2 \leq ... \leq n_c$. Given a balanced pattern of synchrony, it is always

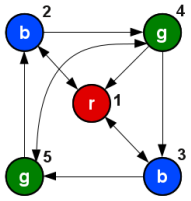

Figure 4: A balanced synchronous state with a corresponding adjacency matrix identical to the one on the right in figure 3. The numeration outside of the cells corresponds to the indexing of the cells and the numeration inside corresponds to the indexing of the clusters.

possible, as argued above, to find a corresponding reordered adjacency matrix A with numeration of the cells such that

$$\chi_\delta \quad = \quad \{n_{\delta-1}+1, ..., n_\delta\}$$

This means, for example, that according to this reordered adjacency matrix A cells indexed by 1 to n_1 belong to cluster 1, those indexed by n_1+1 to n_2 belong to cluster 2, or in general, cells indexed by $n_{\delta-1}+1$ to n_δ belong to cluster δ

$$\begin{aligned} \widetilde{\varphi}_i(t) = \widetilde{\varphi}_j(t) \quad &\Longleftrightarrow \quad i \bowtie j \\ &\Longleftrightarrow \quad n_{\delta-1} < i, j \leq n_\delta \end{aligned} \tag{15}$$

According to Theorem 1 a pattern of synchrony is balanced if each cell that belongs to a given cluster, say cluster δ, receives the same input from any cluster ϵ. Regarding the structure of the reordered matrix A, this assures that it is always a block matrix

$$A = \begin{pmatrix} \sigma_{\alpha\alpha} & \sigma_{\alpha\beta} & \cdots & \sigma_{\alpha c} \\ \sigma_{\beta\alpha} & \sigma_{\beta\beta} & \cdots & \sigma_{\beta c} \\ \vdots & \vdots & \ddots & \vdots \\ \sigma_{c\alpha} & \sigma_{c\beta} & \cdots & \sigma_{cc} \end{pmatrix}. \tag{16}$$

Here, $\sigma_{\delta\epsilon}$ is a $n_\delta \times n_\epsilon$ rectangular matrix describing the incoming connections from cluster ϵ towards cluster δ. From Theorem 1 it follows directly that

$$\sum_{j=1}^{n_\epsilon} (\sigma_{\delta\epsilon})_{ij} = \iota_{\delta\epsilon} \ \forall i \in [1, ..., n_\delta] \tag{17}$$

where $\iota_{\delta\epsilon}$ denotes the corresponding number of inputs.

Figure 4 gives an example of a balanced pattern of synchrony with 3 clusters on the 5-cell network from figure 3. Here, the reordered adjacency matrix A is identical to the one in equation (14). In the chosen cluster indexing r, b, g (for red, blue and green respectively), the clusters comprise

$$\chi_r = \{1\}, \ \chi_b = \{2, 3\}, \ \chi_g = \{4, 5\} \tag{18}$$

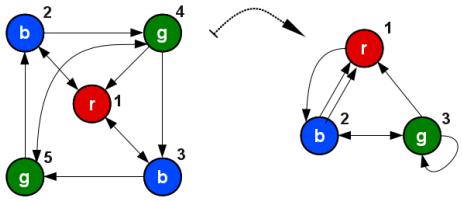

Figure 5: Reduction of a 5-cell system to a 3-cell system for balanced pattern of synchrony.

and therefore

$$A = \begin{pmatrix} \sigma_{rr} & \sigma_{rb} & \sigma_{rg} \\ \sigma_{br} & \sigma_{bb} & \sigma_{bg} \\ \sigma_{gr} & \sigma_{gb} & \sigma_{gg} \end{pmatrix} \tag{19}$$

$$= \begin{pmatrix} 0 & 1 & 1 & 1 & 0 \\ 1 & 0 & 0 & 0 & 1 \\ 1 & 0 & 0 & 1 & 0 \\ 0 & 1 & 0 & 0 & 1 \\ 0 & 0 & 1 & 1 & 0 \end{pmatrix}$$

For example, the matrix

$$\sigma_{rb} = \begin{pmatrix} 1 & 1 \end{pmatrix}$$

describes the coupling from the blue cluster towards the red one. The matrix

$$\sigma_{bg} = \begin{pmatrix} 0 & 1 \\ 1 & 0 \end{pmatrix}$$

describes the coupling from the green towards the blue cluster and the matrix

$$\sigma_{gg} = \begin{pmatrix} 0 & 1 \\ 1 & 0 \end{pmatrix}$$

describes the coupling within the green cluster. Condition (17) posed on the submatrices becomes also clear in the example. Considering σ_{bg}, for instance, it can be seen that (17) is fulfilled, such that each cell from the blue cluster receives one input from the green cluster. If one of the blue cells would receive input from two red ones and the other, only from one (i.e. if (17) is violated), the pattern of synchrony wouldn't be balanced according to Theorem 1. It is important to remark that the reordering of the adjacency matrix is only meaningful when considering a specific, balanced, pattern of synchrony.

Another very important concept is the cluster reduction. The pattern of synchrony from figure 4 can be reduced to a 3-cell system as shown in figure 5. The number of arrows in the reduced system (on the right) indicates the number of inputs

between cells of different clusters in the initial system (on the left): as described by $\iota_{\delta\epsilon}$ in (17). Therefore, we can write a generalized adjacency matrix for the reduced system

$$\begin{aligned} R &= \begin{pmatrix} \iota_{rr} & \iota_{rb} & \iota_{rg} \\ \iota_{br} & \iota_{bb} & \iota_{bg} \\ \iota_{gr} & \iota_{gb} & \iota_{gg} \end{pmatrix} \\ &= \begin{pmatrix} 0 & 2 & 1 \\ 1 & 0 & 1 \\ 0 & 1 & 1 \end{pmatrix}. \end{aligned} \tag{20}$$

A reduced adjacency matrix describes the coupling topology of the system on the $\Delta_{\bowtie}$ polydiagonal where the N-dimensional system (12) becomes $\dim\Delta_{\bowtie} = c$-dimensional

$$\frac{d}{dt}\varphi_i = g(\varphi_i) + \kappa \sum_{j=1}^{c} R_{ij}\Gamma(\varphi_j - \varphi_i)\,. \tag{21}$$

For further examples see section 3.2.

In the example here, the 5-dimensional system is reduced, on the polydiagonal corresponding to (18), to a system of three globally coupled phase oscillators. We can easily think of another network $\widetilde{A}$, consisting of five cells, and a pattern of synchrony reducible to the same 3-cell system with adjacency matrix R as in (20). An example of such a system is given on the right of figure 6. The corresponding reordered adjacency matrix takes the form

$$\widetilde{A} = \begin{pmatrix} \widetilde{\sigma}_{rr} & \widetilde{\sigma}_{rb} & \widetilde{\sigma}_{rg} \\ \widetilde{\sigma}_{br} & \widetilde{\sigma}_{bb} & \widetilde{\sigma}_{bg} \\ \widetilde{\sigma}_{gr} & \widetilde{\sigma}_{gb} & \widetilde{\sigma}_{gg} \end{pmatrix}.$$

The only difference between the adjacency matrix A in (19) of the "old" network (on the left) and the adjacency matrix $\widetilde{A}$ of the "new" network (on the right) is in the submatrix

$$\widetilde{\sigma}_{bg} = \begin{pmatrix} 1 & 0 \\ 0 & 1 \end{pmatrix}$$

describing the coupling from the green cluster towards the blue one. It is important to remark that A and $\widetilde{A}$ share the same submatrix structure in the sense that $\widetilde{\sigma}_{\delta\epsilon}$ is a $n_\delta \times n_\epsilon$ matrix as is $\sigma_{\delta\epsilon}$ $(\forall\delta,\epsilon)$ and

$$\sum_{j=1}^{n_\epsilon}(\widetilde{\sigma}_{\delta\epsilon})_{ij} = \sum_{j=1}^{n_\epsilon}(\sigma_{\delta\epsilon})_{ij} = \iota_{\delta\epsilon}\ \forall i \in [1,...,n_\delta] \tag{22}$$

This is, in general, a necessary and sufficient condition for two patterns of synchrony (subject to equations of motion as in (12)) to be reducible to the same network. Therefore, on the reduced phase space, for the given patterns of synchrony, both systems exhibit the same dynamics. As we have argued above the reordering of the adjacency matrix via a permutation can be considered as a map from one phase space to another. Choosing the same reordered form for the adjacency matrices A

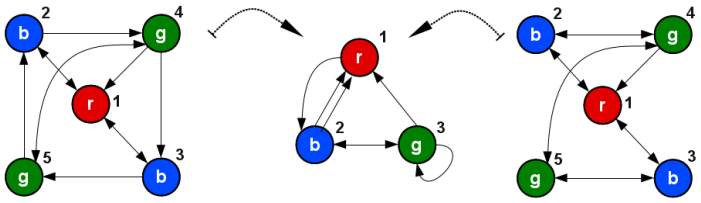

Figure 6: Two non isomorphic 5-cell systems (on the right and left) reducible to the same 3-cell system (in the middle).

and $\widetilde{A}$ of the two systems assures that the trajectories of the synchronous solution will coincide. This can be seen directly from condition (15)

$$\varphi_i^{A*}(t) = \varphi_i^{\widetilde{A}*}(t) := \varphi_i^*(t)$$

However, outside of the reduced (synchronous) phase space the trajectories of A and $\widetilde{A}$ will in general be different. Therefore, there is no reason to expect (and for this example, in general, it is indeed not the case) that the stability properties of those synchrony states are identical on the two networks. Figure 7 represents schematically this idea.

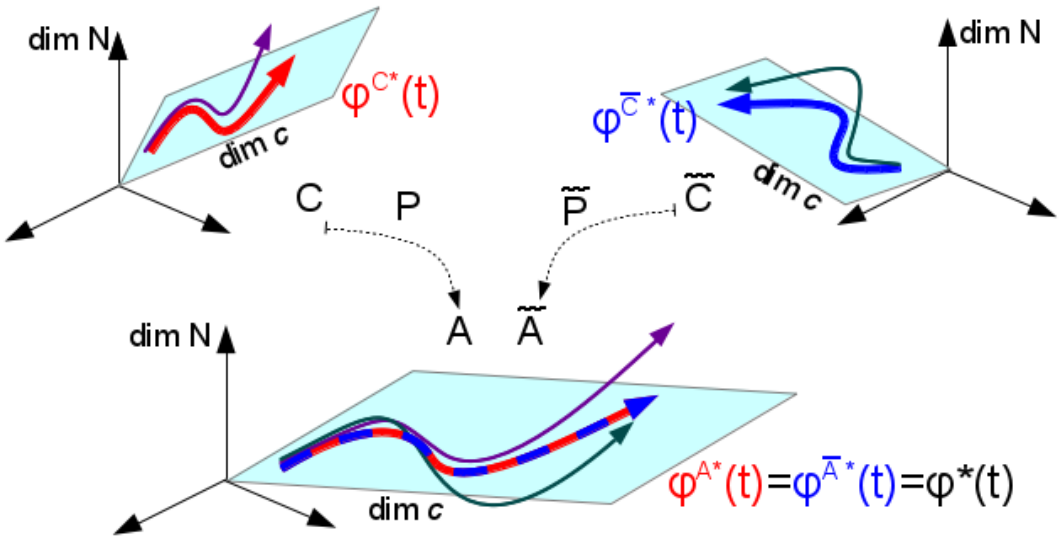

Figure 7: The figure represents two N-dimensional networks C and $\widetilde{C}$ with identical dynamics on the corresponding synchronous c-dimensional subspaces. The permutation matrices P, and $\widetilde{P}$, capture the synchronous structure in the reordered A and $\widetilde{A}$, respectively, and map the initial phase spaces to a joint phase space where the synchronous subspaces coincide.

2 Phase Dynamics on Small Hexagonal Lattices with Repulsive Coupling

In this section we study a system of sinusoidally coupled "active rotators" [91] on hexagonal lattices. As we will see below, for low eigenfrequency $\omega < 1$, each active rotator possesses a stable and an unstable steady states. For a sufficiently large perturbation caused, for example, by the interaction with its neighbors the transient of the trajectory back to the stable state is non-monotonic, imitating a spike. Therefore, the model of "active rotators" describes an excitable system. We restrict the investigation to relatively small lattice sizes and periodic boundary conditions. This restriction is motivated by the fact that for a finite number of clusters on infinitely large regular plane lattices with nearest neighbor coupling, such as the hexagonal lattice, the patterns of synchrony are periodic in space with finitely large repetitive motives [4]. This means that by investigating small latices with periodic boundary conditions we also capture patterns of synchrony for larger lattices. However, as we will see, the stability properties of the otherwise identical patterns, and therefore their realization, strongly depend on the lattice size.

2.1 General Characteristics

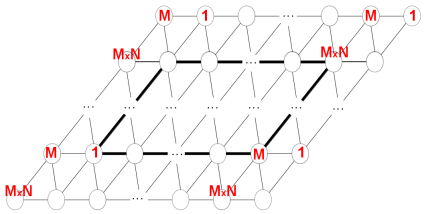

Figure 8: Hexagonal lattice with periodic boundary conditions of size $M \times N$

The Kuramoto and Shinomoto model of sinusoidally coupled "active rotators" [91] is described by the following dynamical system:

$$\dot{\phi}_i = \omega - b\sin\phi_i + \frac{\kappa}{6}\sum_j A_{ij}\sin(\phi_j - \phi_i), \quad i = 1, ..., MN\,. \tag{23}$$

Here, κ denotes the coupling strength normalized over 6 (the number of neighbors for the hexagonal lattice) and A_{ij} is the adjacency matrix describing the hexagonal topology, with $A_{ij} = 1$ if there is a link between nodes i and j, otherwise $A_{ij} = 0$ and $A_{ii} = 0$. The constant $b \neq 0$, denoting the level of excitability, can always be chosen to be positive, by otherwise shifting the phases of all oscillators by π. Furthermore, without loss of generality, after rescaling the time, the natural frequencies and the coupling strength, b can be set to 1. The natural frequencies of the identical oscillators are denoted by ω. At large values of $|\omega| > |b| + |\kappa|$ the right hand side of equation (23) does not change sign and the system performs monotonic oscillations. Being interested in collective dynamical phenomena we chose $|\omega| < 1$, see next paragraph. Figure 8 shows schematically a hexagonal lattice with periodic

boundary conditions of spatial periods M and N. The total number of elements is respectively MN and the resulting phase space is the $(2\pi)^{MN}$- torus, T_{MN}.

We start the investigation by considering the decoupled system, i.e. $\kappa = 0$. In this case the equations of motion (23) are reduced to

$$\dot{\phi}_i = \omega - \sin\phi_i\,, \quad i = 1, ..., MN\,. \tag{24}$$

It can be seen that for $|\omega| < 1$ each oscillator has 2 steady states. Considering the sign of the eigenvalue λ of the Jacobi matrix of (24), the stable steady state is at

$$\phi_s^{(0)} = \arcsin\omega \Longrightarrow \lambda = -\sqrt{1-\omega^2}$$

and the unstable one at

$$\phi_u^{(0)} = \pi - \arcsin\omega \Longrightarrow \lambda = \sqrt{1-\omega^2},$$

whereby for $|\omega| > 1$ no stationary states are possible. Considering the whole MN-dimensional system this results in a total of 2^{MN} steady states. Each steady state corresponds to different combination where individual oscillators are either at $\phi_s^{(0)}$ or at $\phi_u^{(0)}$. Among these, there are only two completely synchronous, 1-cluster solutions: a totally stable solution with $\phi_i = \phi_s^{(0)}$ for $\forall i$ and a totally unstable one with $\phi_i = \phi_u^{(0)}$ for $\forall i$. The remaining $2^{MN} - 2$ steady states are saddle points and correspond to 2-cluster solutions, comprising one stable and one unstable clusters with oscillators locked at $\phi_s^{(0)}$ and $\phi_u^{(0)}$ respectively. For the 2-cluster solutions, a perturbation of a single oscillator belonging to the unstable cluster will urge this oscillator towards the stable cluster revealing a heteroclinic connection between the initial 2-cluster state and the "new" 2-cluster state in which the perturbed oscillator belongs to the initially stable cluster and not to the initially unstable one. The vast number of saddle points in the phase space provides a network of heteroclinic connections. The dynamical flow along those heteroclinics is such that stable clusters can only grow in size and unstable clusters decrease. In contrast to the two 1-cluster solutions, from above, which exist for all coupling strengths, albeit not with the same stability properties as in the decoupled case, for $\kappa \neq 0$ most of the 2-cluster solutions are disintegrated and transformed to 3- or more cluster solutions. This is because for $\kappa \neq 0$ the nontrivial coupling topology, determined by A, restricts the invariant subspaces as discussed in section 1.2. It is, however, important to remark that all $2^{MN} - 2$ saddle states, being hyperbolic (none of the eigenvalues is at zero for $\kappa = 0$), are preserved, along with their stability properties, also for sufficiently small coupling strengths. At larger negative coupling strengths, the bifurcations along the heteroclinics connecting those saddles ensure interesting dynamical phenomena. A complete investigation of all those bifurcations in a system with symmetries, like (23), requires the application of equivariant bifurcation theory [47, 48] which studies the correlation between bifurcating branches and the underlying symmetry breaking. However, most of the bifurcations that take place lead to unstable solutions and have little to no effect on the observable dynamics. Therefore, we concentrate only on those bifurcation branches directly involved in dynamical changes. At the end of section 2.2, in appendix 2.2, we discuss in detail the connection between the flow-invariant synchronous states and the underlying symmetry breaking for the smallest possible hexagonal lattice 3×3.

Before proceeding with the investigation of the relevant bifurcation scenarios for the coupled system, we can beforehand say what we can not expect. Equation (23) can be rewritten in a purely gradient form

$$\frac{d}{dt}\phi_i = -\frac{\partial}{\partial \phi_i} V_i$$

with the corresponding potential function (or Liapunov function) given by

$$V_i = -\omega\phi_i - b\cos\phi_i - \frac{\kappa}{6}\sum_j A_{ij}\cos(\phi_j - \phi_i)\,.$$

Because of the existence of a Liapunov function no Hopf bifurcations may appear in the system [53]. This means that only periodic orbits which result from the periodicity of the toroidal phase space can be observed: i.e. at least one of the oscillators should perform full-scale rotations with amplitude not smaller than 2π. Given that, in the following investigation of the coupled system the only bifurcations which may be expected to lead to periodic orbits are local saddle-node, pitchfork and/or transcritical bifurcations, or global homoclinic and/or heteroclinic bifurcations. Indeed, we observe all these bifurcations in the investigated system, something quite remarkable for a single dynamical model.

As usual, we start the bifurcation analysis by considering the Jacobi matrix for the coupled system (23) given by

$$J_{ik} = \frac{\partial \dot{\phi}_i}{\partial \phi_k} = \begin{cases} -\cos\phi_i - \frac{\kappa}{6}\sum_j A_{kj} & i = k \\ \frac{\kappa}{6} A_{ik}\cos(\phi_k - \phi_i) & i \neq k \end{cases}.$$

From above we know that the $\phi_s^{(0)}$ 1-cluster solution is the only stable state for sufficiently small coupling strengths $|\kappa| \approx 0$. At this equilibrium the Jacobian takes the form

$$J = \frac{\kappa}{6}A - (\sqrt{1-\omega^2} + \kappa)\mathbb{I}$$

where $\mathbb{I}$ denotes the identity matrix of size MN. The corresponding eigenvalues λ_i can be calculated after diagonalization and are given by

$$\begin{aligned} \lambda_i &= \frac{\kappa}{6}\lambda_i^A - (\sqrt{1-\omega^2} + \kappa) \\ &= -\kappa(1 - \frac{\lambda_i^A}{6}) - \sqrt{1-\omega^2}\,, \end{aligned} \tag{25}$$

where λ_i^A denote the eigenvalues of the hexagonal adjacency matrix. From graph theory [20] it is known that for any connected regular graph the maximal eigenvalue of the graph equals the degree of the graph. Accordingly, for the hexagonal lattice of any size the maximal eigenvalue of the graph is $\lambda_{max}^A = 6$. From (25) follows that for positive coupling strength $\kappa \geq 0$ the $\phi_s^{(0)}$ synchronous 1-cluster solution remains stable. For negative coupling strength $\kappa < 0$ the stability properties are governed by the minimal eigenvalue λ_{min}^A. At a critical value of the coupling strength

$$\kappa_{crit} = -\frac{\sqrt{1-\omega^2}}{1 - \lambda_{min}^A/6} \tag{26}$$

the considered 1-cluster solution loses stability in a symmetry breaking bifurcation. At the bifurcation point the dimension of the center manifold is given by the number of eigenvalues crossing zero and corresponds to the multiplicity of λ^A_{min}. For the hexagonal lattice this multiplicity depends on the lattice size and it is for this reason that the observed dynamical phenomena for coupling strengths below κ_{crit} depend on the size of the hexagonal lattice. Numerical computations show the following dependence of the multiplicity $d(M,N)$ of λ^A_{min} on the lattice size:

$$d(M,N) = \begin{cases} 9 & \text{for } M = N = 4 \\ 6 & \text{for } M = N \neq 4 \text{ and } M \neq 3k \\ 4 & \text{for } M = kM \text{ with } k > 1 \text{ and } M \neq 3 \\ 2 & \text{otherwise} \end{cases} \tag{27}$$

with $k \in \mathbb{N}$. In the rest of this section we consider different cases for the multiplicity. We begin, in the next subsection 2.2, with the 3×3 lattice. It is the smallest possible hexagonal lattice and its multiplicity $d = 2$ can be seen as an exception since it is the only square lattice with this property. In subsection 2.3 we consider the 4×3, 5×3 and 5×4 lattices as representatives of multiplicity $d(M,N) = 2$. There, we will see that the observed dynamical phenomena are similar, despite the different lattice sizes. The case of $d(M,N) = 4$ was also investigated within the 4×12 lattice with results comparable to those from the 4×3 and partially the 4×4 hexagonal latices. Those results are not presented separately. The 4×4 hexagonal lattice is a special case both from graph theoretical and dynamical point of view and is considered in subsection 2.4.

For the numerical studies for all lattice sizes the natural frequency was set to $\omega = 0.7$ and the coupling strength κ was varied towards strongly negative values starting from values slightly above κ_{crit} (to detect possible hysteresis with the 1-cluster solution). The investigation of the attractors in the phase space was performed by choosing for each coupling strength a set of not less than 2×10^4 initial conditions from a homogeneous random distribution on the $(2\pi)^{MN}$- torus. Below κ_{crit} no steady states were observed: Depending on the cluster size and especially on the multiplicity of λ^A_{min} the dynamics was either periodic, quasiperiodic or chaotic.

As we will see in the following sections, at κ_{crit} multiple saddle states collide simultaneously with the fix point of the synchronous 1-cluster solution. Each of the saddles corresponds to a clustered state. On the corresponding polydiagonal of the (clustered) reduced system such saddle collides with the fix point of the synchronous 1-cluster solution either in a pitchfork or in a transcritical bifurcation. Taking into account the high number of saddle states participating in the bifurcation, by abusing the conventional terminology we say that the synchronous 1-cluster solution loses stability at κ_{crit} in degenerate pitchfork, respectively, degenerate transcritical bifurcation. In section 6 we investigate in detail those pitchfork and transcritical bifurcations.

2.2 The 3×3 Hexagonal Lattice

The 3×3 hexagonal lattice is the smallest possible hexagonal lattice with periodic boundary conditions, since all smaller lattices result in globally coupled systems. In

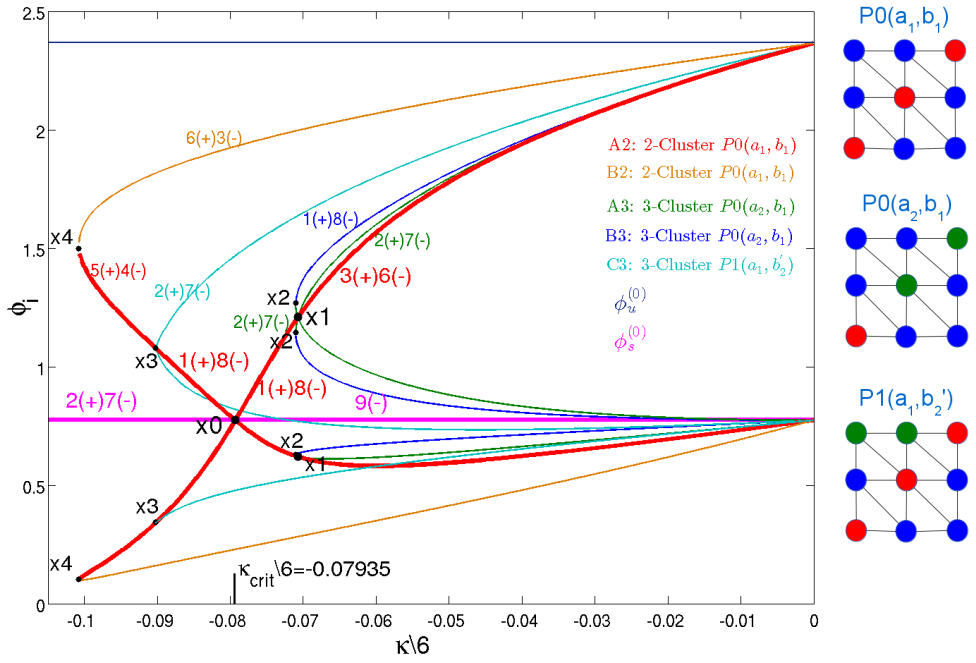

Figure 9: Bifurcation diagram for steady states on the 3×3 hexagonal lattice. The points $X0$ to $X4$ show five bifurcations taking place at different κ values. The number of positive $(+)$ and negative $(-)$ eigenvalues is indicated next to the corresponding branch. For the characterization of the synchronous states $P..(a.., b..)$, see appendix 2.2. *The color-coding representing the synchrony patterns on the hexagonal lattices is not connected to the color-coding representing the different bifurcation branches.*

this case the number of oscillators is 9 and each unit is coupled to all but 2 of the remaining units.

As discussed above, for $\kappa \neq 0$ most of the 2-cluster solutions, present at $\kappa = 0$, are disintegrated and transformed to 3- or more clusters. In appendix 2.2, based on the groupoid formalism presented in section 1.2, we investigate the balanced polydiagonals corresponding to flow-invariant synchronous states and the underlying symmetry breaking. An extended bifurcation analysis of all $2^{MN} - 2$ steady states for $\kappa \leq 0$ reveals, however, that only few synchronous states are directly involved in bifurcations leading to stable states. All the rest remain unstable and therefore have little to no effect on the observable dynamics.

Figure 9 shows the bifurcation diagram for synchronous steady states directly involved in observable dynamical changes for $\kappa < 0$. The patterns of synchrony on the right of the diagram represent the corresponding placement of the synchronous oscillators on the lattice. Remark that the synchronous states are represented up to symmetry-transformations: for example, because of the periodicity of the hexagonal lattice, there are three symmetric synchronous states $P0(a_1, b_1)$– $\{A2_1, A2_2, A2_3\}$– as shown in figure 10A. For $\kappa > \kappa_{crit}$ all investigated initial conditions end up at the stable synchronous 1-cluster solution $\phi_s^{(0)}$. At κ_{crit} this solution loses stability in a degenerate transcritical bifurcation, indicated by the point $X0$ in figure 9. According to (26) and (27) the center manifold at κ_{crit} is 2-dimensional, corresponding to the

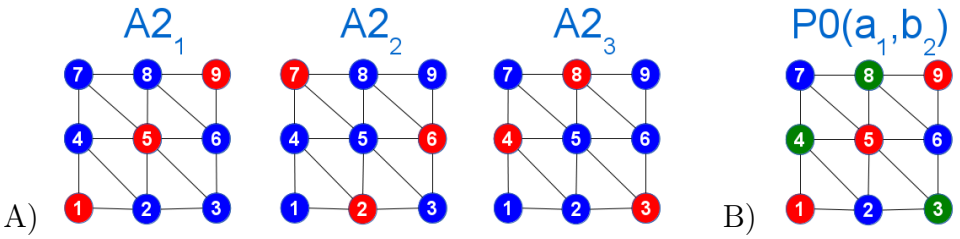

Figure 10: A) The three symmetry related cluster states $A2_i$ of the $P0(a_1, b_1)$ synchrony pattern. B) The $P0(a_1, b_2)$ pattern of synchrony. For the characterization of the synchronous states $P..(a.., b..)$, see appendix 2.2.

multiplicity of λ^A_{min}. Each of the three synchronous states $A2$ involved in the transcritical bifurcation at κ_{crit} originates, respectively, from a saddle at $\kappa = 0$ with three positive and six negative eigenvalues. Such saddle corresponds to a 2-cluster state with three oscillators comprising the unstable cluster and six oscillators comprising the stable cluster. Accordingly, on the 2-dimensional polydiagonal corresponding to the reduced system of $A2$, the saddle node has one stable and one unstable directions. Transverse to the polydiagonal, the remaining eigenvalues indicate two unstable and five stable direction, corresponding to perturbations, disturbing the integrity of the clusters.

In figure 9 at $X1$, each of the three synchronous states $A2$ undergoes a degenerate transcritical bifurcation, whereby two of the three positive eigenvalues of $A2$ become negative. Those eigenvalues correspond to the two unstable directions transverse to the polydiagonal: the smaller cluster comprising three oscillators becomes stable w.r.t. perturbations disturbing its integrity, i.e. w.r.t perturbations orthogonal to the synchronous polydiagonal. This can be seen from a direct computation of the eigenvectors of the Jacobi matrix, at the point $X1$, but also by considering the synchrony pattern of the involved $A3$ states. Observe that $A3$ (i.e. $P0(a_2, b_1)$) results from a symmetry breaking of the small cluster in $A2$ (i.e. $P0(a_1, b_1)$). Furthermore, for a given pattern $A2$ there are three (symmetric) possibilities to break the smaller cluster into a pattern $A3$. Figure 9, pattern A3 (i.e. $P0(a_2, b_1)$), shows only one of the three possibilities where the second and third oscillators of the small cluster from pattern $A2$ (i.e. $P0(a_1, b_1)$) remain identical; however, it is also possible that the first and the second or the first and the third oscillators remain identical in the symmetry breaking. Indeed, at the bifurcation point $X1$ each of the three $A2$ synchrony states collides, respectively, with three corresponding $A3$ states. Each of those $A3$ states comes from a direction transverse to the 2-dimensional polydiagonal of the reduced $A2$ system, resulting in a center manifold at $X1$ transverse to the $A2$ polydiagonal. The cluster comprising the six oscillators, corresponding to the stable directions, remains in the process unchanged, and therefore the stability change takes place in the two initially unstable directions of $A2$ transverse to the polydiagonal. After the bifurcation $A2$ remains, on the polydiagonal, a saddle with one stable and one unstable directions.

In figure 9 at $X0$ (i.e. at κ_{crit}), the three symmetric $A2$ states (shown in figure 10A) undergo simultaneously with the 1-cluster solution $\phi^{(0)}_s$ a degenerate transcritical bifurcation. As in the $X1$ bifurcation from above, the three $A2$ saddles

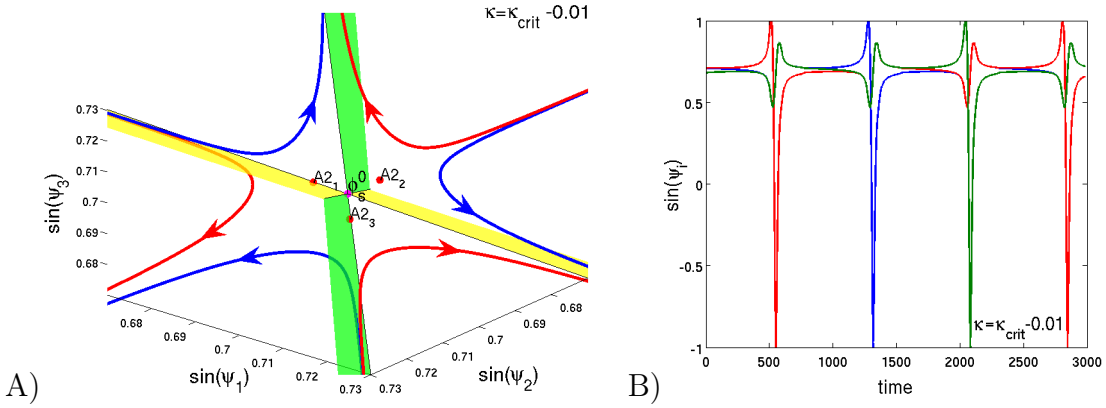

Figure 11: A) Segment of the two symmetric limit cycles (shown in red and blue) in the reduced 3-dimensional system in the vicinity of the bifurcation point after the bifurcation $X0$. The yellow and green planes represent the polydiagonals of $A2_1$ and $A2_3$, respectively. B) Phase plot of the periodic solution. The colors correspond to those of the synchrony pattern $P0(a_1, b_2)$ shown in figure 10.

come to the stable node $\phi_s^{(0)}$ from different directions, along the corresponding 2-dimensional polydiagonals. Because of the symmetry between the $A2$ states, we can naturally introduce new variables along the polydiagonals

$$\begin{aligned} \psi_1 &\equiv \phi_1 = \phi_5 = \phi_9 \\ \psi_2 &\equiv \phi_2 = \phi_6 = \phi_7 \\ \psi_3 &\equiv \phi_3 = \phi_4 = \phi_8 \ . \end{aligned} \tag{28}$$

Those variables correspond to the invariant subspaces of the synchrony pattern $P0(a_1, b_2)$, shown in figure 10B. On the $P0(a_1, b_2)$ polydiagonal the 9-dimensional system is reduced to a system of three globally coupled identical phase oscillators

$$\dot{\psi}_i = \omega - \sin\psi_i + \frac{3\kappa}{6} \sum_{j=1}^{3} \sin(\psi_j - \psi_i) \ . \tag{29}$$

After the bifurcation at $X0$ (i.e. at κ_{crit}), for $\kappa < \kappa_{crit}$ the synchronous 1-cluster solution $\phi_s^{(0)}$, the only observed attractor in the system above κ_{crit}, becomes unstable and all investigated initial conditions end up on one of two symmetric limit cycles. On the limit cycles the system is in a clustered state with a pattern of synchrony corresponding to $P0(a_1, b_2)$. Figure 11A shows the two symmetric limit cycles in the 3-dimensional phase space of the reduced system (29). Observe in figure 11B that the phases of the oscillators are shifted by a third of the period. This is a consequence of the symmetry group (the S_3 permutation group / D_3 dihedral group) of the reduced system, an effect well understood in arrays of identical phase oscillators [10]. A cyclic permutation of the oscillators corresponds to a spatio-temporal symmetry-transformation along a limit cycle, while a non-cyclic permutation corresponds to symmetry-transformation from the one limit cycle to the other [49]. In the following lines we explain the origin of the limit cycles and their symmetries.

The degenerate transcritical bifurcation at $X0$ (i.e. at κ_{crit}), in figure 9, takes place on the three dimensional polydiagonal of the reduced system (29) and therefore

has an S_3 symmetry. This bifurcation is known as the S_3 transcritical/homoclinic bifurcation (S_3-THB) [11], represented schematically in figure 12. The edges of the triangle represent the three 2-dimensional polydiagonals $A2_i$ and the vertices represent the replicas of the 1-cluster solution $\phi_s^{(0)}$ shifted by 2π. At the bifurcation point, along each polydiagonal $A2_i$, the 1-cluster solution $\phi_s^{(0)}$ collides with a corresponding saddle $A2_i$ giving rise to homoclinic connections. Simultaneously there is stability exchange between the 1-cluster solution $\phi_s^{(0)}$ and $A2_i$ saddles in direction transverse to the polydiagonals $A2_i$. After the bifurcation the previously stable transverse directions of the $A2_i$ saddles become unstable, and the homoclinics simultaneously give rise to periodic orbit, as shown in figure 12. The trajectories of the limit cycle passes along the 2-dimensional invariant polysynchronous subspaces $A2_i$ (according to the initial homoclinics). In the vicinity of a saddle $A2_i$ the transverse instabilities dominate and the trajectory is forced away from the current polydiagonal towards another one, resulting in a subsequent visit of each of the three saddle states $A2_i$. This behavior can be seen in figure 11A (at $\kappa = \kappa_{crit} - 0.01$) and also in the schematic representation in figure 12. We can now understand the symmetries of the two limit cycles, mentioned above. Each of the two limit cycles $\mathcal{L}_{red/blue}$, from figure 11A, can be characterized by the subsequent order of the saddles $A2_i$ along the trajectory. The possible arrangements of the three saddles $A2_1, A2_2$, and $A2_3$ are given by the permutation group S_3. However, because of the periodicity of the trajectory, cyclic permutations, like $(A2_1, A2_2, A2_3) \mapsto (A2_3, A2_1, A2_2)$, would correspond to transformations along the same limit cycle (i.e. spatio-temporal symmetry-transformations); anti-cyclic permutations, like $(A2_1, A2_2, A2_3) \mapsto (A2_1, A2_3, A2_2)$, would correspond to transformations from one limit cycle to the other (i.e. spatial symmetry-transformations). Therefore, because of the symmetries, not one but two limit cycles are born at the THB bifurcation.

Remarkably, the asymptotics of the period of the limit cycles follow neither the logarithmic law, typical for a homoclinic bifurcation of hyperbolic saddle points nor the inverse square law, typical for homoclinics to saddle-nodes [46]. Here, the period is inversely proportional to the distance from the critical parameter value (see figure 13A)

$$T \sim \frac{1}{(\kappa_{crit} - \kappa)} \ . \tag{30}$$

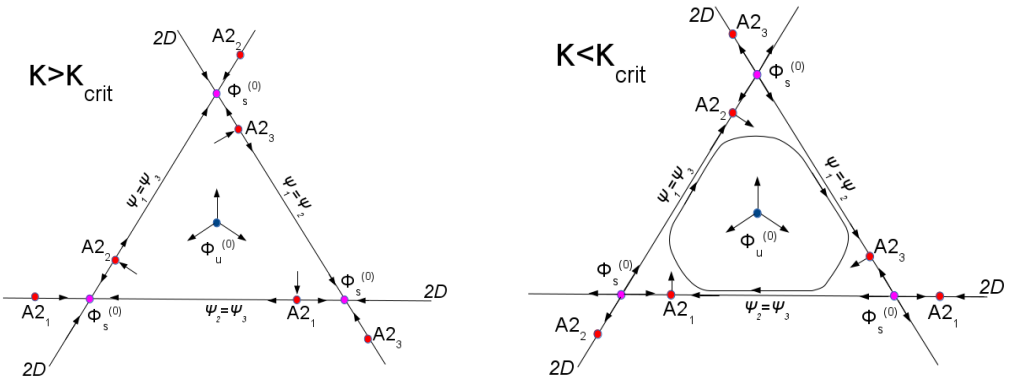

Figure 12: Schematic representation of the S_3-THB bifurcation.

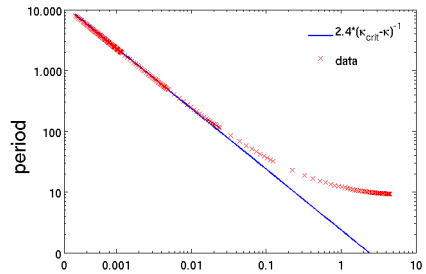

A)

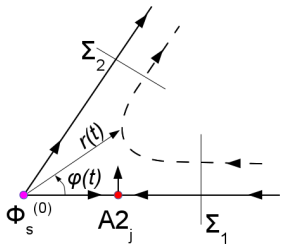

B)

Figure 13: A) Asymptotics of the period of the observed limit cycles. B) Polar coordinates for the normal form of the S_3-THB bifurcation.

We were unable to find in the literature a derivation of this kind of asymptotics. In what follows we show that (30) is indeed the right asymptotics for the more general case S_N.

In polar coordinates (r, φ), as in figure 13B, the normal form of the bifurcation can be written as

$$\dot{r} = \mu r - r^2 \cos(N\varphi) \tag{31}$$
$$\dot{\varphi} = r \sin(N\varphi) \tag{32}$$

rendering a stable (unstable) fixed point at the origin $r^* = 0$ for $\mu < 0$ ($\mu > 0$) and respectively N saddles on each of the invariant submanifolds $\varphi^*_m = m\pi/N$ $(m = 1, .., N)$ at $r^* = \mu$. For $\mu > 0$, the time spend along the periodic orbit, in the vicinity of the bifurcating points, is much larger than the transient time between their 2π- shifted replicas. Therefore, we can choose the latter to be of order 1. The time spend near the fixed points equals the time that $\varphi(t)$ needs to get from the Poincare section Σ_1 to Σ_2; see figure 13B. We can estimate this time, if we could rewrite $\dot{\varphi}(t)$ as a function of $\varphi(t)$ only:

$$\frac{\mathrm{d}\varphi}{\mathrm{d}t} = \mu \, \mathrm{F}(\varphi) \tag{33}$$
$$\hookrightarrow T = \int_{\Sigma_1}^{\Sigma_2} (\mu \mathrm{F}(\varphi))^{-1} \, \mathrm{d}\varphi$$

with $\mathrm{F}(\varphi)$ a function independent on μ. In this case, we would expect

$$\frac{\mathrm{d}^2\varphi}{\mathrm{d}t^2} \sim \mu^2 \ .$$

Taking the time derivative of (32) and substituting back (31) and (32) renders

$$\ddot{\varphi}(t) = (N-1)\frac{\cos(N\varphi)}{\sin(N\varphi)}\dot{\varphi}^2 + \mu\dot{\varphi} \ . \tag{34}$$

And indeed, substituting (33) in (34) gives

$$\frac{\mathrm{d}^2\varphi}{\mathrm{d}t^2} = \mu^2 \left((N-1) \, \frac{\cos(N\varphi)}{\sin(N\varphi)} \, \mathrm{F}(\varphi)^2 + \mathrm{F}(\varphi) \right) \ .$$

The fact that by rescaling the time $t \mapsto \mu t$ entirely absorbs the parameter μ in both equations of motion (31) and (32) shows that the asymptotics of the period is indeed given by (30).

Appendix
Invariant Subspaces on the 3×3 Hexagonal Lattice

In this section we determine the invariant subspaces, i.e. the possible clustered states, for system (23) on the 3×3 hexagonal lattice, taking into account symmetry breaking leading from one clustered state to another. This approach aims to combine (in a non strictly mathematical way) aspects from equivariant bifurcation theory [47, 48] and the groupoid formalism, discussed in section 1.2. In [5] and the proceeding [6, 7] Antoneli and Stewart discuss the connection between equivariant bifurcation theory and groupoid formalism. There, they show that on a network with coupling topology based on a symmetry group Γ it is possible to have balanced patterns of synchrony (called *exotic*) that do not correspond to any fixed point subspace of Γ. Therefore, it is convenient to consider not merely the fixed point subspace of Γ, as it is usual within equivariant bifurcation theory, but rather the balanced patterns of synchrony and the underlying symmetry breaking.

System (23) is equivariant under the symmetry group of the corresponding hexagonal lattice, denoted here by Γ:

$$F(\gamma\phi) = \gamma F(\phi) \;\; \forall \phi \in T_{MN},\, \gamma \in \Gamma.$$

From equivariant bifurcation theory [48, 49] it is known that fixed-point spaces

$$\mathrm{Fix}(\Sigma) = \{\phi \in T_{MN} \,|\, \sigma\phi = \phi \;\forall \sigma \in \Sigma\}$$

with $\Sigma \subseteq \Gamma$, correspond to flow-invariant subspaces of the system:

$$F(\mathrm{Fix}(\Sigma)) \subseteq \mathrm{Fix}(\Sigma)\,.$$

In order to understand the bifurcation scenarios in such equivariant systems, i.e. in order to determine bifurcation branches for a given solution, it is necessary to investigate the isotropy lattice of the system. The isotropy group of a given solution, say $\bar{\phi}$, is defined as

$$\Sigma_{\bar{\phi}} = \left\{\gamma \in \Gamma \,|\, \bar{\phi} = \gamma\bar{\phi}\right\}\,.$$

The isotropy lattice is the partially ordered set of all (conjugate) isotropy subgroups: i.e. each isotropy group is a node on the lattice and there is a (directed) link from one isotropy group to another isotropy group if and only if the first is a subgroup of the second. Being a subgroup of Γ each isotropy group also defines a fixed point space $\mathrm{Fix}(\Sigma_{\bar{\phi}})$ and under some restrictions on $\Sigma_{\bar{\phi}}$ and $\mathrm{Fix}(\Sigma_{\bar{\phi}})$ given by the 'Equivariant Branching Lemma' [48, 49] it is possible to determine symmetry breaking bifurcation branches for the solution $\bar{\phi}$. And vice versa, if we know the symmetry breaking leading from one clustered state to another, we will be able to determine possible bifurcating branches.

In [98] Stewart proves that the invariant subspaces of any coupled cell system form a lattice, in the sense of a partially ordered set, similar to the isotropy lattice. In successive works different methods, both analytical [68, 67, 1] and computational [2, 1], were developed in order to characterize and determine the lattice of invariant subspaces for a coupled system with given topology. Though, even for the smallest case of the 3×3 lattice, because of the relatively high dimensionality and the multiplicity of the graph eigenvalues, the implementation of these methods is very technical and computationally expensive. Moreover, these methods determine the full lattice of invariant subspaces (i.e. all 2^{MN} invariant states), whereas, we are interested in the isotropy lattice of the system comprising the invariant subspaces up to symmetry conjugation. Here, we explicitly determine the invariant subspaces based on simple considerations. Starting from the smallest nontrivial invariant subspaces (the 2-cluster states) we subsequently break the symmetry determining the proceeding higher dimensional states.

On the 3×3 lattice every unit is coupled to almost all other units: to six out of the eight remaining. For a 2-cluster state, say a blue and a red clusters, this means that the smaller cluster (the red one) should comprise exactly three units. If there are less than three red units, there will be at least one blue unit which does not receive input from a red one, while the others do, and if there are four red units there will be at least one blue unit which receives more red input than the rest of the blue units. It can be easily verified that, up to symmetry-transformations, there are only three possible 2-cluster balanced patterns of synchrony, shown in the lower part of figure 14 with the characterizations P_0, Q_0 and R_0, respectively. In order to determine the possible symmetry breaking, it is convenient to consider not only the whole 9-dimensional system but rather the corresponding reduced systems, shown by the networks in the upper part of figure 14. The nodes represent the clusters, indexed by the number of oscillators comprising the cluster and the edges correspond to the inter (intra) cluster connections. In the case of all to all coupling between (within) clusters, i.e. all oscillators from a cluster are coupled to all oscillators of another (the same) cluster, the edges are continuous. Otherwise, the edges are dashed, indexed by the number of connections each oscillator of a given cluster receives from oscillators of a corresponding cluster. The nontrivial coupling topology in this cases depends on the symmetry (P_i, Q_j, R_k) of the synchronous pattern on the whole 3×3 lattice. Observe, for example, the reduced system (a_1, b_1) of the 2-cluster state P_0 shown in the top part of the right block. The coupling within the a_1 cluster is trivial (it is absent), resulting in a symmetry within the a_1 cluster corresponding to the permutation group S_3. Furthermore, because the coupling between the two clusters a_1 and b_1 is all to all, a symmetry breaking within the a_1 cluster will always result in a balanced pattern of synchrony, independent on the symmetry group of the b cluster. Contrary, the coupling within the b_1 cluster is nontrivial and a symmetry breaking of b_1 is always connected to a change in the symmetry pattern on the whole 3×3 lattice. In the case of $P_3(a_1, b_2)$ symmetry, the symmetry groups of each of the three clusters (a_1, b_2) is S_3 and because of the all to all coupling between the clusters, a symmetry breaking within any of those clusters will result in a balanced pattern of synchrony, independent of the other two clusters. This is not the case for the P_1 and P_2 symmetries, where the coupling between (and within) the clusters

is nontrivial. Here, a symmetry breaking in only one of the clusters can not result in a balanced pattern of synchrony unless the symmetry of the other clusters is appropriately broken as well.

The other two 2-cluster states Q_0 and R_0 both reduce to identical systems (c_1, d_1), shown in the top part of the left block. It is interesting to observe that subsequently, the patterns of synchrony resulting from a symmetry breaking also reduce to identical systems although the symmetry groups of Q and R are different. The same considerations are valid here as for the P symmetry. In particular, as for P_3, the symmetry breaking within single clusters for Q_2 and R_2 always leads to balanced patterns of synchrony. Therefore, if the underlying symmetry groups allows it, symmetry breaking between patterns from Q_2, R_2 and P_3 might also be possible: for example $P_3(a_1, b_2)$ can also break in $Q_2(c_3, d_3)$ or $R_2(c_3, d_3)$.

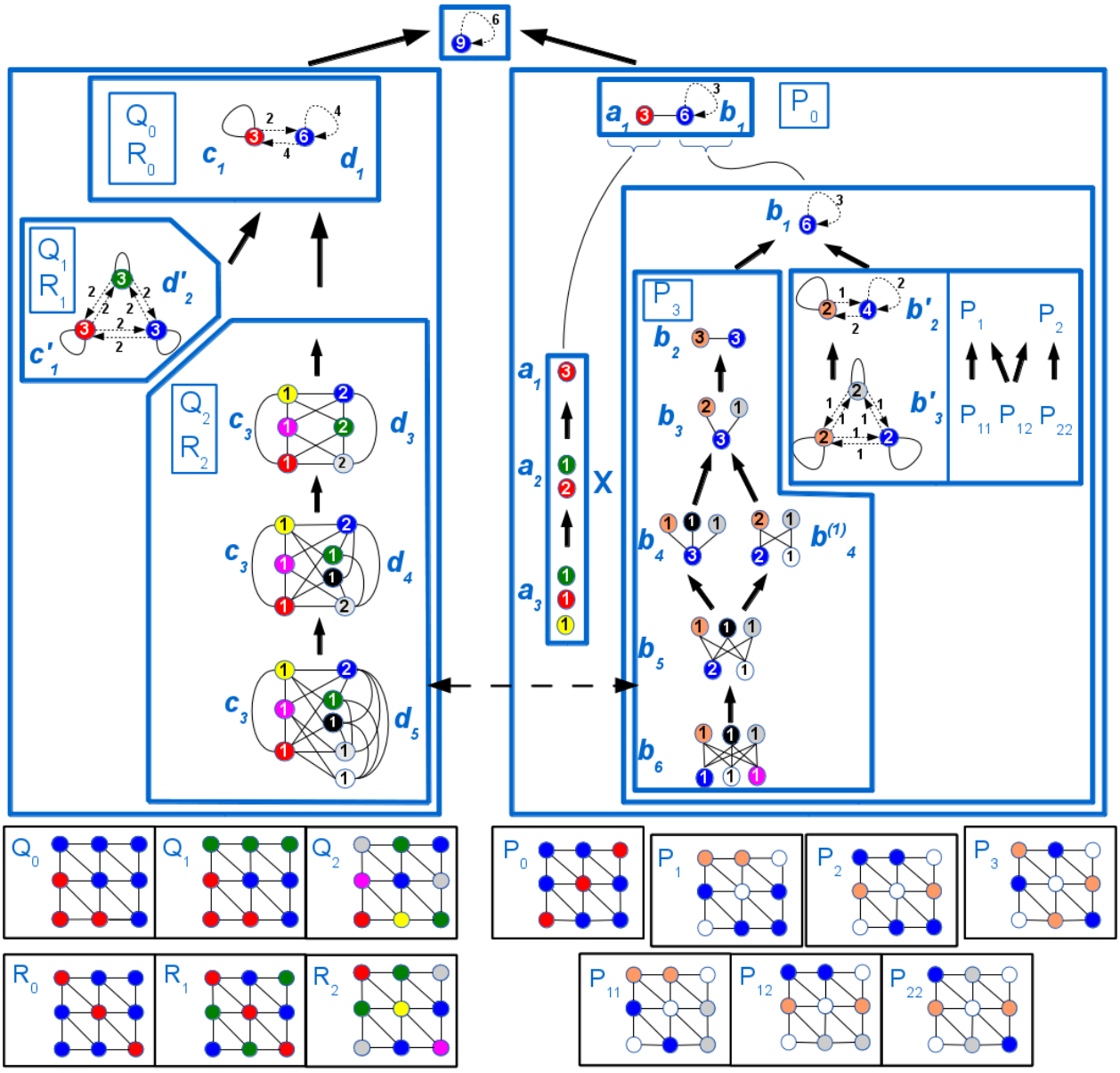

Figure 14: Lattice of symmetry breaking for the balanced patterns of synchrony for the 3×3 hexagonal lattice. The characterizations $X_i(y_j, z_k)$ stand for different symmetries on the whole 3×3 hexagonal lattice (see text). The small networks indicate the reduced system, whereby each node illustrates a cluster and the number inside corresponds to the number of oscillators comprising the cluster. Continuous edges indicate all to all coupling between (within) the clusters. Dashed edges indicate a nontrivial coupling topology between (within) clusters and the edge index indicates the number of connections each oscillator from the given cluster receives from oscillators of the corresponding cluster. In the case of dashed edges the nontrivial coupling topology becomes clear when considering the symmetry characterization $X_i(y_j, z_k)$ on the whole 3×3 hexagonal lattice.

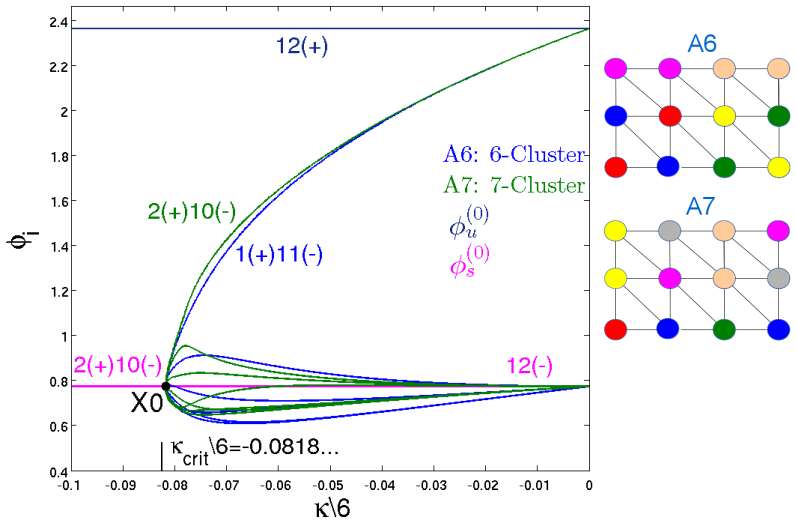

Figure 15: Bifurcation diagram for steady states on the 4×3 hexagonal lattice. The number of positive $(+)$ and negative $(-)$ eigenvalues is indicated next to the corresponding branch. *The color-coding representing the synchrony patterns on the hexagonal lattices is not connected to the color-coding representing the different bifurcation branches.*

2.3 Non-Square Lattices $M \times N$ with Multiplicity $d(M, N) = 2$

In this subsection we consider small non-square hexagonal lattices with multiplicity (27) of λ^A_{min} $d(M, N) = 2$. As representatives we have investigated lattices of sizes 4×3, 5×3 and 5×4. The obtained results have shown that the dynamical phenomena on all those lattices are similar. Therefore, we will describe in detail only the case of the 4×3 lattice.

At first, it appears that for $\kappa > \kappa_{crit}$ the only observed attractor is the stable synchronous 1-cluster solution $\phi_s^{(0)}$ which loses stability at κ_{crit}. Figure 15 represents on the left, up to symmetry-transformations, the bifurcation diagram for the steady states involved in the bifurcation and on the left the balanced patterns of synchrony of those states on the hexagonal lattice. The connectivity networks, corresponding to the reduced systems of $A6$ and $A7$ are, of course, different but have the same eigenvalues identical to the six (up to multiplicity) unique eigenvalues of the whole hexagonal lattice. Most importantly, they share the same minimal eigenvalue as the hexagonal lattice, enabling the bifurcation at $X0$. An investigation of all $2^{MN} - 2$ saddles that exist at $\kappa = 0$ has shown that depending on the initial configuration of the "stable" (placed at $\phi_s^{(0)}$) and "unstable" (placed at $\phi_u^{(0)}$) oscillators, the initial 2-cluster states give rise to nontrivial 2-, 3- , 4- , 6- and 7-cluster states at non-zero coupling strength. Beside $A6$ and $A7$, together with their symmetric copies, some of the reduced systems of the remaining clustered states do share eigenvalues with the whole hexagonal lattice and do take part in bifurcations with the 1-cluster solution $\phi_s^{(0)}$ for $\kappa < \kappa_{crit}$. Nevertheless, only $A6$ and $A7$ have the same eigenvalue λ^A_{min} as the hexagonal lattice (26) and therefore they are the only ones taking part at the bifurcation at $X0$. Observe also that the patterns of synchrony $A6$ and $A7$ are

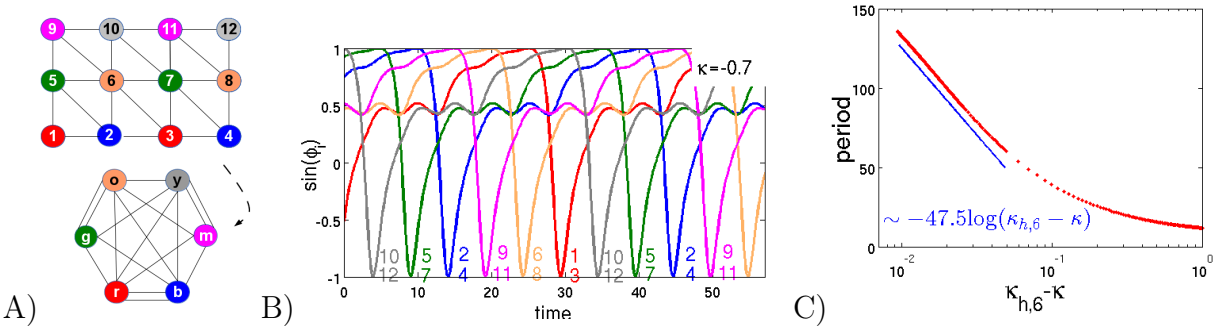

Figure 16: The 6-cluster limit cycle 6LC. A) Pattern of synchrony on the 4×3 hexagonal lattice (top). The corresponding reduced system (bottom). B) Phase plot of the periodic solution. C) Asymptotics of the period.

not subject to nontrivial symmetry-transformations. Therefor, each of them has 12 symmetric copies which take part in the bifurcation. From this point of view, the bifurcation at $X0$ can be regarded as two degenerate pitchfork bifurcations taking place at the same point. Contrary to the 3×3 lattice with a degenerate transcritical bifurcation, the bifurcations here can only be pitchfork because of the high number (2×12) of colliding steady states [45].

At the beginning of the previous paragraph, we mentioned that the only observed attractor for $\kappa > \kappa_{crit}$ appears to be the stable synchronous 1-cluster solution $\phi_s^{(0)}$. In fact, for κ values slightly above κ_{crit} less than half a dozen of more than 2×10^4 randomly chosen initial conditions did not converge to the 1-cluster solution $\phi_s^{(0)}$. Instead, within a very narrow κ region a hysteresis with $\phi_s^{(0)}$ and a limit cycle comprising 12 clusters was observed. For κ below this region, still above κ_{crit}, very few initial conditions showed chaotic behavior and all the rest ended at the still stable 1-cluster solution $\phi_s^{(0)}$. For different κ values below κ_{crit}, with the 1-cluster solution $\phi_s^{(0)}$ being unstable, various dynamical states were observed: limit cycles with 6, 7 and 12 clusters, quasi-periodicity and chaos. In what follows, we describe the observed limit cycles and their transitions to quasi-periodic and chaotic dynamical states. We also explain the hysteresis observed above κ_{crit}.

The limit cycle with 6-clusters, which we call 6LC, is shown, up to symmetry-transformations, in figure 16. Figure 16A represents the synchrony pattern on the 4×3 hexagonal lattice and the corresponding reduced system. It is interesting to observe that the spatio-temporal symmetry of the periodic solution is the dihedral group D_6: the phases of the oscillators belonging to different clusters are shifted by one sixth of the period (see figure 16B). This is not surprising since in the reduced system (figure 16A, bottom) the pairs r-b, g-o, and y-m are symmetric with a symmetry group Z_2 (interchanging the oscillators within each pair does not affect the system). Furthermore, there is a symmetry D_3 corresponding to a permutation of those pairs (observe that if the oscillators of each pair were identical, we would have a (reduced) system of three coupled oscillators). Combining the two groups we end up with the dihedral group $D_6 \simeq D_3 \otimes Z_2$. The phase shift between oscillators belonging to the same pair is half the period, corresponding to the Z_2 symmetry.

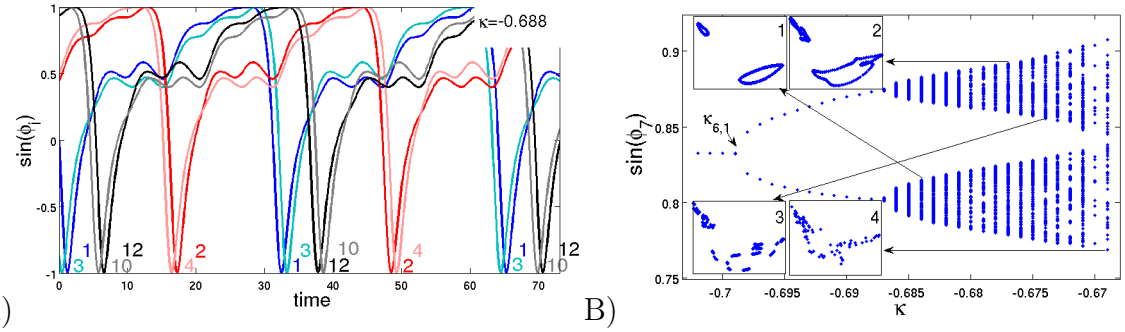

Figure 17: A) Phase plot of the 12-cluster limit cycle born at $\kappa_{6,1}$ from the period doubling bifurcation of the 6-cluster limit cycle. For the sake of better visibility, only 6 out of the 12 different phases are shown:1, 3, 2, 4, 10 and 12. B) Intersection of ϕ_7 with a Poincare section $\phi_1 = \pi$ at different κ values. Insets: Segments of 2-dimensional projection of the intersection points on the Poincare section for ϕ_4 and ϕ_7 at different κ values.

For example,

$$\psi_r(t) \quad = \quad \psi_b(t + \frac{T}{2})$$

where ψ_i denotes the phase in the reduced system and T the period. The phase shift between oscillators belonging to different pairs is, respectively, a third of half the period, corresponding to the D_3 symmetry. For example

$$\psi_r(t) \quad = \quad \psi_y(t + \frac{T/2}{3}) = \psi_g(t + 2\frac{T/2}{3})\,. \tag{35}$$

The logarithmic asymptotics exhibited by the period, shown in figure 16C, indicates a heteroclinic bifurcation at $\kappa_{h,6} = -0.55... < \kappa_{crit}$ from which the periodic solutions originates. At the bifurcation point the new born periodic solutions is strongly unstable with a pair of complex conjugated multipliers, as well as, two real negative multipliers outside the unit circle. Decreasing κ below $\kappa_{h,6}$ gradually retracts the multipliers towards the unit circle, down to $\kappa_{6,3} = -0.61..$, where one real negative multiplier enters the unit circle in a period doubling bifurcation. At $\kappa_{6,2} = -0.62..$ the pair of complex conjugated multipliers also reaches the unit circle in a Neimark-Sacker bifurcation and finally the last real negative multiplier enters the unit circle also in a period doubling bifurcation at $\kappa_{6,1} = -0.69..$. For all κ values lower than this, the 6-cluster limit cycle 6LC remains stable.

Seen the other way around, considering an increase in κ from strongly negative values, a new periodic orbit, comprising 12 clusters, is born from the period doubling bifurcation at $\kappa_{6,1}$. Figure 17A shows a phase plot for 6 out of the 12 different phases. Not surprisingly, the period of the new limit cycle equals twice the period of the 6LC limit cycle at the bifurcation point. However it is interesting that the spatio-temporal symmetry of the new limit cycle corresponds to a symmetry breaking of the spatio-temporal symmetry of the old one. Here, each of the 6 clusters from figure 16A is split into two, which is depicted in the spatio-temporal symmetry and the period

doubling. In figure 17A, the phase shift between oscillators, previously belonging to the same cluster (figure 16A,B), is half the new period (or approximately the whole period of the 6LC limit cycle). This corresponds to a Z_2 spatio-temporal symmetry. For example,

$$\phi_1(t) = \phi_3(t + \frac{T}{2})$$

where T denotes the period of the new born 12-cluster limit cycle. Furthermore, the phase shift between oscillators previously belonging to the pairs r-b, g-o, and y-m from the previous section is, respectively, one half of half the new period, corresponding to a further Z_2 symmetry:

$$\phi_1(t) = \phi_2(t + \frac{T/2}{2}) = \phi_4(t + 3\frac{T/2}{2})\,.$$

Finally, the D_3 symmetry from above is also present:

$$\phi_1(t) = \phi_{12}(t + \frac{\frac{T/2}{2}}{3}) = \phi_{10}(t + 7\frac{\frac{T/2}{2}}{3})\,. \tag{36}$$

Therefore, it is not surprising that the spatio-temporal symmetry of the new born 12-cluster limit cycle is the dihedral group $D_{12} \simeq D_3 \otimes Z_2 \otimes Z_2$.

Increasing κ further, above $\kappa_{6,1}$, gradually deforms the "doubled period" 12-cluster limit cycle, as represented in figure 17B. At $\kappa = -0.687..$ a Neimark-Sacker bifurcation takes place, giving birth to a stable quasiperiodic orbit on a "double" torus (figure 17B- Inset 1). Further increase of κ forces a progressive folding of the torus (figure 17B- Inset 2). This leads to a shift in the winding number of the trajectory on the torus: it takes more time to complete a full cycle on the Poincare section of the torus, as it can be seen by the finite number of intersections in figure 17B- Inset 3. Eventually, the winding number becomes rational and stable limit cycles with high period multiplicity are formed, marking the Arnold tongues in parameter space. Figure 17B- Inset 4 represents a limit cycle with period multiplicity 80. This process indicates the formation of a chaotic set. However, this region of phase space gradually loses stability with the increase of κ and before the chaotic set becomes observable, trajectories become attracted to another 12-cluster limit cycle, which we call 12LC(A).

The 12LC(A) limit cycle appears to be the only remaining attractor after the chaotic set, originating from the 6LC periodic orbit, loses stability. It is also the limit cycle which remains stable for the largest κ interval; it is the one observed in the hysteresis with the 1-cluster solution $\phi_s^{(0)}$ above κ_{crit}; and it gives rise to a chaotic set on its own. From the logarithmic low of the period asymptotics, represented in figure 18A, it becomes clear that 12LC(A) originates from a heteroclinic bifurcation at $\kappa_{h,12A} = -0.475..$ *above* κ_{crit}. At this point, it is strongly unstable with a single positive real eigenvalue outside the unit circle. A decrease in κ, down to $\kappa_{12A,3} = -0.476.. > \kappa_{crit}$, leads to a subcritical pitchfork bifurcation of limit cycles and 12LC(A) becomes stable, coexisting with the still stable 1-cluster steady solution $\phi_s^{(0)}$. The fact, that at this point very few initial conditions, out of more than 2×10^4 randomly chosen, end up at 12LC(A) indicates a very small basin of attraction. The hysteresis remains down to $\kappa_{12A,2} = -0.476.. > \kappa_{crit}$ where the limit cycle

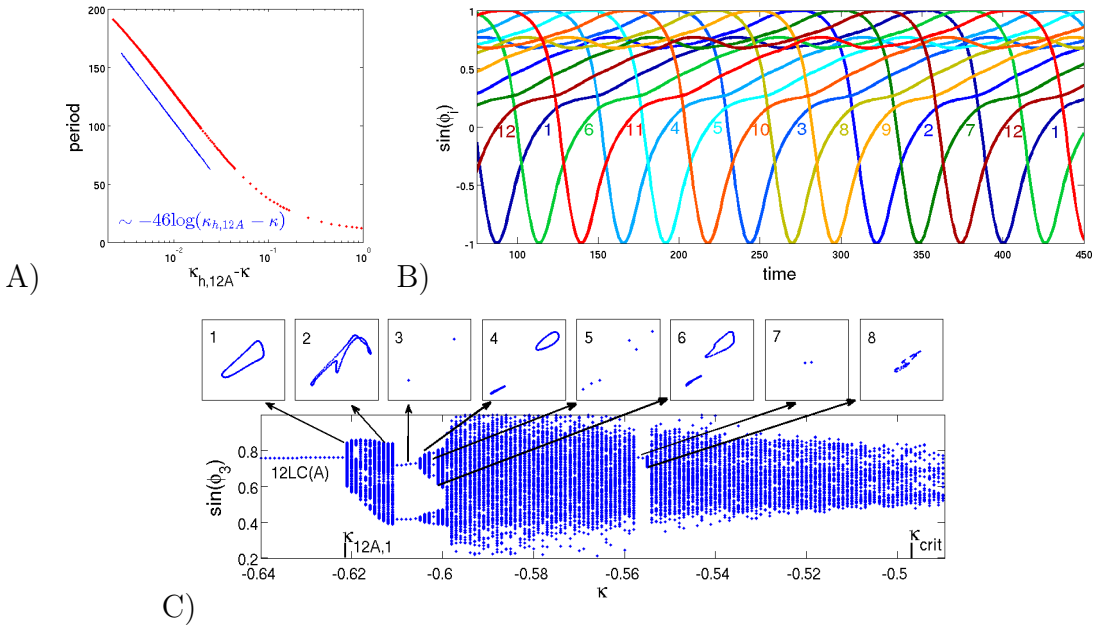

Figure 18: A) Period asymptotics of the 12-cluster limit cycle 12LC(A). B) Phase plot of the 12 clusters. C) Intersection of ϕ_3 with a Poincare section $\phi_1 = \pi$ at different κ values. Insets: Segments of 2-dimensional projection of the intersection points on the Poincare section for ϕ_4 and ϕ_3 at different κ values.

loses stability in a Neimark-Sacker bifurcation with a pair of complex conjugated multipliers reaching the unit circle. At this point a quasiperiodic orbit emerges on the newborn torus. Similar to the formation of the chaotic set from the previous paragraph, a chaotic set starts to form at decreasing κ values from the folding of the torus. Because of the instabilities of the initial torus, the forming chaotic set remains, at first, unstable. Further decrease of κ gradually suppresses those instabilities, whereby transiently chaotic orbits are observed. When κ becomes smaller than κ_{crit}, the 1-cluster solution $\phi_s^{(0)}$ loses stability and for certain κ region $[\kappa_{12A,1}, \kappa_{crit}]$ the only attractor of the system remains the chaotic set, represented in figure 18C. At different values of κ the chaotic set changes and various stability islands with invariant tori and limit cycles of higher period multiplicity are formed and disintegrate, once again, indicating the Arnold tongues in parameter space. In a decrease of κ towards $\kappa_{12A,1}$ the chaotic set is gradually formed back to torus, originating from a Neimark-Sacker bifurcation at $\kappa_{12A,1}$ where the two complex conjugated eigenvalues of 12LC(A) are pulled back within the unit circle and the 12-cluster periodic orbit regains its stability. From this point on, it remains stable and down to $\kappa_{6,1}$, where the 6-cluster limit cycle 6LC from above stabilizes as well, it is the only observed attracting state in phase space. The spatio-temporal symmetry of the 12LC(A) periodic solution is once again the dihedral group D_{12} (see figure 18B). However, in this case the symmetry does not originate from a subsequent symmetry breaking. The reason is that, here, the 12-cluster limit cycle 12LC(A) is born directly from a heteroclinic bifurcation, contrary to the 12-cluster limit cycle with $D_{12} \simeq D_3 \otimes Z_2 \otimes Z_2$ born from the period doubling bifurcation of 6LC.

The two stable limit cycles 6LC and 12LC(A) do not remain the only attractors

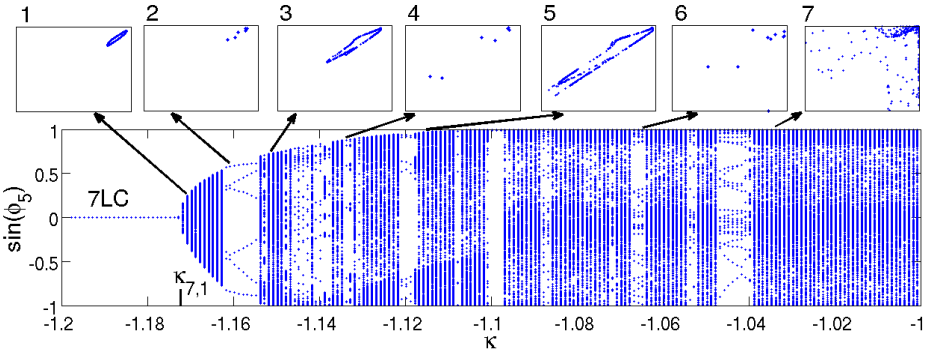

Figure 19: Intersection of ϕ_5 with a Poincare section $\phi_1 = \pi$ at different κ values within a chaotic attractor originating from a Neimark-Sacker bifurcation of a 7-cluster solution 7CL. Insets: Segments of 2-dimensional projection of the intersection points on the Poincare section for ϕ_7 and ϕ_3 at different κ values.

in the system for $\kappa < \kappa_{6,1}$. Decreasing κ further, down to $\kappa = -0.92..$, reveals a new chaotic set, represented in figure 19. At first, transiently chaotic trajectories, ending on the stable 12LC(A) limit cycle, are observed and for lower κ values the chaotic set becomes stable. As in the cases from above, various stability islands appear at different κ values, some of them represented in the insets of the figure. From figure 19 it becomes clear that, here as well, by considering an increase of κ from below, the chaotic set originates from the folding of a torus born from a Neimark-Sacker bifurcation of a limit cycle at $\kappa_{7,1} = -1.17..$: a 7-cluster periodic orbit, which we call 7LC. Despite the similarity with the previous cases, the bifurcation curve of the 7LC periodic solution, represented in figure 20A ,is more complicated than the one of the 6LC limit cycle. The 7LC limit cycle originates from a saddle node bifurcation of limit cycles at $\kappa_{SN,7} = -0.86...$ The saddle node bifurcations along the bifurcation curve, together with subsequent period doubling and pitchfork bifurcations (not shown explicitly) attest the intricate topology in phase space. Decreasing κ from higher values towards $\kappa = -0.92..$ forces a folding in phase space, deforming the limit cycles in this region and gradually leading to quasiperiodic and chaotic solutions. It is interesting to observe (see figure 20B) that in the stable region the 7-cluster solution does not possess any spatio-temporal symmetries, which is to be expected since the reduced system does not have any symmetries either (see figure 20C).

At each of the pitchfork bifurcations in 20A limit cycles with 12-clusters are born. Most of those 12-cluster periodic solutions remain unstable within the investigated κ region, exhibiting themselves Neimark-Sacker, pitchfork and period doubling bifurcations. Nevertheless some of those 12-cluster limit cycles become stable for sufficiently low κ values. Similar to the 12-cluster limit cycle originating from the period doubling bifurcation of 6LC, the spatio-temporal symmetries of the periodic solutions originating from pitchfork bifurcations of 7LC correspond to symmetry breaking of the 7-cluster solutions, whereby the phases of oscillators previously belonging to the same cluster are shifted by half the period of the new 12-cluster limit cycles.

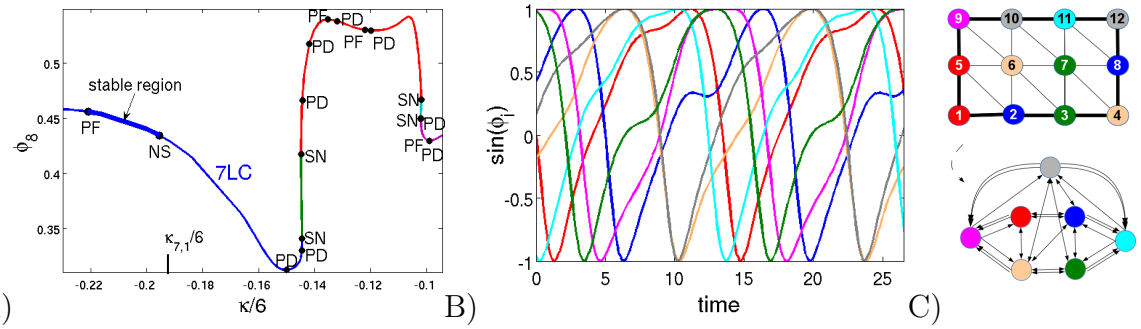

Figure 20: A) Fragment of the bifurcation curve for the 7LC limit cycle showing the intersection of ϕ_8 with the Poincare section $\phi_1 = \pi$. Abbreviations: (NS) Neimark-Sacker; (PD) Period Doubling; (PF) PitchFork; (SN) Saddle Node. B) Phase plot of the 7 clusters for the 7LC limit cycle in the stable region at $\kappa = -1.19$. The colors correspond to the pattern of synchrony in C). C) Pattern of synchrony for the 7LC limit cycle on the 3×4 hexagonal lattice and the corresponding reduced system.

2.4 The 4×4 Hexagonal Lattice

The 4×4 hexagonal lattice seems to be a special case not only from graph theoretical point of view, where it is distinguished by its own name– "The Shrikhande Graph" [20]– but also from dynamical point of view, as we will see in this section.

The hexagonal lattice of any size with periodic boundary conditions is a regular graph, since every element has the same number of neighbors. However, the Shrikhande graph is *strongly regular*, meaning that additionally, every two adjacent elements have p common neighbors and every two nonadjacent elements have q common neighbors: here, $p = q = 2$. Because of this peculiarity, the multiplicity of the graph eigenvalues (see (27)) is also exceptional: among all doubly periodic hexagonal lattices, only the 4×4 hexagonal lattice has a minimal eigenvalue of multiplicity $d(4, 4) = 9$. As a consequence, the center manifold at the bifurcation point κ_{crit}, where the 1-cluster synchronous solution $\phi_s^{(0)}$ loses stability, has the unusually high dimension 9.

Figure 21 represents the bifurcation diagram for the steady states involved in the bifurcation at $\kappa_{crit} = -0.5356...$ (the X0 point in the diagram). Up to symmetry-transformations, besides the 1-cluster solution $\phi_s^{(0)}$, there are eight entangled steady states. The remaining points, X.. in figure 21, denote bifurcations along the corresponding polydiagonals which do not influence directly the X0- bifurcation; therefore, those bifurcations won't be discussed in detail here. Considering the exceptionally high dimension of the center manifold at the bifurcation point X0, it is not surprising that the bifurcation diagram is much more complex than in the previous cases. Nevertheless, it shows similar features. Recall from above that on the 3×3 lattice there was a single degenerate transcritical bifurcation and on the 4×3 lattice there were two degenerate pitchfork bifurcations. In figure 21 at X0, there are two degenerate pitchfork bifurcations, along the invariant subspaces of the B3 and A5 patterns of synchrony, and six degenerate transcritical bifurcations, respectively, along the invariant subspaces of the remaining six patterns of synchrony. In section 6 we will investigate in greater detail the question whether the 1-cluster solution $\phi_s^{(0)}$,

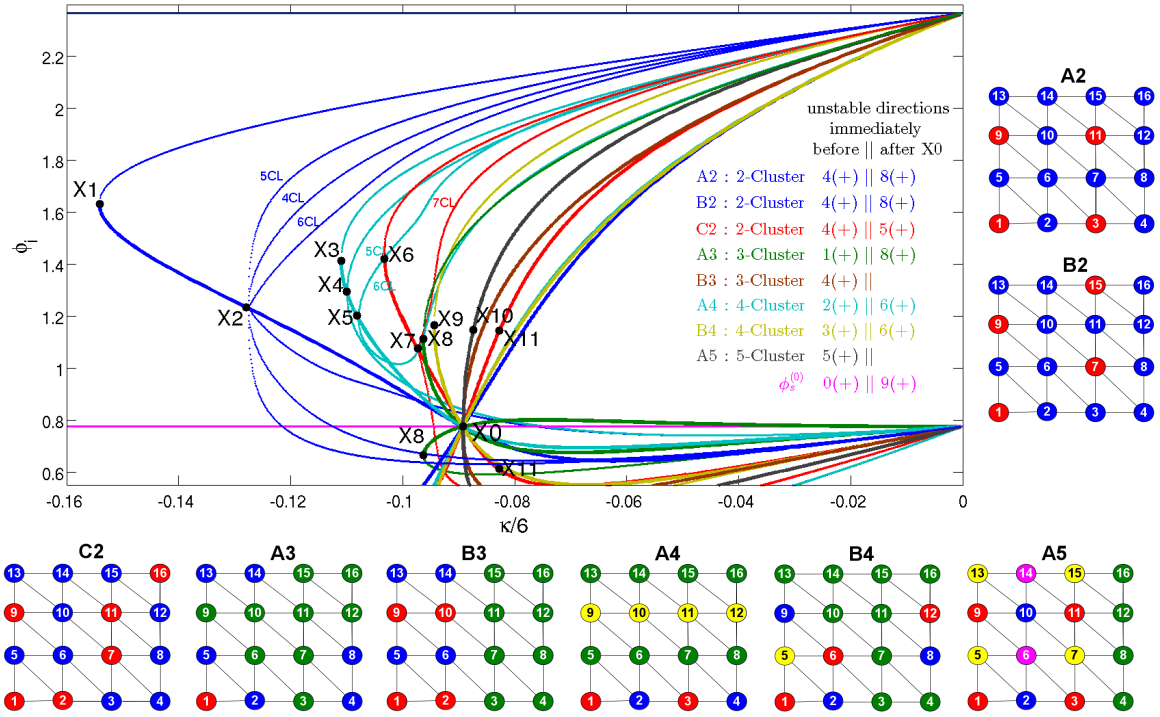

Figure 21: Bifurcation diagram for eight steady states taking part at the bifurcation of the 1-cluster solution $\phi_s^{(0)}$ on the 4×4 hexagonal lattice. The different patterns of synchrony on the hexagonal lattice are shown, up to symmetries, on the side and below the bifurcation diagram, whereby *the colors of the patterns do not correspond to the colors used in the bifurcation diagram.* In the bifurcation diagram, different colors indicate the whole bifurcation scenario (including secondary bifurcation branches as in X2, for example) for a given pattern of synchrony, indicated by the same color of the inscriptions on the right. For each bifurcation branch the positions of only two oscillators are shown.

in specific networks of coupled phase oscillators with sinusoidal repulsive coupling (such as the Kuramoto and Shinomoto model (23)), bifurcates in a transcritical or in a pitchfork bifurcation. There, we will see that the "typical" bifurcation for such systems is the transcritical one, which explains why in figure 21 there are more transcritical than pitchfork bifurcations. Even without going into in-depth mathematical calculations, this can be intuitively expected after a simple consideration. From the center manifold theorem [53] it is known that a system can be expanded in terms of Taylor series, in the vicinity of the bifurcation point, bringing the bifurcation to its normal form. In its normal form the pitchfork bifurcation has a linear and a cubic term, while the transcritical has a quadratic term as well. In general, there is no reason to expect that the quadratic term should disappear in the expansion. And indeed, as we will see, only in certain cases, depending among others on the number of oscillators in the network and the connectivity matrix, this term disappears leading to pitchfork bifurcation. Besides the similarities between this and the preceding bifurcation diagrams, there are also dynamical states on the 4×4 lattice, which are similar to the ones from the previous sections. In what follows, we first discuss those

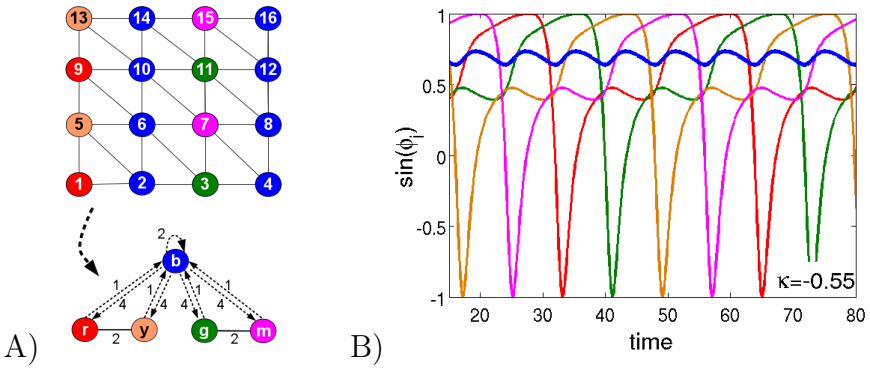

Figure 22: The 5-cluster limit cycle 5LC. A) Pattern of synchrony, up to symmetry-transformations, on the 4×4 hexagonal lattice (top). The corresponding reduced system (bottom). B) Phase plot of the weak-chimera-like periodic solution. The colors in the phase plot correspond to the colors from the synchrony pattern.

states and concentrate afterward on an intriguing phenomena observed only on the Shrikhande Graph.

Similar to the 4×3 lattice, here on the 4×4 lattice, at kappa values slightly *above* κ_{crit} a hysteresis with the still stable 1-cluster solution $\phi_s^{(0)}$ and a limit cycle comprising 5 clusters was observed (see figure 22A). This limit cycle, which we call 5LC, is born stable in a saddle node bifurcation at $\kappa_{5,1} = -0.48.. > \kappa_{crit}$ and vanishes at $\kappa_{5,3} = -0.68.. < \kappa_{crit}$, again in a saddle node bifurcation. From the reduced network in figure 22A it becomes clear that the pattern of synchrony of the 5LC limit cycle possesses symmetries: i) the pairs of oscillators r-y and g-m are interchangeable with a symmetry Z_2; ii) the oscillators within each pair are interchangeable as well, with an additional Z_2 symmetry. Expectably, this leads to a spatio-temporal symmetry $D_4 \simeq Z_2 \otimes Z_2$, as shown in figure 22B: oscillators belonging to the same pair, r-y or g-m, are shifted by half of the period and oscillators belonging to different pairs are shifted by a multiple of a quarter of the period. More surprising is the fact that the large (blue) cluster, comprising eight oscillators, does not perform full-scale rotations but only small-scale librations. In the literature [12] this effect has been called a "weak-chimera state": a state in a system of coupled identical phase oscillators with weighted coupling, such that there are pairs of oscillators with bounded phase differences over time (in our case, those are the phase differences between the small clusters) and there are pairs with unbounded phase differences (in our case, the phase differences between the large and the small clusters). After the lost of stability of the 1-cluster solution at κ_{crit}, the 5LC limit cycle seems to overtake the whole basin of attraction of $\phi_s^{(0)}$ and remains the only observed attractor down to $\kappa_{5,1} = -0.61..$; there, it loses stability in a Neimark-Sacker bifurcation. Again similar to the previous section, this bifurcation gives rise to a quasiperiodic solution which gradually becomes chaotic at lower kappa values and on its turn remains the only observed attractor of the system down to approximately $\kappa = -0.7$. At around this kappa value new attractors appear in the phase space, comprising families of 4-cluster periodic solutions. Remarkably, this families are continua of periodic states, something exceptional in a non-conservative system. In the remaining part of this

section we investigate this continua and explain their origins and peculiarities.

In section 1.2 as well as in sections 2.2 and 2.3, we have seen that in a synchronous clustered state the dynamics of the full system is identical to the dynamics of the reduced system constrained on the corresponding flow-invariant polydiagonal. Furthermore, in the previous cases, when we have spoken of clustered states– for instance such as a limit cycles or steady states– and have represented their patterns of synchrony on the hexagonal lattice, we have noted that the corresponding representations are shown up to symmetry-transformations. In those cases, the reduced system could be "lifted" (distributed) on the hexagonal lattice in different ways, resulting in different patterns of synchrony connected via the hexagonal symmetry-transformations on the lattice (for example, see figure 10A in section 2.2). Accordingly, in the full-dimensional phase space each of those symmetric patterns defines its own invariant polydiagonal, all of them being, on their turn, also connected via the corresponding symmetry-transformations. The existence of such transformations in the full-dimensional phase space ensures not only that the dynamical states on the polydiagonals are identical, but also that their stability properties in directions transverse to the polydiagonals (for example, the whole sets of multipliers in the case of limit cycles) are also identical. Contrary, at the end of section 1.2, we have argued that a reduced system being "lifted" on a larger network, to patterns of synchrony that are not symmetry connected (or even more generally to different networks), do not implicitly lead to dynamical states with identical stability properties in directions transverse to the otherwise dynamically identical polydiagonals. Such is the example of the patterns Q_i and P_i on the 3×3 lattice in figure 14: two synchrony patterns, which are not symmetry connected, leading to identical reduced systems. Remarkably, this is also the case for the patterns of synchrony in the continua of the 4-cluster periodic solutions, which we are interested in. Figure 23 shows six examples of such patterns of synchrony on the 4×4 hexagonal lattice, which correspond to flow-invariant polydiagonals hosting the continua of periodic solutions. Observe that the patterns are not connected via symmetry-transformation but nevertheless reduce to the same system.

In what follows, we first consider only one representative of such patterns and concentrate on the 4-dimensional reduced system. This will help us understand the origin of the continua of limit cycles in the otherwise non-conservative system. Besides, it will give us hints about the bifurcation at which the continua of periodic solutions originate, which turns out to be at κ_{crit}. Finally, investigating this bifurcation in the full 16-dimensional phase space will help us understand the similarities and differences between the stability properties of the different 4-cluster periodic solutions.

Consider the pattern of synchrony (P1), shown in figure 23. On the synchronous subspace corresponding to this pattern

$$\begin{aligned} \psi_1 &\equiv \phi_1 = \phi_3 = \phi_9 \ = \phi_{11} \\ \psi_2 &\equiv \phi_2 = \phi_4 = \phi_{10} = \phi_{12} \\ \psi_3 &\equiv \phi_5 = \phi_7 = \phi_{13} = \phi_{15} \\ \psi_4 &\equiv \phi_6 = \phi_8 = \phi_{14} = \phi_{16} \end{aligned} \tag{37}$$

the equations of motions (23), governing the dynamics of the system, take the re-

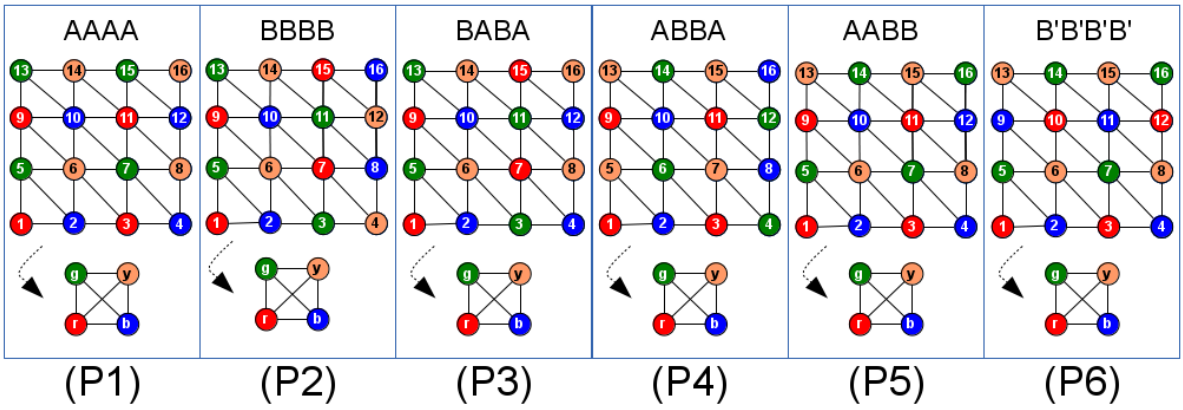

Figure 23: Examples of 4-cluster synchronous states on the 4×4 hexagonal lattice, which corresponds to flow-invariant polydiagonals hosting the continua of periodic solutions.

duced form

$$\dot{\psi}_i = \omega - \sin\psi_i + \frac{4\kappa}{6} \sum_{j=1}^{4} \sin(\psi_j - \psi_i) \ . \tag{38}$$

Unexpectedly, similar to the 3×3 hexagonal lattice from section 2.2, we observe a spontaneous onset of global coupling in a setup with local coupling. We will investigate this intriguing phenomena further in sections 3 to 6. Remark also that the coupling function in (38) includes only the first Fourier harmonics. Therefore, the celebrated result of Watanabe and Strogatz holds: a system of N globally sinusoidally coupled phase oscillators possesses N–3 constants of motion (WS- Integrals) [111, 112]. In our case: $N = 4$, the number of the four clusters, and we have a single constant of motion. In these early works Watanabe and Strogatz show that the reduction of the N-dimensional system to a 3-dimensional system corresponds to a 3-dimensional foliation of the originally N-dimensional manifold of the phase space. Accordingly, there are only three degrees of freedom and the remaining N–3 dynamically invariant directions are parametrized by constants of motion: i.e. each leaf of the foliation is characterized by N–3 WS-integrals. In a later work [78], Marvel, Mirollo and Strogatz show that the reduction is related to the 3-dimensional *Möbius group of transformations* consisting of the fractional linear transformations of the complex unit disc onto the complex plane and vice verse. In particular, by connecting the temporal evolution of the N-dimensional system to the one-parameter family of Möbius transformations, they show that the phases of the N oscillators evolve according to the action of the group. As a consequence, they reveal a connection between the WS-integrals from the previous works and the cross ratios of any four phases ψ_i, ψ_j, ψ_k and ψ_l

$$R(i,j,k,l) = \frac{\sin(\frac{\psi_i - \psi_k}{2})}{\sin(\frac{\psi_i - \psi_l}{2})} \frac{\sin(\frac{\psi_j - \psi_l}{2})}{\sin(\frac{\psi_j - \psi_k}{2})} \tag{39}$$

which are conserved quantities under Möbius transformations. Therefore, all R's, derived by permutation of the indices, are constants of motion. As expected, not

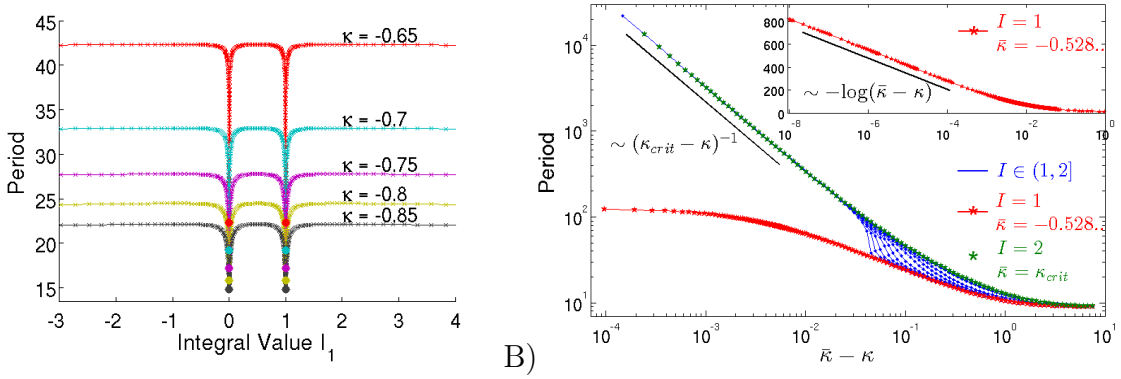

Figure 24: A) Period vs. integral value I for different fixed κ values. B) Asymptotics of the period for the continuum of limit cycles. Main figure: A log-log plot for different values of the integral $I \in [1, 2]$. Inset: A log-linear plot for integral value $I = 1$.

all constants of motion obtained in such a way are linearly independent. Observe that in our case, with $N = 4$, from all 4! permutations of the indices there are six nontrivial (non-cyclic) ones. Those can be expressed for example as

$$\begin{array}{ll} I_1 = R(i,j,k,l) & I_4 = R(i,k,l,j) \\ I_2 = R(i,j,l,k) & I_5 = R(i,l,k,j) \\ I_3 = R(i,k,j,l) & I_6 = R(i,l,j,k)\ . \end{array} \tag{40}$$

It can be easily verified that, according to (39), $I_2, ..., I_6$ can be expressed in terms of I_1. In particular,

$$\begin{array}{llll} I_1 & & I_4 = & 1/(1-I_1) \\ I_2 = & I_1^{-1} & I_5 = & I_1/(I_1-1) \\ I_3 = & 1-I_1 & I_6 = & (I_1-1)/I_1 \quad . \end{array} \tag{41}$$

This means that each 3-dimensional leaf of the foliation is characterized by a fixed value of I_1 and each point on the corresponding leaf is determined by three phases; for example ψ_i, ψ_j, ψ_k. The fourth phase, respectively ψ_l, is implicitly given by (39)

$$\psi_l\left(\psi_i, \psi_j, \psi_k;\, I_1\right) = 2\arctan\left(\frac{\sin(\frac{\psi_j}{2})\sin(\frac{\psi_i-\psi_k}{2}) - I_1\sin(\frac{\psi_i}{2})\sin(\frac{\psi_j-\psi_k}{2})}{\cos(\frac{\psi_j}{2})\sin(\frac{\psi_i-\psi_k}{2}) - I_1\cos(\frac{\psi_i}{2})\sin(\frac{\psi_j-\psi_k}{2})}\right) \bmod 2\pi\,.$$

This explains the observation of continua of limit cycles for fixed κ values: in the reduced system (38) on each leaf of the foliation there is a limit cycle; each leaf– therefore, each limit cycle– is characterized by the corresponding integral value (39) and a continuous variation of the integral value leads to a continuum of limit cycles.

Since the limit cycles are characterized by the integral values I, it is not surprising that for fixed κ values the periods of the limit cycles also change with respect to I. This is represented in figure 24A for five different values of κ within the integral region from -3 to 4. From equation (39) it becomes clear that I takes values from minus to plus infinity. However, because of the invariance of the globally coupled reduced system with respect to phase permutations, the whole integral range

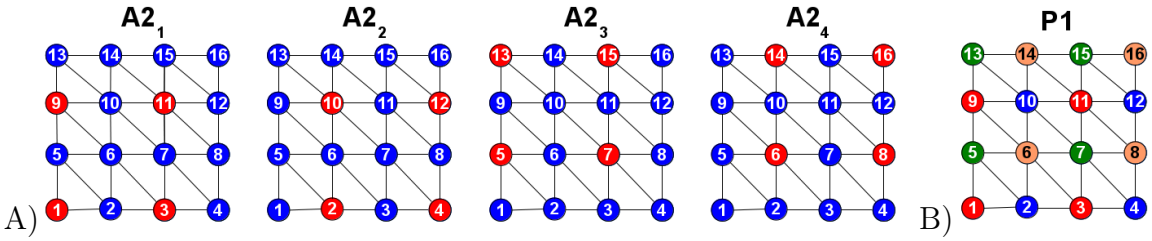

Figure 25: A) The four symmetric copies of the $A2$ pattern of synchrony from figure 21. B) The corresponding 4-cluster pattern of synchrony P1.

$I \in (-\infty, +\infty)$ corresponds to symmetric copies of one of the following region: $(-\infty, -1]$, $[-1, 0]$, $[0, 0.5]$, $[0.5, 1]$, $[1, 2]$, $[2, +\infty]$. This follows from the integral relations (41) and is confirmed in figure 24A. Therefore, when considering the reduced 4-dimensional system, it is sufficient to concentrate only on one of those integral regions. Observe also that the value $I = 1$ (as well as $I = 0, \pm\infty$), where the period gradually takes its lowest value, stands out from the rest. This is due to the fact that those integral values are degenerate and the four phases are pairwise equal: for example, at $I_1 = 1$ we have $\psi_1 = \psi_2$ and $\psi_3 = \psi_4$. In this case(s) the limit cycles are 2-clusters periodic solutions with corresponding 2-dimensional reduced systems. The dynamical properties on the leaves characterized by those integral values also differ from the rest. Figure 24B represents in a log-log plot the asymptotics of the periods of limit cycles, at different integral values from the continuum. The log-linear plot in the inset of figure 24B shows an explicit logarithmic asymptotics and reveals that the limit cycle characterized by $I = 1$ is born in a heteroclinic bifurcation above κ_{crit} at $\kappa = -0.528...$. Contrary, the periods of the remaining limit cycles belonging to the continuum and characterized by integral values $I \in (1, 2]$ have the asymptotics

$$T \sim \frac{1}{(\kappa_{crit} - \kappa)} .$$

In section 2.2, equation 30, we have seen that this kind of asymptotics indicates a transcritical/homoclinic bifurcation (THB). Recall that on the 3×3 hexagonal lattice from section 2.2 there were three symmetric copies of the saddle state corresponding to the $A2_i$ patterns of synchrony (see figure 10A). Those saddles gave rise to stable periodic orbits after exchanging stability with the synchronous 1-cluster solution $\phi_s^{(0)}$ at κ_{crit}. A schematic representation of the corresponding S_3-THB bifurcation in the reduced 3-dimensional system was shown in figure 12. Here, in analogy to the S_3-THB, we have an S_4-THB bifurcation. In section 6 we investigate these bifurcations in more detail. To see this here, consider further a 4-cluster limit cycle with pattern of synchrony corresponding to P1, as shown in figure 25B. The configuration of the four clusters in P1 corresponds to four symmetric copies of the saddle state $A2$ undergoing a bifurcation at X_0 in figure 21. This is represented in figure 25: each symmetric copy $A2_i$ of the saddle $A2$ corresponds to a 2-cluster pattern of synchrony, where three of the four phases ψ_i in P1 are identical. Therefore, each copy $A2_i$ lies within the 4-dimensional polydiagonal $(\psi_1, ..., \psi_4)$ from equation (37) and the THB bifurcation takes place in the reduced 4-dimensional system from equation (38). In figure 21, we see that in the full 16-dimensional system, before the

bifurcation at κ_{crit}, each saddle state $A2_i$ has 4 unstable and 8 stable directions. Accordingly, in the reduced system (38), each symmetric copy of the saddle $A2_i$ has a 1-dimensional invariant unstable manifold and a 3-dimensional stable manifold. Thereby, two of those three stable directions are transverse to the 2-dimensional polydiagonal $A2_i$ and the third remaining stable direction lies within this polydiagonal, together with the 1-dimensional unstable manifold– the latter connecting the saddle and the 1-cluster solution $\phi_s^{(0)}$. Observe that this setup, on each of the 2-dimensional polydiagonals $A2_i$ hosting a corresponding saddle $A2_i$ and the 1-cluster solution $\phi_s^{(0)}$, is analogous to the case from section 2.2. Here, at the bifurcation at κ_{crit}, the four saddles $A2_i$ collide with the 1-cluster synchronous solution $\phi_s^{(0)}$ and homoclinic connections along each of the $A2_i$ polydiagonals are formed. Furthermore, at the bifurcation, there is a stability exchange between the 1-cluster solution $\phi_s^{(0)}$ and the four saddles $A2_i$: the directions of the saddles within polydiagonals $A2_i$ become stable, while the transverse directions become unstable, simultaneously giving rise to periodic orbits originating from the corresponding homoclinics (see section 2.2). The only difference here is that the corresponding transverse manifolds are 2-dimensional, whereas in section 2.2 they were 1-dimensional. However, this difference is suppressed by the symmetry of the globally coupled 4-dimensional system (38). A perturbation in direction transverse to a polydiagonal $A2_i$ disturbs, independent of the fourth oscillator, the integrity of the cluster containing the three oscillators with identical phases. If we consider this subsystem of three (globally) coupled oscillators with identical phases, we see that in this state there is always an eigenvalue corresponding to perturbations respecting the integrity of the cluster (this is the eigenvalue which lies within polydiagonal $A2_i$) and another degenerate eigenvalue with two symmetric eigenvectors that disturb the integrity of the cluster (those are the eigenvalues transverse polydiagonal $A2_i$). This symmetry is not broken by the bifurcation and accordingly at the bifurcation point not one but both transverse direction exchange stability with the 1-cluster state $\phi_s^{(0)}$. This explains also that after the bifurcation, in the full 16-dimensional system, the saddles $A2$ have not four but eight unstable directions.

Until now we have considered only the pattern of synchrony P1 in figure 23. We have seen that on the associated polydiagonals the saddle nodes correspond to symmetric copies of $A2$ and give rise to periodic orbits after the S_4-THB bifurcation. The remaining patterns in figure 23 also describe 4-cluster synchrony-states of periodic orbits born in analogous S_4-THB bifurcations. From figure 23, we see that their polydiagonals also host four saddles equivalent to copies of the saddles $A2$ and/or $B2$ from figure 21. The four-letter notations above the patterns of synchrony in figure 23 indicate the copies of A2 and/or B2 within the pattern. For example, pattern P3 in figure 23 is indicated by BABA and comprises two copies of the saddle $B2$ (corresponding to the configuration of the red and green clusters, respectively) and two copies of the saddle $A2$ (corresponding to the configuration of the blue and yellow clusters, respectively). In fact, on the 4×4 hexagonal lattice, any pattern of synchrony which is reducible to a system of four globally coupled phase oscillators corresponds to a combination of four copies of the patterns $A2$ and/or $B2$. Accordingly, on the associated polydiagonals the solutions undergo a S_4-THB bifurcation at κ_{crit} from which the periodic orbits originate. After the bifurcation each

periodic orbit is characterized by the sequence of four of the saddles: the trajectories of the limit cycles pass subsequently in the vicinity of the saddles $A2_i$ and/or $B2_k$ along 2-dimensional polydiagonals (according to the initial homoclinics). The other way around, considering not the phase space but the patterns of synchrony $A2$ and/or $B2$ on the 4×4 hexagonal lattice, we can find all patterns up to symmetry-transformations. For example, let the firs cluster be red, the second blue, the third green and the fourth yellow: (r, b, g, y). Starting from the first oscillator, we place either pattern $A2$ or $B2$ and obtain the configuration on the 4×4 hexagonal lattice of the four oscillators that belong to the red cluster. Subsequently, on the next oscillator, that does not belong to previous (red) cluster, we place $A2$ or $B2$, if possible, a.s.o. Let us consider patterns P2 and P3. In both cases, we choose to start with a $B2$ configuration for the red cluster and therefore it comprises oscillators $\{1, 7, 9, 15\}$. The next oscillator that does not belong to this group is oscillator 2, which gives the initial position of the blue cluster. For the configuration of the blue cluster we can choose either $A2$ or $B2$. In pattern P2 it is $B2$ and in pattern P3 it is $A2$. In both cases, the next oscillator that does belong neither to the red nor to the blue clusters is oscillator 3, which gives the initial position of the green cluster. In both patterns P2 and P3, for the green cluster, it is only possible to choose the $B2$ configuration. The yellow cluster comprises the remaining oscillators. Considering all possible configurations of the patterns $A2$ and/or $B2$ on the 4×4 hexagonal lattice we acquire that up to symmetry-transformations there are only six possible patterns, represented in figure 23.

In section 2.2 we have seen that the S_3-THB bifurcation gives rise to two symmetric limit cycles. This is due to the structure of the undergone bifurcation where each periodic orbit subsequently passes in the vicinity of the three saddles $A2_1, A2_2, A2_3$; see figure 12. There, a non-cyclic permutation of the oscillators, $(1, 2, 3) \to (1, 3, 2)$, corresponds to a symmetry-transformation from the one periodic orbit $(A2_1, A2_2, A2_3)$ to the other $(A2_1, A2_3, A2_2)$, and a cyclic permutation to a spatio-temporal symmetry-transformation along the same orbit. These (discrete) symmetry-transformations are a direct consequence of the S_3 symmetry of the reduced system (29) [49, 10]. In analogy, based on the S_4 permutation group, we might expect similar phenomena after the S_4-THB bifurcation. However, here it is even more interesting because of the different synchrony patterns and the additional integral dependence within the continuum of Watanabe-Strogatz reduction. In (40), we have seen that for all 4! permutations of the oscillators there are six non-trivial ones leading to the six permutation-related integral values. Moreover, for each integral value I_k there are four (trivial) permutations which leave the integral value unchanged and therefore would correspond to transformations on the same foliation leaf. Let the set of four indices (r, b, g, y) correspond to an arbitrary permutation of the set $(1, 2, 3, 4)$. From equation (39) follows that

$$\begin{aligned} I &= R(r, b, g, y) = R(g, y, r, b) \\ &= R(b, r, y, g) = R(y, g, b, r) \end{aligned} \tag{42}$$

Observe that on the first row in (42), respectively on the second row, the integral relations are connected via pairwise cyclic permutations, while the first and second rows are connected via anti-cyclic permutations.

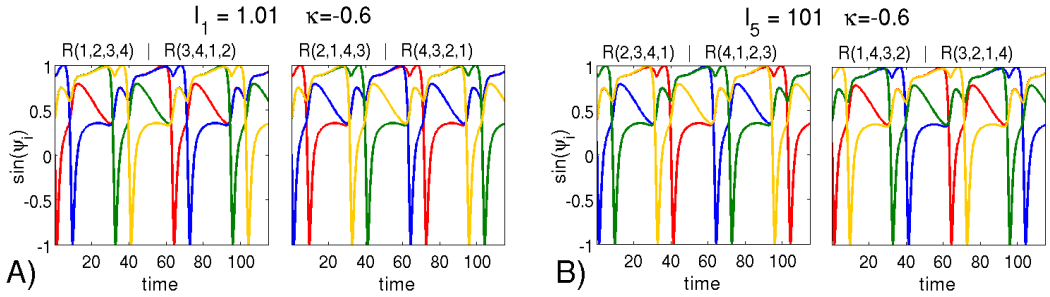

Figure 26: Phase plots of symmetric limit cycles connected via cyclic and anti-cyclic permutations. The color coding in all cases is as follows: $\psi_1 \equiv \psi_r$- ***r***ed, $\psi_2 \equiv \psi_b$- ***b***lue, $\psi_3 \equiv \psi_g$- ***g***reen, $\psi_4 \equiv \psi_y$- ***y***ellow. A) The two symmetric limit cycles belonging to the same foliation leaf characterized by the integral value $I = 1.01$. B) The corresponding symmetry connected limit cycles belonging to the foliation leaf characterized by the integral value $I = 101$.

Each of the figures 26A and 26B represents two limit cycles, characterized by two different integral values, respectively $I = 1.01$ and $I = 101$. At each of the two integral values, the limit cycles are obtained by permutations of the oscillators according to (42). The four permutation-relations (42) indicate that the S_4 symmetry of the system is manifested as a Z_2 spatio-temporal symmetry and a Z_2 spatial symmetry of the periodic orbits. For a fixed integral value, for example $I = 1.01$ in Figure 26A, the pairwise cyclic permutations, $(r, b, g, y) \to (g, y, r, b)$, correspond to Z_2 spatio-temporal symmetry-transformation along the same orbit. In figure 26A(left) this Z_2 spatio-temporal symmetry is

$$\psi_r(t) = \psi_g(t + \frac{T}{2}) \text{ and } \psi_b(t) = \psi_y(t + \frac{T}{2}) \tag{43}$$

and corresponds to the permutation-relation

$$R\left(\psi_r(t), \psi_b(t), \psi_g(t), \psi_y(t)\right) = R\left(\psi_g(t + \frac{T}{2}), \psi_y(t + \frac{T}{2}), \psi_r(t + \frac{T}{2}), \psi_b(t + \frac{T}{2})\right) .$$

In the last equations T denotes the period of the limit cycle. From the point of view of the phase shifts, we can pair the oscillators (r, g) and (b, y). The anti-cyclic symmetry-transformations, for a fixed integral value, indicate a spatial Z_2 symmetry, such that *on each foliation leaf there are two distinct symmetric periodic orbits*. For example, the permutation $(r, b, g, y) \to (b, r, y, g)$ correspond to an exchange of the oscillator pairs (r, g) and (b, y), see figure 26A. The same observations are true for figure 26B as well as for any other integral value (39) with the relations (42).

The symmetry relations resulting from permutations corresponding to different integral values are even more interesting. Similar to cases from the previous sections (see for example, the limit cycles in equations (35) and (36), as well as the 5LC limit cycle in figure 22), we might have expected, from the S_4 symmetry of the 4-dimensional system and the fact that $D_4 \simeq Z_2 \otimes Z_2$, that the spatio-temporal symmetry here is D_4 and not simply Z_2. For example, we might have expected

$$\psi_r(t) = \psi_g(t + \frac{T}{2}) \text{ and } \psi_r(t) = \psi_b(t + \frac{T/2}{2}) , \tag{44}$$

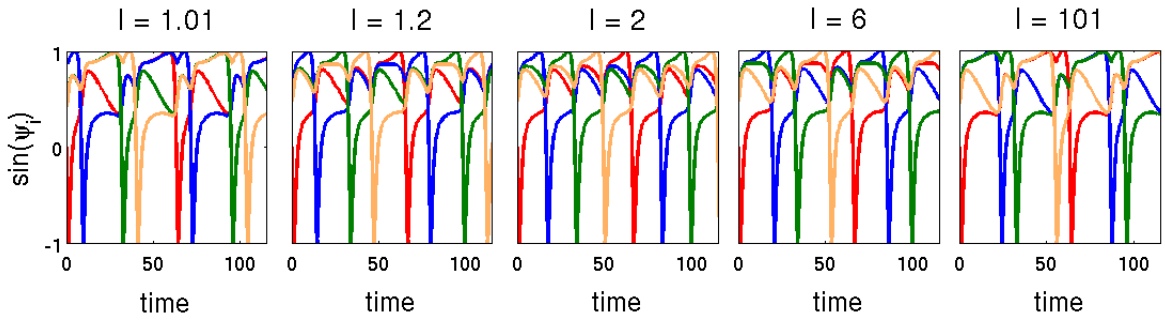

Figure 27: Phase plots of limit cycles characterized by five different integral values. The color coding in all cases is as follows: $\psi_1 \equiv \psi_r$- ***r***ed, $\psi_2 \equiv \psi_b$- ***b***lue, $\psi_3 \equiv \psi_g$- ***g***reen, $\psi_4 \equiv \psi_y$- ***y***ellow.

whereby the ψ_r and ψ_g relation expresses the Z_2 symmetry corresponding to exchange of oscillators belonging to the same pair and the ψ_r and ψ_b relation expresses the Z_2 symmetry corresponding to exchange between the pairs. However, this is not the case: in general, arbitrary S_4 permutations lead to different integral values and can not correspond to spatio-temporal symmetry-transformations along the same limit cycle. Nevertheless, limit cycles characterized by different (permutation-related) integral values belong to the same continuum. Therefore, we can consider a continuous shift of the integral value from $I \to I'$. From this point of view, a (discrete) permutation, for example such as $(r, b, g, y) \to (b, g, y, r)$, seems as a continuous transformation from one integral region in the other. Figure 27 represents the phase plots for limit cycles characterized by five different integral values, indicating five steps along a continuous integral shift $1.01 \to 101$. In the figure, the integral values $1.01 \leftrightarrow 101$, as well as $1.2 \leftrightarrow 6$, are permutation-related. Remark that the shift of the integral value does not influence the Z_2 spatio-temporal symmetry which was observed for a fixed integral value: the phase relations (43) between oscillators belonging to the same pair (in the example (r, g) or (b, y)) remains half of the period. Contrary, the phase relations between oscillators belonging to two different pairs gradually changes with respect to the shift of the integral value. In the given example, only at $I = 2$ (in general $I = 2, 0.5, -1$) the spatio-temporal symmetry becomes $D_4 \simeq Z_2 \otimes Z_2$ with the corresponding phase relations (44), where the phases of the oscillators are shifted by a quarter of the period. Otherwise, for $I \in (1, 2) \cup (2, \infty)$, it gets broken to a Z_2 spatio-temporal symmetry and Z_2 spatial symmetry. A comparison of the plots on the left of $I = 2$ with those on the right of $I = 2$ shows that the Z_2 spatial symmetry is not lost: it corresponds to an exchange of the pairs (r, g) and (b, y). In figure 27 we can also see that a further shift of the integral value, for example to the "left" $I \searrow 1$, would lead to a degeneracy. At $I = 1$ the otherwise 4-cluster limit cycle becomes a two cluster solution at which the pairs (r, g) and (b, y) overlap:

$$\psi_r(t) = \psi_b(t) = \psi_g(t + \frac{T}{2}) = \psi_y(t + \frac{T}{2}) \tag{45}$$

and the symmetry of the system becomes $D_2 \simeq Z_2$. Recall from above that the integral values $I = 1$ (as well as $I = 0, \pm\infty$), where the four phases of the oscillators

Integral Region									
$-\infty$	Region 1 $(-\infty,-1]$	Region 2 $[-1,0)$	0	Region 3 $(0,0.5]$	Region 4 $[0.5,1)$	1	Region 5 $(1,2]$	Region 6 $[2,+\infty)$	$+\infty$
	(b,g,r,y) (i,l,j,k)	(g,r,y,b) (i,k,j,l)		(g,r,b,y) (i,k,l,j)	(r,b,y,g) (i,j,l,k)		(r,b,g,y) (i,j,k,l)	(b,g,y,r) (i,l,k,j)	
$r=y$ $b=g$	(r,b) (g,y) $\psi_r(t)=\psi_b(t+T/2)$ $\psi_g(t)=\psi_y(t+T/2)$		$r=g$ $b=y$	(r,y) (b,g) $\psi_r(t)=\psi_y(t+T/2)$ $\psi_b(t)=\psi_g(t+T/2)$		$r=b$ $g=y$	(r,g) (b,y) $\psi_r(t)=\psi_g(t+T/2)$ $\psi_b(t)=\psi_y(t+T/2)$		$r=y$ $b=g$

Table 1: Upper part of the table: Permutation-relations $R(\blacksquare,\blacksquare,\blacksquare,\blacksquare)$ between the six integral regions. On the first row: The permutation sets of the indices indicate the continuous transformation of a limit cycle w.r.t. a shift of the integral value. On the second row: using the four trivial permutations that leave the integral value unchanged, we show the corresponding reordered permutation sets, in terms of the six integrals $I_1,..,I_6$ from equation (40). Lower part of the table: Phase relations between the clusters in the different integral regions.

are pairwise equal, were exceptional. Because of this degeneracy, at $I=1$ (as well as $I=0,\pm\infty$) there are not four permutation-relations (42), that leave each of those integral values unchanged, but eight. For example, because of $\psi_r(t)=\psi_b(t)$ and $\psi_g(t)=\psi_y(t)$ we would have

$$\begin{aligned} I &= R(r,b,g,y)=R(g,y,r,b) \\ &= R(b,r,y,g)=R(y,g,b,r) \\ &\equiv \\ I &= R(b,r,g,y)=R(g,y,b,r) \\ &= R(r,b,y,g)=R(y,g,r,b)\,. \end{aligned} \tag{46}$$

Remark that in the general case (42) (with $I\neq 0,1,\pm\infty$) those eight permutation-relations correspond to two pairs of two symmetric limit cycles at two distinct integral values: each of the four rows in (46) characterizes a limit cycle and the permutations on each row correspond to Z_2 spatio-temporal symmetry-transformations along this limit cycle. For a shift of the integral value $I=1\pm\delta$, those four limit cycles can be considered as a result of the $D_2\simeq Z_2$ symmetry breaking into the observed Z_2 spatio-temporal symmetry and Z_2 spatial symmetry. In the example from above, we can see that the first two rows in (46) would correspond to the two limit cycles from figure 26A at $I=1+\delta$: there the pairs of oscillators shifted by half of the period (43) were (r,g) and (b,y). Accordingly, the last two rows in (46) would correspond to two limit cycles at $I=1-\delta$ with phase relations between the oscillators given by

$$\psi_b(t)=\psi_g(t+\frac{T}{2}) \text{ and } \psi_r(t)=\psi_y(t+\frac{T}{2}) \tag{47}$$

or oscillator pairs (r,y) and (b,g). In a similar way, we can investigate all permutation-relations in terms of smooth transitions between the six integral regions. These are represented in table 1 for a limit cycle continuously transformed w.r.t. a shift of the

integral value. Remark that it is more convenient instead of using the six integrals $I_1, .., I_6$ from equation (40) to denote the six integral regions depending on the integral value: Region 1,...,Region 6 as in the table. This is because in the reduced 4-dimensional system (38) the four oscillators are indistinguishable and depending on the initial choice of correspondence between the set (r, b, g, y) and the index set of the oscillators (i, j, k, l), we can choose the integral value I_1 to lie in any of the regions. Nevertheless, when we speak of the permutation-relations between integral regions, we mean the relations between fixed integral values: i.e. always referring to a set of fixed values of the oscillator phases $\{\psi_1, \psi_2, \psi_3, \psi_4\}$. In the case of limit cycles this set might be chosen to represent the intersection of the periodic orbit and the Poincaré section.

Now we can address the question of stability. Due to the presence of the neutral direction "along" the continuum, each periodic orbit has a Floquet multiplier equal to 1. Below, we call an orbit stable, if all other Floquet multipliers lie within the unit circle and unstable otherwise. According to the theory of Γ- equivariant systems [49, 47, 48, 5], if Γ is the symmetry group associated with the coupling topology of the network, two dynamical states, x and γx, are equivalent if they are connected via a symmetry-transformation $\gamma \in \Gamma$. Until now we were interested in the symmetries from the point of view of the integral value. As we have seen in the last paragraphs, in the reduced system, each limit cycle has in total 12 symmetric copies, two for each of the six permutation-related integral values. On the reduced graph of four identical globally coupled phase oscillators, the interchange between the permutation-related integral values does not play any role: the permutations correspond to trivial symmetry-transformations on the graph and result in the same pattern of synchrony. From this point of view the 12 limit cycles are identical and have the same dynamical properties. Indeed, all periodic orbits from the continuum born at the S_4-THB bifurcation are stable within the corresponding 4-dimensional polydiagonal. The only exceptions are the limit cycles with $I = 0, 1, \pm\infty$, which were born in the heteroclinic bifurcations as discussed above. However, this does not hold in the full 16-dimensional system. There, the stability properties of a limit cycle depend, in general, both on the permutation-related integral values and on the corresponding patterns of synchrony on the 4×4 hexagonal lattice. Figure 28 represents schematically the idea. It represents two different patterns of synchrony (P1 and P3) and indicates that the associated 4-dimensional polydiagonals correspond to different subspaces in the 16-dimensional phase space. Observe that there is no symmetry-transformation on the hexagonal lattice which can transform pattern P1 into P3. Therefore, there is no symmetry-transformation in phase space between the polydiagonals and, in general, we can not expect that limit cycles associated with those patterns will have the same stability properties in the 16-dimensional system, even if the integral value is fixed. On the other hand, an exchange, for example of the red and blue oscillators in pattern P3, which would correspond to a change in the integral value, say $I_j \to I_k$ (just a permutation in the reduced system), leads to a configuration of the oscillators which, on the lattice, is not symmetry connected to the original one, although it belongs to the same polydiagonal. Therefore, if there is no such symmetry-transformation on the lattice, we can not expect that the stability properties of the limit cycles characterized by those two integral values (I_j and I_k)

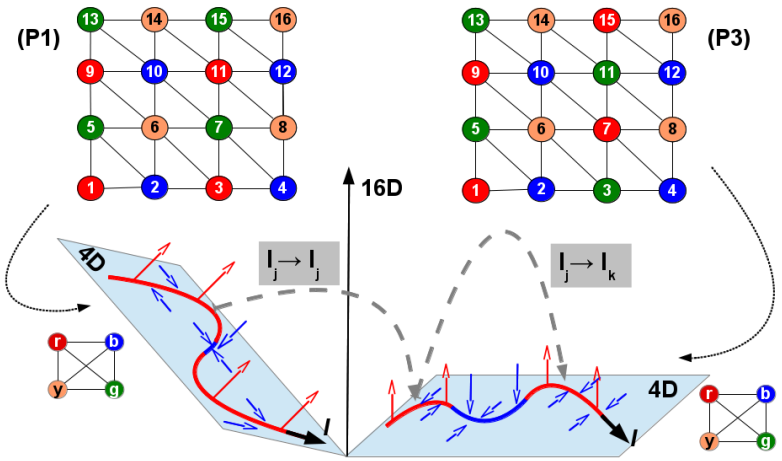

Figure 28: Schematic representation of two different 4-dimensional polydiagonals corresponding to a reduced system of four globally coupled phase oscillators, together with with their defining patterns of synchrony on the 4×4 hexagonal lattice. The curves on each of the 4-dimensional subspaces represent the continua of periodic solutions. The colors along the curves indicate different stability properties depending on the integral value.

are the same in the 16-dimensional system. An indeed, for a fixed κ value, the limit cycle corresponding to the pattern of synchrony P1 may be stable, while the limit cycle corresponding to the pattern of synchrony P3 may be unstable. However, an exchange of the blue and yellow oscillators in P3 (another change in the integral value, say $I_j \to I_l$) leads to a configuration of the oscillators which, on the lattice, is symmetry connected to the original one. Therefore, the limit cycles characterized by I_j and I_l are also symmetry connected and do have the same stability properties in the 16-dimensional system. A natural question to ask is, what is the connection between the different integral values, the different patterns from figure 23 and the stability properties of the corresponding limit cycles.

For a fixed pattern of synchrony and different integral values the answer to this question is a direct consequence of the theory of Γ- equivariant dynamical systems. Let Γ denote the symmetry group of the 4×4 hexagonal lattice. Remark that the group Γ is a subgroup of the permutation group S_{16}. Each pattern Pk from figure 23 is invariant under a subgroup Σ_k: i.e. $\Sigma_k \subset \Gamma \subset S_{16}$. Each permutation $\pi_{mn} \in S_4$, corresponding to a change in the integral value $I_m \to I_n$, can be naturally lifted to a permutation $\Pi^{(k)}_{mn} \in S_{16}$: the transformation on the 4-dimensional polydiagonal associated with Pk is also a transformation in the full 16-dimensional system. Therefore, if $\Pi^{(k)}_{mn}$ is an element of the symmetry subgroup Σ_k then, on the polydiagonal associated with Pk, the limit cycle characterized by the integral values I_m and I_n have identical dynamical properties. In particular they have the same stability properties in terms of the sets of multipliers. Consider the example of pattern P3. In figure 23 as well as in figure 28 the colors of the clusters are chosen such that the first cluster is red, the second blue, the third green and the fourth yellow: (r, b, g, y). Therefore, for simplicity, we can associate this ordering with the indexing used in table 1. There, it corresponds to integral region 5, or in terms of the indexing of the

six integrals, to $(r, b, g, y) \equiv (i, j, k, l)$. The symmetry on the lattice w.r.t. exchange of the blue and yellow oscillators ($b \leftrightarrow y$), corresponds to a permutation invariance w.r.t. exchange of index j and l ($j \leftrightarrow l$). Thus, according to table 1 the equivalence between the integral regions for pattern P3 is as follows

$$\begin{array}{ccccc} j \leftrightarrow l & \text{Pattern P3} & & & \\ (i,j,k,l) \equiv (i,l,k,j) & \Leftrightarrow & \text{Region } 5 \equiv \text{Region } 6 & s3(I) & \\ (i,l,j,k) \equiv (i,j,l,k) & \Leftrightarrow & \text{Region } 1 \equiv \text{Region } 4 & s3(II) & \\ (i,k,l,j) \equiv (i,k,j,l) & \Leftrightarrow & \text{Region } 3 \equiv \text{Region } 2 & s3(III)\,. & \end{array} \tag{48}$$

In particular, on the polydiagonal associated with P3 a limit cycle characterized by $I = R(i, j, k, l)$ has the same stability properties as a limit cycle characterized by $I^{'} = R(i, l, k, j)$. This identifications show that on P3 the stability properties of limit cycles are classified in three stability classes $s3(I)...s3(III)$. In a similar way, we can see that the same holds for patterns $P2, ..., P6$ from figure 23. For example, in pattern P4 the exchange of the blue and green oscillators leads to a symmetry connected configuration of the clusters. Using the same identification $(r, b, g, y) \equiv (i, j, k, l)$, on the lattice, the symmetry $b \leftrightarrow g$ of P4 corresponds to a permutation invariance $j \leftrightarrow k$. From table 1 follows that the resulting equivalence between the integral regions for pattern P4 is

$$\begin{array}{ccccc} j \leftrightarrow k & \text{Pattern P4} & & & \\ (i,j,k,l) \equiv (i,k,j,l) & \Leftrightarrow & \text{Region } 5 \equiv \text{Region } 2 & s4(I) & \\ (i,l,j,k) \equiv (i,l,k,j) & \Leftrightarrow & \text{Region } 1 \equiv \text{Region } 6 & s4(II) & \\ (i,k,l,j) \equiv (i,j,l,k) & \Leftrightarrow & \text{Region } 3 \equiv \text{Region } 4 & s4(III)\,. & \end{array} \tag{49}$$

Here, the stability properties of limit cycles are also classified in three stability classes $s4(I)...s4(III)$, although, the equivalence between the integral regions is not the same. Remark that pattern P1 is an exception since any exchange of the clusters leads to a symmetric copy of the original pattern. Therefore, for P1, the limit cycles from different integral regions have identical stability properties, classified in a single stability class $s1$:

$$\begin{array}{c} \text{Pattern P1} \\ (i,l,j,k) \equiv (i,k,j,l) \equiv (i,k,l,j) \equiv (i,j,l,k) \equiv (i,j,k,l) \equiv (i,l,k,j) \\ \Leftrightarrow \\ \text{Region } 1 \equiv \text{Region } 2 \equiv \text{Region } 3 \equiv \text{Region } 4 \equiv \text{Region } 5 \equiv \text{Region } 6 \end{array}$$

It is interesting to observe, from the numerical investigation of the system, that the stability classes associated to different patterns are also related. Consider, for example, the stability class $s3(III)$ from equations (48). From the point of view of the permutation group S_4 (accordingly its lift to S_{16}) the equivalence relation within the stability class $s3(III)$ corresponds to the permutation $(i_1, i_2, i_3, i_4) \mapsto (i_1, i_2, i_4, i_3)$, or to the S_4 group element $(3, 4)$. A comparison to the stability classes of pattern P4 from equations (48) shows that this is the same equivalence relation as in $s4(II)$. And indeed, the limit cycles characterized by permutation-related integral values from integral regions 2 and 3 on the polydiagonal P3 have the same

		Integral Region					
		Region 1	Region 2	Region 3	Region 4	Region 5	Region 6
P1	$r \leftrightarrow g$ $r \leftrightarrow b$ $r \leftrightarrow y$	$\mathcal{A}$	$\mathcal{A}$	$\mathcal{A}$	$\mathcal{A}$	$\mathcal{A}$	$\mathcal{A}$
P2 P3	$r \leftrightarrow g$ $b \leftrightarrow y$	$\mathcal{B}$	$\mathcal{C}$	$\mathcal{C}$	$\mathcal{B}$	$\mathcal{D}$	$\mathcal{D}$
P4	$r \leftrightarrow y$ $b \leftrightarrow g$	$\mathcal{C}$	$\mathcal{B}$	$\mathcal{D}$	$\mathcal{D}$	$\mathcal{B}$	$\mathcal{C}$
P5 P6	$r \leftrightarrow b$ $g \leftrightarrow y$	$\mathcal{D}$	$\mathcal{D}$	$\mathcal{B}$	$\mathcal{C}$	$\mathcal{C}$	$\mathcal{B}$

Table 2: Classification of the combinations of different patterns and integral regions into the stability classes $\mathcal{A}$, $\mathcal{B}$, $\mathcal{C}$, $\mathcal{D}$. The symmetry-transformation resulting from pairwise exchange of the clusters ($c_i \leftrightarrow c_j$) are shown for the different patterns.

stability properties as the limit cycles characterized by permutation-related integral values from integral regions 1 and 6 on the polydiagonal P4. An investigation of the symmetries of all patterns under exchange of clusters and the corresponding permutation-relations reveals that there are, in total, four stability classes $\mathcal{A}$, $\mathcal{B}$, $\mathcal{C}$, $\mathcal{D}$. The results are summarized in Table 2. Each of the stability classes corresponds to equivalence relation expressed in terms of group element of S_4:

$$\begin{aligned} \mathcal{A} &\equiv (1,2,3,4) \\ \mathcal{B} &\equiv (1,4)(2,3) \\ \mathcal{C} &\equiv (1,3)(2,4) \\ \mathcal{D} &\equiv (1,2)(3,4) \end{aligned}$$

Observe, once again, the manifestation of D_4 and $Z_2 \otimes Z_2$ symmetry groups. Here, it is a direct consequence of the lift of the network of four globally coupled oscillators to the Shrikhande graph.

It remains to investigate how the stability of the continua changes in the full 16-dimensional phase space with respect to κ. Each limit cycle from a continuum, independent on the integral value characterizing it or the pattern of synchrony it belongs to, is born at κ_{crit}. However, depending on the integral value and the pattern of synchrony (i.e. the corresponding stability class), each limit cycle becomes stable at different κ below κ_{crit}. When we speak of the stability of the continuum, we mean an integral region within the continuum comprising stable, respectively, unstable limit cycles. From table 2 we can see that it is sufficient to consider the stability of each class only in a single integral region since the remaining integral values can be obtained by the integral relations (41). Figure 29 represents, for integral region 3 ($I \in [0, 0.5]$), the stability changes of the four stability classes with respect to the coupling parameter κ. The figures represent a κ range from $\kappa = -0.65$ down to $\kappa = -1$. The red color indicates unstable regions and the blue color, respectively, stable regions. At the boundary between stable and unstable regions, green color indicates a transitions of a single multiplier in/out the unit circle and light blue (cyan) indicates a transition of a pair of complex conjugate multipliers

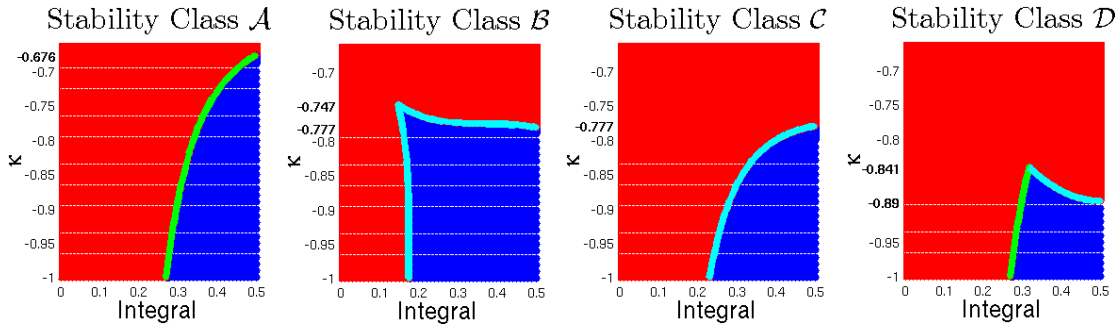

Figure 29: Dependence of the four stability classes from table 2 on the integral value and on κ. The red color indicates unstable regions and the blue color, respectively, stable regions. At the boundary between stable and unstable regions, green color indicates a transitions of a single multiplier in/out the unit circle and light blue (cyan) indicates a transition of a pair of complex conjugate multipliers in/out the unit circle.

in/out the unit circle. For κ values above the upper boundary shown in the figure, $\kappa = -0.65$, up to κ_{crit} the corresponding stability classes are unstable for the whole integral range. From the figure we can see that the four stability classes "stabilize" at different κ values. For example, in stability class $\mathcal{A}$ the first stable limit cycle appears at $\kappa = -0.676...$ and integral value $I = 0.5$, while in stability class $\mathcal{B}$ the first stable limit cycle appears at $\kappa = -0.747...$ and integral value $I \approx 0.146....$ Further decrease of κ extends the stability region and gradually shifts the boundary of the stable region towards $I = 0$. The integral values $I = 0, 1, \pm\infty$, as we have seen, are exceptional. From equation (45) and the corresponding discussion we know that at those integral values the degeneracy of the system is higher than at any other value: the 4-dimensional system becomes 2-dimensional. Asymptotically, for $\kappa \to -\infty$, all stability classes become stable within the whole integral region, however, the corresponding 2-dimensional limit cycles at $I = 0, 1, \pm\infty$ remain unstable for $\kappa \ll \kappa_{crit}$.

Phase Dynamics on Small Hexagonal Lattices with Repulsive Coupling: Conclusions

In this part of the work we have investigated the phase dynamics of coupled "active rotators" on small hexagonal lattices with repulsive coupling. We have seen that the symmetries of the underlying graph are emphasized in the symmetries of the dynamical states and play a crucial role in synchronization, by determining the flow-invariant polydiagonals and therefore, admissible clustered states. As a result, a network with local symmetries, describing a non-globally coupled system, may exhibit stable dynamical states with reduced symmetries, or even reduce to a globally coupled system. In such cases the dynamics takes place on the corresponding polydiagonal and the dimensionality of the initial system is strongly reduced. The variety of dynamical states may range from synchronized steady states and periodic solutions, quasi-periodicity and chaos, to weak-chimera states. It is remarkable that in the single model of a doubly periodic hexagonal lattice we could observe so many different dynamical states, accompanied by a various bifurcation scenarios: period doubling bifurcations, Neimark-Sacker bifurcation, saddle-node bifurcations, pitchfork bifurcations, transcritical bifurcations, homoclinic bifurcations and also the not so common transcritical/homoclinic (THB) bifurcations.

In particular, we have seen that spatio-temporal symmetries of synchronous states are directly connected to symmetries, not of the full, but of the corresponding reduced networks. Nevertheless, we have observed that bifurcation scenarios, in terms of symmetry breaking, do not depend solely on the local symmetries of the network or corresponding reduced system, but also on global characteristics of the full network, such as the network size, for instance. The reason is that a symmetry breaking of a synchronous state, in general, leads to a different synchronous state; and the existence of the latter state is restrained by the network topology of the full system.

Furthermore, if the synchronous state corresponds to a globally coupled system and the coupling function belongs to the class of "sinusoidally coupled" systems, compatible with the Watanabe-Strogatz reduction [111, 112, 78], the dimensionality is reduced further to three dimensions with a corresponding set of constants of motion (integral values). In the investigated system, this reduction takes place in the case of the 4×4 hexagonal lattice leading to the emergence of continua of limit cycles. There, we observed connections between the discrete symmetries of the network topology and continuous shifts in the integral value, both influencing the spatio-temporal symmetries of synchronous states.

3 Watanabe-Strogatz Reduction and Cluster Reduction

In this section we investigate general necessary conditions allowing the Watanabe-Strogatz (WS) reduction in networks with local non-trivial coupling topology. In the subsection 3.1 we indicate a general structure of the equations of motion compatible with the WS reduction [111, 112, 78]. In subsection 3.2 we recall some notions and conditions about cluster reduction [97, 50] which were introduced in section 1.2 and combine them in section 3.3 with the conditions derived in subsection 3.1 to obtain a class of network topologies compatible with the WS reduction. In sections 4 and 5 we give examples of networks with such topologies and discuss their dynamical properties. In section 6 we present a generic analysis of bifurcations taking place on the WS submanifold, explaining the observations from previous sections.

3.1 Watanabe-Strogatz Reduction

In [111] Watanabe and Strogatz show that a dynamical system of N phase oscillators with global cosine coupling is integrable and possesses N–3 integrals of motion. In a subsequent publication [112], investigating the dynamical properties of Josephson junction arrays, the authors show that the results hold for a general class of ODE's. Any system of N "sinusoidally coupled" phase oscillators, i.e.

$$\dot{\varphi}_j = g + f e^{i\varphi_j} + \bar{f} e^{-i\varphi_j} \quad j = 1, ..., N \ , \tag{50}$$

can be reduced to 3-dimensional system with $N-3$ constants of motion. Here, f is a smooth complex valued 2π-periodic function of the phases $\varphi_1, ..., \varphi_N$, and g is a real valued function. The important condition for the reduction is that the functions f and g are the same for all oscillators and thus do not depend on the index j. In a latter work [78], Marvel, Mirollo and Strogatz prove the connection of the WS reduction to the 3-dimensional Möbius group of transformations. In this subsection, without going into details about the reduction itself, we emphasize the form of the coupling topology compatible with the WS reduction.

Let us consider a general class of equations of motion describing a system of diffusively coupled phase oscillators with interactions depending not on the values of the instantaneous phases but on their differences

$$\begin{aligned}
\dot{\varphi}_j &= \omega_j + \sum_{l\geq 1} p_{j,l} e^{il\varphi_j} + \bar{p}_{j,l} e^{-il\varphi_j} + \\
&\qquad \sum_{k=1}^{N} D_{jk} \left\{ \sum_{l\geq 1} q_{jk,l} e^{il\varphi_k} e^{-il\varphi_j} + \bar{q}_{jk,l} e^{-il\varphi_k} e^{il\varphi_j} \right\} \qquad (51) \\
&= \omega_j + \sum_{l\geq 1} \left\{ p_{j,l} + \sum_{k=1}^{N} D_{jk} \bar{q}_{jk,l} e^{-il\varphi_k} \right\} e^{il\varphi_j} + \\
&\qquad \sum_{l\geq 1} \left\{ \bar{p}_{j,l} + \sum_{k} D_{jk} q_{jk,l} e^{il\varphi_k} \right\} e^{-il\varphi_j}
\end{aligned}$$

Here, ω_j, which can be time dependent, denotes the eigenfrequency of oscillator j; the Fourier coefficients $p_{j,l}$ (and their complex conjugate) determine the form of the function that describes the internal dynamics of oscillator j; D_{jk} denotes the adjacency matrix coefficients that determines the coupling strength between oscillators j and k; and the Fourier coefficients $q_{jk,l}$ determine the form of the coupling function between those oscillators.

In order to mach the normal form in (50), only coupling functions including the first harmonic $l = 1$ are allowed. Furthermore, all oscillators should have the same eigenfrequency $\omega_j = \omega \, \forall j$, and the same dynamics in the decoupled case $p_j = p \, \forall j$. The coefficients $q_{jk,l=1}$ do not depend on l any more and can be absorbed in the matrix C by rewriting it as $C_{jk} = D_{jk} q_{jk}$. Finally, the matrix C should not depend on j which leads to the most general form:

$$\dot{\varphi}_j = \omega + \{p + \sum_{k=1}^{N} \bar{c}_k e^{-i\varphi_k}\} e^{i\varphi_j} + \{\bar{p} + \sum_{k=1}^{N} c_k e^{i\varphi_k}\} e^{-i\varphi_j}. \tag{52}$$

The coupling matrix C determines, for each oscillator k, coupling strength and coupling function which can be a sine, a cosine or a combination of those. This means that for a given oscillator k all other oscillators should be coupled to it with same coupling function and the same coupling strength. This renders the general form of the coupling matrix C

$$C = \begin{pmatrix} \widetilde{c}_1 & c_2 & \dots & \dots & c_N \\ c_1 & \widetilde{c}_2 & \dots & \dots & c_N \\ \vdots & \vdots & \ddots & & \vdots \\ \vdots & \vdots & & \ddots & \vdots \\ c_1 & c_2 & \dots & \dots & \widetilde{c}_N \end{pmatrix} \tag{53}$$

Each of the c_k's describes the "external" coupling and can be written as

$$c_k = \alpha_k \frac{1}{2\mathrm{i}} + \beta_k \frac{1}{2} \tag{54}$$

where $\alpha_k \in \mathbb{R}$ determines the coupling strength w.r.t. to the sine part and $\beta_k \in \mathbb{R}$ w.r.t. the cosine part of the coupling function. The $\widetilde{c}_k$'s in (53) describe the self coupling and can be written as

$$\widetilde{c}_k = \widetilde{\alpha}_k \frac{1}{2\mathrm{i}} + \widetilde{\beta}_k \frac{1}{2}. \tag{55}$$

Remark that we distinguish between *internal dynamics* of the oscillators, described by the coefficients p (and $\bar{p}$); and *self coupling*, described by the $\widetilde{c}_k$'s. At this point, this might seem superficial and the self coupling function might seem trivial. However, in section 3.3, when we consider the reduced system, corresponding to synchronous state on a flow-invariant polydiagonal, the equivalent to the coefficients $\widetilde{c}_k$ will describe the coupling within the same cluster, differentiating it from the internal dynamics of the single oscillators. Observe also that the coupling strength

$\widetilde{\alpha}_k \in \mathbb{R}$, w.r.t. the sine part of the self coupling function, can in general differ from the remaining α_k in the k-th column. This is because in (52) it will result in

$$\widetilde{\alpha}_k \sin(\varphi_k - \varphi_k) = 0 \ .$$

The coupling strength $\widetilde{\beta}_k \in \mathbb{R}$ w.r.t. the cosine part of the self coupling renders a constant

$$\widetilde{\beta}_k \cos(\varphi_k - \varphi_k) = \widetilde{\beta}_k \ ,$$

which can be seen as a shift in the eigenfrequency of oscillator k. Though, all oscillators should have the same eigenfrequency, and therefore $\widetilde{\beta}_k = \bar{\omega} \ \forall k$.

It is important to observe that if any of the c_k entries is zero, because of $c_{jk} = c_k \ \forall j$, the given oscillator will be decoupled from the system. Thus, the WS reduction is compatible only with system of identical oscillators with (not necessarily uniform) *global* coupling. Nevertheless, as we have seen in section 2.4, the WS reduction is also manifested on submanifolds in systems with non-global topologies, i.e. with C_{jk} depending both on j and k. In those systems the reduction is physically relevant if there exist clustered solutions whose associated polydiagonal is transversely stable and the corresponding reduced system has the from (52).

3.2 Cluster Reduction

In this subsection we shortly recall the notion of cluster reduction [97, 50] and give examples additional to those already introduced in section 1.2.

Two oscillators j and k belong to the same cluster if and only if $\varphi_j(t) = \varphi_k(t) \ \ \forall t$. Considering a given dynamical system, and analyzing an emerging clustered state, we can introduce an equivalence relation $\sim_{Cl}$ on the index set $\mathcal{C}$ of oscillators such that two oscillators j and k belong to the same $\sim_{Cl}$- equivalence class (i.e. $j \sim_{Cl} k$) if and only if j and k belong to the same cluster. Accordingly, the equivalence relation $\sim_{Cl}$ defines a "polysynchronous" subspace in the phase space $\mathcal{P}$ of the system

$$\Delta_{\sim_{Cl}} = \{\vec{\varphi} \in \mathcal{P} \,|\, j \sim_{Cl} k \Longleftrightarrow \varphi_j(t) = \varphi_k(t) \ \ \forall t\}.$$

It is important to remark that the polysynchronous subspace, determined in such a way, is flow-invariant per definition: i.e. we observe a clustered state and identify with it a subspace, or in particular, an equivalence relation. Yet, this is not the case for an arbitrary subspace. Following the notation in [97, 50] we introduce an equivalence relation $\bowtie$ on the index set $\mathcal{C}$ which defines a generic polysynchronous subspace (or polydiagonal)

$$\Delta_{\bowtie} = \{\vec{\varphi} \in \mathcal{P} \,|\, j \bowtie k \Longrightarrow \varphi_j = \varphi_k\}.$$

Generally, this polysynchronous subspace is not flow-invariant and a trajectory which lies on $\Delta_{\bowtie}$ at a given time t' will not remain on $\Delta_{\bowtie}$. In section 1.2 we have shown in Theorem 1, in analogy to [97, 50], that a polysynchronous subspace defined by an equivalence relation $\sim$ on the index set $\mathcal{C}$ is flow-invariant if and only if all oscillators that belong to the same equivalence class have the same internal dynamics and receive the same external input: i.e. if the equivalence relation is balanced. Furthermore, on the flow-invariant polysynchronous subspaces the dynamics

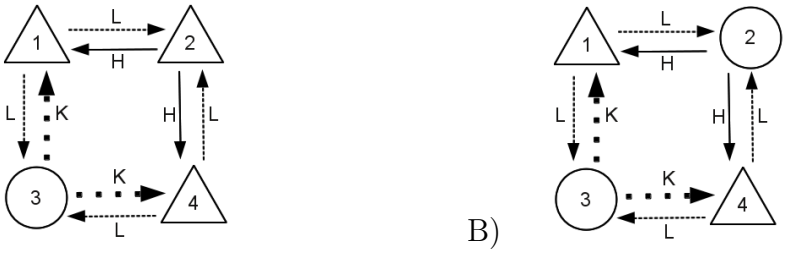

Figure 30: Two systems of four coupled phase oscillators

of the original N-dimensional system can be reduced to a P-dimensional dynamics, with P denoting the number of clusters (i.e. the dimension of the polysynchronous subspace). This cluster reduction takes place because all oscillators that belong to the same cluster have identical dynamics and, since the clustered state is flow-invariant, a single representative of each of the clusters is sufficient to describe the behavior of all other elements of the same cluster.

We consider two simple examples of systems comprising four coupled phase oscillators (figures 30A and 30B).

Example 1: Consider first the system in figure 30A. Its most general form is given by:

$$\begin{aligned}
\dot{\varphi}_1 &= \Omega + G(\varphi_1) + \alpha H(\varphi_2 - \varphi_1) + \beta K(\varphi_3 - \varphi_1) \\
\dot{\varphi}_2 &= \Omega + G(\varphi_2) + \gamma L(\varphi_1 - \varphi_2) + \gamma L(\varphi_4 - \varphi_2) \\
\dot{\varphi}_3 &= \omega + g(\varphi_3) + \gamma L(\varphi_1 - \varphi_3) + \gamma L(\varphi_4 - \varphi_3) \\
\dot{\varphi}_4 &= \Omega + G(\varphi_4) + \alpha H(\varphi_2 - \varphi_4) + \beta K(\varphi_3 - \varphi_4)
\end{aligned}$$

where ω, Ω denote the eigenfrequency, and the 2π-periodic functions $g(x)$, $G(x)$, respectively $H(x)$, $K(x)$, $L(x)$, describe the internal dynamics, respectively the coupling between the oscillators. Observe that only oscillators 1 and 4 are identically coupled to the network. In any other case the involved oscillators would have either different internal dynamics (for example oscillators 2 and 3) and/or different external input (for example oscillators 2 and 4). Therefore, in the only possible clustered state of this system, oscillators 1 and 4 belong to the same cluster and the dynamics can be restricted to the polydiagonal

$$\Delta = \{\vec{\varphi} \in \mathcal{P} \,|\, 1 \sim 4 \Longrightarrow \varphi_1 = \varphi_4\}.$$

It can be easily seen, after substitution, that the polydiagonal $\mathcal{P}$ is flow-invariant and the system can be reduced to a 3-dimensional system: choosing oscillator 1 as a representative for the cluster $\{1, 4\}$ and rescaling the coupling constant $\gamma \mapsto \gamma' = 2\gamma$

$$\begin{aligned}
\dot{\varphi}_1 &= \Omega + G(\varphi_1) + \alpha H(\varphi_2 - \varphi_1) + \beta K(\varphi_3 - \varphi_1) \\
\dot{\varphi}_2 &= \Omega + G(\varphi_2) + \gamma' L(\varphi_1 - \varphi_2) \\
\dot{\varphi}_3 &= \omega + g(\varphi_3) + \gamma' L(\varphi_1 - \varphi_3)
\end{aligned}$$

Example 2: In figure 30B oscillators 2 and 3 have identical internal dynamics and the system is described by

$$\begin{aligned}
\dot{\varphi}_1 &= \Omega + G(\varphi_1) + \alpha H(\varphi_2 - \varphi_1) + \beta K(\varphi_3 - \varphi_1) \\
\dot{\varphi}_2 &= \omega + g(\varphi_2) + \gamma L(\varphi_1 - \varphi_2) + \gamma L(\varphi_4 - \varphi_2) \\
\dot{\varphi}_3 &= \omega + g(\varphi_3) + \gamma L(\varphi_1 - \varphi_3) + \gamma L(\varphi_4 - \varphi_3) \\
\dot{\varphi}_4 &= \Omega + G(\varphi_4) + \alpha H(\varphi_2 - \varphi_4) + \beta K(\varphi_3 - \varphi_4)
\end{aligned}$$

This system allows 3- cluster states which lie on the corresponding flow-invariant polydiagonals:

$$\Delta_{14} = \{\vec{\varphi} \in \mathcal{P} \,|\, 1 \sim 4 \Longrightarrow \varphi_1 = \varphi_4\}$$

$$\Delta_{23} = \{\vec{\varphi} \in \mathcal{P} \,|\, 2 \sim 3 \Longrightarrow \varphi_1 = \varphi_4\}$$

$$\Delta_{14,23} = \Delta_{14} \cap \Delta_{23}.$$

In the last case, for example, the reduced system is 2-dimensional and the dynamics is given by

$$\begin{aligned}
\dot{\varphi}_1 &= \Omega + G(\varphi_1) + \alpha H(\varphi_2 - \varphi_1) + \beta K(\varphi_2 - \varphi_1) \\
\dot{\varphi}_2 &= \omega + g(\varphi_2) + 2\gamma L(\varphi_1 - \varphi_2).
\end{aligned}$$

It is interesting to remark that the reduction on the $\Delta_{14,23}$ polydiagonal would also be possible in the case of different coupling strengths γ:

$$\begin{aligned}
\dot{\varphi}_2 &= \omega + g(\varphi_2) + \gamma_{21} L(\varphi_1 - \varphi_2) + \gamma_{24} L(\varphi_4 - \varphi_2) \\
\dot{\varphi}_3 &= \omega + g(\varphi_3) + \gamma_{31} L(\varphi_1 - \varphi_3) + \gamma_{34} L(\varphi_4 - \varphi_3)
\end{aligned}$$

provided that $\gamma_{21} + \gamma_{24} = \gamma_{31} + \gamma_{34}$. But on the other hand, this difference would spoil the flow invariance of Δ_{23}. This last observation shows that it is possible to "switch on and off" certain clustered states by varying the corresponding coupling strengths. Moreover, this shows that the coupling strength controls the stability properties along the synchronous subspaces.

Here, we are interested in N-dimensional systems that do not obey equation (52) but, nevertheless, allow the WS reduction in synchronous states such that their dynamics on the corresponding P-dimensional polysynchronous subspaces becomes 3-dimensional with $P - 3$ constants of motion.

3.3 Requirements on the System of Coupled Phase Oscillators

In this section, we investigate how the requirement– that a system should obey equation (52), not in general, but only on a flow-invariant polydiagonal– constrains the dynamical properties of a generic system (51). The cluster reduction from the total phase space to the polydiagonal only rescales the coupling strengths, according

to the size of the corresponding clusters, and leaves the involved coupling functions unchanged. Therefore, the functions governing the dynamics of the whole N-dimensional system should have the same form as those in equation (52); i.e. we have to consider phase oscillators with identical internal dynamics and sinusoidal coupling:

$$\dot{\varphi}_j = \omega + \{p + \sum_{k=1}^{N} \bar{\Theta}_{jk} e^{-i\varphi_k}\} e^{i\varphi_j} + \{\bar{p} + \sum_{k=1}^{N} \Theta_{jk} e^{i\varphi_k}\} e^{-i\varphi_j} \quad \text{with } j = 1, .., N \ . \quad (56)$$

Here, the entries of the $N \times N$ coupling matrix Θ should have the following form

$$\theta_{jk} = a_{jk} \frac{1}{2\mathrm{i}} + b_{jk} \frac{1}{2}.$$

For later convenience we write the coupling matrix as $\Theta = \frac{1}{2\mathrm{i}} A + \frac{1}{2} B$ with A and B real valued matrices. Moreover, recall from section 1.2 that the coupling matrix is invariant w.r.t. renumbering of the oscillators. Accordingly, here, the oscillators belonging to the same cluster are chosen have subsequent indices, see equation (15) from section 1.2.

From above we know that oscillators belonging to the same cluster should have identical internal dynamics and receive the same external input. The first of these conditions is already fulfilled in equation (56). The second condition is a restriction on the coupling matrix, which on the polydiagonal should coincide with the form of equation (53). In equation (52) each variable φ_j stands for a single oscillator but on the polydiagonal it would stand for a whole cluster. This means that instead of the c_k's in (53) there would be a matrix. Therefore, Θ takes the following form

$$\Theta = \frac{1}{2i} \begin{pmatrix} [\widetilde{A}_{11}] & [A_{12}] & \cdots & [A_{1P}] \\ [A_{21}] & [\widetilde{A}_{22}] & \cdots & [A_{2P}] \\ \vdots & \vdots & \ddots & \vdots \\ [A_{P1}] & [A_{P2}] & \cdots & [\tilde{A}_{PP}] \end{pmatrix} + \frac{1}{2} \begin{pmatrix} [\widetilde{B}_{11}] & [B_{12}] & \cdots & [B_{1P}] \\ [B_{21}] & [\widetilde{B}_{22}] & \cdots & [B_{2P}] \\ \vdots & \vdots & \ddots & \vdots \\ [B_{22}] & [B_{P2}] & \cdots & [\widetilde{B}_{PP}] \end{pmatrix} \quad (57)$$

On the diagonals, $[\widetilde{A}_{kk}]$ and $[\widetilde{B}_{kk}]$ are block matrices and have dimension S_k corresponding to the size of the k-th cluster. Those matrices describe the coupling topology between the oscillators within the same cluster. The off diagonal matrices $[A_{jk}]$ and $[B_{jk}]$ are $S_k \times S_j$ rectangular matrices and have dimension corresponding to the sizes S_j and S_k of the j-th and k-th cluster respectively. They describe the coupling topology between the elements of clusters j and k. From (54) we know that for a given oscillator k all other oscillators should be coupled to it with the same coupling function and the same coupling strength. On the polydiagonal this means that for a given cluster k all other oscillators belonging to a different cluster j should receive the same input from cluster k. Combining this with the observation in example 2 from the previous section, that a polydiagonal can be left flow-invariant also for different coupling strengths, provided that their sums are identical, we deduce the following condition for the coefficients describing the inter cluster coupling:

$$\begin{array}{l} \sum_{n=1}^{S_k} (a_{jk})_{mn} = \alpha_k \ \ \forall j,\ j \neq k;\ \forall m = 1, .., S_j \\ \sum_{n=1}^{S_k} (b_{jk})_{mn} = \beta_k \ \ \forall j,\ j \neq k;\ \forall m = 1, .., S_j \end{array} \quad (58)$$

where $(a_{jk})_{mn}$ and $(b_{jk})_{mn}$ denote the entries of the matrices $[A_{jk}]$ and $[B_{jk}]$ respectively. The constants α_k and β_k describe the coupling strengths between the clusters of the reduced system (see equation (22) from section 1.2), and are in one to one correspondence to those in equation (54).

Consider now the coupling within the clusters given by $[\widetilde{A}_{kk}]$ and $[\widetilde{B}_{kk}]$. From (55) we know that the odd (sine) part of the coupling function between elements of the same cluster does not affect the dynamics and therefore does not impose any condition on the $[\widetilde{A}_{kk}]$ matrices. The even (cosine) part $[\widetilde{B}_{kk}]$ of the coupling strengths can be seen as a shift in the eigenfrequencies, which should be identical for all oscillators and therefore leads to

$$\sum_n (\widetilde{b}_{kk})_{mn} = \bar{\omega} \;\; \forall k; \forall m.$$

In the following sections we first give examples of systems with non-global coupling topology where the WS reduction is, initially, not expected but, nevertheless, takes place on submanifolds corresponding to reduced systems compatible with condition (58). We will see that in some cases those manifolds become transversely stable and the reduction is directly observable. In section 4 we consider coupled phase oscillators with different ring topologies. In section 5 we investigate a class of semi-globally coupled systems with a topology naturally compatible with the WS reduction. Finally, in section 6 we present a generic analysis of bifurcations taking place on the WS submanifold, explaining the observations from previous sections.

General Form of the Investigated Systems

In analogy to section 2, we choose, for the dynamics of the phase oscillators, a system of excitable sinusoidally coupled "active rotators" [91]:

$$\dot{\phi}_i = \omega - \sin\phi_i + \frac{\kappa}{\mathcal{N}} \sum_j \mathcal{A}_{ij} \sin(\phi_j - \phi_i), \;\; i = 1, ..., N \; . \tag{59}$$

where $\mathcal{A}_{ij}$ describes the corresponding topology and κ the coupling strength. In the examples, where $\mathcal{A}$ is a regular graph, the normalization factor $\mathcal{N}$ equals the degree of the graph $\mathcal{N} = D = \sum_j \mathcal{A}_{kj}$, otherwise, it equals the total number of oscillators $\mathcal{N} = N$. The Jacobi Matrix of the system is given by

$$J_{ik} = \frac{\partial \dot{\phi}_i}{\partial \phi_k} = \begin{cases} -\cos\phi_i - \frac{\kappa}{\mathcal{N}} \sum_j \mathcal{A}_{kj} & i = k \\ \frac{\kappa}{\mathcal{N}} \mathcal{A}_{ik} \cos(\phi_k - \phi_i) & i \neq k \end{cases}$$

Recall from section 2, that in the attractive regime (i.e. $\kappa > 0$), the synchronous 1-cluster solution given by $\phi_i = \arcsin\omega = \phi_s^{(0)}$ is stable. This solution remains stable also for negative κ and loses stability at $\kappa_{crit} < 0$. For this 1-cluster state the Jacobi Matrix reads

$$J = \frac{\kappa}{\mathcal{N}} \mathcal{A} - \sqrt{1 - \omega^2}\,\mathbb{E} - \frac{\kappa}{\mathcal{N}} \mathbb{D} \tag{60}$$

where $\mathbb{E}$ is the identity matrix and $\mathbb{D}$ is the degree matrix of the graph; i.e. $\mathbb{D}$ is a diagonal matrix with diagonal elements $\sum_j \mathcal{A}_{kj} = d_k$ and zeros otherwise. It is

convenient to use the Laplace matrix of the graph, given by

$$L(A) = (\mathbb{D} - \mathcal{A}) \,,$$

and its eigenvalues Λ_i. The eigenvalues of the Jacobi matrix (60) become

$$\lambda_i = \frac{-\kappa}{\mathcal{N}} \Lambda_i - \sqrt{1-\omega^2} \ . \tag{61}$$

The critical value of κ, where the 1-cluster synchronous solution loses stability, is calculated at $\lambda_i = 0$ and corresponds to the largest eigenvalue Λ_{max}

$$\kappa_{crit} = -\frac{\mathcal{N}\sqrt{1-\omega^2}}{\Lambda_{max}}. \tag{62}$$

Remark that $0 = \Lambda_0 \leq \Lambda_1 \leq ... \leq \Lambda_{N-1} = \Lambda_{max}$ [23]. At κ_{crit} the synchronous 1-cluster solution with $\phi_i = \phi^{(s)} = \arcsin\omega \ \forall i$ becomes unstable but remains a fixed point for the system at any κ value. At each subsequent smaller eigenvalue Λ_i a corresponding bifurcation takes place affecting further the stability of the synchronous 1-cluster solution.

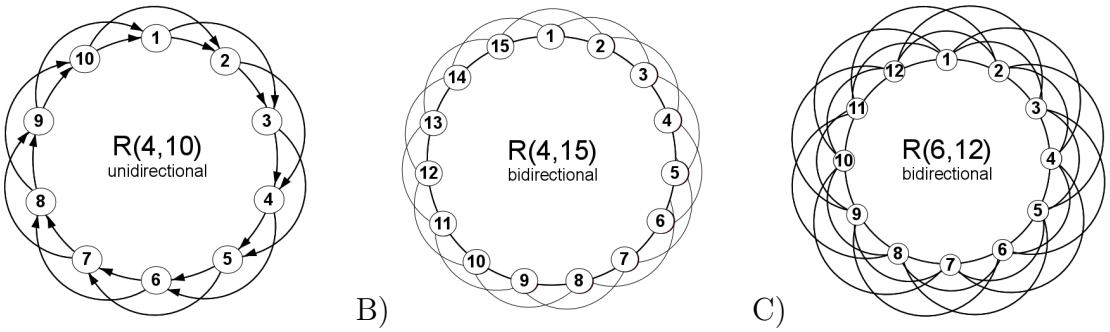

Figure 31: Examples for ring topologies. A) Unidirectional ring $R(4, 10)$. B) Bidirectional ring $R(4, 15)$. C) Bidirectional ring $R(6, 12)$.

4 Ring Topologies and the Watanabe-Strogatz Reduction

In this section we investigate systems of sinusoidally coupled phase oscillators with different ring topologies. Figure 31 illustrates different examples of such ring topologies. From a graph theoretical point of view, what we call here a regular ring $R(D, N)$, corresponds a special case of a circulant graph [115]. It is a graph constructed as equally-spaced vertices on a circle, where each vertex v_k is coupled to the preceding m vertices $v_{k-m}, ..., v_{k-1}$ and the subsequent n vertices $v_{k+1}, ..., v_{k+n}$. Such a ring has degree $D = m+n$ and is denoted by $R(D, N)$, where N corresponds to the number of nodes. Here we consider unidirectional rings with $m = 0$ (see figure 31A) and bidirectional rings with $m = n$ (see figures 31B and 31B). We show that on a regular ring $R(D, N)$, depending on the degree D of the nodes, for a given number of oscillators N, it is possible to build P clusters of size m such that the dynamics of the reduced P- cluster system becomes, according to the SW reduction, 3-dimensional with $P-3$ constants of motion. As we have seen in section 3.3, a necessary condition for the WS reduction is that in the cluster reduced state the system becomes globally coupled: i.e. each element of a given cluster should be coupled to at least one element of a different cluster and arbitrary many elements of its own cluster. From the examples of figure 31, it is easy to see that on the ring this requirement is fulfilled if the elements belonging to different cluster alternate, whereby all possible permutations are allowed (for the $R(4, 15)$ example, see figure 32). Hence, each cluster should have the same number of elements and therefore the number of internal/external connections between/within clusters should be, respectively, the same.

This leads to the following algebraic dependence

$$mP = N \tag{63}$$

$$E(P-1) + I = D \tag{64}$$

whit the additional conditions

- for bidirectional ring:
  $D = 2d$, $I = 2i$, $I \leq E \leq I + 2$

Bidirectional coupling $D = 8$

I	$P = \frac{D-I}{E} + 1$	Condition for E	E	P
0	$P = \frac{8}{E} + 1$	$E \in \{1, 2\}$	1	9
			2	5
2	$P = \frac{6}{E} + 1$	$E \in \{2, 3, 4\}$	2	4
			3	3
4	$P = \frac{4}{E} + 1$	$E \in \{4, 5, 6\}$	4	2

Unidirectional coupling $D = 4$

I	$P = \frac{D-I}{E} + 1$	Condition for E	E	P
0	$P = \frac{4}{E} + 1$	$E \in \{1\} < 2$	1	5
1	$P = \frac{3}{E} + 1$	$E \in \{1, 2\}$	1	4
2	$P = \frac{2}{E} + 1$	$E \in \{2, 3\}$	2	2

Table 3: Cluster states for regular ring of degree 8 for bidirectional coupling and degree 4 for unidirectional.

- for unidirectional ring: (global coupling condition)
  $P \leq D + 1$; $I = i$, $I \leq E \leq I + 1$.

Here, D denotes the degree of each node, P is the number of clusters, m is the size of the clusters, E is the number of external connections between an element of a given cluster towards every other cluster, and I is the number of internal connections within the same cluster; all of them being positive integers. Remark, once again, that those requirements describe only clustered states leading to globally coupled reduced systems, compatible with the WS reduction. On a given ring $R(D, N)$ there are, in general, other balanced polydiagonals corresponding to non-globally coupled clustered states. In the examples below, we will see that such non-globally coupled clustered states might appear as stable states in the system, however, we will mainly concentrate on those states leading to the WS reduction.

Table 3 gives examples for the possible cluster states compatible with the WS reduction requirements for two regular rings : one of degree 8 with bidirectional coupling and the other of degree 4 with unidirectional coupling. From (64) follows that without specification of the total number N of oscillators, for a given D, we can vary the number of internal connections I, which confines the number of possible external connections E, the latter additionally restricted by the fact that $\frac{D-I}{E}$ should always be an integer.

From the examples in table 3, we see that for given ring topology $R(D, N)$ there might be several possible clustered states compatible with the WS reduction. As we will see below, in the reduced P-dimensional system, for a given number of clusters P, the total number N, of oscillators on the ring, plays a secondary role: a change in the size m of the clusters does not influence the dynamical properties on the reduced phase space. However, in the full N-dimensional phase space this change will, in general, influence the stability properties transverse to the corresponding P-dimensional polydiagonal and affect whether or not the system reaches the state compatible with the WS reduction. The questions we are interested in are, on the one side, how the ring size affects the stability properties of the different admissible P-dimensional polydiagonals, and on the other side, for a fixed ring size allowing the existence of more than one P-dimensional polydiagonal, which of these polydiagonals, if any, are manifested as stable states.

Here, we concentrate on bidirectional rings with dynamics governed by equation (59) with $\mathcal{N} = D$. In the clustered state with P clusters the equations of motion (59) are reduced to a globally coupled system of P oscillators with identical coupling

and take the form

$$\dot{\psi}_i \;=\; \omega - \sin\psi_i + E\frac{\kappa}{D}\sum_{\substack{j=1\\ j\neq i}}^{P}\sin(\psi_j - \psi_i),\;\; i = 1, ..., P\ . \tag{65}$$

The synchronous 1-cluster solution $\psi_i = \arcsin\omega\ \forall i$ remains a fixed point also for the reduced system. However, on the corresponding polydiagonal, it changes stability at a critical value κ_{crit}^{diag} calculated with respect to the Jacobi matrix

$$J^{diag} = E\frac{\kappa}{D}\mathbb{I} - (\sqrt{1-\omega^2} + E\frac{\kappa}{D}(P-1))\mathbb{E}\ . \tag{66}$$

Here $\mathbb{E}$ is the P-dimensional identity matrix. The $P \times P$ matrix $\mathbb{I}$ is defined as

$$(\mathbb{I})_{ij} = \begin{cases} 0 & i = j \\ 1 & i \neq j \end{cases}$$

and has $P-1$ degenerate eigenvalues $\lambda_l^{\mathbb{I}} = -1\ l = 1, .., P-1$ and one eigenvalue $\lambda_{max}^{\mathbb{I}} = P-1$. Therefore the eigenvalues of the Jacobi matrix (66) are given by

$$\lambda_i^{diag} = -\frac{E\kappa}{D}(P - 1 - \lambda_i^{\mathbb{I}}) - \sqrt{1-\omega^2},\;\; i = 1, ..., P$$

and

$$\kappa_{crit}^{diag} = -\frac{D\sqrt{1-\omega^2}}{EP}\ . \tag{67}$$

Remark that the eigenvalues of the reduced system are also eigenvalues of the full N-dimensional system.

In the following subsections we investigate bidirectional rings of degree $D = 4$ and $D = 6$, whereby different ring sizes are chosen allowing for clustered states compatible with the WS reduction. In each of the considered cases, numerical investigations were performed at different values of κ below κ_{crit}; however, κ values slightly above κ_{crit} were also investigated, in order to search for possible hysteresis with the still stable synchronous 1-cluster state. For each of the κ values more than 2×10^3 initial conditions were chosen from a homogeneous random distribution on the corresponding $(2\pi)^N$ torus. Additionally, in all cases, we have investigated the stability properties of the dynamical states on the P-dimensional polydiagonals where the WS takes place for $P > 2$. There, the reduced P-dimensional globally coupled system (see equation (65)) undergoes a transcritical/homoclinic bifurcation, at the corresponding κ_{crit}^{diag}, giving birth to periodic orbits. For $P > 3$ each of these orbits belongs to a continuum and is characterized by $P-3$ constants of motion. As described in section 2.4, each constant of motion can take values within $(-\infty, +\infty)$, whereby the whole interval can be divided into six integral regions (see section 2.4, equations (39) to (41)). In section 2.4 figure 29, we have seen how the stability properties of the continuum change with respect to κ: once a stable region within the continuum of limit cycles appears, a shift of κ leads to a shift of the borders of the stable region. Expecting a similar behavior here, in order to investigate the stability properties of the continua of limit cycles, we have taken for each integral region

Bidirectional ring of degree $D = 4$

I	$P = \frac{D-I}{E} + 1$	Condition for E	E	P
0	$P = \frac{4}{E} + 1$	$E \in \{1, 2\}$	1	5
			2	3
2	$P = \frac{2}{E} + 1$	$E \in \{2\}$	2	2

Table 4: Cluster states for a bidirectional regular ring of degree 4.

five fixed values (in total 30 values per constant of motion): within the integral region $(0, 0.5]$ the values were chosen to be $[0 + \epsilon,\ 0.125,\ 0.25,\ 0.375,\ 0.5 - \epsilon]$; the values within the remaining five regions were derived via the integral relations from section 2.4, equation (41). At different κ values below the corresponding κ_{crit}^{diag}, we have considered all possible combinations of the $P - 3$ constants of motion at those values and investigated the stability properties of the corresponding limit cycles.

4.1 Rings of degree $D = 4$

Regarding the WS reduction requirement, a bidirectional ring of degree $D = 4$ allows cluster states with 2, 3 and 5 clusters, see table 4. Here, we concentrate on the only case where the dimension of the reduced phase space in the clustered state is greater than 3, i.e. $P = 5$. Restricting the investigation on small ring sizes, with $N = mP$, we consider the three rings with N =10, 15 and 25 oscillators, allowing the existence of five clusters comprising, respectively, m =2, 3 and 5 elements. Observe that in the case $m = 3$ (on $R(4, 15)$), besides $P = 5$, a reduced globally coupled clustered state $P = 3$ is also possible (see figure 32); for $m = 2$ (on $R(4, 10)$) and for $m = 5$ (on $R(4, 25)$) the only globally coupled clustered state, compatible with the WS reduction, is $P = 5$.

As discussed above, the WS reduction becomes apparent if and only if the corresponding polydiagonal of the reduced P-dimensional system is transversely stable for some $\kappa < \kappa_{crit}$, which in general depends on the ring size. In contrast, from equation (65), we see that the dynamics of the reduced system, on the polydiagonal, is independent of the ring size. A calculation of the critical coupling strength from (62) and (67) shows that on all three investigated rings $\kappa_{crit}^{diag\,(P=3,5)} < \kappa_{crit}$: i.e. the synchronous 1-cluster state loses stability in the full N-dimensional system at κ_{crit} but remains stable on the corresponding reduced polydiagonals. For the investigated κ values above κ_{crit}, in none of the three cases, a hysteresis with the still stable 1-cluster solution was observed. Similar to the examples from section 2, immediately after the loss of stability of the synchronous 1-cluster state, at κ_{crit}, chaotic dynamics takes place. Decreasing the coupling strength further reveals, in all three cases, desynchronized stable limit cycles corresponding to rotating waves with spatio-temporal symmetry, respectively, the dihedral group D_N: for $N = 10$, the symmetry group of the solution is $D_{10} = D_5 \otimes D_2$, whereby $\phi_i(t) = \phi_{(i+N/2)\mathrm{mod}N}(t + T/2)$; for $N = 15$, $D_{15} = D_5 \otimes D_3$, $\phi_i(t) = \phi_{(i+N/3)\mathrm{mod}N}(t + T/3)$; and surprisingly, for $N = 25$, $D_{25} \neq D_5 \otimes D_5$, the phase shift in this case is given by $\phi_i(t) = \phi_{(i+N/5)\mathrm{mod}N}(t + 3T/5) = \phi_{(i+2N/5)\mathrm{mod}N}(t + T/5)$. Similar to the cases of desynchronized periodic states from section 2, these non-trivial spatio-temporal

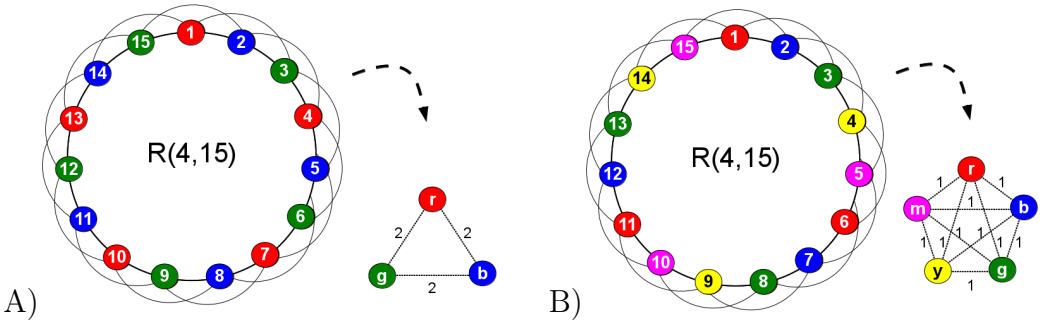

Figure 32: Patterns of synchrony on the $R(4,15)$ ring. A) 3-cluster pattern of synchrony. B) 5-cluster pattern of synchrony.

symmetries suggest that, here, the limit cycles are born from bifurcations leading to symmetry breaking of preceding limit cycles comprising smaller clusters.

In the cases, where $P > 2$ is allowed by the ring size, an S_P- THB bifurcation takes place: respectively, at $\kappa_{crit}^{diag\,(P=3,5)}$. As a result, in analogy to the examples from sections 2.2 and 2.4, periodic orbits are born (together with their symmetry related copies). For $P > 3$ the periodic orbits build a continuum and for $P = 3$ there is a single periodic orbit. Figure 32 gives an example of the resulting 3- and 5-cluster patterns of synchrony on the $R(4,15)$ ring. At the bifurcation, P symmetric copies of saddles collide with the fixed point of the synchronous 1-cluster state. Those saddles originate from 2- cluster states at $\kappa = 0$, whereby oscillators belonging to $P-1$ of the clusters are at $\phi^{(s)}$ and the oscillators comprising the remaining cluster are at $\phi^{(u)}$. However, unlike the examples from sections 2.2 and 2.4 where κ_{crit}^{diag} was equal to κ_{crit}, here, the fixed point of the synchronous 1-cluster state is already unstable. Hence, the periodic orbits resulting from the S_P- THB bifurcation, which are born stable in the reduced P-dimensional system, are inevitably unstable with respect to perturbations in the full N-dimensional phase space. For example, for $N = 15$, the limit cycle comprising three clusters, that is born at the S_3- THB bifurcation at $\kappa_{crit}^{diag\,(P=3)} = -0.4761$, becomes stable in a Neimark-Sacker bifurcation at $\kappa = -0.825 < \kappa_{crit}^{diag\,(P=3)}$. In contrast, recall from section 2.2 that there the corresponding limit cycle was immediately born stable in the full 9-dimensional space of the 3×3 hexagonal lattice. As we will see in sections 5 and 6, the 3×3 hexagonal lattice is a special case of a *complete k- partite graph* (with k=3) and for a given class of those graphs the limit cycles are always born stable at the THB bifurcation.

On the three rings $R(4,10)$, $R(4,15)$ and $R(4,25)$, the numerical investigations, based on the randomly distributed initial conditions in the full N-dimensional phase space, reveal that for certain $\kappa < \kappa_{crit}^{diag\,(P=5)}$ only few, if any, of the initial conditions converged towards the corresponding continuum of limit cycles on the 5 -dimensional polydiagonal. In all three cases, the additional investigation of the stability properties of the continua of limit cycles, based on the combinations of different values of the $P-3=2$ constants of motion, show that for some of the investigated κ values below $\kappa_{crit}^{diag\,(P=5)}$ there are integral pairs belonging to stable parts of the continuum. However, unlike the examples from section 2.4 where a shift of κ towards $-\infty$ grad-

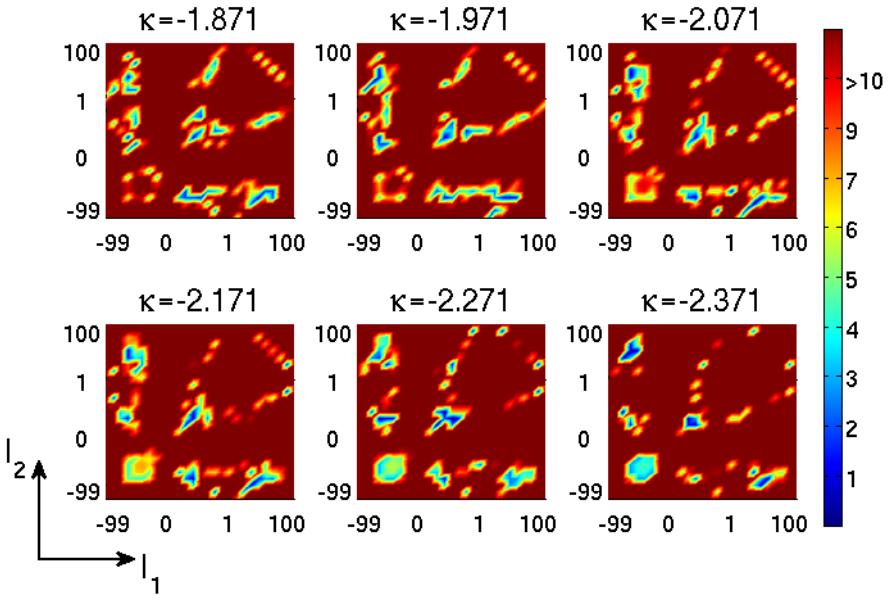

Figure 33: Change of the stability regions of the continua of limit cycles for the investigated pairs of integral vales at different κ vales in the case of $N = 10$, $P = 5$. The color corresponds to the absolute value of the largest multiplier.

ually enlarged the stability region (see figure 29), here, the stability regions appear in some κ ranges and then disappear again for lower κ values. The analysis of the multipliers of limit cycles shows that at the stability change, depending on the corresponding integral values, either pairs of complex conjugated multipliers cross the unit circle or single multipliers become greater than one. In the cases of $N = 15$, and $N = 25$ those stability regions appeared in very narrow intervals of the investigated κ values. For $N = 10$, the κ intervals are broader. Figure 33 represents the change of the stability region for the investigated pairs of integral vales at six subsequent κ values in the case of $N = 10$. The color in the figure corresponds to the absolute value of the largest multiplier, whereby the multipliers corresponding to the invariant directions of the continuum of limit cycles are not considered. Observe also that the integral regions are rescaled to the same size. This reveals a symmetry along the diagonal $I_1 = I_2$ which is due to permutation of the indices within the integral relations. We do not investigate these symmetries in more details here.

4.2 Rings of degree $D = 6$

For bidirectional rings of degree $D = 6$ there are four possible clustered states ($P = 2, 3, 4, 7$) which lead to globally coupled reduced systems, see table 5. For $P = 4$ and $P = 7$ the dimension of the corresponding reduced systems is greater than 3 and a WS reduction takes place. For each of those two cases we choose $m = 2, 3$. In total we investigate four rings $R(6, 8)$, $R(6, 12)$, $R(6, 14)$ and $R(6, 21)$. For $N = 8, 12$, the $P = 4$- cluster state is possible, and for $N = 14, 21$, the $P = 7$. Remark that here, once again, for $m = 3$, i.e. on $R(6, 12)$ and $R(6, 21)$, a $P = 3$ state of a reduced globally coupled system is also possible. Using equations (62) and

Bidirectional ring of degree $D = 6$

I	$P = \frac{D-I}{E} + 1$	Condition for E	E	P
0	$P = \frac{4}{E} + 1$	$E \in \{1, 2\}$	1	7
			2	4
2	$P = \frac{2}{E} + 1$	$E \in \{2\}$	2	3
			4	2

Table 5: Cluster states for a bidirectional regular ring of degree 6.

(67) we can see that for $P = 4$ $\kappa_{crit}^{diag\,(P=4)} = \kappa_{crit}$, while for $P = 7$ $\kappa_{crit}^{diag\,(P=7)} < \kappa_{crit}$ and for $P = 3$ $\kappa_{crit}^{diag\,(P=3)} < \kappa_{crit}$.

The observed dynamical phenomena on the rings $R(6, 14)$ and $R(6, 21)$ are, in general, similar to the those described in the previous section. For the investigated κ values above κ_{crit} no hysteresis was found with the still stable 1-cluster solution. In both cases, immediately after the loss of stability of the synchronous 1-cluster solution at κ_{cirt} the only observed dynamical states are chaotic. Further decrease of κ reveals desynchronized stable limit cycles corresponding to rotating waves with spatio-temporal symmetry, respectively, the dihedral group D_N. In the case of $N = 14$ the symmetry group is $D_{14} = D_7 \otimes D_2$ with a phase shift between the oscillators given by $\phi_i(t) = \phi_{(i+N/2)\mathrm{mod}N}(t + T/2)$ and for $N = 21$, $D_{15} = D_7 \otimes D_3$ with $\phi_i(t) = \phi_{(i+N/3)\mathrm{mod}N}(t + T/3)$. At the corresponding κ_{crit}^{diag} THB bifurcations take place giving birth to periodic solutions. However, unlike the examples from the previous section, here, the numerical investigation at κ values below $\kappa_{crit}^{diag\,(P=7)}$ did not reveal any stable integral regions of the continuum of limit cycles. Furthermore, in the case $N = 21$, the 3-cluster limit cycle born at $\kappa_{crit}^{diag\,(P=3)}$ in a THB bifurcation also remains unstable.

The two investigated rings $R(6, 8)$ and $R(6, 12)$, allowing the existence of $P = 4$-clustered states, also show dynamical phenomena similar to those observed in the previous sections, albeit with some peculiarities. The case of $N = 8$ is very much alike, up to the dimensionality, to the 3×3 hexagonal lattice from section 2.2. Here, for negative coupling strengths above κ_{crit} the only stable state is the 1-cluster synchronous solution. At $\kappa_{crit}^{diag\,(P=4)} = \kappa_{crit}$ a THB bifurcation takes place giving birth to a continuum of limit cycles. The similarity to the 3-dimensional case from section 2.2 is that, here, the whole continuum of limit cycles is immediately stable after the bifurcation. In fact, the $R(6, 8)$ ring is also a special case of a *complete k- partite graph* (with k=4) and belongs to a class of such graphs, where the limit cycles born at the corresponding THB bifurcation are always stable; see sections 5 and 6.

The $R(6, 12)$ ring exhibits very rich dynamics with dynamical states similar to those observed on the 4×4 hexagonal lattice in section 2.4. From all investigated rings this is the only one where the numerical investigation reveals a hysteresis for coupling strengths slightly above κ_{crit}: a stable 3-cluster limit cycle coexists with the still stable 1-cluster state. Figure 34 represents the corresponding 3-cluster pattern of synchrony and a phase plot of the periodic solution. Similarly to the hysteresis observed on the 4×4 hexagonal lattice, the limit cycle, here, is also a weak-chimera state [12]: the large (red) cluster comprising eight elements performs only small-

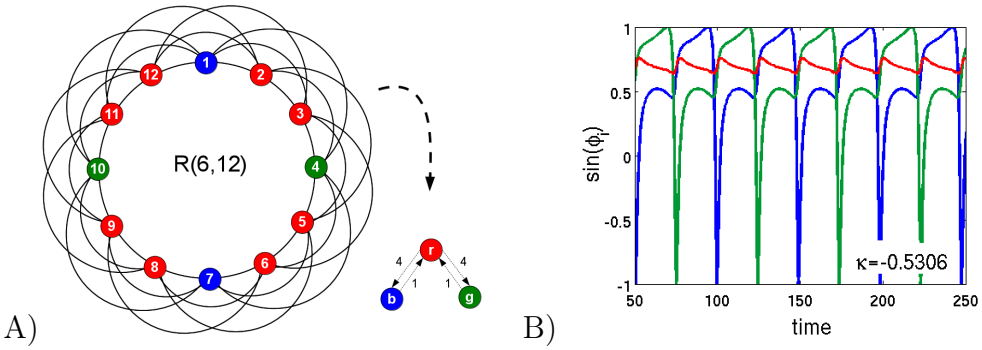

Figure 34: A) 3-cluster pattern of synchrony on $R(6,12)$ and the corresponding reduced system. B) Phase plot of the weak-chimera-like periodic solution.

scale librations, while the two small remaining clusters perform full-scale rotations with a phase shift corresponding to half of the period. Furthermore, here as well, the weak-chimera limit cycle is born stable in a saddle node bifurcation above κ_{crit}. It also remains stable in a certain κ range below κ_{crit}, where it coexists with a chaotic attractor in the system, until it loses stability in the Neimark-Sacker bifurcation and the system enters a purely chaotic state. Decreasing κ further reveals stable periodic solutions with different patterns of synchrony: 12 clusters (i.e. desynchronized state) which we call 12LC; 6 clusters which we call 6LC; as well as, the stable region of the continuum of 4-cluster limit cycles on the $P = 4$ polydiagonal. The spatio-temporal symmetry group of the desynchronized periodic solution 12LC is Z_2 with phase dynamics indicating that the limit cycle originates from the symmetry breaking of the 6-cluster state represented in figure 35A. The phase shift between the oscillators is such that oscillators previously belonging to the same cluster are now shifted by half of the period: for example $\phi_1(t) = \phi_8(t+T/2)$. Figure 35B represents the pattern of synchrony for the observed 6-cluster solution 6LC. Remark that its reduced system is globally coupled, however, it is not subject to the WS reduction since the reduced matrix does not have the form required from equation (53): the requirement that a given oscillator from the reduced system coupes to all other oscillators with the same coupling strength is not fulfilled. Its spatio-temporal symmetry is $D_6 = D_3 \otimes D_2$, whereby the clusters that are coupled by the doubled coupling strength in the reduced system have phases shifted by half of the period: those are the pairs (r,m), (b,g), (k,y) and, for example, $\phi_b(t) = \phi_g(t+T/2)$. Observe that if we would identify further the oscillators belonging to those pairs (i.e. $\phi_b(t) = \phi_g(t)$ a.s.o) we would end up with a reduced globally coupled system of three oscillators which would live on the $P = 3$ polydiagonal (see figure 35C). Because of those symmetry properties if might be expected that the 6-cluster periodic solution is somehow connected to the 3-cluster limit cycle born from the THB bifurcation at $\kappa_{crit}^{diag\,(P=3)} = -0.7141$. However, the 6-cluster periodic solution is born unstable within the chaotic set for κ above $\kappa_{crit}^{diag\,(P=3)}$ and becomes stable at $\kappa = -0.847 > \kappa_{crit}^{diag\,(P=3)}$ after a series of period doubling and Neimark-Sacker bifurcations. The 3-cluster limit cycle born at $\kappa_{crit}^{diag\,(P=3)}$ from the THB bifurcation remains unstable for all investigated κ values.

Here, on the ring $R(6,12)$, the continuum of periodic solutions, born at $\kappa_{crit}^{diag\,(P=4)} = \kappa_{crit}$, is initially unstable with respect to perturbations in the full 12-dimensional

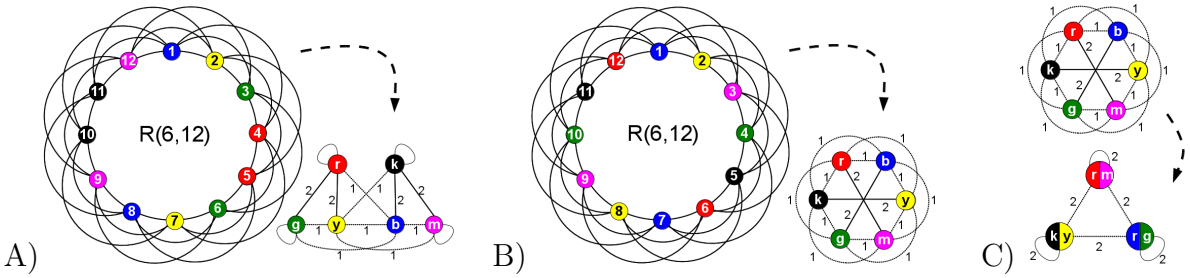

Figure 35: Different 6-cluster patterns of synchrony on the $R(6,12)$ ring and their reduced systems.

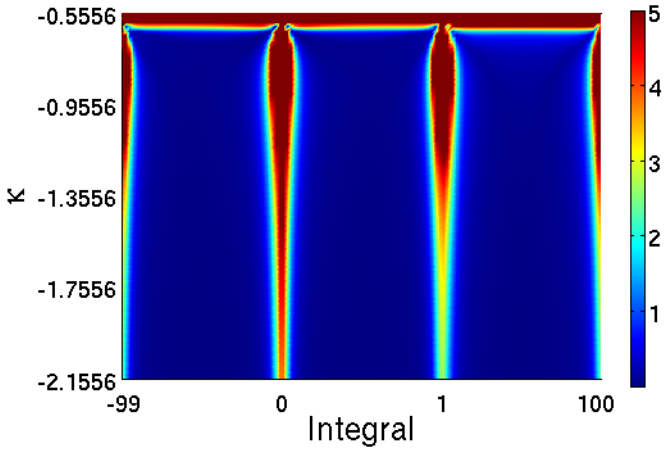

Figure 36: Change of stability regions for the continuum of limit cycles on the $P = 4$ polydiagonal on the $R(6,12)$ ring. The color corresponds to the absolute value of the largest multiplier.

phase space. Similar to the continuum on the 4×4 hexagonal lattice discussed in section 2.4, at $\kappa < \kappa_{crit}^{diag\,(P=4)}$ parts of the continuum become stable, whereby decreasing the κ value results in a shift of the stability region and when κ is further decreased towards $-\infty$ the whole continuum gradually becomes stable. Figure 36 represents the stability change of the continuum with respect to κ. The color in the figure corresponds to the absolute value of the largest multiplier, whereby the multipliers corresponding to the invariant directions of the continuum of limit cycles are not considered and the six integral regions are rescaled to the same size.

5 Semi-Globally Coupled Systems: Complete k- Partite Graphs

In this section we investigate systems with underlying graphs representing a natural choice for a coupling topology compatible with the WS reduction, as required in equation (57). In the case of "active rotators", where the coupling function has only a sine (odd) part, the coupling matrix from equation (57) becomes

$$A = \begin{pmatrix} [\widetilde{A}_{11}] & [A_{12}] & \cdots & [A_{1P}] \\ [A_{21}] & [\widetilde{A}_{22}] & \cdots & [A_{2P}] \\ \vdots & \vdots & \ddots & \vdots \\ [A_{P1}] & [A_{P2}] & \cdots & [\tilde{A}_{PP}] \end{pmatrix}$$

where $[\widetilde{A}_{jj}]$ are block matrices of dimension S_j and the off diagonal matrices $[A_{ij}]$ are $S_j \times S_i$ rectangular matrices. It seems natural to choose the off diagonal matrices $[A_{jk}]$ with $j \neq k$ to have entries $(a_{jk})_{mn} = 1 \ \forall m, n$ and all on diagonal matrices $[A_{kk}]$ to be zero matrices. For example,

$$A = \begin{pmatrix} 0&0&0 & 1&1&1&1 & 1&1&1&1&1 \\ 0&0&0 & 1&1&1&1 & 1&1&1&1&1 \\ 0&0&0 & 1&1&1&1 & 1&1&1&1&1 \\ \\ 1&1&1 & 0&0&0&0 & 1&1&1&1&1 \\ 1&1&1 & 0&0&0&0 & 1&1&1&1&1 \\ 1&1&1 & 0&0&0&0 & 1&1&1&1&1 \\ 1&1&1 & 0&0&0&0 & 1&1&1&1&1 \\ \\ 1&1&1 & 1&1&1&1 & 0&0&0&0&0 \\ 1&1&1 & 1&1&1&1 & 0&0&0&0&0 \\ 1&1&1 & 1&1&1&1 & 0&0&0&0&0 \\ 1&1&1 & 1&1&1&1 & 0&0&0&0&0 \\ 1&1&1 & 1&1&1&1 & 0&0&0&0&0 \end{pmatrix}$$

with the corresponding reduced matrix, according to equation (58), given by

$$A_R = \begin{pmatrix} 0&4&5 \\ 3&0&5 \\ 3&4&0 \end{pmatrix} .$$

From graph theoretical point of view, such graphs corresponds to a *complete k-partite graphs* [37]. Per definition, the vertices in such graphs can be partitioned into k disjoint sets, such that there are no adjacent vertices within the same set and every pair of vertices belonging to different sets are adjacent. Figure 37 gives two examples of such graphs: a 3- partite graph $K(3, 5, 4)$ and a 4- partite graph $K(2, 3, 3, 3)$. Here, we use the notation $K(S_1, S_2, S_3, ...)$, where S_j denotes the size of the j-th disjoint set.

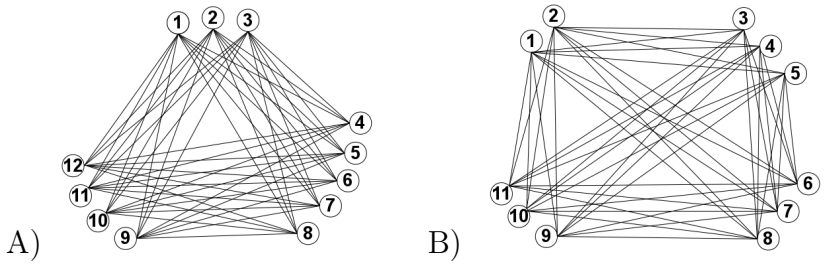

Figure 37: Examples for k- partite graphs. A) 3-partite graph $K(3,5,4)$. B) 4-partite graph $K(2,3,3,3)$.

In the full N-dimensional system, the critical value of κ for the synchronous 1- cluster solution $\phi_i = \arcsin\omega \ \forall i$ can be determined by (62) with $\mathcal{N} = N$. The Laplace matrix of the N-dimensional semi-globally coupled system is given by

$$L = \begin{pmatrix} \begin{bmatrix} N-S_1 & 0 & 0 \\ 0 & \ddots & 0 \\ 0 & 0 & N-S_1 \end{bmatrix} & \cdots & [-1] \\ \vdots & \ddots & \vdots \\ [-1] & \cdots & \begin{bmatrix} N-S_P & 0 & 0 \\ 0 & \ddots & 0 \\ 0 & 0 & N-S_P \end{bmatrix} \end{pmatrix}$$

and has the following degenerate eigenvalues

$$\begin{aligned} \Lambda_0 &= 0 \quad \text{with multiplicity } 1 \\ \Lambda_i &= N - S_i, \ i = 1, ..., P \quad \text{with multiplicity } S_i - 1 \\ \Lambda_{max} &= N \quad \text{with multiplicity } P - 1 \end{aligned}$$

Substituting Λ_{max} in (62) gives the critical coupling strength of the system:

$$\kappa_{crit} = -\sqrt{1-\omega^2} \ . \tag{68}$$

Naturally, such systems exhibit, besides the synchronous one cluster state, also balanced clustered states where oscillators that are not coupled belong to the same cluster. The size of the corresponding clusters is therefore given by the size of the diagonal block matrices: cluster k has size S_k, with $k = 1, ..., P$. For those clustered states each oscillator of a given cluster couples to S_k oscillators of a different cluster k. Therefore, in the reduced system, the equations of motion (59) take the form

$$\dot{\phi}_i = \omega - \sin\phi_i + \frac{\kappa}{N} \sum_{\substack{j=1 \\ j \neq i}}^{P} S_j \sin(\phi_j - \phi_i), \ \ i = 1, ..., P \tag{69}$$

with a coupling matrix given by

$$A_R = \begin{pmatrix} 0 & S_2 & ... & S_P \\ S_1 & 0 & ..... & S_P \\ \vdots & \vdots & \ddots & \vdots \\ S_1 & S_2 & ..... & 0 \end{pmatrix} \ . \tag{70}$$

The corresponding reduced Laplace matrix, which we denote by $\mathbb{S}$, is therefore

$$\begin{aligned}\mathbb{S} &= \begin{pmatrix} \sum_j S_j - S_1 & -S_2 & ... & -S_P \\ -S_1 & \sum_j S_j - S_2 & ..... & -S_P \\ \vdots & \vdots & \ddots & \vdots \\ -S_1 & -S_2 & ..... & \sum_j S_j - S_P \end{pmatrix} \\ &= N\mathbb{E} - \widetilde{A}_R \end{aligned} \tag{71}$$

with

$$\widetilde{A}_R = \begin{pmatrix} S_1 & S_2 & ... & S_P \\ S_1 & S_2 & ..... & S_P \\ \vdots & \vdots & \ddots & \vdots \\ S_1 & S_2 & ..... & S_P \end{pmatrix}$$

The synchronous 1- cluster solution $\phi_i = \arcsin\omega \ \forall i$ remains a fixed point on the P-dimensional polydiagonal, where its stability is determined by the eigenvalues of

$$\begin{aligned} J^{diag} &= -\frac{\kappa}{N}\mathbb{S} - (\sqrt{1-\omega^2})\mathbb{E} \\ &= -\frac{\kappa}{N}\widetilde{A}_R - (\sqrt{1-\omega^2} - N)\mathbb{E} \ . \end{aligned}$$

The matrix $\widetilde{A}_R$ has $P-1$ eigenvalues $\lambda_{min}^{\widetilde{A}_R} = 0$ and one eigenvalue $\lambda_{max}^{\widetilde{A}_R} = N$. Accordingly, the Laplace matrix (71) of the reduced system has $P-1$ eigenvalues $\lambda_{max}^{\mathbb{S}} = N$ and one eigenvalue $\lambda_{min}^{\mathbb{S}} = 0$.

Now we can calculate the critical value κ_{crit}^{diag} of the coupling strength for the reduced system (i.e. on the diagonal subspace defined by the clusters). Unlike some of the examples from section 4, where the 1- cluster solution might lose stability on the reduced diagonal subspace at a value κ_{crit}^{diag} different from κ_{crit}, here, the critical value on the diagonal subspace always equals κ_{crit}

$$\begin{aligned} \kappa_{crit}^{diag} &= \frac{-N\sqrt{1-\omega^2}}{\lambda_{max}^{\mathbb{S}}} \\ &= -\sqrt{1-\omega^2} \ . \end{aligned} \tag{72}$$

Remarkably, for all semi-globally coupled systems the critical value of the coupling strength (68) depends neither on the size of the different clusters nor on the number of clusters. This is due to the fact that in (59) the coupling strength is normalized over the total number of oscillators N and we sum over the adjacency matrix. In fact, this is the same critical coupling strength as for a globally coupled system.

Nevertheless, there is a remarkable difference between the globally coupled and the semi-globally coupled systems. In the former case the Laplace matrix has one eigenvalue $\Lambda_{min} = 0$ and $N-1$ eigenvalues $\Lambda_{max} = N$; this means that the center manifold at the bifurcation point κ_{crit} is $(N-1)$-dimensional making the one cluster solution unstable with respect to all possible perturbations. In the case of semi-globally coupled systems the center manifold is $(P-1)$-dimensional. Furthermore, here, at the bifurcation point the center manifold lies within the diagonal subspace defined by the reduced system (69). This means that after the bifurcation the

synchronous 1-cluster solution remains stable in all directions which are transverse to the diagonal subspace.

For $\kappa < \kappa_{crit}$, the observed dynamical states in semi-globally coupled systems with *complete P- partite graph* topologies depend on the respective size of the P clusters and can be, accordingly, divided in three classes. Let $K(S_1, S_2, ..., S_P)$ denote the complete P- partite graph and let the sizes of the clusters be such that $S_1 \leq S_2 \leq ... \leq S_P$. i.e. the P-th cluster always has the maximal size. Then the three classes are

$$\begin{aligned} \text{Class I} &\Leftrightarrow \sum_{i=1}^{P-1} S_i > S_P \\ \text{Class II} &\Leftrightarrow \sum_{i=1}^{P-1} S_i = S_P \\ \text{Class III} &\Leftrightarrow \sum_{i=1}^{P-1} S_i < S_P \ . \end{aligned} \tag{73}$$

In the following, based on corresponding examples, we describe the dynamical properties of each of these classes. As representatives for Class I we consider $K(2,3,4,5)$ and $K(2,3,4,7)$; for Class II we consider $K(2,3,4,9)$; and for Class III we consider $K(2,3,4,11)$ and $K(2,3,4,13)$. On each of those 4-partite graphs, there are balanced 4-cluster states with clusters, respectively, comprising the oscillators that are not coupled. In the following, we denote by Ψ_k the reduced variable corresponding to the cluster of size k.

Figure 38 represents bifurcation diagrams for each of the considered graphs. In all diagrams, the bifurcation branches correspond to 2-cluster fix points, whereby three of the four clusters are identical. As we know from previous sections, at $\kappa = 0$, those fixed points correspond to saddle states, where the oscillators belonging to the one ("stable") cluster have phases equal $\arcsin\omega$ and those belonging to the second ("unstable") cluster have phases equal $\pi - \arcsin\omega$. The bifurcation branches are continuations of those saddle states and different colors in the figures indicate different configurations of the 2-cluster states. For example, in figure 38A1, the fix point of the 2-cluster state (Ψ_5) and $(\Psi_2 = \Psi_3 = \Psi_4)$ is represented in red. The dots along the branches indicate bifurcation points which we discuss in more detail in the next paragraphs. Remark that in the considered cases the sizes of the first three clusters are always $S_1 = 2$, $S_2 = 3$ and $S_3 = 4$, while the size of the fourth cluster changes, from case to case, in order to match the three different classes from (73). Here, we consider equation (69) as the result of a cluster reduction and, accordingly, the entries S_k of the reduced coupling matrix (70) are natural numbers. In general, we can think of (69) as an independent system of P- globally coupled phase oscillators with weighted coupling, in which case, the weights S_k can be arbitrary real numbers. As we will see in section 6, in both cases, the bifurcation scenarios at κ_{crit} are generic and correspond to the three classes from (73). From the bifurcation diagrams 38A1 and 38A2, for class I graphs, we can see that an increase of S_4, here the size of the largest cluster, leads to a shift of the bifurcation branches. At first, this shift does not lead to any remarkable structural changes and

all branches undergo a transcritical bifurcation at κ_{crit}, where the corresponding saddles collide with the fix point of the 1-cluster synchronous solution. In the case, when $S_4 = \sum_{i=1}^{3} S_i$, class II ,represented in figure 38B, the bifurcation branches are shifted further; the red branch bifurcates at κ_{crit} in a pitchfork, while the remaining branches undergo transcritical bifurcations. For $S_4 > \sum_{i=1}^{3} S_i$, class III, represented in 38C1 and 38C2, the bifurcation branches are shifted further and the red branch as well as the remaining ones undergo, again, a transcritical bifurcation. As we will see in the next section, it is the number of positive and negative eigenvalues of the fix point as well as the weights S_k from the reduced system, that determines whether or not a given branch undergoes a transcritical or a pitchfork bifurcation at κ_{crit}.

Table 6 represents all stability changes along the branches for the graphs $K(2,3,4,5)$, $K(2,3,4,9)$ and $K(2,3,4,13)$ shown, respectively, in figure 38A1, 38B and 38C2. The stability changes for the remaining two graphs $K(2,3,4,7)$ and $K(2,3,4,11)$ are comparable. In the table, the bifurcation at κ_{crit} with the synchronous 1-cluster solution is underlined with a "wavy underbar". Observe that the branches bifurcating at κ_{crit} with the 1-cluster fix point correspond initially (at $\kappa = 0$) to the saddle states where the 2-cluster configuration is least unstable. Furthermore, in all cases, a branch undergoing a transcritical bifurcation at κ_{crit} ends in a saddle node bifurcation at $\kappa < \kappa_{crit}$, colliding with its "counterpart"; the latter originating at $\kappa = 0$ from the saddle corresponding to the most unstable 2-cluster configuration. For example, for the graph $K(2,3,4,5)$ belonging to class I, the red branch is the saddle at $\kappa = 0$, where the *sheer* cluster Ψ_5 is "unstable" and the second *compound* cluster $(\Psi_2 = \Psi_3 = \Psi_4)$ is "stable"; respectively, having 5 positive and 9 negative eigenvalues (see Table 6, column $(\Psi_5)\,(\Psi_2 = \Psi_3 = \Psi_4)$, row BP1). The last bifurcation of this branch (see Table 6, column $(\Psi_5)\,(\Psi_2 = \Psi_3 = \Psi_4)$, row BP6) is a saddle node bifurcation: the branch collides with its "counterpart"– the saddle state where the *sheer* cluster Ψ_5 is "stable" and the *compound* cluster $(\Psi_2 = \Psi_3 = \Psi_4)$ is "unstable"– respectively, having 5 negative and 9 positive eigenvalues. In the case of the $(\Psi_9)\,(\Psi_2 = \Psi_3 = \Psi_4)$ branch, in the graph $K(2,3,4,9)$ from class II, both the initial saddle and its "counterpart" saddle have the same number of positive and negative eigenvalues. On the corresponding 2-dimensional polydiagonal $(\Psi_9)\,(\Psi_2 = \Psi_3 = \Psi_4)$ those two saddles are symmetric and collide simultaneously at κ_{crit} with the 1-cluster fix point in a pitchfork bifurcation. Observe that, in the graph $K(2,3,4,13)$ from class III, at the initial saddle state corresponding to the red branch $(\Psi_{13})\,(\Psi_2 = \Psi_3 = \Psi_4)$ it is the *compound* cluster $(\Psi_2 = \Psi_3 = \Psi_4)$ that is initially "unstable" while the *sheer* cluster Ψ_{13} is "stable"; this is contrary to the graph $K(2,3,4,5)$ from class I (see Table 6, column $(\Psi_{13})\,(\Psi_2 = \Psi_3 = \Psi_4)$, row BP1). This switch between the initial stability of the *sheer* and the *compound* clusters, when going from class I to class III graphs, can also be seen in the bifurcation diagrams from figure 38 as the shift of the red branch caused by the increase of S_4. Remarkably, the transcritical bifurcation of this branch leads to a stable fix point which dominates the dynamics until the succeeding saddle node bifurcation (see Table 6, column $(\Psi_{13})\,(\Psi_2 = \Psi_3 = \Psi_4)$, rows BP4 and BP5).

A closer look at the stability changes along the different branches from table 6 reveals that it is not so much the whole graph that belongs to a given class (73) but much more the single branches. In the above lines we have introduced the

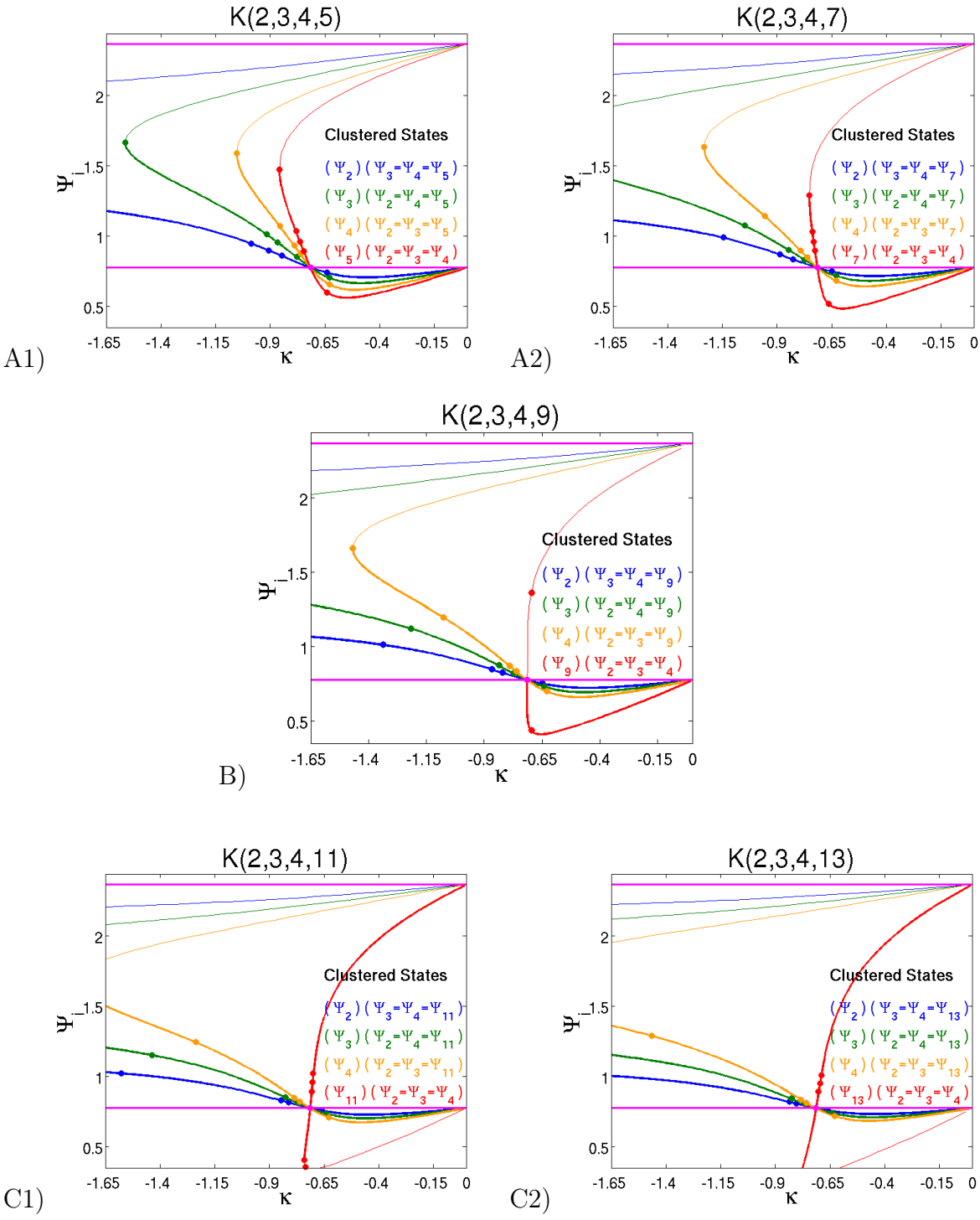

Figure 38: Bifurcation diagrams representing 2-dimensional branches of fixed points for different complete 4- partite graphs. In all diagrams Ψ_k indicates the reduced variable of the cluster of size k. The dots along each of the branches indicate bifurcations (for the cases from plots A1, B and C2, see table 6).
A) Class I: 1) $K(2,3,4,5)$, 2) $K(2,3,4,7)$.
B) Class II: $K(2,3,4,9)$.
C) Class III: 1) $K(2,3,4,11)$, 2) $K(2,3,4,13)$.

K(2,3,4,5)

$(\Psi_2)\,(\Psi_3=\Psi_4=\Psi_5)$		$(\Psi_3)\,(\Psi_2=\Psi_4=\Psi_5)$		$(\Psi_4)\,(\Psi_2=\Psi_3=\Psi_5)$		$(\Psi_5)\,(\Psi_2=\Psi_3=\Psi_4)$	
BP1	(+)2(−)12 ↦ (+)1(−)13	BP1	(+)3(−)11 ↦ (+)1(−)13	BP1	(+)4(−)10 ↦ (+)1(−)13	BP1	(+)5(−)9 ↦ (+)1(−)13
BP2	(+)1(−)13 ↦ (+)2(−)12	**BP2**	(+)1(−)13 ↦ (+)2(−)12	**BP2**	(+)1(−)13 ↦ (+)2(−)12	**BP2**	(+)1(−)13 ↦ (+)2(−)12
BP3	(+)2(−)12 ↦ (+)4(−)10	BP3	(+)2(−)12 ↦ (+)3(−)11	BP3	(+)2(−)12 ↦ (+)3(−)11	BP3	(+)2(−)12 ↦ (+)3(−)11
BP4	(+)4(−)10 ↦ (+)7(−)7	BP4	(+)3(−)11 ↦ (+)6(−)8	BP4	(+)3(−)11 ↦ (+)5(−)9	BP4	(+)3(−)11 ↦ (+)5(−)9
BP5	(+)7(−)7 ↦ (+)11(−)3	BP5	(+)6(−)8 ↦ (+)10(−)4	BP5	(+)5(−)9 ↦ (+)9(−)5	BP5	(+)5(−)9 ↦ (+)8(−)6
BP6	(+)11(−)3 ↦ (+)12(−)2	BP6	(+)10(−)4 ↦ (+)11(−)3	BP6	(+)9(−)5 ↦ (+)10(−)4	BP6	(+)8(−)6 ↦ (+)9(−)5

K(2,3,4,9)

$(\Psi_2)\,(\Psi_3=\Psi_4=\Psi_9)$		$(\Psi_3)\,(\Psi_2=\Psi_4=\Psi_9)$		$(\Psi_4)\,(\Psi_2=\Psi_3=\Psi_9)$		$(\Psi_9)\,(\Psi_2=\Psi_3=\Psi_4)$	
BP1	(+)2(−)16 ↦ (+)1(−)17	BP1	(+)3(−)15 ↦ (+)1(−)17	BP1	(+)4(−)14 ↦ (+)1(−)17	BP1	(+)9(−)9 ↦ (+)1(−)17
BP2	(+)1(−)17 ↦ (+)2(−)16	**BP2**	(+)1(−)17 ↦ (+)2(−)16	**BP2**	(+)1(−)17 ↦ (+)2(−)16	**BP2**	**Pitchfork**
BP3	(+)2(−)16 ↦ (+)4(−)14	BP3	(+)2(−)16 ↦ (+)3(−)15	BP3	(+)2(−)16 ↦ (+)3(−)15		
BP4	(+)4(−)14 ↦ (+)7(−)11	BP4	(+)3(−)15 ↦ (+)6(−)12	BP4	(+)3(−)15 ↦ (+)5(−)13		
BP5	(+)7(−)11 ↦ (+)15(−)3	BP5	(+)6(−)12 ↦ (+)14(−)4	BP5	(+)5(−)13 ↦ (+)13(−)5		
BP6	(+)15(−)3 ↦ (+)16(−)2	BP6	(+)14(−)4 ↦ (+)15(−)3	BP6	(+)13(−)5 ↦ (+)14(−)4		

K(2,3,4,13)

$(\Psi_2)\,(\Psi_3=\Psi_4=\Psi_{13})$		$(\Psi_3)\,(\Psi_2=\Psi_4=\Psi_{13})$		$(\Psi_4)\,(\Psi_2=\Psi_3=\Psi_{13})$		$(\Psi_{13})\,(\Psi_2=\Psi_3=\Psi_4)$	
BP1	(+)2(−)20 ↦ (+)1(−)21	BP1	(+)3(−)19 ↦ (+)1(−)21	BP1	(+)4(−)18 ↦ (+)1(−)21	BP1	(+)9(−)13 ↦ (+)6(−)16
BP2	(+)1(−)21 ↦ (+)2(−)20	**BP2**	(+)1(−)21 ↦ (+)2(−)20	**BP2**	(+)1(−)21 ↦ (+)2(−)20	BP2	(+)6(−)16 ↦ (+)4(−)18
BP3	(+)2(−)20 ↦ (+)4(−)18	BP3	(+)2(−)20 ↦ (+)3(−)19	BP3	(+)2(−)20 ↦ (+)3(−)19	BP3	(+)4(−)18 ↦ (+)3(−)19
BP4	(+)4(−)18 ↦ (+)7(−)15	BP4	(+)3(−)19 ↦ (+)6(−)17	BP4	(+)3(−)19 ↦ (+)5(−)17	**BP4**	(+)3(−)19 ↦ (+)0(−)22
BP5	(+)7(−)15 ↦ (+)19(−)3	BP5	(+)6(−)16 ↦ (+)18(−)4	BP5	(+)5(−)17 ↦ (+)17(−)5	BP5	(+)0(−)22 ↦ (+)13(−)9
BP6	(+)19(−)3 ↦ (+)20(−)2	BP6	(+)18(−)4 ↦ (+)19(−)3	BP6	(+)17(−)5 ↦ (+)18(−)4		

Table 6: Stability changes at the bifurcation points along the branches for $K(2,3,4,5)$, $K(2,3,4,9)$ and $K(2,3,4,13)$ represented in figure 38A1, 38B and 38C2, respectively. In each case, the bifurcation at κ_{crit} with the synchronous 1-cluster solution is underlined with a "wavy underbar".

implicit notion of the "*sheer*" and "*compound*" clusters. Strictly speaking, this notation makes sense only in the reduced P-dimensional phase space; in the full N-dimensional phase space the *sheer* cluster itself comprises a *subcluster* of S_k oscillators, and the *compound* cluster comprises $P-1$ *subclusters* of totally $N-S_k$ oscillators. Depending on whether S_k of the *sheer* cluster is smaller, equal, or greater than the sum of the S_k's of the *compound* cluster, we can say that a branch belongs to class I, II or III, respectively. From table 6 we can see that branches belonging to class I, for instance, undergo basically identical transcritical bifurcations at κ_{crit}. We rigorously prove in section 6 that the this is indeed the case. Moreover, the stability changes at the remaining bifurcation points, for all branches, also share a common feature: all those bifurcations do not take place in the reduced P-dimensional system. In the reduced P-dimensional system, the only bifurcations that take place are those at κ_{crit} and the final saddle node bifurcations. All other bifurcations affect the internal stability of the *subclusters* and take place on manifolds transverse to the P-dimensional polydiagonal of the reduced system. For a subcluster comprising S_k oscillators there are S_k directions determining its internal stability. One of those directions corresponds to a perturbation where the integrity of the *subcluster* is not disturbed (this direction is along the polydiagonal of the reduced system), and the remaining (S_k-1) directions (transverse to the polydiagonal of the reduced system) disturb the integrity of the *subcluster*. Observe that at all stability changes (except the bifurcations at κ_{crit} and the final saddle node bifurcations) the number of positive/negative eigenvalues changes by the number (S_k-1). Consider, for example, the $(\Psi_4)\,(\Psi_2=\Psi_3=\Psi_{13})$ branch in the graph $K(2,3,4,13)$. Initially, the *sheer* cluster Ψ_4 is completely "unstable" and at the BP1 bifurcation three of the four unstable directions are stabilized. After the bifurcation the Ψ_4 cluster becomes stable with respect to perturbations transverse to the polydiagonal of the reduced 4-dimensional $\{\Psi_2,\Psi_3,\Psi_4,\Psi_{13}\}$ system. The following bifurcation BP2, at κ_{crit}, takes place in the reduced 4-dimensional system: the single positive eigenvalue becomes negative and simultaneously 2 of the 17 initially negative eigenvalues become positive. Those two eigenvalues correspond to perturbations disturbing the integrity of the *compound* cluster $(\Psi_2=\Psi_3=\Psi_{13})$, but not the integrity of the single *subclusters* $\{\Psi_2,\Psi_3,\Psi_{13}\}$. Therefore, after the bifurcation at κ_{crit} the polydiagonal of the reduced 4-dimensional system $\{\Psi_2,\Psi_3,\Psi_4,\Psi_{13}\}$ remains locally transversely stable. This is true for all branches; and indeed, in all cases, the observed dynamics immediately after the bifurcation at κ_{crit} takes place on the 4-dimensional polydiagonal of the reduced system. Furthermore, from the table we can see that for branches of class I the subsequent bifurcations follow the same pattern: the integrity of the single *subclusters* is subsequently disturbed, starting from the smallest towards the largest. For branch $(\Psi_{13})\,(\Psi_2=\Psi_3=\Psi_4)$ of class III it is the opposite: in the bifurcations before κ_{crit} the single *subcluster* are subsequently stabilized, starting from the largest towards the smallest. Here, the three positive eigenvalues before the BP4 bifurcation at κ_{crit} (see Table 6, column $(\Psi_{13})\,(\Psi_2=\Psi_3=\Psi_4)$, row BP4) correspond to perturbations of the *compound* cluster within the 4-dimensional polydiagonal.

As mentioned above and as expected by the different scenarios in the bifurcation diagrams, the dynamics of the systems, for κ values below κ_{crit}, depend on the corresponding class (73) of the complete P- partite graphs.

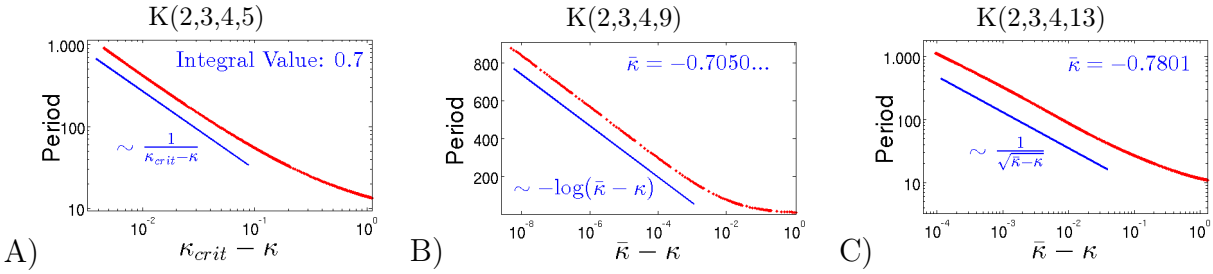

Figure 39: Asymptotics of the period of limit cycles observed on the different complete 4- partite graphs: A) $K(2,3,4,5)$ (log-log plot). B) $K(2,3,4,9)$ (log-linear plot). C) $K(2,3,4,13)$ (log-log plot).

For graphs of class I, at κ_{crit} a THB bifurcation takes place resulting in periodic solutions. For $P > 3$ those solutions form a continuum, whereby each periodic orbit is characterized by $P-3$ constants of motion. For example, in the case of the $K(2,3,4,5)$ graph from above, there are four clusters and each periodic solution is characterized by one constant of motion. Figure 39A represents the asymptotics for the periodic solution with integral value $I = 0.7$: it is the typical asymptotics for a THB bifurcation (see section 2.2; [11]). Remarkably, for all graphs of class I, the periodic solutions are born stable at the THB bifurcation with respect to perturbations in the full N-dimensional space. Although the stability of a periodic orbit is a global phenomenon, according to the observations from the previous paragraph and the fact that at the bifurcation point the center manifold lies within the diagonal subspace defined by the reduced system (69), the P-dimensional polydiagonal remains locally transversely stable. This transverse stability has an effect on the stability of the newly formed periodic orbits.

Let us consider the symmetries of the periodic orbits. Recall the examples from sections 2.2 and 4.2. There the 3×3 hexagonal lattice was a complete 3- partite graph $K(3,3,3)$, respectively, the $R(6,8)$ ring was a complete 4- partite graph $K(2,2,2,2)$ and in those cases the THB bifurcations were symmetric: the S_3-THB, respectively, the S_4-THB. Furthermore, in the example discussed in section 2.4– on the 4×4 hexagonal lattice– the THB bifurcation was also symmetric. There, we have seen that the S_4 permutation symmetries of the four oscillators in the reduced system were connected to spatial and spatio-temporal symmetries of the periodic solutions, and also to changes in the integrals of motion characterizing the leafs of the WS foliation. For a generic complete P- partite graph (with clusters of different sizes) the coupling topology (70) of the reduced P-dimensional system (69) does not imply any symmetries between the saddles. An interesting question is whether the periodic orbits born at non-symmetric THB bifurcations in P- partite graphs are symmetry related or not. Immediately after the bifurcation, the trajectory of a newly born periodic orbit passes cyclically in the vicinity of each of the saddles involved in the THB bifurcation. Hence, a periodic orbit is characterized by the order of the different saddles along the trajectory. For a P- partite graph there are P saddles and we can identify each saddle with the single *subcluster* forming the *sheer* cluster. For example, on the $K(2,3,4,5)$ graph, we might denote a periodic orbit by $L(5,4,3,2)$ which subsequently passes in the vicinity of the saddle $(\Psi_5)(\Psi_2 = \Psi_3 = \Psi_4)$ followed

by the saddle $(\Psi_4)(\Psi_2 = \Psi_3 = \Psi_5)$, followed by $(\Psi_3)(\Psi_2 = \Psi_4 = \Psi_5)$, followed by $(\Psi_2)(\Psi_3 = \Psi_4 = \Psi_5)$, and again by $(\Psi_5)(\Psi_2 = \Psi_3 = \Psi_4)$ a.s.o. There are $P!$ possible ways to order the saddles, suggesting that $P!$ distinct periodic orbits are born at the bifurcation. However, only $(P-1)!$ of all permutations are non-cyclic: for example, on the $K(2,3,4,5)$ graph those might be denoted by $L(2,3,4,5)$, $L(2,3,5,4)$, $L(2,4,3,5)$, $L(2,4,5,3)$, $L(2,5,3,4)$, $L(2,5,4,3)$. Since a periodic trajectory visits all saddles in a cyclic way, we might rather expect that there $(P-1)!$ different periodic orbits, whereas, for example, $L(5,4,3,2)$ would describe the same limit cycle as $L(2,5,4,3)$. Because of the WS-integrals this is not the case! Recall from section 2.4 that in the reduced system generic cyclic permutations of the oscillator-indices lead to different integral values. The only permutations that do leave the integral value I unchanged are given by

$$\begin{aligned} I &= R(i,j,k,l) = R(k,l,i,j) \\ &= R(j,i,l,k) = R(l,k,j,i) \end{aligned} \tag{74}$$

with $R(i,j,k,l)$ defined as

$$R(i,j,k,l) = \frac{\sin(\frac{\Psi_i - \Psi_k}{2})}{\sin(\frac{\Psi_i - \Psi_l}{2})} \frac{\sin(\frac{\Psi_j - \Psi_l}{2})}{\sin(\frac{\Psi_j - \Psi_k}{2})} \ .$$

In equation (74) on the first row, respectively on the second row, the integral relations are connected via pairwise cyclic permutations, while the first and second rows are connected via anti-cyclic permutations. In section 2.4 we have seen that– for fixed value of κ and fixed integral value– on the corresponding sheet of foliation there were two distinct periodic orbits. In the reduced 4-dimensional system of identical oscillators those two periodic orbits were symmetry connected: the pairwise cyclic permutations within the first (second) row in (74) corresponded to spatio-temporal symmetries and permutations between the first and second rows corresponded to spacial symmetries of the system. For a generic P- partite graph, in the reduced P-dimensional phase space, the oscillators are coupled with different coupling strengths and are therefore not interchangeable. Nevertheless, on each foliation leaf (i.e. for a given fixed integral value) there are two limit cycles. Here, the pairwise cyclic permutations within the first (second) row in (74) also correspond to spatio-temporal symmetries, but the spacial symmetries, due to permutations between the first and second rows, do not exist since the reduced system is in general not symmetric. Remark that the spacial-temporal symmetries result from the peculiarities of the THB bifurcation and not from symmetries due to the topology of the reduced network.

It is interesting to remark that it is also possible to determine the basin of attraction for each of each limit cycle. It is defined by order of the oscillators within the interval $[0, 2\pi]$. This order is always preserved (modulo 2π). The WS reduction is connected to the 3-dimensional Möbius group, such that the phases of the oscillators evolve according to the action of the group [78], i.e. the temporal evolution of the system corresponds to a Möbius transformations. The Möbius transformations have the property to preserve the initial order of the oscillators and since each limit cycle is characterized by this order, this allows us to define its basin of attraction. For example, the basin of attraction $\mathcal{B}(2,4,3,5)$ of the $L(2,4,3,5)$ limit cycle is given

by

$$\mathcal{B}(2,4,3,5) = \left\{(\Psi_2,\Psi_3,\Psi_4,\Psi_5) \in \mathcal{T}^2 \otimes \mathcal{T}^3 \otimes \mathcal{T}^4 \otimes \mathcal{T}^5 \,|\, \Psi_2 < \Psi_3 < \Psi_4 < \Psi_5\right\} \ .$$

For complete P- partite graphs of class III, there is always a single bifurcation branch of class III where the corresponding saddle undergoes a transcritical bifurcation at κ_{crit} resulting in a stable fix point. After the bifurcation the 1-cluster solution becomes unstable and within a certain κ range the new stable fix point remains the only (global) attractor of the system. Decreasing κ further leads to a saddle node bifurcation (see the discussion above; Table 6, column $(\Psi_{13})\,(\Psi_2 = \Psi_3 = \Psi_4)$, rows BP4 and BP5). At the saddle node bifurcation a stable 2-cluster limit cycle is born, not surprisingly, with the same cluster configuration as the colliding branches: a *sheer* cluster comprising the largest *subcluster* and a *compound* cluster comprising the remaining $P-1$ *subclusters.* In the case of the $K(2,3,4,13)$ graph, the saddle node bifurcation takes place at $\bar{\kappa} = -0.7801... < \kappa_{crit}$ and the asymptotics of the 2-cluster limit cycle is represented in figure 39C. It has the inverse square root law typical for limit cycles born at saddle node bifurcation [46]. Recall from above that all branches of class I and III, end in saddle node bifurcation. It is interesting to remark that in all those cases corresponding 2-cluster limit cycles are born, although most of them remain unstable.

For complete P- partite graphs of class II, there is always a single bifurcation branch of class II undergoing a pitchfork bifurcation at κ_{crit} with the 1-cluster solution. The observed dynamics, immediately after the bifurcation, corresponds to two symmetric 2-cluster periodic solutions with the same cluster configuration as the branch of class II: : a *sheer* cluster comprising the largest *subcluster* and a *compound* cluster comprising the remaining $P-1$ *subclusters.* Unlike the previous case, here, the limit cycles are born in a heteroclinic bifurcation at $\bar{\kappa}$ above κ_{crit}. In the case of the $K(2,3,4,9)$ graph, the branch of class II corresponds to the 2-cluster state $(\Psi_9)\,(\Psi_2 = \Psi_3 = \Psi_4)$, and the heteroclinic bifurcation takes place at $\bar{\kappa} = -0.7050... > \kappa_{crit}$. The period asymptotics of the resulting limit cycles, represented in figure 39B, follows the logarithmic law typical for limit cycles born at heteroclinic bifurcation [46]. The first row in figure 40 represents, at different κ values above $\bar{\kappa}$, the changes of the flow leading to the heteroclinic bifurcation on the reduced 2-dimensional polydiagonal $(\Psi_9)\,(\Psi_2 = \Psi_3 = \Psi_4)$ in the $K(2,3,4,9)$ graph. The second row in the figure shows the newly born limit cycles at two different κ values with $\kappa_{crit} < \kappa \lesssim \bar{\kappa}$. The four quadrants on each plot represent the toroidal phase space shifted by 2π, respectively.

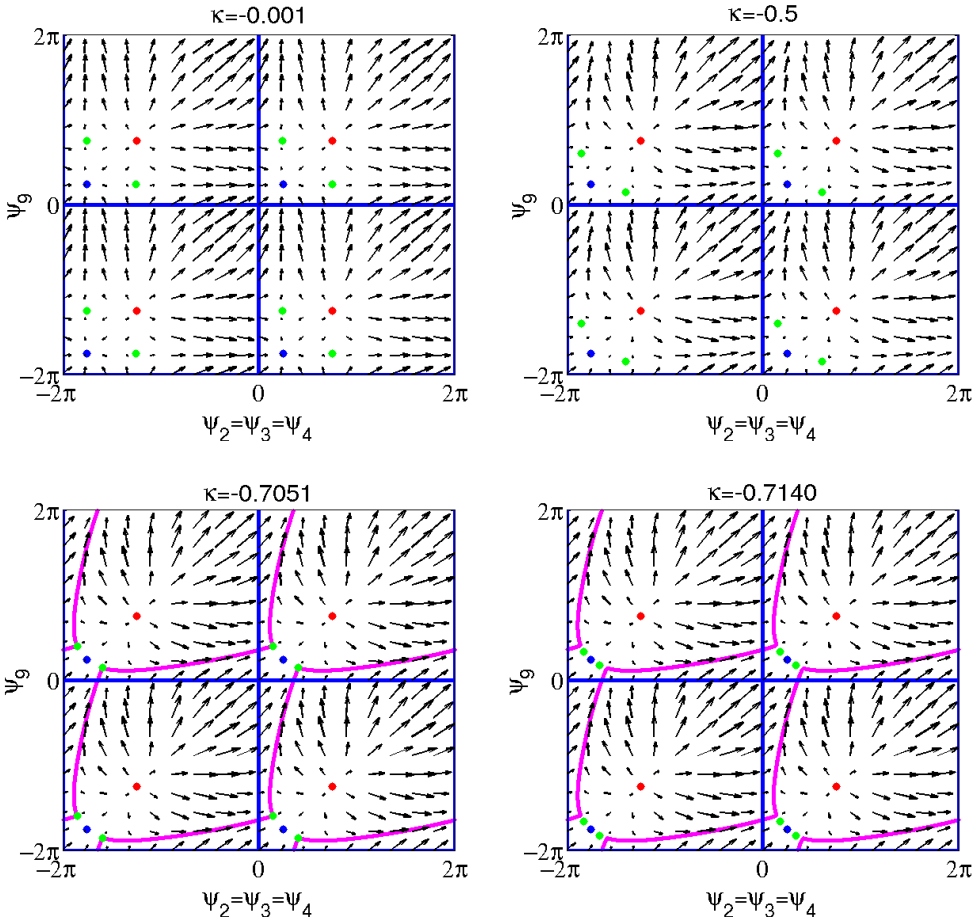

Figure 40: Flow on the reduced 2-dimensional polydiagonal $(\Psi_9)\,(\Psi_2 = \Psi_3 = \Psi_4)$ in the $K(2,3,4,9)$ graph at different κ values above κ_{crit}. The four quadrants on each plot represent the toroidal phase space shifted by 2π, respectively. The two symmetric copies of the limit cycles born from the heteroclinic bifurcation at $\bar{\kappa} = -0.7050...$ are shown in the plots on the second row.

6 From Local to Global Coupling: Transition to Watanabe-Strogatz dynamics and Conditions for Transcritical Bifurcations Leading to Limit Cycles

In the previous sections we have given examples of dynamical systems of coupled phase oscillators which, in general, are not compatible with the WS requirements represented in section 3 but, nevertheless, allow P- cluster states such that the dynamics on the corresponding reduced P-dimensional polydiagonal becomes, according to the WS reduction, 3-dimensional with $P-3$ constants of motion. As we have seen, it depends on the coupling topology of the total N- dimensional system, whether or not this P- dimensional (WS-) polydiagonal becomes transversely stable for some coupling strengths κ, manifesting the WS dynamics as observable (stbale) dynamical states. In this section we neglect those transverse directions and concentrate on the P-dimensional (WS-) polydiagonal itself. We prove some general facts about the bifurcations at κ_{crit}^{diag} which govern the dynamical state of the system after the lost of stability of the synchronous 1-cluster solution on the P-dimensional (WS-) polydiagonal.

Consider a P-dimensional reduced system (56), whose reduced dynamics on a flow-invariant P-dimensional polydiagonal is given by

$$\begin{aligned}\dot{\varphi}_j &= \omega + \{p + \sum_{k=1}^{P} \bar{\gamma}_k e^{-i\varphi_k}\} e^{i\varphi_j} + \{\bar{p} + \sum_{k=1}^{P} \gamma_k e^{i\varphi_k}\} e^{-i\varphi_j} \quad \text{with } j = 1, .., P \quad (75)\\ &= \frac{\omega}{2} + \{p + \sum_{k=1}^{P} \bar{\gamma}_k e^{-i\varphi_k}\} e^{i\varphi_j} + \text{c.c.}\end{aligned}$$

where the overbar, respectively "c.c.", denotes complex conjugate. Remark that $p, \gamma_k \in \mathbb{C}$. The coefficients γ_k of the reduced coupling matrix are explicitly given by (58), taking the form

$$\gamma_k = \alpha_k \frac{1}{2\mathrm{i}} + \beta_k \frac{1}{2}$$

and the other coefficient

$$p = \frac{s}{2i} + \frac{c}{2}$$

is such that the parameter determining the excitability of the system w.r.t. the sine part of the internal dynamics is s and with respect to the cosine part c.

Let $\vec{\varphi}^* = \{\varphi^*, ..., \varphi^*\}$ be the synchronous *stable* 1-cluster steady state solution. An investigation of the stability properties of this solution requires an expansion of (75) about $\vec{\varphi}^*$. Introducing $x_i = \varphi_i - \varphi^*$, the expansion of (75) is given, up to second order, by

$$\frac{dx_i}{dt} = \varepsilon\, x_i - \frac{1}{2} b\, x_i^2 - \sum_k s_k^{(1)} x_k + \sum_k s_k^{(2)} x_k\, x_i - \frac{1}{2} \sum_k s_k^{(2)} x_k^2 + \dots \qquad (76)$$

with coefficients, respectively,

$$\begin{aligned}
\epsilon &= i\,p\,e^{i\varphi^*} + i\sum_k \bar{\gamma}_k + \text{c.c.} \\
b &= p\,e^{i\varphi^*} + \sum_k \bar{\gamma}_k + \text{c.c.} \\
s_k^{(1)} &= i\,\bar{\gamma}_k + \text{c.c.} \\
s_k^{(2)} &= \bar{\gamma}_k + \text{c.c.}\ .
\end{aligned}$$

In order to simplify the expressions, as well as for latter convenience, we introduce the following notations:

$$\begin{aligned}
P_+(\vec{\varphi}^*) &= p\,e^{i\varphi^*} + \bar{p}\,e^{-i\varphi^*} \\
P_-(\vec{\varphi}^*) &= i(p\,e^{i\varphi^*} - \bar{p}\,e^{-i\varphi^*}) \\
A &= -i\sum_k \gamma_k - \bar{\gamma}_k = -\sum_k \alpha_k \\
B &= \sum_k \gamma_k + \bar{\gamma_k} = \sum_k \beta_k \\
S_1^A &= -i\sum_k (\gamma_k - \bar{\gamma}_k)x_k = -\sum_k \alpha_k x_k \\
S_1^B &= \sum_k (\gamma_k + \bar{\gamma}_k)x_k = \sum_k \beta_k x_k \\
S_2^A &= -i\sum_k (\gamma_k - \bar{\gamma}_k)x_k^2 = -\sum_k \alpha_k x_k^2 \\
S_2^B &= \sum_k (\gamma_k + \bar{\gamma}_k)x_k^2 = \sum_k \beta_k x_k^2\ .
\end{aligned}$$

The expressions for ϵ and b are therefore given by

$$\epsilon = P_- + A \tag{77}$$
$$b = P_+ + B\ . \tag{78}$$

Substituting in (76) and discarding the higher order terms renders

$$\begin{aligned}
\frac{dx_i}{dt} &= (P_- + A)\,x_i - \sum_k \alpha_k x_k - \frac{1}{2}(P_+ + B)\,x_i^2 + \sum_k \beta_k x_k\,x_i - \frac{1}{2}\sum_k \beta_k x_k^2 \qquad (79) \\
&= -\frac{1}{2}b\,x_i^2 + \left(\varepsilon + S_1^B\right)\,x_i - \frac{1}{2}(2S_1^A + S_2^B)
\end{aligned}$$

Remark that the Jacobian at the symmetric equilibrium $\vec{\varphi}^*$, i.e. for $x_i = 0\ \forall i$, is given by

$$J_{ij} = \begin{cases} P_- + A - \alpha_i & \text{for } i = j \\ -\alpha_j & \text{otherwise} \end{cases}$$

and has an eigenvalue $\lambda_1 = \epsilon = P_- + A$, with multiplicity $N - 1$, and a simple eigenvalue $\lambda_2 = P_-$. We are interested in the *stable* 1-cluster steady state solution

$\vec{\varphi}^*$ and the events which accompany its destabilization. Observe that for negative A, the largest eigenvalue is λ_2 and the remaining eigenvalues become zero in a parameter region where the symmetric solution $\vec{\varphi}^*$ is already unstable. Therefore, before the bifurcation we are interested in the case with $P_-(\vec{\varphi}^*) < 0$ and a positive $A = -\sum_k \alpha_k$, which corresponds to a "prevailing repulsive" coupling strength α_k w.r.t. the sine part.

Now we can consider the steady state solutions of (79). At the steady state each oscillator can take one of two states:

$$x_i^{(\pm)} = \frac{\left(\varepsilon + S_1^B\right) \pm \sqrt{\left(\varepsilon + S_1^B\right)^2 - b(2S_1^A + S_2^B)}}{b} \ . \tag{80}$$

Let $\sigma_i = \pm 1$ denote the sign before the square root. The steady solution of the system is therefore characterized by the set $\{\sigma_1, ..., \sigma_P\}$ and depends on the quantities

$$\begin{aligned} Q_A &= \sum_k \alpha_k \sigma_k \\ Q_B &= \sum_k \beta_k \sigma_k \ . \end{aligned}$$

Because of the form of (80) it is convenient also to introduce

$$\begin{aligned} E &= \varepsilon + S_1^B \\ S &= b(2S_1^A + S_2^B) \\ \Delta &= \sqrt{\left(\varepsilon + S_1^B\right)^2 - b(2S_1^A + S_2^B)} \ . \end{aligned} \tag{81}$$

After substituting into $S_{1/2}^{\cdot\cdot}$ we can rewrite the following expressions

$$\begin{aligned} b(2S_1^A + S_2^B) &\equiv S \\ &= 2\sum_k \alpha_k \left(E + \sigma_k \Delta\right) + \frac{1}{b}\sum_k \beta_k \left(E + \sigma_k \Delta\right)^2 \\ &= 2AE + 2Q_A\Delta + \frac{B}{b}E^2 + \frac{B}{b}\Delta^2 + 2\frac{Q_B}{b}E\Delta \end{aligned} \tag{82}$$

and

$$\begin{aligned} \varepsilon + S_1^B &\equiv E \\ &= \epsilon + \frac{1}{b}\sum_k \beta_k \left(E + \sigma_k \Delta\right) \\ &= \epsilon + \frac{B}{b}E + \frac{Q_B}{b}\Delta \ . \end{aligned} \tag{83}$$

We can solve the second of these equations for E

$$E = \left(\frac{b}{b-B}\right)\left(\epsilon + \frac{Q_B}{b}\Delta\right) \ . \tag{84}$$

Combining (82) with (84) and substituting in (81) allows us to derive a self consistent equation for Δ

$$\left(B^2 - b^2 - Q_B^2\right)\Delta^2 - 2b\left(Q_A(b-B) + AQ_B\right)\Delta + b^2\epsilon(\epsilon - 2A) = 0 \ .$$

Observe that the two solutions $\Delta_\pm$ of the quadratic equation depend on the value of ϵ

$$\Delta_\pm = \frac{\left(Q_A(b-B) + AQ_B\right) \pm \sqrt{\left(Q_A(b-B) + AQ_B\right)^2 - \epsilon(\epsilon - 2A)\left(B^2 - b^2 - Q_B^2\right)}}{\frac{1}{b}\left(B^2 - b^2 - Q_B^2\right)}$$

We are interested in the bifurcation of the symmetric equilibrium $\vec{\varphi}^*$ at $\epsilon = 0$. Therefore, we consider only the solution Δ which vanishes at $\epsilon = 0$ and is compatible with $x_i|_{\epsilon=0} = 0$. Expanding about the bifurcation point at small values of ϵ renders

$$\Delta \ = \ \frac{-Ab}{\left(Q_A(b-B) + AQ_B\right)}\epsilon + \mathcal{O}(\epsilon^2) \ . \tag{85}$$

Substituting back in (80) results in

$$x_i = \begin{cases} \frac{Q_A - A}{Q_A(b-B) + AQ_B}\,\epsilon + \mathcal{O}(\epsilon^2) & \text{for } \sigma_i = +1 \\ \frac{Q_A + A}{Q_A(b-B) + AQ_B}\,\epsilon + \mathcal{O}(\epsilon^2) & \text{for } \sigma_i = -1 \ . \end{cases} \tag{86}$$

Remark that, per definition (81), $\Delta \geq 0$. Additionally, as discussed above, we require $P_- < 0$ and $A > 0$ in order for the synchronous 1-cluster solution to be stable before the bifurcation. Observe also that at $\vec{\varphi}^*$, equation (75) is identical to zero and

$$\begin{aligned} b \ &= \ P_+ + B \\ &= \ -\omega < 0 \end{aligned}$$

Therefore, from (85) follows that before the bifurcation (i.e. $\epsilon < 0$)

$$AQ_B \leq Q_A(\omega + B) \ . \tag{87}$$

Pitchfork bifurcations are possible only in the non-generic situation of $AQ_B = Q_A(\omega + B)$; for positive A such pitchforks are subcritical, and their branches lie in the region of $\epsilon < 0$. Otherwise, all branches are transcritical: when approaching $\epsilon = 0$, every coordinate of every steady state decreases asymptotically linearly, and changes sign after passing through the bifurcation value of the parameter. Accordingly, along each branch of solutions the absolute values of Q_A and Q_B remain constant, but each changes sign for$\varepsilon > 0$ and $\varepsilon < 0$.

Let us investigate the stability of the 2-cluster steady states. The synchronous 1-cluster solution $\vec{\varphi}^*$ is stable for $\epsilon < 0$, and becomes unstable with an $(P-1)$-dimensional unstable manifold for $\epsilon > 0$. The spectrum of the 2- cluster steady solution of the system, characterized by the set $\{\sigma_1, ..., \sigma_P\}$, is also highly degenerate. Let us denote by m_+ the number of positive σ_i's and by m_- the number of negative σ_i's. There are $(m_+ - 1)$ eigenvalues equal to $-\Delta$ and $(m_- - 1)$ eigenvalues equal to

$+\Delta$. From equation (85) we can see that at the bifurcation point all those eigenvalues change sign. The remaining two eigenvalues can be calculated in the 2-dimensional reduced system of the two cluster steady solution and are given by

$$\lambda_\pm = -\frac{A}{2} \pm \sqrt{\left(\frac{A}{2}\right)^2 + \Delta\left\{Q_A^{(-)}\left(\frac{2Q_B^{(+)}}{b} - 1\right) - Q_A^{(+)}\left(\frac{2Q_B^{(-)}}{b} - 1\right) - 4\Delta\left(\frac{Q_B^{(+)}Q_B^{(-)}}{b^2} - 1\right)\right\}} \tag{88}$$

where

$$\begin{aligned} Q_A^{(\pm)} &= -\sum_k \delta(\sigma_k \gtrless 0)\alpha_k \\ Q_B^{(\pm)} &= \sum_k \delta(\sigma_k \gtrless 0)\beta_k \end{aligned}$$

with

$$\delta(\sigma > 0) = \begin{cases} 1 & \text{for } \sigma > 0 \\ 0 & \text{otherwise} \end{cases}$$

and

$$\delta(\sigma < 0) = \begin{cases} 1 & \text{for } \sigma < 0 \\ 0 & \text{otherwise} \end{cases} .$$

Observe that at $\epsilon = 0$, i.e. $\Delta = 0$, the eigenvalue λ_- does not change sign. The eigenvalue λ_+, however, might or might not change sign, depending on the coefficients α_k and β_k as well as on the cluster configuration. This is the eigenvalue that distinguishes the class I from the class III branches.

Now we can understand the observations from the previous sections for systems of "active rotators", with solely sinusoidal coupling function. In those cases $B = Q_B = Q_B^{(\pm)} = 0$ and equations (86) and (88), respectively, become

$$x_i = \begin{cases} -\frac{Q_A - A}{Q_A \omega}\epsilon + \mathcal{O}(\epsilon^2) & \text{for } \sigma_i = +1 \\ -\frac{Q_A + A}{Q_A \omega}\epsilon + \mathcal{O}(\epsilon^2) & \text{for } \sigma_i = -1 \ . \end{cases} \tag{89}$$

$$\lambda_\pm = -\frac{A}{2} \pm \sqrt{\left(\frac{A}{2}\right)^2 - \frac{A\epsilon}{Q_A}\left\{Q_A^{(+)} - Q_A^{(-)} - 4\frac{A\epsilon}{Q_A}\right\}} \tag{90}$$

with the condition for a pitchfork bifurcation given by

$$Q_A = 0 \ . \tag{91}$$

In section 5, figure 38 we have pointed out the shift of the branches undergoing transcritical bifurcations with respect to changes of the size of the largest cluster, or equivalently changes in the coupling constants of the reduced system. This shift can comprehended from equation (89) where x_i determines the position of the cluster in the vicinity of the bifurcation point. Remark also that the definition of the class II branches from equation (73) corresponds to the same condition given by

equation (91). Finally, for ϵ in the vicinity of the bifurcation point, i.e. $\epsilon \approx 0$, equation (90) results into

$$\lambda_{\pm} = \frac{(-A \pm A)}{2} - \frac{\left(Q_A^{(+)} - Q_A^{(-)}\right)}{Q_A}\epsilon + \mathcal{O}(\epsilon^2)\,.$$

The sing of λ_+ is determined by $\left(Q_A^{(+)} - Q_A^{(-)}\right)$ reflecting the definition of the class I and the class III branches, whereby for the class III branches the saddle undergoing the transcritical bifurcation becomes a stable fix point. From the examples above, we have seen that for class I systems (i.e. systems where only class I branches exist) the transcritical bifurcation leads to the THB bifurcation resulting in limit cycles.

From Local to Global Coupling: Conclusions

In this part of the work we have investigated general conditions, posed on the network topology and dynamics, enabling the existence of flow invariant polydiagonal subspaces compatible with the Watanabe-Strogatz reduction. Besides the sinusoidal coupling function, a necessary condition for the WS reduction is that in the cluster reduced state, on the polydiagonal, the system becomes globally coupled: i.e. each element of a given cluster should be coupled to at least one element of a different cluster and arbitrary many elements of its own cluster. From the investigated examples we have seen that the existence of such polydiagonals does not ensure their dynamical relevance, since those polydiagonals may remain unstable. Similar to the observations from section 2, here, we have seen that the stability of the reduced system depends not only on the local symmetries of the network but also on global characteristics such as the network size. We have investigated the bifurcations associated with the lost of stability of the 1- cluster state for repulsing coupling. Depending on the reduced network, pitchfork or transcritical bifurcations take place and the resulting desynchronization of the 1- cluster state leads to new clustered states which might be stationary or time-dependent. In particular, if the coupling strengths in the reduced system are of class I (i.e. the largest coupling strength is smaller than the sum of the remaining coupling strengths) a THB bifurcation always takes place. Remarkably, even if the coupling topology of the reduced WS system does not imply any particular symmetries, the periodic orbits born at the THB bifurcation possess a spatio-temporal symmetry due to the peculiarities of bifurcation itself. If the reduced system does have additional symmetries due to its coupling topology, those symmetries are expressed as spatial symmetries between different periodic orbits.

Part II
Sustained oscillations, irregular firing and chaotic dynamics in hierarchical modular networks with mixtures of electrophysiological cell types

In part I of the work we studied dynamical phenomena which emerge as a result of the interplay between network topology and single-node dynamics by focusing on complex network of largely theoretical interest. The network topologies corresponded to regular or structured graphs with comprehensible complexity in terms of symmetries; the single-node dynamics and interaction functions were modeled by coupled phase oscillators enabling the study of collective behavior in terms of synchronization. In part II we investigate similar questions about the interplay between network topology and single-node dynamics, however, concentrating on more realistic dynamical systems describing neuronal cortical-like networks. In line with expectations, both architecture of a neuronal network and dynamics of single neurons is far more complex than the systems presented in part I. The most famous detailed mathematical model of single neuron dynamics is the Hodgkin–Huxley model [58], which takes into account the biophysical characteristics of the cell membrane and describes how action potentials are initiated and propagated. Each neuron is described by a set of several coupled ordinary differential equations and although the Hodgkin–Huxley model is a detailed and accurate mathematical model of a single neuron, it is not always the best choice when considering large neural networks because of the computational expense and analytical complexity. Nevertheless, phase oscillator models similar to those investigated in part I can be derived as phenomenological approximations of the Hodgkin–Huxley model and can be used to describe strongly simplified dynamics of single neurons [26, 64]. This is not surprising since a neuron stimulated with a constant external input current can perform periodic oscillations in the phase space which can be approximated via phase oscillator models (see section 1.1). The *Ermentrout-Kopell canonical model* [40, 41], also called *theta neuron model*, is a simple one-dimensional phenomenological model for a spiking neuron:

$$\frac{d\theta}{dt} = (1 - \cos\theta) + (1 + \cos\theta)\, I(t) \ . \tag{92}$$

Here $I(t)$ is the input to the model and θ is a phase variable with a range $[0, 2\pi]$ such that when θ equals π the neuron spikes. For more details we refer to [40, 41, 64]. Similar to the Kuramoto and Shinomoto model of "active rotators" [91], the theta neuron model describes an excitable system. Recall from section 2, equation (23) that for $\omega \in (0, 1)$ and $b = 1$ the Kuramoto and Shinomoto model of "active rotators" had one stable and one unstable fixed points for $\kappa = 0$, because of the sine function. Depending on the values of ω, b and the term proportional to κ those fixed points are shifted along the unit circle and eventually disappear in the saddle node bifurcation.

Because of the cosine function, the theta neuron model (92) has two fixed points for $I < 0$ which disappear in a saddle node bifurcation at $I = 0$ and the neuron performs periodic oscillations for $I > 0$. Although a network of theta neurons might be analytically comprehensible, similar to those investigated in part I, it describes neurons with identical or similar internal dynamics and does not capture the diversity of firing patterns of cortical neurons [63, 116]. A suitable theoretical model, based on extension of the theta neuron model, which reproduces the behavior of neurons belonging to different electrophysiological classes is the Izhikevich neuron model [62]. In this model a second slow time-scale variable u is introduced describing the recovery process of the membrane potential after a neuron performs a spike [61]:

$$\begin{aligned} \frac{d\theta}{dt} &= (1-\cos\theta) + (1+\cos\theta)\,(I(t)+su) \\ \frac{du}{dt} &= \delta(\theta-\pi) - \eta u \end{aligned} \tag{93}$$

Here, $\eta \ll 1$ enables the time scale separation and δ denotes the Dirac delta function such that the variable u is increased at each spike ($\theta = \pi$) and then slowly relaxes to zero. The sign of s in the first equation determines whether the next firing is advanced or delayed, which results, respectively, in spike facilitation or adaptation. Remark that introducing a variable $v = \tan(\theta/2)$ allows us to rewrite the system (93) in the normal quadratic form of the Izhikevich neuron model [62] (see equation (94) below). Since the new variable v is not periodic it is also necessary to introduce artificially a spike threshold and reset value for v. In section 10 we discuss shortly the dynamical properties in the phase space of the Izhikevich neuron model. For more details we refer to [61, 62, 64].

In the remaining part of this work we use the Izhikevich model as a paradigm for the neuron dynamics and study a global dynamical phenomenon in neural networks, known as self-sustained activity. In particular, we investigate the effect of network architecture and single neuron dynamics on the self-sustained activity of the network.

Sections 7–9 as well as parts of section 12 were published in this form in [103].

7 Self-Sustained Activity in Neuronal Networks

The resting state of the brain, i.e. its state in the absence of sensory stimuli or behavioral tasks, shows sustained ongoing activity characterized by irregular neuronal firing and macroscopic ensemble oscillations covering a broad frequency range, from less than 1 Hz up to more than 100 Hz [9, 19, 105, 22, 42, 87, 92, 54]. Experimental and theoretical work suggests that this ongoing resting state activity may have an important role to endow the brain with flexibility in dealing with diverse cognitive and behavioral situations [72, 52, 73, 76, 88, 33, 96].

Since the cortex during a resting state is essentially disconnected from external stimuli, it is in a dynamic regime in which neural activity is self-sustained [99]. It is important to understand the mechanisms responsible for self-sustained activity (SSA) in the cortical network: the roles of the structural organization of cortical connections as well as of the intrinsic characteristics of neurons that constitute the network.

The architecture of the cortical connections presents different features when viewed from different spatial scales. At a microscopic scale cortical circuitry is highly recurrent with both excitatory and inhibitory neurons involved in many superposed positive and negative feedback loops [38, 16, 15]. At a macroscopic or systems level scale the organization of cortical connections seems to be hierarchical and modular, with dense excitatory and inhibitory connectivity within modules and sparse excitatory connectivity between modules [57, 119, 80, 89].

A number of studies considered effects of the structure of cortical connections on the existence of sustained cortical activity and on variability of the single-cell and population firing rates in that regime. Studies with random networks of sparsely connected excitatory and inhibitory neurons have shown that sustained irregular network activity can be produced when the recurrent inhibitory synapses are relatively stronger than the excitatory synapses [106, 107, 21, 108, 69]. Recently, the random network assumption has been relaxed and it has been shown that networks with clustered [74], layered [32, 85], hierarchical and modular [66, 110, 44] connectivity patterns as well as with local and long-range connections plus excitatory synaptic dynamics [99] can generate cortical-like irregular activity patterns. Other works have focused on the role of signal transmission delays and noise in the generation of such states [30, 31].

Emphasizing the role of the topological structure of the cortical networks, most of these models do not take into account the possible joint role of the multiple firing patterns of the different types of neurons that comprise the cortex. For example, descriptions in terms of the popular leaky integrate-and-fire model (see e.g. [108, 110, 74, 85]), do not capture the diversity of firing patterns of cortical neurons [63, 116]. The exception is the model of [32], where complex intrinsic properties of the employed neurons correspond to electrophysiological measurements.

Intrinsic properties of cortical neurons like types of ion channels, and distributions of ionic conductance densities stand behind a variety of firing patterns. Based on their responses to intracellular current pulses, neurons with different patterns can be grouped into five main electrophysiological classes: regular spiking (RS), intrinsically bursting (IB), chattering (CH, also called fast repetitive bursting), fast spiking

(FS) and neurons that produce low threshold spikes (LTS) [24, 79, 82, 25]. Excitatory cells of the RS, IB and CH classes are mostly pyramidal and glutamatergic, and comprise ∼80% of cortical cells; their majority is of the RS type. On the other hand, inhibitory cells from the FS and LTS classes are of non-pyramidal shapes and GABAergic.

Given the variability of cortical firing patterns, the natural questions are: (i) how does the inclusion of neurons with varying intrinsic dynamics in a hierarchical and modular cortical network model affect the occurrence of SSA in the network? (ii) how does a combination of hierarchical and modular network topology with individual node dynamics influence the properties of the SSA patterns in the network?

To address these questions, we use a hierarchical and modular network model which combines excitatory and inhibitory neurons from the five cortical cell types. Higher complexity in comparison to previous models, in particular mixtures of different neuronal classes in non-random networks, hampers analytical studies. However, it is important to push modeling to these higher complexity situations that are closer to biological reality. Numerical simulations may give us insights on how to construct deeper analytical frameworks and shed light on the mechanisms underlying ongoing cortical activity at rest.

Our simulations show that SSA states with spiking characteristics similar to the ones observed experimentally can exist for regions of the parameter space of excitatory-inhibitory synaptic strengths in which the inhibitory strength exceeds the excitatory one. This is in agreement with the simulations of random networks made of leaky integrate-and-fire neurons mentioned above. However, our simulations disclose additional mechanisms that enhance SSA. The SSA lifetime increases with the number of modules, and when the network is made of LTS inhibitory neurons and a mixture of RS and CH excitatory neurons. These new mechanisms point to a synergy between network topology and neuronal composition in terms of neurons with specific intrinsic properties on the generation of SSA cortical states.

8 Methods and Models

All functions, simulations, and protocols were implemented in C++. Ordinary differential equations were integrated by the fourth order Runge-Kutta method with step size of 0.01ms. Processing of the results was performed in Matlab.

8.1 Neuron models

Neurons in our networks were described by the piecewise-continuous Izhikevich model [62]. The dynamics of the i-th neuron obeys two coupled differential equations,

$$\begin{aligned} \dot{v}_i &= 0.04v_i^2 + 5v_i + 140 - u_i + I_i(t) \\ \dot{u}_i &= a\,(b\,v_i - u_i), \end{aligned} \tag{94}$$

with a firing condition: whenever the variable $v(t)$ reaches from below the threshold value $v_{\rm crit}$=30mV, the state is instantaneously reset, $v(t) \mapsto c,\ u(t) \mapsto u(t) + d$. The variable v represents the membrane potential of the neuron and u is the membrane recovery variable. Each resetting is interpreted as firing a single spike.

Appropriate combinations of the four parameters (a, b, c, d) generate the firing patterns of the five main electrophysiological cortical cell classes listed in the Introduction. We use the following sets of values [62]:

- RS neurons: $a = 0.02$, $b = 0.2$, $c = -65$, $d = 8$ (Figure 41a);
- IB neurons: $a = 0.02$, $b = 0.2$, $c = -55$, $d = 4$ (Figure 41b);
- CH neurons: $a = 0.02$, $b = 0.2$, $c = -50$, $d = 2$ (Figure 41c);
- FS neurons: $a = 0.1$, $b = 0.2$, $c = -65$, $d = 2$ (Figure 41d);
- LTS neurons: $a = 0.02$, $b = 0.25$, $c = -65$, $d = 2$ (Figure 41e).

The term $I_i(t)$ in equation 94 denotes the input received by neuron i

$$I_i(t) = I_{stim,i} + I_{syn,i}$$

where $I_{stim,i}$ stands for the external input, which is independent from the network activity, and $I_{syn,i}$ denotes the synaptic input from other neurons in the network. We modeled the latter as

$$I_{syn,i} = \sum_{j \in \text{presyn}} G_{ij}^{\text{ex/in}}(t)\left(E_{\text{ex/in}} - v_i\right), \tag{95}$$

where the sum extends over all neurons, presynaptic to neuron i, and $G_{ij}^{\text{ex/in}}$ is the conductance of the synapse from neuron j to neuron i, which can be either excitatory or inhibitory. The reversal potentials of the excitatory and inhibitory synapses are $E_{\text{ex}} = 0$mV and $E_{\text{in}} = -80$mV, respectively. We assume that the synaptic dynamics is event-driven without delays: when a presynaptic neuron fires, the corresponding

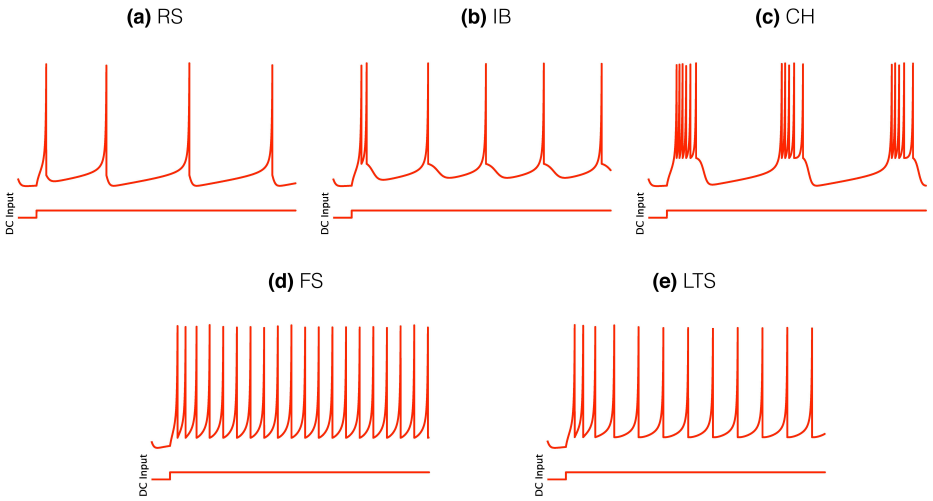

Figure 41: Electrophysiological cell classes as modeled by equation (94). Parameter values are given in the text. (a) Regular spiking (RS) neuron. (b) Intrinsically bursting (IB) neuron. (c) Chattering (CH) neuron. (d) Fast spiking (FS) neuron. (e) Low threshold spiking (LTS) neuron.

synaptic conductance $G_{ij}^{\text{ex/in}}$ is instantaneously increased by a constant amount $g_{\text{ex/in}}$. Otherwise, conductances obey the equation

$$\frac{d}{dt}G_{ij}^{\text{ex/in}}(t) = -\frac{G_{ij}^{\text{ex/in}}(t)}{\tau_{\text{ex/in}}}, \tag{96}$$

with synaptic time constants τ_{ex}=5 ms and τ_{in}=6 ms [29, 65]. The parameters $g_{\text{ex/in}}$ characterize the synaptic strength and are varied throughout the simulations.

8.2 Network models

The hierarchical and modular architecture of our networks was constructed by a top-down method [110]. In this approach, we started with a random network of N neurons connected with probability p and rewired it to obtain hierarchical and modular networks. Here we used two combinations of N and p: N=512 with p=0.02, and N=1024 with p=0.01. In both cases the ratio of excitatory to inhibitory neurons was 4:1. Excitatory neurons were purely of the RS type or a mixture of two types: RS (always present) with either CH or IB cells. Inhibitory cells were all of either FS or LTS type. A random network as the one described above constitutes one module and will be called here a network of hierarchical level H=0. A network of hierarchical level H has 2^H modules [110], hence a network of hierarchical level H=1 has 2 modules, a network with H=2 has 4 modules, and so on.

Networks with $H > 0$ were generated by the following algorithm:

1. Randomly divide each module of the network into two modules of same size;
2. With rebating probability $R_{\text{ex/in}}$, delete each intermodular connection $(i \to j)$ and create a new connection between i and k where k is a randomly chosen neuron from *the same module* as i;

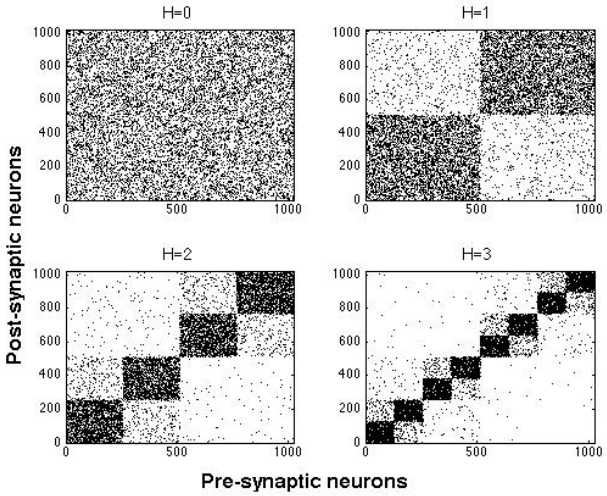

Figure 42: Examples of connection matrices for hierarchical and modular networks at $H = 0, \ldots, 3$ constructed with rebating probabilities given in text. Each dot represents a connection from a presynaptic neuron to a postsynaptic one.

3. Recursively apply steps 1 and 2 to build networks of higher hierarchical levels.

The rebating probabilities had values $R_{\rm ex}$=0.9 and $R_{\rm in}$= 1, rendering the intermodular couplings exclusively excitatory. Figure 42 shows examples of hierarchical and modular networks constructed with the above rebating probabilities.

8.3 Network spiking characteristics

Here, we define the quantities and measures that characterize the spiking properties of single neurons and of the entire network.

The spike train of a neuron i is represented as [43, 29],

$$x_i(t) = \sum_{t_i^f} \delta(t - t_i^f), \tag{97}$$

where $\{t_i^f\}$ is the set of times at which a neuron i fires. The firing rate of neuron i over a time interval T is the number n_i of spikes which it fires during the interval, divided by T:

$$f_i = \frac{n_i}{T} = \frac{1}{T}\int_T x_i(t')dt. \tag{98}$$

Accordingly, the mean firing rate of N neurons in the network, over a time interval T, is given by:

$$\begin{aligned} \langle f \rangle &= \frac{f_i}{N} \\ &= \frac{1}{N}\sum_{i=1}^{N}\frac{1}{T}\int_T x_i(t')dt'. \end{aligned} \tag{99}$$

The time-dependent activity of the network $A(t;\Delta t)$ was defined as the total number of spikes fired by its neurons within a time interval Δt around t:

$$A(t;\Delta t) = \sum_{i=1}^{N} \int_{t}^{t+\Delta t} x_i(t')dt'. \tag{100}$$

Dividing it by the number of neurons, we obtain the time-dependent firing rate of the network:

$$f(t;\Delta t) = \frac{1}{N} \sum_{i=1}^{N} \int_{t}^{t+\Delta t} x_i(t')dt'. \tag{101}$$

Equation (100) provides the variation of the number of active neurons in the network within the interval Δt while equation (101) gives the variation of the proportion of active neurons within Δt. Since Δt in both expressions will be fixed at 1 ms throughout this study, below we denote the time-dependent activity and firing rate of the network simply by $A(t)$ and $f(t)$.

Irregularity of network firing was characterized by two distributions: the distribution of interspike intervals (ISI) of all neurons in the network, and the distribution of the coefficients of variation (CV) of the ISIs of each neuron. The ISI distribution was formed by the set $\{\mathrm{ISI}_i\}$, i=1,..., N for all neurons. To obtain the distribution of the CVs, we calculated for every neuron i the standard deviation $\sigma_{\mathrm{ISI_i}}$ of its ISI_i distribution normalized by the mean $\overline{\mathrm{ISI}}_i$ for this neuron ([43]):

$$CV_i = \frac{\sigma_{\mathrm{ISI_i}}}{\overline{\mathrm{ISI}}_i}, \tag{102}$$

and took the set of CV_i for all network neurons.

Basing on the values of these activity measures extracted from the raster plots of the simulations, we delineated the regions where SSA was observed on the plane of excitatory and inhibitory conductances $(g_{\mathrm{ex}}, g_{\mathrm{in}})$.

9 Results

9.1 Parameter dependence of SSA

Below, "architecture of the network" denotes the topology of the network, i.e. hierarchical level H, plus its composition, i.e. the types and proportions of participating neurons. A given network realization is then a network with fixed architecture, produced randomly by the algorithm from the preceding section.

In the simulations, the network was activated by injecting external current of amplitude I_{stim} into a proportion P_{stim} of the neurons for the time interval T_{stim}. After stimulus termination, the network was left to evolve freely ($I_{stim}(t > T_{stim}) = 0$) until the end of simulation time T_{sim}. While this activation may look adequate enough from a physiological point of view, in the dynamical sense it plays only the role of setting initial conditions. In the course of stimulation, the system is driven to some position in the phase space, from where it is left to evolve on its own. The effect, of course, would be the same if the same starting state for free evolution was explicitly imposed from the beginning. However, external stimulation ensures that initial conditions are not just randomly chosen somewhere in the high-dimensional phase space, but lie close to typical pathways in its "physiologically reasonable" part. In the case of multistability (i.e. quiescent state and one or several kinds of SSA), variation of initial conditions can place the starting points in the attraction domains of different coexisting attractors.

Parameter search.

To gain insight into properties of the system, such as duration of SSA and firing rates, at different synaptic strengths, we conducted a preliminary study with small networks of 512 neurons and short simulation times T_{sim}=350 ms. These investigations were performed in the parameter region of synaptic strengths $g_{\text{ex}} \in [0, 1]$, $g_{\text{in}} \in [0, 5]$, discretizing it with Δg_{ex}=0.1 and Δg_{in}=0.5. For each network realization and each parameter pair $(g_{\text{ex}}, g_{\text{in}})$ in this range, we took eight initial conditions in different regions of phase space. This was achieved by changing the proportion of stimulated neurons (either half of the neurons or all of them: P_{stim}=1/2, 1), the amplitude of external current (I_{stim}=20, 30) and the stimulation interval (T_{stim}=80 ms, 120 ms).

Figure 43 represents a corresponding typical example: in this case, a network of two modules (hierarchical level H=1) where 20% of the excitatory neurons were of the CH class, all inhibitory neurons were of the LTS class, and the activation parameters were P_{stim}=1, I_{stim}=20 and T_{stim}=80 ms. Figure 43A shows the resulting duration and type of network activity for different synaptic strengths. The blue region corresponds to fast decay of activity after termination of the external input with network activity lasting not longer than 50 ms. We call this type of behavior *rapid decay*. The yellow region indicates large-scale network activity oscillations, when, for a certain time after activation, different groups of neurons fire synchronously, and decay afterward. We call this behavior *temporary oscillatory activity*. The red region corresponds to the same type of network behavior as in the yellow one, but lasting until the end of the simulation, and we call it *persistent oscillatory SSA*.

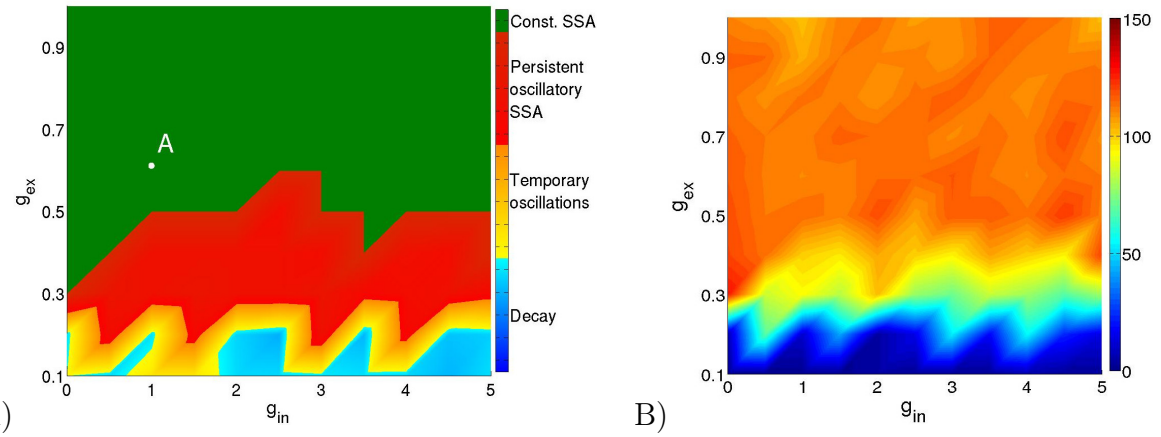

Figure 43: Types of activity for a network of 512 neurons in 2 modules. Neuronal types: 64% RS, 16% CH, 20% LTS. Activation parameters: P_{stim}=1, I_{stim}=20, T_{stim}=80 ms.
A) Duration of network activity. Green: constant SSA; Red: persistent oscillatory SSA; Yellow: temporary oscillatory SSA, Blue: rapid decay. (see also figure 44)
B) Mean firing rate of the network during the active period. Firing rate ranges in Hz: see colorbox on the right.

The green region indicates SSA with strongly irregular individual neuronal firing and more or less constant overall network activity; this behavior is referred to as *constant SSA*. Examples of these four behavioral patterns are visualized in figure 44.

Figure 43B represents the mean firing rate $\langle f \rangle$ of the neurons in the active period. The latter was defined as the time interval between the end of external stimulation and the time of the last spike in the network. If by the end of simulation neurons were still spiking, the whole duration of the free evolution was taken as the length of the active period. The regions corresponding to SSA yield somewhat unrealistic mean firing rates above 70 Hz in comparison with lower values found in cortex [95, 108, 59, 32, 77, 55]. These high mean frequencies owe to CH and LTS neurons, which, in the green region of the diagram, can display firing rates as high as 600 Hz. In these regions, even individual RS neurons can possess very high firing rates, in some cases as high as 200 Hz.

Regardless of those high firing rates, we studied the effects of changes in the network architecture, its realizations and initial conditions on the SSA. As a rough measure of the latter, we regarded the area occupied by the SSA regions on the parameter plane of $(g_{\text{ex}}, g_{\text{in}})$. For this small networks, we summarize our observations as follows:

- Increase of the hierarchical level H (i.e. the number of network modules) under fixed other conditions led to growth of the SSA area;
- If the second excitatory neuron type (besides the RS neurons) was CH, increase of its proportion led to growth of the SSA area;
- If the second excitatory neuron type was IB, variation of its proportion displayed no clear influence on the SSA area;

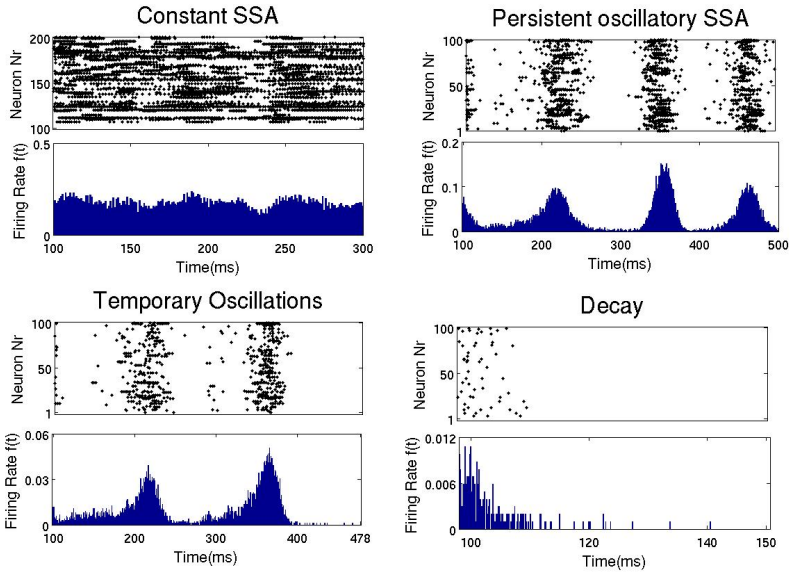

Figure 44: Four types of network activity patterns. Each panel shows the raster plot of the spiking activity for a sample of 100 network neurons (top), and the firing rate $f(t)$ of all neurons (bottom). Constant SSA: point A in figure 43 ($g_{\rm ex}$=0.6, $g_{\rm in}$=1). Persistent oscillatory SSA: point B in figure 45 ($g_{\rm ex}$=0.12, $g_{\rm in}$=0.6). Temporary oscillations: point C in figure 45 ($g_{\rm ex}$=0.09, $g_{\rm in}$=0.5). Decay: point D in figure 45 (g_{ex} = 0.06, g_{in} = 0.2).

- Under fixed other characteristics, replacement of FS inhibitory neurons by LTS inhibitory neurons increased the SSA area.

We did not observe noticeable changes in the SSA area for different network realizations and/or activation parameters. The few observed changes were mostly seen as small displacements along the border between the red and yellow regions in the top diagram of figure43 (data not shown). These changes became significant in the lower left part of the diagram (data also not shown), where the mean firing rates were closer to biological values. Therefore, below we concentrate on this parameter region, which we call the region of low synaptic strengths.

9.2 SSA for low synaptic strengths

From now on we consider a larger network consisting of 1024 neurons within the parameter range of weaker synaptic strengths: $g_{\rm ex} \in [0.05, 0.15]$, $g_{\rm in} \in [0, 1]$.

Figure 45 gives an example of the $(g_{\rm ex}, g_{\rm in})$ diagram for low synaptic strengths (discretized on a 50×50 grid with $\Delta g_{\rm ex}$=0.002 and $\Delta g_{\rm in}$=0.02). It corresponds to a network with hierarchical level H=1, 20% of its excitatory neurons of the CH type, inhibitory neurons of the LTS type, and the following activation parameters: $P_{\rm stim}$=1/2, 10$\leq$ $I_{\rm stim}$ <20 and $T_{\rm stim}$=100 ms. The simulation was prolonged up to 1000 ms. The lifetime of activity strongly depends on the initial conditions: for a given network realization, some initial conditions would result in SSA while others would not. Therefore, only a statistical characterization of activity makes

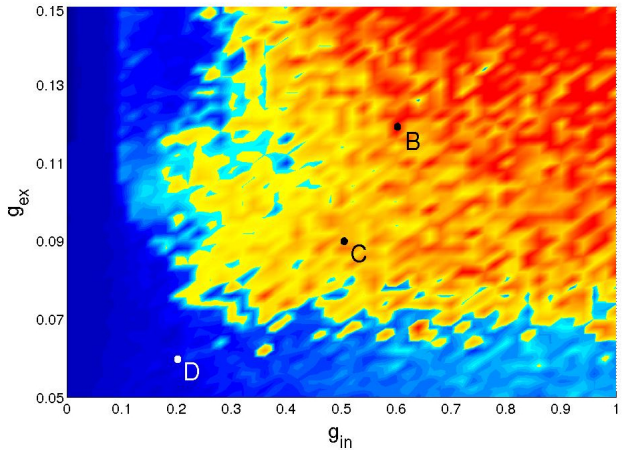

Figure 45: Network activity on the parameter plane of low synaptic strengths: a typical distribution of network activity patterns for 2^{10} neurons. Network parameters and coloring scheme as in figure 43A.

sense. In each point of the parameter grid we chose 10 different initial conditions, followed the evolution and plotted the maximal lifetime. The resulting diagram captures the generic properties of all studied network architectures in the region of low synaptic strengths: in all cases no constant SSA was detected, and self-sustained activity, if present, was oscillatory. The striking feature is the highly fragmented shape of the SSA region which is located in the upper right corner of the diagram. Changing the activation protocol, under the fixed network architecture, we observed similar fragmented structures with slightly different configurations (not shown). For neighboring initial conditions, prepared by varying the stimulation time within several integration steps, the lifetime of network activity varied over the range from few milliseconds up to 10^4 ms. Notably, even at low values $g_{\rm ex}$ (the bottom part of the diagram) there is some probability to observe SSA with three or four subsequent epochs of high synchronous activity.

High sensitivity with respect to initial conditions is a hallmark of dynamical chaos. On the other hand, at least within the range of low synaptic strengths, the chaotic regime is hardly an attractor, since activity typically dies out after a long or short transient: trajectories end up at the trivial stable state where all neurons are at their resting potential. Systems which, for typical initial conditions, exhibit chaos up to a certain time and then, often abruptly, switch to non-chaotic dynamics, are known as transiently chaotic [71]. In section 11.2 we discuss in more details features of this transient dynamics.

Based on our observations, we may say with a high certainty that the SSA states in the domain of low synaptic strengths are due to transient chaos and therefore have finite lifetimes. Increasing the synaptic strengths to higher parameter values, e.g. ($g_{\rm ex} \sim 1$, $g_{\rm in} \gtrsim 2$) may lead to a situation where the transient chaotic set turns into an attractor and the SSA becomes incessant. However, as remarked above, this would result in very high firing frequencies and, hence, would hardly correspond to biologically realistic cases.

The fact that we are dealing with transient SSA makes the analysis somewhat

ambiguous: there seems to be no definite way to draw a sharp boundary in the parameter space, between the domains with SSA and those without it. However, under each fixed set of parameters, we can evaluate the probability of having SSA with a given duration. This, of course, requires statistics for a sufficient number of initial conditions.

First, we partitioned the $(g_{\rm ex}, g_{\rm in})$ diagram of low synaptic strengths into sixteen distinct domains, corresponding to sixteen fixed $(g_{\rm ex}, g_{\rm in})$ pairs. For all network architectures and each of the domains we tested 120 different initial conditions, prepared by external stimulation: we varied the proportion of stimulated neurons $P_{\rm stim}$=1, 1/2, 1/8, 1/16, the input current $I_{\rm stim}$=10, 20 and the stimulation time $T_{\rm stim}$=50, 52,. . .,78 ms. In this way we intended to lead the system to distinct regions of the phase space (presumably governed by the number of stimulated neurons), and then, by varying $T_{\rm stim}$, to gather statistics within these regions. Each run ended when the activity died out completely, or else at 10^4 ms.

We observed that regardless of the network architecture in the absence of inhibition ($g_{\rm in}$=0) or at very low excitatory synaptic strength ($g_{\rm ex}$=0.05) no cases of SSA occurred and the system relaxed towards the fixed point in a non-chaotic way for all 120 tested initial conditions. Figure 6 displays extended statistics for a network with four modules (H=2) where 20% of the excitatory neurons are CH, and the inhibitory neurons are LTS. For each of the sixteen $(g_{\rm ex}, g_{\rm in})$ pairs, over a thousand different initial conditions were used. Figure 6A shows the corresponding lifetime distributions. At sufficiently high inhibition and excitation, for most of the network architectures these distributions display exponential decay. This observation is confirmed in figure 6B which shows the distributions for the nine cases in the upper right corner of figure 6A, replotted on the logarithmic scale of the ordinate. The probability of finding a chaotic transient SSA with lifetime τ decays exponentially in τ, at a rate which depends on the network parameters. Such exponential distributions of the lifetime of chaotic transients are typical and characteristic for systems with transient chaotic behavior [71].

Concentrating on the four pairs $(g_{\rm ex}, g_{\rm in})$ from the far upper right corner in figure 46 ($g_{\rm ex}$=0.12, 0.15 and $g_{\rm in}$=0.7,1) which showed most cases of transient SSA, we performed additional simulations for all architectures, creating in each case a few thousands initial conditions by varying the stimulation time in the range of 50ms to 175ms and/or the amplitude of the stimulus in the range of 10 to 30 and/or the proportion of stimulated neurons $P_{\rm stim}$=1, 1/2, 1/8, 1/16.

In the next subsection we present the obtained results and demonstrate that dependence of SSA on the values of $g_{\rm ex}$ and $g_{\rm in}$ varies strongly in response to changes in the network architecture.

9.3 Changes with respect to network architecture

Here, we describe the changes in the SSA states caused by variation of the network architecture in the region of low synaptic strengths. Below, we basically refer to the four investigated pairs $(g_{\rm ex}, g_{\rm in})$ ($g_{\rm ex}$=0.12, 0.15 and $g_{\rm in}$=0.7, 1) corresponding to the most active domain of the parameter plane, since there the changes are better visible, and the tendencies can be better inferred from the statistics based on few

A)

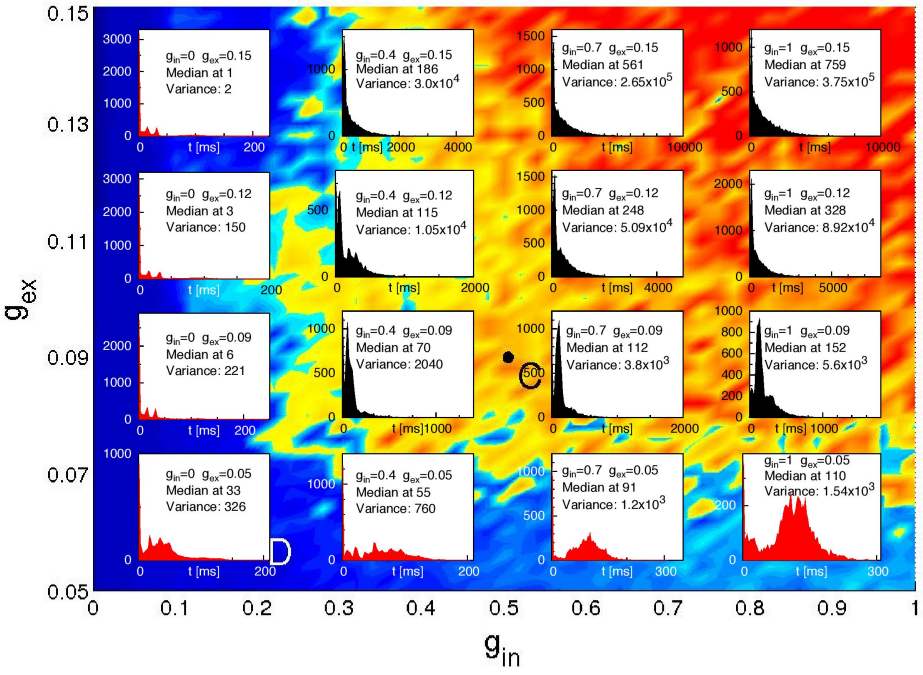

B)

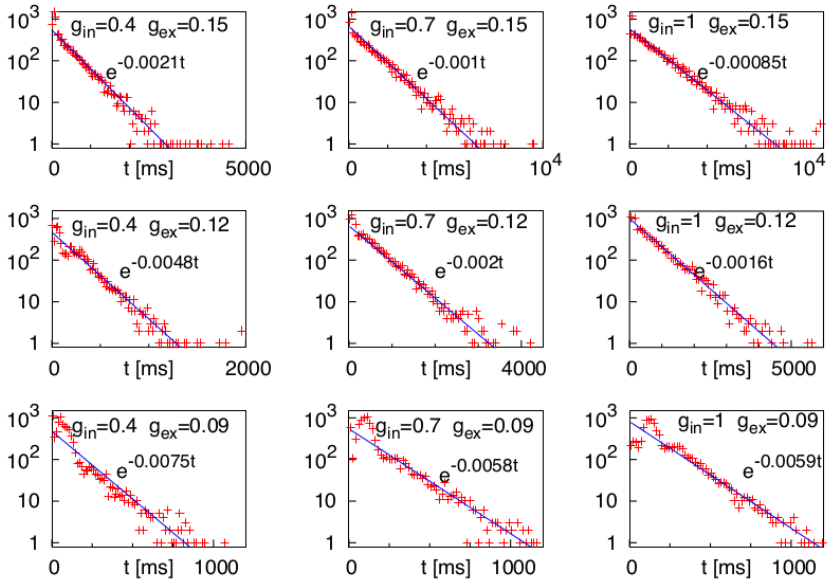

Figure 46: Lifetime distributions for a network of 2^{10} neurons with four modules (H=2); 20% of the excitatory neurons are CH; the inhibitory neurons are LTS. A) Histograms of lifetimes, with medians and variances, for 10^4 different initial conditions at sixteen pairs $(g_{\rm ex}, g_{\rm in})$. B) Ordinate values on the logarithmic scale for 9 upper right ("black") histograms from the top panel. Straight lines: fitted exponential dependencies.

thousands initial conditions for each of the parameter pairs and each of the network architectures. Results based on the statistics gathered for the 120 initial conditions for the neighboring regions display similar tendencies but are less distinct.

The findings are summarized in Table 7. There, we used as observable the value of the median for the distribution of the lifetimes of SSA. Being interested only in SSA cases, we excluded all trials which resulted in rapid decay or very short oscillatory activity: only the datasets for which, after the end of the stimulation, the lifetime exceeded 300 ms, were processed. From a dynamical point of view this corresponded to a choice of trajectories that for a certain time lived on the chaotic set. Remarkably, this cut off of the short-lived trajectories led to a drastic reduction of the number of trials in the analyzed distributions. Especially in the case of architectures and synaptic parameters under which the probability of long-lived SSA was low, this increased the influence of statistical outliers on the calculated values. Therefore, in the following we can only speak about tendencies. A systematic quantitative research would require a huge amount of trials, beyond our current computational capabilities. We point out that altogether over 10^6 initial conditions where simulated and analyzed.

We start the analysis with networks where all excitatory neurons are RS, whereas inhibitory neurons are either LTS or FS (see rows in Table 1 corresponding to RS neurons). In this range of synaptic strengths and for hierarchical level H=0 the combination RS-FS could hardly lead to SSA: the activity was seldom longer than 100 ms, and was followed by direct decay to the stable state. In contrast, the RS-LTS combination delivered cases of SSA. Albeit relatively rare (recall the exponential distribution in figure 46), for the RS-LTS networks some SSA states could display lifetimes longer than 1000 ms. Changing the number of modules had little effect on SSA duration for RS-FS networks due to low probability of finding SSA in this case (see above). Nevertheless, in the network with four modules (H=2) we observed many cases of SSA with lifetimes longer than 500ms, while none was observed for a random network with H=0. For RS-LTS networks the effect of increase in the number of modules was more articulate: The longest lifetimes of the SSA grew from a few hundred ms for random networks (H=0) to a few thousand ms for modular networks (H=1,2).

Introduction of CH neurons as a second type of excitatory neurons led to a noticeable increase in the lifetime expectancy of SSA for the H=0 case, both for LTS and FS inhibitory neurons. In the former case, the increase was more pronounced. For the case of LTS inhibitory neurons, the presence of just 20% of CH neurons in the excitatory population slightly expanded the SSA domain of synaptic conductances towards lower values of the $(g_{\mathrm{ex}}, g_{\mathrm{in}})$ diagram (not shown). Besides this, in the upper right part of the diagram (see rows in Table 1 corresponding to LTS cases with H=0 and 20%CH or 40%CH) the probability to get a durable (over 1000 ms) SSA became higher. Increase of the percentage of CH neurons to 40% confirmed the tendency of growing SSA lifetime expectancy in the middle part of the $(g_{\mathrm{ex}}, g_{\mathrm{in}})$ diagram (not shown). Remarkably, in the upper right region of the diagram the distribution was no longer exponential, at least not in the examined range of lifetimes. The median of the lifetime distribution became significantly higher (above 2000 ms at g_{ex}=0.15, and at high modularity it became more probable to get SSA with duration up to 10^4ms

Medians [ms]

Excitatory neurons	H	Inhibitory neurons: LTS (g_{ex}, g_{in}) (0.12, 0.7)	(0.15, 0.7)	(0.12, 1)	(0.15, 1)
RS	0	408	365	544	431
	1	506	428	707	535
	2	603	674	850	834
20%CH	0	372	500	421	573
	1	449	583	519	653
	2	618	1011	756	1209
40%CH	0	729	2343	759	2258
	1	1027	3821	1086	3566
	2	2866	9907	4344	9907
20%IB	0	339	359	368	374
	1	385	360	435	385
	2	474	527	582	607
40%IB	0	317	379	330	380
	1	360	360	376	364
	2	417	557	484	632

Excitatory neurons	H	Inhibitory neurons: FS (g_{ex}, g_{in}) (0.12, 0.7)	(0.15, 0.7)	(0.12, 1)	(0.15, 1)
RS	0	xxx	xxx	xxx	xxx
	1	346	329	372	357
	2	423	519	490	554
20%CH	0	xxx	375	355	368
	1	343	363	356	370
	2	441	521	475	555
40%CH	0	397	663	396	565
	1	379	434	379	439
	2	1036	1735	1210	1734
20%IB	0	xxx	xxx	xxx	xxx
	1	xxx	xxx	337	333
	2	403	457	430	490
40%IB	0	xxx	xxx	xxx	xxx
	1	xxx	xxx	335	327
	2	370	442	409	471

Table 7: Effect of the network architecture on SSA for four different pairs of synaptic strengths g_{ex} and g_{in}. Medians of activity lifetimes are restricted to cases of SSA exceeding 300ms after the end of stimulation. 'xxx' denotes networks for which such cases did not occur or were very seldom.

(which means over 100 subsequent epochs of collective activity) than not to observe SSA at all. In the case of networks with FS inhibitory neurons, the presence of CH neurons as the second type of excitatory neuron had a similar effect of increasing the SSA lifetime expectancy, but by far not so strong. In fact, for the middle part of the diagram the effect was barely noticeable, even when the proportion of CH neurons was 40% (not shown), and it hardly makes sense to speak of SSA in this case. In the upper right corner of the diagram (see rows in Table 1 corresponding to FS cases with H=0 and 20%CH or 40%CH), cases of SSA were detected but the respective lifetime medians indicate that lifetimes longer than a few hundred milliseconds are seldom. At higher modularity levels the effect of CH neurons as a second type of excitatory neurons became more visible. In the configuration with RS and CH excitatory neurons and LTS inhibitory neurons, hierarchical levels H=1,2 allowed the SSA lifetime to reach values $\sim 10^4$ms in the upper right corner of the diagram (see rows in Table 1 corresponding to LTS cases with H=1,2 and 20%CH or 40%CH) and a few thousand ms in the middle part of the diagram (not shown). The same tendency, but with a weaker effect, was observed when the inhibitory neurons belonged to the FS class (see Table 1 rows corresponding to FS cases with H=1,2 and 20%CH or 40%CH): here at H=2 and with 40% of CH neurons the distributions of activity lifetimes had medians that exceeded 1000ms and some initial conditions resulted in SSA states with lifetimes $\sim 10^4$ ms.

At H=0, the effect of IB neurons as a second type of excitatory neuron, compared to purely RS excitatory neurons, was relatively weak, especially when the inhibitory neurons were of the FS class since in that case SSA was almost absent (see Table 1 rows corresponding to FS cases with H=0 and 20%IB or 40%IB). This is not surprising, since the difference between RS and IB neurons is not so strong as the difference between RS and CH neurons, especially in presence of irregularity of synaptic currents in the network. The effect was modest for LTS inhibitory neurons as well. However, noticeably and, somewhat surprisingly, this case displayed a clear *negative* tendency on the SSA lifetime (see Table 1 rows corresponding to LTS cases with H=0 and 20%IB or 40%IB). In all configurations with IB neurons, growth of the number of modules resulted in the increase of the SSA lifetime (see rows in Table 1 corresponding to H=1,2 and 20%IB or 40%IB).

Our calculations unambiguously confirmed that modularity of the network favored SSA and extended its average lifetime (compare in Table 1 rows for H=0 with rows for H=1,2). This effect is well seen e.g. at $g_{\rm ex}$=0.12, $g_{\rm in}$=0.7 in an exemplary network of 1024 neurons in which the inhibitory neurons are of the LTS type, and the CH neurons make 20% of the excitatory ones. At these parameter values (see figure 46B) the probability to find an SSA with duration τ decays as $\exp(-\alpha\tau)$. For H=0,1,2 the fitted values of α were, respectively, 7.47×10^{-3}, 3.74×10^{-3} and 1.74×10^{-3}ms^{-1}: each modularity level approximately doubles the expectancy of SSA duration.

9.4 Quantitative characteristics

Below we present characteristics of spiking dynamics in the studied networks: activities, frequency spectra, firing rates, interspike intervals and coefficients of variation

(see Sec. 8.3), both globally and for different subpopulations of neurons.

We start with computation of these measures for several initial conditions in a network with fixed architecture and values of $(g_{\rm ex}, g_{\rm in})$ which ensure sufficiently long SSA.

Figure 47 presents characteristics for an example network of four modules (H=2), with RS excitatory neurons and LTS inhibitory neurons at $g_{\rm ex}$=0.15, $g_{\rm in}$=0.7, computed between the end of the external input and the last network spike. For all runs the duration of SSA exceeded 500 ms. Each column of the figure stands for a different set of initial conditions, whose SSA lifetime is shown in the activity plots on the first row. In all cases the type of activity pattern is oscillatory SSA (the only observed SSA type at low synaptic strengths). Further rows in the figure show the global frequency distribution of the network activity calculated via the Fourier transform, distributions of the neuronal firing rates f_i, of the interspike intervals (ISI) with their coefficients of variation (CV) and, in the last row, of the CVs for the ISIs of individual neurons.

The measures presented in figure 47 disclose little reaction to variation of initial conditions; in general, this observation holds for networks with other kinds of architecture as well. In several examples, especially for higher hierarchical levels, variability was more pronounced; this referred to amplitudes of the leading frequencies in the spectra (whereby the frequencies themselves stayed nearly constant), and can be attributed to non-coincidence of durations of oscillatory epochs in different modules. Notably, in all studied network architectures at all combinations of synaptic strengths we found no indicator that would signalize the approaching abrupt cessation of the SSA: from the point of view of average characteristics of activity, there is no visible difference between the short and the durable SSA.

Weak sensitivity of the SSA characteristics with respect to initial conditions supports our assumption that the state of SSA corresponds to wandering of all trajectories in the phase space over the same chaotic set which possesses well defined statistical characteristics but is (at least, in the domain of weak synaptic strengths) not an ultimate attractor of the system. Within the high-dimensional phase space of the network, this set appears to lie in a kind of relatively low-dimensional "channel"; nearby trajectories are quickly attracted by this channel, move along it for a certain time, and finally escape to the equilibrium.

Regarding the type of spiking behavior, the measures shown in Figure 47 reveal an irregular network activity. The distribution of the neuronal firing rates, clearly non-Gaussian, is asymmetric and long-tailed. The ISI distribution, non-Gaussian as well, is close to exponential, as can be expected for nearly Poissonian behavior. The distribution of the CVs of the ISIs is broad and asymmetric with average value $\gtrsim 1$. We recovered these features in all encountered SSA states in the region of low synaptic strengths.

Given this point, we proceed to the description of how different network compositions affect the activity characteristics. The general results on the effect of network architecture are summarized in Table 8 for excitatory neurons and Table 9 for inhibitory neurons. In these tables, each of the activity characteristics is calculated from the average over 10 different initial conditions resulting in SSA with lifetimes above 700ms.

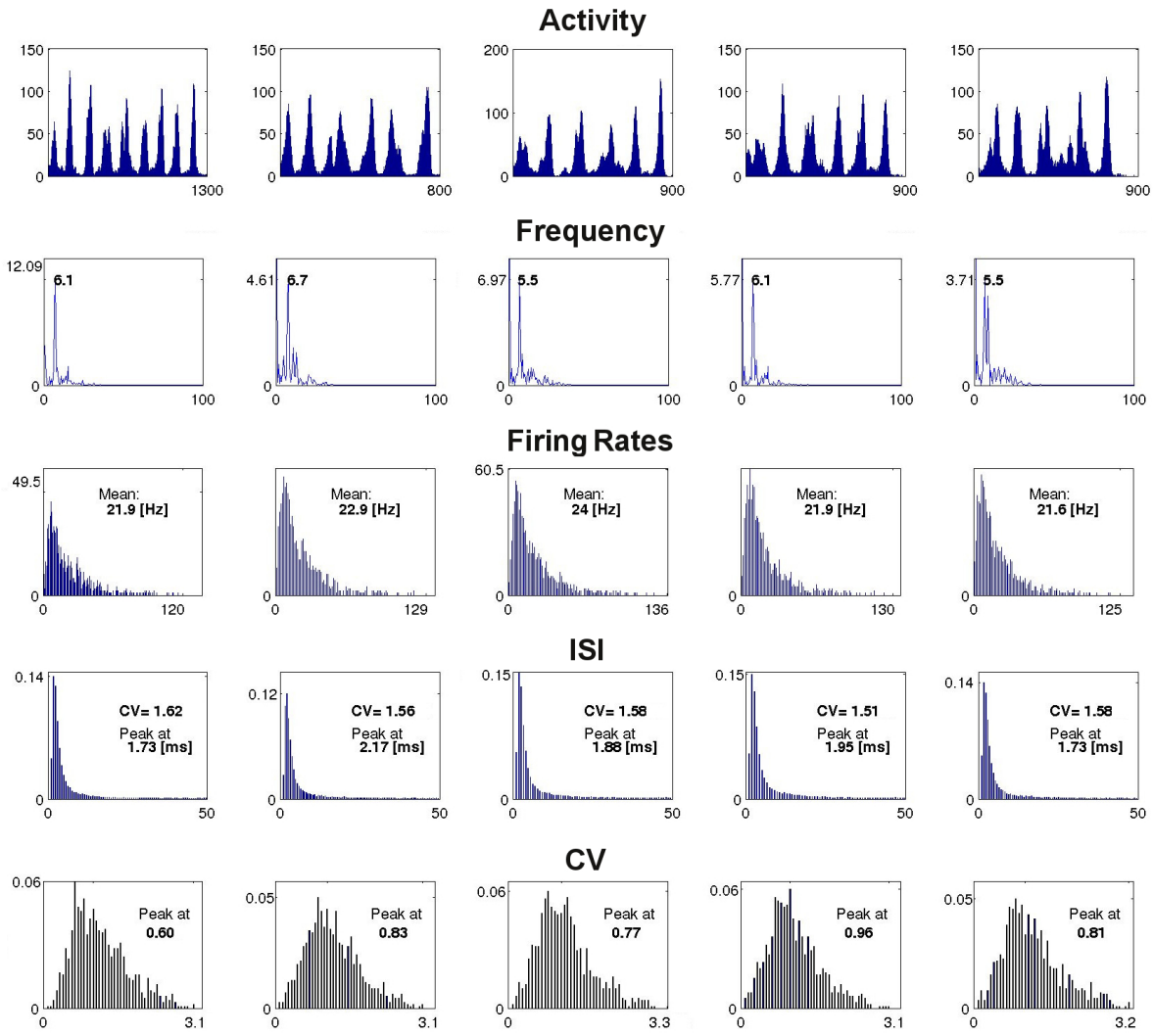

Figure 47: Example of dependence of the spiking properties on the initial conditions. The figure shows the network measures for a fixed network architecture: H=2, RS excitatory neurons, LTS inhibitory neurons, $g_{\rm ex}$=0.15, $g_{\rm in}$=0.7, and five different initial conditions, one for each column. The first row: network activity $A(t)$ over the active period, from the end of the external stimulation (time 0 in the horizontal axis) until last spike of a network (indicated by the number under the right end of the time axis, in ms). The second row: global frequency spectrum of the activity (horizontal axis: frequency in Hz, vertical axis: amplitude). The third row: distribution of the firing rates over the ensemble of neurons in the active period (the mean of each distribution is shown inside the corresponding plot and the maximal rate is shown at the extreme right of the horizontal axis). The fourth row: distribution of the ISIs (in ms) over the ensemble of neurons for the active period (with CV and the peak value of the distribution indicated inside each plot). The fifth row: distribution of the CVs of the ISIs of the network neurons; the peak of each distribution is shown inside the plot.

For networks with excitatory neurons of RS type only, comparisons between the cases with LTS and FS inhibitory neurons for fixed synaptic strengths and various initial conditions showed no significant difference in the mean firing rates of the excitatory neurons (see in Table 8 rows for RS cases). Introduction of CH neurons as the second type of excitatory neuron led to a significant increase in the firing rate of excitatory RS neurons (see Table 8 rows for 20%CH or 40%CH). In networks with LTS inhibitory neurons, when the CH neurons comprised 20% of all excitatory neurons the median firing rate of RS neurons doubled and when the proportion of CH reached 40% the median firing rate of RS neurons tripled. In networks with FS inhibitory neurons these increments in RS neurons firing rate were less pronounced, the growth factors being approximately 1.7 (20%CH) and 2.3 (40%CH). On the other hand, the efect of IB neurons was much weaker and (based on the few relevant data for FS inhibitory neurons) independent of the type of inhibitory neuron (see Table 8 rows corresponding to 20%IB or 40%IB). Remarkably, the effect of modularity on the firing rate of excitatory neurons was not very pronounced (see Table 8), and median firing rates for $H > 0$ levels remained in the same range as in the case of a random network topology (H=0).

In the preceding subsection we noted that presence or absence of particular types of neurons strongly influences the probability of SSA. Intuitively, this could be expected, due to the different amounts of excitation and inhibition they provide to the network, an effect also known for leaky integrate-and-fire neurons ([21, 69]). However, if this were the only reason, the lifetime distributions for networks with LTS inhibitory neurons should be similar to those for FS neurons at lower inhibitory synaptic strength, which was not confirmed by numerics (see 7).

Effect of the type of inhibitory neuron on the amounts of excitation and inhibition produced by the network is shown in Table 9. The first two columns of Table 9 (for LTS and FS neurons respectively) represent the total excitation and the total inhibition produced by the network, measured respectively as the total number of spikes produced by excitatory and inhibitory neurons normalized over the activity period. The other columns represent the activity measures for networks with LTS or FS neurons as introduced above. Remarkably, the exchange of LTS and FS neurons at fixed modularity level and percentage of the second type of excitatory neurons did not have a significant effect on the total excitation produced by the network. This can be seen in a comparison of the first column in Table 9 for LTS or FS neurons respectively. However, the maximal firing rates (and hence, quite often, the corresponding mean values) of the FS neurons were consistently higher than for the LTS neurons (see columns for maximum and mean firing rates in Table 9). At the same time many FS neurons displayed very low firing rates, which resulted in lower medians of the distributions for FS neurons than for LTS neurons (see columns for median firing rates in Table 9). This tendency was preserved not only when all excitatory neurons were RS but also in the cases with a second type of excitatory neurons and also for different modularity levels (see Table 9).

These characteristics suggest that the firing rate distribution of LTS neurons is more uniform, both in space and time, than the firing rate distribution of FS neurons. This is not indeed surprising: As the name suggests, a LTS neuron needs less excitatory input in order to reach a spiking threshold ($\sim$2.8 mV) in comparison to

a FS neuron (∼3.4 mV). On the other hand, once the threshold is reached, a FS neuron spikes much more often (at a frequency ∼140 Hz for an input of I=10) compared to the LTS neuron (∼80 Hz for the same input). Therefore, when embedded in a network, the LTS neurons require less correlated excitatory input in order to spike, which makes them more sensitive. The FS neurons, in contrast, respond only to relatively high correlated excitation, hence their population includes many non-active neurons along with few ones with very high spiking rates. As a consequence, while the total inhibition produced by the network is comparable for both types of inhibitory neurons (see the second column in Table 9 for LTS or FS neurons respectively), the inhibitory spreading in the case of networks with FS neurons is less efficient than in networks with LTS neurons, being concentrated on the few relevant postsynaptic neurons. The end result is that networks built of LTS cells possess more inhibitory neurons with moderate spiking frequencies than networks built of FS cells.

Presence (both of 20% or 40%) of CH neurons in the network did not affect the tendency described above in different behavior of the two types of inhibitory neurons: the mean firing rate and the corresponding maximal firing rate of the FS neurons was higher than for the LTS neurons; however, the median of the firing rate distribution was still lower for FS neurons than for LTS neurons (see Table 9). This again meant presence of a few very active FS inhibitory neurons on one side of the distribution and of many weakly active FS neurons on its other side. In comparison, most of the LTS neurons were active with moderate firing rates.

Further, we considered the firing rates of the different populations of neurons, measured not only over the duration of SSA as a whole but also over each of the active epochs of the oscillatory activity. This allowed us to extract the global silent epochs from the statistics, making the comparison between different cases more accurate. In fact, measurements of individual frequencies of the neurons confirmed that the active individual neurons shared the leading frequency with the whole module they belonged to, and only the weakly active neurons (with a firing rate of a few Hz) fired independently (not shown).

Similarly to the firing rate of excitatory RS neurons, when 20% of all excitatory neurons were of the CH type the firing rate of the inhibitory neurons (both of the LTS or FS types) doubled, and when the proportion of CH neurons reached 40% the firing rate of these inhibitory neurons tripled. This can be seen directly from the columns in Table 9 representing the corresponding firing rates. The presence (both of 20% or 40%) of CH neurons in the network did not alter the tendency described above of greater uniformity in the distribution of firing rates of the two types of inhibitory neurons: the mean firing rate and the corresponding maximal firing rate of the FS neurons was higher than for the LTS neurons; however, the median of the firing rate distribution was still lower for FS neurons than for LTS neurons (see Table 9). This again meant presence of a few very active FS inhibitory neurons on one side of the distribution and of many weakly active FS neurons on its other side. In comparison, most of the LTS neurons were active with moderate firing rates.

The effect of introducing excitatory neurons of the IB type in the network was not as impactant on the firing rates of inhibitory neurons (both of LTS or FS types) as the effect of CH excitatory neurons but nevertheless networks with IB excitatory

CHARACTERISTIC MEASURES FOR EXCITATORY NEURONS

Excitatory Neurons	H	LTS Inhibitory neurons				FS Inhibitory neurons			
		Firing Rate Median		ISI CV		Firing Rate Median		ISI CV	
		RS	CH / IB	RS	CH / IB	RS	CH / IB	RS	CH / IB
RS	0	15	—	1.2	—	xxx	—	xxx	—
	1	14	—	1.2	—	15	—	1.2	—
	2	13	—	1.4	—	13	—	1.5	—
20%CH	0	31	79	1.9	3.2	29	63	2.0	3.2
	1	30	79	1.8	3.0	26	64	2.0	3.1
	2	26	69	1.9	3.0	22	56	2.0	3.2
40%CH	0	48	124	2.2	3.3	40	94	2.5	4.0
	1	46	122	2.2	3.3	34	82	2.4	3.7
	2	43	114	2.1	3.3	31	84	2.6	4.1
20%IB	0	22	35	1.7	2.3	xxx	xxx	xxx	xxx
	1	19	28	1.5	2.0	xxx	xxx	xxx	xxx
	2	16	28	1.7	2.2	16	27	1.7	2.2
40%IB	0	26	41	2.1	2.7	xxx	xxx	xxx	xxx
	1	24	38	1.9	2.5	xxx	xxx	xxx	xxx
	2	21	36	2.0	2.5	19	33	2.0	2.5

Table 8: Effect of the network architecture on characteristic measures of the excitatory neurons at synaptic strengths g_{ex}=0.15, g_{in}=1. Measures are computed from average over 10 different trials with lifetimes of the SSA over 700ms. 'xxx' denotes networks in which such lifetimes were observed in less than 10 trials.

neurons displayed small increments in the firing rates of their inhibitory neurons, which were stronger for 40% than for 20% of IB neurons. The same ocurred with the total excitation and inhibition produced by the network, as can be seen from Table 9.

Finally, and also akin to the firing rate of RS excitatory neurons, the effect of modularity on the activity measures shown in Table 9 was not so strong. For non-zero hierarchical levels, the total inhibition and excitation produced by a network and the firing rate of its inhibitory neurons with otherwise fixed neuron types remained in the same range as for a network with H=0. The same was accordingly true for the distributions of the firing rates of the different types of inhibitory neurons (not shown). Difference in total excitation and inhibition was also not strongly influenced by merely exchanging the type of inhibitory neurons and keeping all other network parameters fixed (see Table 9).

CHARACTERISTIC MEASURES FOR INHIBITORY NEURONS

		Inhibitory neurons: LTS							
Excitatory neurons	H	Total		Firing Rate			ISI		CV
		Excitation	Inhibition	Mean	Median	Max	Peak	CV	Peak
RS	0	0.015	0.037	38	32	121	1.7	1.7	1.2
	1	0.015	0.039	39	32	129	1.9	1.6	1.2
	2	0.016	0.040	40	33	119	1.7	1.7	1.1
20%CH	0	0.046	0.076	76	59	268	1.2	2.4	1.5
	1	0.044	0.077	77	61	264	1.2	2.4	1.6
	2	0.044	0.077	77	66	246	1.3	2.3	1.7
40%CH	0	0.093	0.123	123	98	367	1.2	2.7	1.8
	1	0.087	0.123	123	104	384	1.2	2.7	2.0
	2	0.085	0.118	118	99	346	1.2	2.7	2.0
20%IB	0	0.025	0.050	50	37	179	1.1	2.2	1.3
	1	0.023	0.049	49	38	170	1.2	2.1	1.3
	2	0.025	0.051	51	40	171	1.2	2.1	1.1
40%IB	0	0.036	0.061	61	43	208	1.0	2.6	1.7
	1	0.033	0.060	60	44	216	1.0	2.5	1.6
	2	0.035	0.064	64	50	212	1.1	2.3	1.5

		Inhibitory neurons: FS							
Excitatory neurons	H	Total		Firing Rate			ISI		CV
		Excitation	Inhibition	Mean	Median	Max	Peak	CV	Peak
RS	0	xxx	xxx	xxx	xxx	xxx	xxx	xxx	xxx
	1	0.017	0.043	43	30	181	1.4	1.9	1.4
	2	0.018	0.042	42	30	150	1.2	2.2	1.0
20%CH	0	0.047	0.085	85	51	368	1.1	2.9	2.2
	1	0.043	0.083	83	49	350	1.1	2.9	1.7
	2	0.041	0.080	80	53	315	1.0	3.1	1.5
40%CH	0	0.079	0.127	127	79	491	0.9	3.9	1.8
	1	0.074	0.128	128	66	493	1.0	3.8	2.2
	2	0.072	0.125	125	75	471	0.8	4.4	1.9
20%IB	0	xxx	xxx	xxx	xxx	xxx	xxx	xxx	xxx
	1	xxx	xxx	xxx	xxx	xxx	xxx	xxx	xxx
	2	0.026	0.054	54	35	227	1.0	2.6	1.2
40%IB	0	xxx	xxx	xxx	xxx	xxx	xxx	xxx	xxx
	1	xxx	xxx	xxx	xxx	xxx	xxx	xxx	xxx
	2	0.035	0.068	68	43	279	0.9	2.9	1.3

Table 9: Effect of the network architecture on characteristic measures of the inhibitory neurons at synaptic strengths g_{ex}=0.15, g_{in}=1. Measures are computed from average over 10 different trials with lifetimes of the SSA over 700ms. 'xxx' denotes networks in which such lifetimes were observed in less than 10 trials.

10 Phase Space Analysis of the Single Neuron

In this section we consider the dynamical properties of the Izhikevich neurons represented in equation (94) and discuss their connection to the observations from the previous sections.

Recall that the internal properties of a single neuron are described by two coupled differential equations,

$$\begin{aligned} \dot{v} &= \underbrace{0.04v^2 + 5v + 140}\, -u + I(t) \\ &= \qquad \mathrm{f}(v) \qquad\quad - u + I(t) \\ \dot{u} &= a\,(b\,v - u), \end{aligned} \tag{103}$$

together with the reset condition at a threshold at $v_{crit} = 30\mathrm{mV}$

$$\begin{aligned} v(t) &\mapsto c \qquad\quad \text{if } v(t) = 30\mathrm{mV} \\ u(t) &\mapsto u(t) + d \qquad \text{if } v(t) = 30\mathrm{mV} \end{aligned} \tag{104}$$

The four parameters (a, b, c, d) generate the firing patterns of the five cell classes used in the simulations, as represented in section 8.1 (see table 10).

Let us first consider the case of a constant input current $I = const.$ The dynamics of the 2-dimensional system (103) is determined by the position of the two nullclines

$$\dot{v} = 0 \iff \bar{u} = \mathrm{f}(v) + I \tag{105}$$

$$\dot{u} = 0 \iff u^* = bv\,. \tag{106}$$

The nullcline of the first equation, which we denote by $\bar{u}$, describes a quadratic parabola separating the phase space region with $\dot{v} < 0$ (above the parabola) from the region with $\dot{v} > 0$ (below the parabola). The nullcline of the second equation, denoted by u^*, is a straight line.

Figure 48 gives example of the phase portraits of RS and CH neurons. Observe that the first nullcline, $\bar{u}$ in (105), does not depend on any of the four parameters (a, b, c, d) but only on the input current I which controls the shift of the quadratic parabola. For zero or sufficiently small input I the nullclines intersect indicating the positions of one stable and one unstable fixed points. Figure 48A represents the case for $I = 0$ where the stable fixed point is indicated by the blue dot. The second nullcline, u^* in (106), depends on the parameter b which controls the gradient of the straight line and therefore determines, at $I = 0$, the resting state of the neuron.

	a	b	c	d
RS	0.02	0.2	-65	8
CH	0.02	0.2	-50	2
IB	0.02	0.2	-55	4
FS	0.1	0.2	-65	2
LTS	0.02	0.25	-65	2

Table 10: Parameters (a, b, c, d) characterizing the five electrophysiological cell classes used in the simulations.

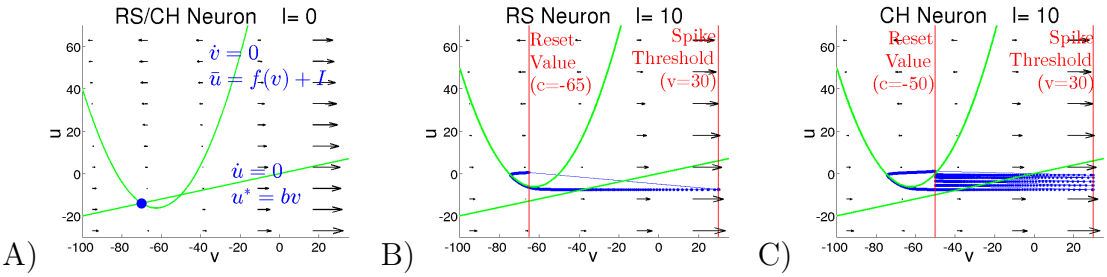

Figure 48: Phase portraits of RS and CH neurons with corresponding nullclines in green. A) $I = 0$. The two intersection points of the nullclines indicate the positions of the fixed points. The stable fixed point is marked by a blue dot. B) Phase portraits of a RS neuron with $I = 10$. C) Phase portraits of a CH neuron with $I = 10$. In B) and C) the two vertical red lines indicating the reset value $v_{reset} = c$ and the spike threshold $v_{spike} = 30$mV, respectively. The trajectories are in blue.

From the parameters (a, b, c, d) given in table 10 we can see that the RS and CH neurons have the same b value which makes also the phase portraits for $I = 0$ identical. For higher (constant) I the two fixed points disappear in a saddle node bifurcation and the neuron spikes. Figures 48B and 48C represent, respectively, the phase portraits for the RS and CH neurons for $I = 10$. The difference between the two neuron types is given on the one hand by the increment of the u variable (controlled by the parameter d) after each spike which is considerably higher for the RS neuron and on the other hand by the reset value c. The effect of this can be clearly seen in the plots: while the RS neuron is instantaneously reset above the parabola, the CH neuron has to perform several spikes until its u value is large enough and lies above the $\bar{u}$ nullcline.

The time scale separation between the v and u variables, caused by the small parameter a in (103), is clearly visible by the arrows indicating the phase space flow: while the v variable is rapidly changing during the spiking process, the u variable remains approximately constant. Only when the trajectory is in the vicinity of the $\bar{u}$ nullcline the velocity $\dot{v}$ becomes small and the two time scales are comparable.

Let us consider the case of a time dependent input current $I(t)$ generated by a presynaptic spike train. As an example, we analyze the behavior of a RS neuron embedded in a network of modularity level $H = 0$ where 20% of all excitatory neurons are of CH type and the inhibitory neurons are of LTS type. The synaptic strengths (g_{ex}, g_{in}) are (0.15, 1) and the stimulation procedure corresponds to SSA with lifetime above 2000ms. We concentrate on a time interval about one of the periods of high network activity lasting from $t \approx 890$ to $t \approx 990$. We are considering the behavior of a highly active RS neuron which receives only excitatory input during the active period. This is not the generic case, however, it underlines an important dynamical feature of the network behind the large scale oscillations, as we will see in section 11.

Figure 49 represents the solely excitatory presynaptic spike train and the change of the variables $v(t)$, $u(t)$ and $G(t)$ of the RS neuron. The green dots in the plot indicate the incoming presynaptic spike train and the blue dots correspond to the spike times of the RS neuron. Figure 50 shows the corresponding snapshots of the

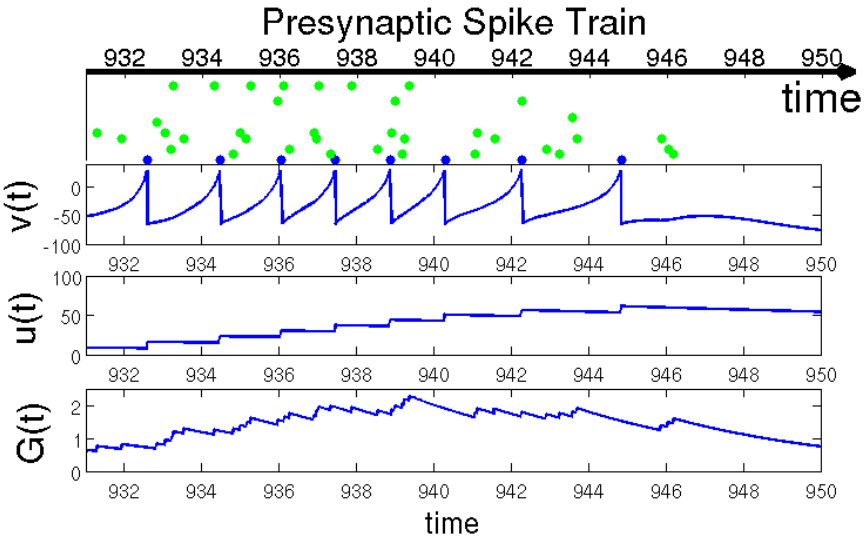

Figure 49: Change of the variable $v(t)$, $u(t)$ and $G(t)$ of a RS neuron with respect to an excitatory presynaptic spike train indicated by the green dots. The blue dots indicate the spikes of the RS neuron of interest.

phase space, at different times, for the same RS neuron. The left and right insets above each snapshot in figure 50 display, respectively, the presynaptic input current $I(t)$ (its instantaneous value indicated by red dot) and the synaptic conductance $G(t)$ (its instantaneous value indicated by the vertical line). In the phase space plots the instantaneous position is indicated by a red dot and the blue line shows the tail of the recent trajectory. As in figure 48 the green lines show the position of the nullclines. The u^* nullcline is time independent but the $\bar{u}$ nullcline is shifted. From equation (105) we see that in phase space the position of the whole $\bar{u}$ nullcline depends on $I(t)$. However, $I(t)$ itself depends on the one side on the voltage variable $v(t)$ and on the other side on the synaptic conductance $G(t)$; see section 8.1

$$I(t) = (E_{ex} - v)G(t) \tag{107}$$

$$\frac{dG(t)}{dt} = -\frac{G(t)}{\tau_{ex}} + g_{ex}\sum_{t_j^f<t}\delta(t-t_j^f)\,. \tag{108}$$

Therefore, the important quantity is given by

$$\bar{u}(t) = \mathrm{f}(v(t)) + I(t) \tag{109}$$

which is denoted by green dot on the parabola in figure 50. Observe that the vertical distance between the green and red dots corresponds to $\dot{v}(t)$:

$$\dot{v}(t) = \bar{u}(t) - u(t)\,. \tag{110}$$

The first two plots in figure 50 represent, respectively, the state of the RS neuron before (figure 50 $t = 880$) and at the beginning of the active period (figure 50 $t = 916$). During the silent period ($t \in [870, 900]$) the synaptic input of the RS neuron is approximately zero and the trajectory slides slowly along the $\bar{u}$ nullcline towards

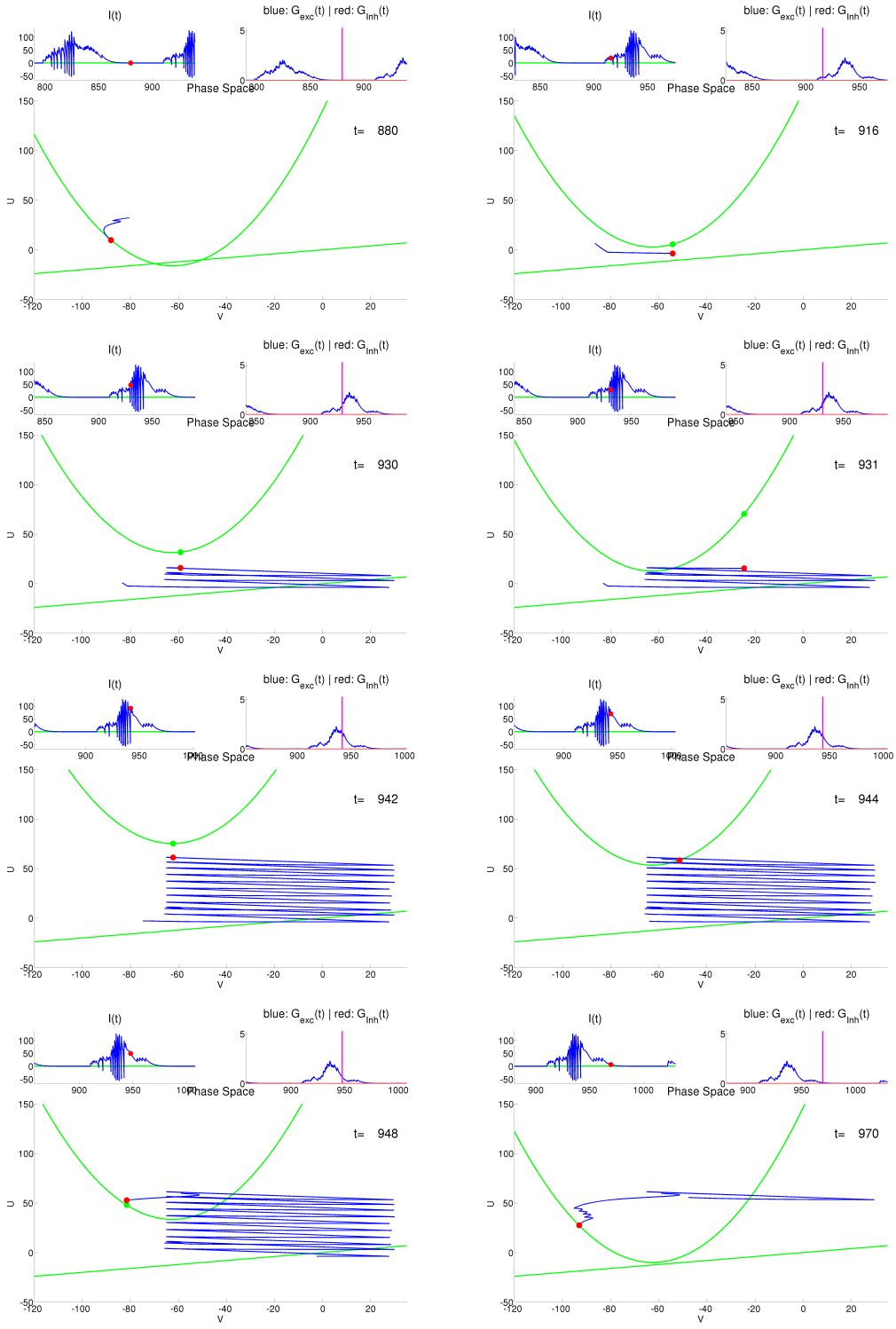

Figure 50: Snapshots of the phase space of a RS neuron embedded in the network during the simulation. For description of the plots see text.

the stable state; during this slow transition both $\dot{v}(t)$ and $\dot{u}(t)$ are very small with comparable time scales. At the beginning of the active period (figure 50 $t = 916$) the excitatory synaptic input shifts the $\bar{u}$ nullcline upwards and the neuron is free to spike. Observe in the next two plots (figure 50 $t = 930$ and $t = 931$) that while $G_{ex}(t)$ is fluctuating weakly, $I(t)$ performs great rapid shifts caused by the fast v-variable and its reset after each spike (see equation 107). During this active phase the $I(t)$ oscillations result in large oscillations of the $\bar{u}$ nullcline (see equation 109). Along with this, the synaptic input increases, mirroring the increasing activity of the network, causing an ongoing additional positive shift of the $\bar{u}$ nullcline. Contrary to the constant input case ($I = const$) of figure 48 this additional shift in the $\bar{u}$ nullcline sets the increased u variable $u \mapsto u + d$ below the parabola allowing for another spike. This explains why the RS neurons tend to behave like CH neurons during the active periods (see figure 50 $t = 930$ to $t = 942$). This bursting behavior is observed for all highly active neurons independent of their electrophysiological class. It is important to observe that while the network activity is increasing the spiking frequency of the neuron of interest is approximately constant during the whole process (see figure 49): the distance $\Delta v = v_{crit} - c$ is constant and the velocity $\dot{v}$ seen as in equation (110) does not change radically after each spike since both u and $\bar{u}$ are growing. This bursting-like process endures either until the trajectory is instantaneously reset above the $\bar{u}$ nullcline after a spike or until the trajectory $(v(t), u(t))$ is trapped by the $\bar{u}$ nullcline (see figure 50 $t = 944$). The neuron enters a slow time scale dynamics $\bar{u}(t) \approx u(t)$ (see equation 110) with very small $\dot{v}$ leading to long lasting transient towards the stable state (see figure 50 $t = 948$ and $t = 970$).

In the following lines we show that the higher $u(t)$ becomes after each spike ($u \mapsto u + d$), the higher the presynaptic excitatory input $G_{ex}(t)$ should be in order to ensure the next spike. Considering the time scale separation between the u and v variable during the spiking process we can assume that during a spike, i.e. for $v(t) \in [c, v_{crit}]$, u remains approximately constant: $u_{spike} \approx$ const; see figure 49. Making this assumption, we should also consider that during a spike $G(t)$ is decaying according to (108) with a time scale determined by τ which is of the same order of magnitude as the time scale of v. Assume that the trajectory $(v(t), u_{spike})$ gets trapped by the $\bar{u}$ nullcline for some u_{spike}:

$$\dot{v} = 0 = \alpha v^2 + \beta v + \gamma - u_{spike} + (E_{ex} - v)G_{ex} + (E_{in} - v)G_{in} \ .$$

Solving for v renders

$$\begin{aligned} v_{\pm} &= \frac{G_{ex} + G_{in} - \beta}{2\alpha} \pm \\ &\frac{1}{2\alpha}\sqrt{(\beta - G_{in})^2 - 2(\beta + G_{in})G_{ex} + G_{ex}^2 - 4\alpha\left(\gamma - u_{spike} - |E_{in}|\, G_{in} + E_{ex}G_{ex}\right)} \ . \end{aligned} \tag{111}$$

The fixed points exist if the term under the square root is positive or

$$(\beta - G_{in})^2 - 2(\beta + G_{in})G_{ex} + G_{ex}^2 - 4\alpha\left(\gamma - u_{spike} - |E_{in}|\, G_{in} + E_{ex}G_{ex}\right) = 4\delta \tag{112}$$

with $\delta > 0$. Solving for G_{ex} renders

$$\begin{aligned} G_{ex}^{\pm} &= (\beta + 2\alpha E_{ex} - G_{in}) \pm \\ &2\sqrt{\alpha(\beta - G_{in})E_{ex} + \alpha^2 E_{ex}^2 + \alpha(\gamma - u_{spike} - |E_{in}|\, G_{in}) + \delta} \ . \end{aligned} \tag{113}$$

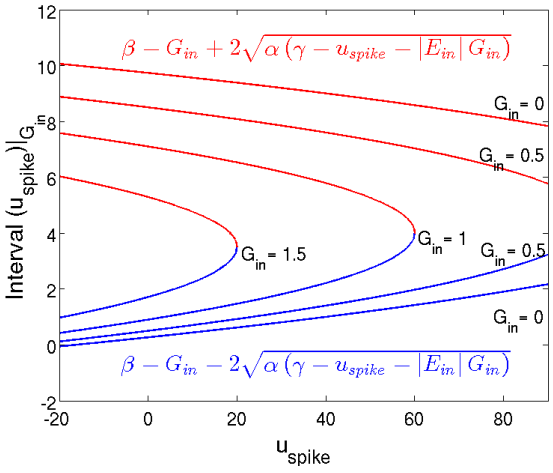

Figure 51: The lower and upper boundaries of the G_{ex} interval from equation (114) as function of u_{spike} for different G_{in} values.

Assuming that $E_{ex} = 0$, as in the simulations, the last expression simplifies and we derive the following condition for G_{ex}

$$\begin{aligned} \beta - G_{in}(t) - 2\sqrt{\alpha\,(\gamma - u_{spike} - |E_{in}|\,G_{in}(t))} \;\; < \\ G_{ex}(t) \\ < \;\; \beta - G_{in}(t) + 2\sqrt{\alpha\,(\gamma - u_{spike} - |E_{in}|\,G_{in}(t))} \quad . \end{aligned} \tag{114}$$

If $G_{ex}(t)$ is within this interval the $\bar{u}$ nullcline does not intersect the constant u_{spike} line and the two fixed points in (111) do not exist. Observe that for

$$G_{in}(t) = \frac{\gamma - u_{spike}}{|E_{in}|} \tag{115}$$

the two boundaries of the interval coincide and for $G_{in}(t)$ greater than this value, the fixed points always exist.

The interval (114) depends not only on $G_{in}(t)$ but also on the value of u_{spike} during the spike: the higher the value of u_{spike},the narrower the interval. Figure 51 illustrates the behavior of the G_{ex} interval as function of u_{spike} and G_{in}. Knowing that

$$G(t) = G_0 \mathrm{e}^{-\frac{t}{\tau}} \underset{t\to\infty}{\longrightarrow} 0$$

means that if we choose $G_{ex,0}$ at the beginning of the spike to lie within the interval (114) (i.e. assuring $\dot{v}(c, t = 0; G_0) > 0$), does not automatically assure that the neuron will perform a spike, i.e. that at a latter time ($T > 0$) $G(T)$ would not escape from the interval causing the $\bar{u}$ nullcline to intersect the constant u_{spike} leading to the appearance of the two fixed points. In figure 48 this happens both for the times ($t = 930 \mapsto t = 931$) and for ($t = 941 \mapsto t = 944$). In the first case the neuron does perform a spike, while in the second case it does not. Although the interval condition (114) itself is not sufficient to ensure that a neuron will perform a spike for given initial $G_{ex,0}$ and $G_{in,0}$ at $v = c$, it shows a clear tendency: the higher u_{spike} is, the higher the excitation should be. Furthermore, we can also see that even in the case of zero inhibition the bursting-like behavior can not endure for high u_{spike} if $G_{ex}(t)$ does not grow sufficiently.

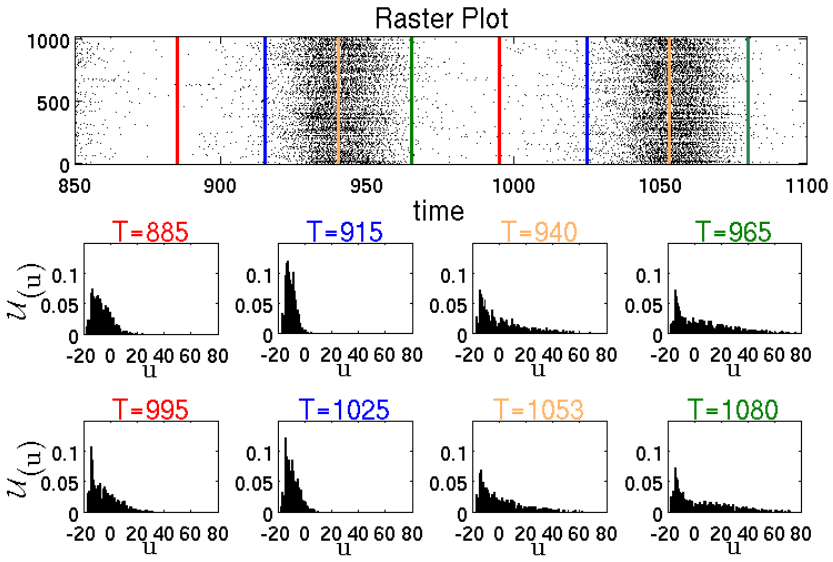

Figure 52: Distribution $\mathcal{U}(u, \delta u; T)$, with $\delta u = 1$, as given by equation 116, at different times T. The times corresponding to the red lines in the raster plot are chosen to lie between two active periods. The blue, yellow and green lines correspond, respectively, to times at the beginning, in the middle and at end of an active period.

11 Global Phase Space Analysis of the Network

Above we discussed the dynamics of a single neuron and considered the role of the u variable. In the first part of this section, we implement the previous considerations on the whole network and determine different dynamical states during the SSA process. In the second part of the section we discuss features of the transient chaotic dynamics associated with the SSA in section 9.2.

11.1 Different Stages of the SSA Process

Let $\mathcal{U}(u, \delta u; t)$ be the distribution of the u variables of the neurons comprising the network at time t:

$$\mathcal{U}(u, \delta u; t) = \frac{1}{N} \sum_{i=1}^{N} \int_{u}^{u+\delta u} \delta(u_i(t) - x) dx \ . \tag{116}$$

Figure 52 represents the $\mathcal{U}(u, \delta u; t)$ distribution at different times T for the same network and the same simulation as in figure 49 and figure 50. The times are chosen to lay, respectively, between two active periods or at the beginning, in the middle and at end of an active period.

Consider first, in figure 52, the times ($T = 940$, $T = 1053$) in the middle and ($T = 965$, $T = 10800$) at the end of an active period, respectively, indicated by the yellow and green lines in the raster plot. As expected, from the corresponding distributions we can see that during an active period the number of neurons occupying high u values increases. Let us consider such highly active neuron, like the RS neuron from figure 49 and figure 50. Suppose that at the peak of an active period all neurons

presynaptic to the neuron of interest (in this case all of them being excitatory) are highly active and spike similarly to the neuron of interest. Since all of them spike with an approximately constant frequency the total synaptic input into the neuron of interest reaches a constant (*maximal*) level. This means that while u is growing ($u \mapsto u + d$) the $\bar{u}$ nullcline of the neuron of interest does not receive the additional shift any more ($G_{ex}(t)$ is not growing any more) leading to an end of the bursting-like regime. As a consequence, the neuron of interest can not instantaneously produce another spike causing a drop in its spiking frequency which subsequently leads to a drop in the $\bar{u}$ nullclines of all its postsynaptic neighbors. Its presynaptic neighbors experience eventually the same and the $\bar{u}$ nullcline of the neuron of interest starts dropping. A potential new presynaptic excitatory input may shift the $\bar{u}$ nullcline once again above $u(t)$ leading to a positive but very small $\dot{v}$ which may or may not result in a new spike. Overall, this process leads to a definite drop in the spiking frequency of the whole network leading to a drop of the nullclines of most neurons, slowing their spiking frequency further. Eventually all highly active neurons are trapped by their $\bar{u}$ nullclines and enter a slow transient dynamics towards their resting states. This marks the end of the active period. Nevertheless, in figure 52, from the distributions ($T = 965$, $T = 10800$) at the end of the active periods, we see that there are still neurons occupying low u values. We call them moderately active neurons. The peak of the distributions is located near the corresponding u values of the resting states. Most of those moderately active neurons are postsynaptic to previously active inhibitory neurons, the latter being at the end of the active period in a long lasting transient state. At the end of the active period the moderately active neurons receive less presynaptic inhibition and being near their resting state do not need much excitation in order to spike. Remark that in this state a large number of neurons postsynaptic to the moderately active neurons are in a transient state and, therefore, most of the newly produced spikes will not lead to spikes in the postsynaptic neurons. This is a crucial state for the SSA since most of the newly produced network activity gets absorbed by the transient neurons. The activity of the network is sustained only within the "pool" of moderately active neurons. Observe that if the inhibition during the highly active periods is insufficient there will be less moderately active neurons at the end of the active periods which leads to a lower probability of sustaining the activity. From the distributions in figure 52 at times ($T = 885$, $T = 995$) between the active periods, indicated by the red lines in the raster plot, we see that the tail of the distribution is shifted from high towards low u values. This shift corresponds to the transition of previously active neurons towards their resting states. As result, the number of neurons which are able to contribute to the network activity is growing. At the beginning of the active periods ($T = 915$, $T = 1025$), the blue lines in the raster plot, the distributions are concentrated at low u values towards the resting states which marks the end of the transient process. At this stage the network becomes highly excitable. Here, most neurons occupy low u values and, therefore, newly produced spikes lead with a higher probability of subsequent spikes in the postsynaptic neurons.

11.2 Global Phase Space and the Resulting Transient SSA

In section 9 we have seen that in the region of low synaptic strengths the observed SSA states are always "oscillatory" corresponding to large-scale network activity oscillations. Those states emphasized transient chaotic-like dynamics indicated by the high sensitivity with respect to initial conditions and the corresponding exponential distributions of the lifetimes; see section 9.2. In this section we investigate features of this transient dynamics and the corresponding phase space region. A rigorous mathematical investigation of such a region in this highly dimensional phase space, taking also into account the discontinuity (104) and (108) of the differential equations (103) and (107), is beyond the scope of this work. The following analysis intends to give insights into the possible structure of the region. In the following we refer to this region as a chaotic set, which is the topological structure underlying transient chaotic dynamics. Such chaotic sets are also called chaotic saddles. We remark that although both high sensitivity with respect to initial conditions and the corresponding exponential distributions of the lifetimes characterize transient chaos, they are not sufficient to prove its existence [71] and distinguish it from other transient dynamical states, for example, such due to heteroclinic connections between saddle states in the phase space. The following observations are valid for both a chaotic set and a heteroclinic network. Remark that in section 2 we have seen examples where chaos originates from heteroclinic networks.

In the previous section we analyzed different states of the global network activity referring to the phase space analysis of single neurons discussed in section 10. Here, we consider the dynamics of the system in the highly-dimensional *global* phase space. The previous considerations remain valid since the phase space of a single neuron corresponds to a subspace of this global phase space. Accordingly, the trajectory from figure 50 discussed in section 10 is a projection of the trajectory of the whole system on the 2- dimensional subspace describing the state of the RS neuron of interest embedded in the network. Remark that the transients, discussed in the previous section, from highly active states of single neurons towards their resting states, should not be confused with the transient chaotic regime in the global phase space.

In the observed oscillatory SSA states, the system exhibits chaotic-like behavior over a certain time period, whose duration strongly depends on the initial condition, and abruptly switches into a non-chaotic state corresponding to a stable fixed point where all neurons are at their resting potential. During the oscillatory chaotic regime, in the global phase space, the trajectory of the system remains in the vicinity of a chaotic set, which is not an attractor. Strictly speaking, the chaotic set itself is invariant and a trajectory lying in the set can not escape. In the case of heteroclinic networks this set corresponds to heteroclinic cycles between saddles. The trajectories we are referring to visit and remain for certain time T within a phase space region Γ which contains the chaotic set. Since the set is not an attractor, once a trajectory leaves the region Γ it can not return to it. Consider a large number of initial conditions N_0 taken with a given distribution ρ_0 within a phase space region R. By an appropriate choice of R many of the initial conditions would lead to trajectories visiting the region Γ which contains the chaotic set. The number of trajectories

which remain in the region Γ after some period of time T is given by

$$N(T) \sim \mathrm{e}^{-\kappa T} \tag{117}$$

where κ is called the escape rate. The escape rate is independent of the distribution ρ_0 or of the choice R and Γ and, therefore, characterizes the chaotic set itself [71]. However, the constant of proportionality in (117) does depend on ρ_0, R and Γ. This is not surprising since trajectories originating from initial conditions distributed in the region R comprise the transients towards the region Γ and hence alter the lifetime T. The escape rate is the same exponent characterizing the lifetime distributions of the SSA from section 9.2. Recall that there, for all network architectures, the initial conditions were not chosen as random distributions ρ_0 within the highly dimensional phase space but as the result of a stimulation procedure of the network by changing the amplitude of the external input current I_{stim}, the proportion of stimulated neurons P_{stim} and the duration of stimulation T_{stim}. We argued that this stimulation procedure ensures that the initial conditions lie close to typical pathways in a "physiologically reasonable" part of the phase space, i.e. presumably close to long living SSA trajectories. Since the position of the initial conditions defines the region R, we intended to choose R as broad as possible, by leading the system to distinct regions of the phase space (governed by the number of stimulated neurons and the amplitude of the external current) but simultaneously assuring that many of the initial conditions would lead to typical pathways visiting the region Γ containing the chaotic set. Remark that the escape rate gives only global information about the chaotic set. It is a global measure of its instability: the higher the escape rate, the more unstable the chaotic set is, resulting in a higher probability that a random trajectory would escape its comprising region Γ within a given time.

In the remaining part of this section we investigate the local structure of the chaotic set– or, to be more precise– the local structure of its comprising region Γ. To facilitate the comparison of the following results with those from the previous section, we take the same example network of modularity level $H = 0$ where 20% of all excitatory neurons are of CH type and the inhibitory neurons are of LTS type. The synaptic strengths (g_{ex}, g_{in}) are $(0.15, 1)$ and the stimulation procedure corresponds to the same initial condition with lifetime of SSA above 2000ms. This high lifetime ensures that the corresponding trajectory remains within the phase space region Γ for sufficiently long time period. In what follows we refer to this trajectory as the *initial trajectory* and denote it symbolically by $\mathcal{I}(t)$. After the stimulation the system was left to evolve freely along the initial trajectory for a time $\tau = 370$ms, corresponding to more than three oscillatory periods of high global network activity, ensuring that the trajectory has reached the region Γ. Once in the Γ region the system was systematically perturbed at fifty different perturbation positions $\mathcal{P}_k$, $k = 1, .., 50$. The perturbation positions $\mathcal{P}_k$ were chosen to lie at equidistant time intervals along the initial trajectory such that

$$\mathcal{P}_k = \mathcal{I}(\tau + k\,\Delta t) \tag{118}$$

with $\Delta t = 7$ms. Starting from each perturbation position the system was perturbed, respectively, six hundred times, by stimulating each time a proportion $P = 1/8$ of different randomly chosen neurons with an external input current $I_{ext} = 10$ for a time

period $t_{stim} = 3$ms. After each perturbation the system was left to evolve once again freely and the corresponding new lifetime was recorded. This local perturbation procedure provided sets of "secondary" initial conditions, each containing six hundred points densely placed about the corresponding perturbation position $\mathcal{P}_k$. Remark that each of those sets of "secondary" initial conditions lies at a different place along the initial trajectory, i.e. it provides a local distribution of "secondary" initial conditions at distinct local regions within the region Γ. Therefore, each of the sets alone is not sufficient to provide a global information about the whole region. However, taken together, these sets cover the tubular neighborhood of the initial trajectory. As mentioned above, the escape rate provides information about the global instability of the region Γ. Here, our intention is to test the local instability of the region Γ. In particular we are interested to see whether the whole region Γ is unstable or there is a smaller local unstable subregion within Γ, something like a "hole", from where the trajectories tend to escape. If the former case the lifetimes of trajectories originating from different local sets would be comparable, since they would be able to escape from anywhere, regardless the position of the corresponding local set within the Γ region. In the latter case, however, trajectories originating from local sets situated near the "hole" would tend to have shorter lifetimes than trajectories originating from local sets situated far away from the "hole". Remark that there might be more than one "hole", especially for a heteroclinic network, with "holes" eventually situated in the vicinity of the corresponding saddle points.

Figure 53 represents graphically the results from the "local" investigation. The raster plot on the left of figure 53 shows the spiking activity of the network along the initial trajectory. It can be considered as a representation of the initial trajectory $\mathcal{I}(t)$. The green lines within the raster plot correspond to times $(\tau + k\,\Delta t)$ from equation (118) defining the positions of perturbation. On the right side of figure 53 are given examples of the lifetime distributions of different (local) sets of "secondary" initial conditions at different perturbation positions $\mathcal{P}_k$. Observe that the distributions are not smooth like those discussed in section 9.2 but exhibit instead local maxima (peaks). The diagram in the middle of figure 53 represents the lifetimes for the first and second local peak (respectively in blue and red) at the different perturbation positions. The perturbation positions in the middle diagram are aligned with the corresponding times in the raster plot, according to equation (118).

Consider first the raster plot in figure 53. Observe that the time between two periods of high network activity can be roughly estimated to be about 100ms. As we have seen in section 9.4, for a given network architecture and fixed conductivity strengths, this time does not depend strongly on the initial conditions leading to the corresponding SSA states. Therefore, we can assume that it is a feature roughly characterizing a "typical" time period within the set Γ. In the case of heteroclinic network this "typical" time period may be associated with the period between two saddle points and in the case of a chaotic set it can be associated with the "typical" time period a trajectory needs in order to perform one oscillation within the set Γ. We should remark that, in either case, this is an oversimplified point of view since the topology of the Γ region within the highly dimensional phase space is unknown. Furthermore, for a chaotic set in such system it would be difficult to strictly define a period of oscillation by means of techniques such as the Poincare

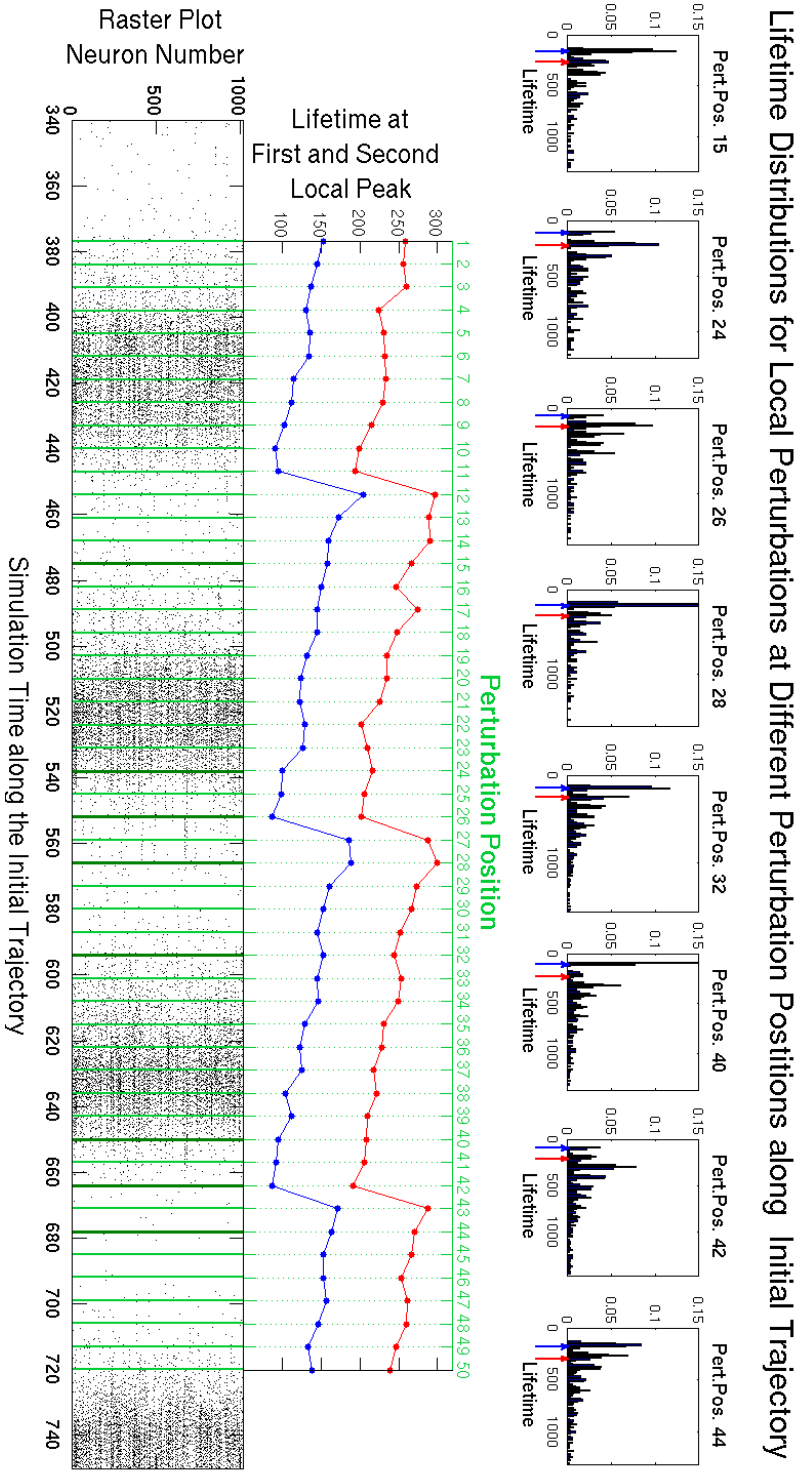

Figure 53: Results from the investigation of the local structure of the phase space region Γ comprising the chaotic set. On the left: Raster plot of the spiking activity of the network along an initial trajectory $\mathcal{I}(t)$. Green lines represent the time of the perturbation positions along the initial trajectory (see text). In the middle: Change of the lifetimes at the first and second peak of the distributions resulting from the local perturbations at the perturbation positions along the trajectory (see text). On the right: Examples of the distributions at different perturbation positions.

Section for example (see part I, section 2). Nevertheless, this viewpoint seems to be compatible with the observations. In the diagram in the middle of figure 53, the distance between the lifetimes of the first and second peaks corresponds to the same "typical" time period of about 100ms. The same is true for the distance between the lifetimes of any subsequent peaks in the distributions on the right side of the figure. The peaks in the distributions show that certain lifetimes are favored and therefore indicate that trajectories do not escape the region Γ anywhere. Observe, in the diagram in the middle of figure 53, the change of lifetimes with respect to the perturbation positions. Despite the fluctuations between subsequent initial conditions there is a clear tendency which indicates decrease in the lifetime followed by large jumps. Those jumps and the peaks in the distributions indicate that there is/are subregion/s in Γ from where trajectories tend to escape, i.e. "hole(s)". Because of the oscillation of the initial trajectory within the Γ region $\mathcal{I}(t)$ repeatedly passes in the vicinity of a "hole". Each of the perturbed trajectories originating from a "secondary" initial condition performs similar dynamics along the phase space flow within the Γ region and also passes in the vicinity of a "hole". Consider a position along the initial trajectory after it has passed near a "hole", i.e. such that $\mathcal{I}(t)$ has to perform a whole oscillation until it reaches again a "hole". Accordingly, all perturbed trajectories originating from this perturbation position have to perform a whole oscillation themselves until they reach a "hole". At each passage near a "hole" a proportion of all trajectories originating from a local set of "secondary" initial conditions escapes the Γ region trough the "hole". The closer the perturbation position is to the "hole", the shorter becomes the lifetime of the trajectories that escape the region Γ at the first passage, i.e. the lifetime at the first peak. The lifetime of the subsequent peaks is accordingly shifted by the "typical" time period, since the remaining trajectories have to perform another oscillation until they reach a "hole" again. When the perturbation position passes the "hole" there is a jump in the lifetimes which corresponds to the "typical" time period (see perturbation positions $\mathcal{P}_{12}$, $\mathcal{P}_{27}$ and $\mathcal{P}_{43}$). The amplitudes of the different peaks within the distributions indicate the topological complexity of the region Γ. For example, in the distribution corresponding to perturbation position $\mathcal{P}_{40}$, the amplitude of third peak is distinctly higher than of the second peak. This might be due to the fact that there are, respectively, two different "holes" with two different local escape rates corresponding, for example, to two saddles with different instabilities or due to a complex folding and stretching of the topology of the chaotic set within Γ. Nevertheless, the escape rate, as global characteristics of the whole region, is still well defined, when considering the lifetime distribution of all fifty local set of "secondary" initial conditions together, as represented in figure 54.

It is important that this local perturbation procedure allows us to determine the position of a "hole" along an initial trajectory $\mathcal{I}(t)$: it is always situated at the end of high global network activity period. A comparison with the results from section 11.1 shows that a "hole" corresponds to a state of the network with a high proportion of neurons occupying high u values (compare figure 52 and figure 53). This is the crucial dynamical state since the activity of the network is sustained only within the "pool" of moderately active neurons and most of the newly produced network activity gets absorbed by the "transient neurons", i.e. many of the newly produced

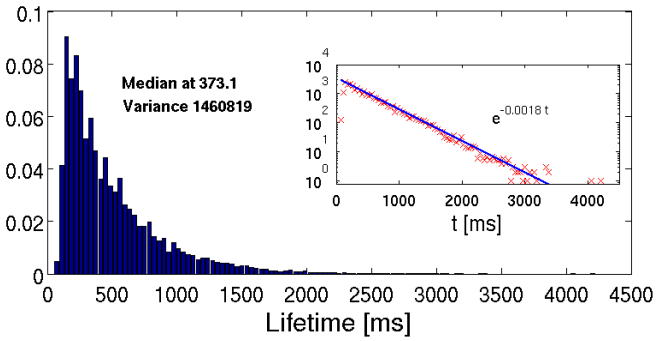

Figure 54: Global lifetime distribution of all fifty local set each comprising six hundred "secondary" initial conditions considered together. Inset: The corresponding histogram in linear - logarithmic plot.

spikes do not lead to spikes in the postsynaptic neurons.

12 Discussion

Our main finding is that the neuronal composition of the network, i.e. the types and combinations of excitatory and inhibitory cells that comprise the network, has an effect on the properties of SSA in the network, which acts in conjunction with the effect of network topology. Previous theoretical studies have emphasized the role of the structural organization (topology) of the cortical network on its sustained activity [66, 110, 44, 74, 85]. Here we have shown that the electrophysiological classes of the cortical neurons and the percentages of these neurons in the network composition also affect the dynamics of the sustained network activity. Specifically, we found that networks comprising excitatory neurons of the RS and CH types have higher probability of supporting long-lived SSA than networks with excitatory neurons only of the RS type. In addition, the type of the inhibitory neurons in the network also has a significant effect. In particular, LTS inhibitory neurons stronger favor long-lived SSA states than FS inhibitory neurons.

A possible mechanism that would render networks made of RS and CH excitatory cells more prone to long-lived SSA is due to the pattern of spikes exhibited by the CH cells, which consists of spike bursts followed by strong afterhyperpolarizations. During a phase of high network activity neurons with high spiking frequency exhibit bursting-like behavior independent of their electrophysiological class; see section 10. At the end of the high-activity period such neurons enter slow transient depolarization leading to global decrease of the network activity. In this state, none of the transient neurons is able to perform a spike and the network activity is sustained by moderately active neurons postsynaptic to previously active inhibitory neurons. The presence of CH neurons in the network would then enhance and coordinate the postsynaptic responses of other network cells, which would contribute to prolongation of network activity. As a consequence, the low-activity periods would become shorter and the global network activity would become more oscillatory and better synchronized with corresponding increases in the global network frequency and the mean firing frequency of the individual neurons, effects reported in Sect.9. This mechanism is more effective in networks with inhibitory neurons of the LTS class rather than of the FS class because of the higher temporal and spatial uniformity of the inhibition provided by LTS neurons, as discussed in Section 9.4. During a high activity phase the LTS neurons ensure a higher number of moderately inhibited neurons, while the FS neurons lead to a lower number of strongly inhibited neurons.

We are aware of just one theoretical study in the literature which has addressed the impact of the specific neuronal composition of the network on its SSA regimes [32]. There, it was shown that a two-layered cortical network in which the layers were composed of excitatory RS and inhibitory FS cells with a small proportion of excitatory LTS cells in the second layer, could produce SSA. Here we have extended the analysis by including neurons of five electrophysiological classes and, in particular, by considering LTS cells that are exclusively inhibitory.

Our study also has shown that modularity favors SSA. In general, independently of neuronal composition, the increase in the hierarchical level of the network (and hence in the number of modules) increases the lifetime expectancy of SSA in the network. This effect can be understood if we imagine that distinct modules are

activated intermittently and non-simultaneously. Each module is a random network which, depending on its specific neuronal composition, can generate SSA with a certain lifetime. Because of the sparse coupling among modules, they activate each other in an alternate way so that there is a probability of each one of them activating a neighbor before decaying to rest. And the larger the number of modules, the greater is this probability. In other words, using the paradigm of a "hole" in the phase space, introduced in section 11, if we consider each module as a random network by itself, it has its own "hole" leading from sustained dynamical activity towards the resting state. Increasing the number of modules it is less probable that all modules would enter a "hole" simultaneously.

The region of the parameter space of excitatory and inhibitory synaptic strengths for which the network SSA states display properties similar to physiological measurements [95, 59, 77, 55] is the lower right corner of what we called the diagram of low synaptic strengths. The spiking properties of the SSA states in this region are remarkably independent of the network architecture and initial conditions. These properties are irregular neuronal firing and low frequency population oscillation with leading frequency often in the range of ∼5 to ∼8 Hz. In this particular region of the ($g_{\rm ex}$, $g_{\rm in}$) plane the ratio $g_{\rm ex}/g_{\rm in}$ has a value between about 4 and 12. This is consistent with the theoretical prediction that irregular activity in a spiking cortical network can be sustained in a balanced excitation-inhibition state, whereby the strength of inhibitory synapses is higher than the strength of excitatory synapses: to compensate for the smaller number of inhibitory neurons and keep the average total synaptic input into a neuron near zero, so that the neuron spikes are caused by the fluctuations around this average [106, 3, 107, 21]. These theoretical studies relied on random networks of sparsely-connected leaky integrate-and-fire neurons. Our study, although more focused on hierarchical and modular networks, also has shown that irregular SSA can occur in random networks (H=0). Since our networks are based on neuron models with richer properties than the leaky integrate-and-fire model, our finding points to a complementary, though secondary in comparison with the excitation-inhibition balance, mechanism for irregular SSA in a random network of spiking neurons, which depends on the mixture and proportions of the different types of excitatory and inhibitory neurons in the network.

Our results strongly suggest that the sustained and irregular firing regimes in our simulations are transiently chaotic. This is consistent with conjectures that the default state of the brain is chaotic [93, 106, 107, 14, 65, 75]. It is important to note that in the biologically relevant range of low synaptic strengths the SSA does not last indefinitely: its lifetime remains finite and abruptly ends with relaxation towards the state of rest. The probability to observe a SSA of a given duration is an exponential function of duration. From this point of view, SSA is a transient phenomenon. In a way, this was already expected because every brain dynamical regime is transient [86]. Duration of the transient depends on the network architecture (hierarchical level, mixture of excitatory-inhibitory neurons) and the synaptic parameters. A direct possibility to prolong the lifetime of the SSA without increasing the synaptic strengths is to increase the number of neurons, since the escape time of transient chaotic trajectories grows exponentially with the growth of the dimension of the system [27, 69, 71, 39]. We observed this effect when proceeding from 2^9 to 2^{10}

neurons; our preliminary results with larger networks confirm this conjecture.

Conclusions

A complex dynamical network is characterized, on the one hand, by the internal dynamics of the single nodes comprising the network and, on the other hand, by the network topology describing the interaction structure between the nodes. In this work we have investigated global dynamical phenomena emerging from the interplay between network topology and single-node dynamics in systems of excitable elements.

Using the paradigm of phase oscillators, in the first part of this work, we focused on the collective behavior of the nodes in terms of synchronization. The network topology alone puts strong constraints on the dynamical flow in the phase space of the system and in particular on the admissible synchronized states which live on flow-invariant submanifolds (polydiagonals) [97, 50, 51, 35]. Identification of flow-invariant polydiagonals corresponding to synchronized states allows a reduction of the initial network to a smaller, reduced network: oscillators belonging to the same cluster in the initial network correspond to a single node in the reduced network and edges between the nodes in the reduced network are weighted according to corresponding cluster sizes. The collective behavior of the nodes from the initial system is emphasized by the reduced network. Moreover, depending on the clustered state, the reduced network may correspond to a globally coupled system and in those cases, for a certain class of coupling functions and single-node dynamics, the dynamics of the network is naturally reduced further and becomes 3- dimensional according to the Watanabe-Strogatz reduction [111, 112, 78]. For the single nodes dynamics we have chosen the Kuramoto and Shinomoto model of sinusoidally coupled "active rotators" [91], which is widely used in studies of collective effects and is compatible with the class of "sinusoidally coupled systems" required by the Watanabe-Strogatz reduction [78]. In the case of identical phase oscillators interacting via the same coupling function, the polydiagonals corresponding to synchronized states remain flow-invariant for all non-vanishing coupling strengths; yet their stability alters, leading to non-generic bifurcation scenarios reflecting the symmetry of the underlying graph. Accordingly, depending on the parameter region, different clustered states gain or lose stability. We have focused our investigation on the parameter region of repulsive coupling, since the traditionally considered opposite, attractive coupling, commonly favors the onset of global synchronization [8], while repulsive coupling is known to result in less trivial effects like clustering and hysteresis [104]. In general, dynamical phenomena, such as transition from globally synchronous state to chaos or cluster synchronization, depend on the eigenvalues of the underlying adjacency matrix whose degeneracy determines the dimension of the center manifold at the bifurcation points. Plane hexagonal lattices with periodic boundary conditions provide a suitable theoretical framework for such investigations, since the degeneracy of the eigenvalues of the adjacency matrix strongly depends on the size of the lattice while keeping the local, hexagonal, symmetries of the system fixed. Investigating different small hexagonal lattices with periodic boundary conditions, we have shown that the dynamical states of the system are not governed solely by the local symmetries of the network but also by its global characteristics. For instance, depending on the network size and the parameter region the dynamically relevant stable states

of the system diversify from various periodic synchronous states, quasi-periodicity and chaos to weak-chimera states [12]. Each of these dynamical states emphases different symmetries induced by the network topology and transitions between those states correspond to breaking of symmetries, whereby different bifurcation scenarios strongly depend on the network size. The observed range of these bifurcation scenarios is remarkable. We have found period doubling bifurcations, Neimark-Sacker bifurcation, saddle-node bifurcations, pitchfork bifurcations, transcritical bifurcations, homoclinic bifurcations and also the not so common transcritical/homoclinic (THB) bifurcations [11]. Periods of limit cycles born at THB bifurcations display neither the logarithmic law, typical for a homoclinic bifurcation of hyperbolic saddle points, nor the inverse square law, typical for homoclinics to saddle-nodes [46]. Here, the observed period is inversely proportional to the distance from the critical parameter value. We discussed the normal form of the THB bifurcation and investigated the asymptotics of the period. Stable synchronized periodic solutions born at THB bifurcations were observed only for certain sizes of the investigated hexagonal lattices: the 3×3 and 4×4 hexagonal lattices. In the case of the 4×4 hexagonal lattice the periodic solutions comprised four identical clusters with a reduced network corresponding to 4- dimensional globally coupled system of four identical nodes. This reduced system is subject to the Watanabe-Strogatz reduction, resulting in 3- dimensional dynamics with the periodic solutions belonging to continua of limit cycles. We studied generic conditions posed on the network topology enabling the Watanabe-Strogatz reduction and investigated systems with such nontrivial topologies. In many of these investigated systems we have found not only symmetric but also non-symmetric THB bifurcations. Finally, we presented a generic analysis of bifurcations taking place on submanifolds associated with the Watanabe-Strogatz reduced system.

While the network models in the first part of this work were of prevailing theoretical interest, in the second part, we investigated more realistic, cortical-like neuronal networks. The focus remained on the question about the interplay between network topology and single-node dynamics. We studied their effects on a global dynamical phenomenon, known as self-sustained activity (SSA). We constructed a spiking network model that captures elements of the architectonic organization of the cortex and of its composition in terms of cells of different electrophysiological classes. The architecture of the network is hierarchical and modular, which arguably [110, 90] represents the generic topological organization of the cortex across many spatial scales, and the excitatory and inhibitory cells of our model belong to five distinct electrophysiological classes that can coexist in the same network [82, 25]. For the dynamics of single neurons we used the Izhikevich neuron model [62]. Our goal was to study the combined effect of these architectonic and physiological elements on the SSA of the network. To do so we performed an extensive computational study of our model by considering network architectures characterized by different combinations of hierarchical and modularity levels, mixture of excitatory-inhibitory neurons, strength of excitatory-inhibitory synapses and network size submitted to distinct initial conditions. In the investigated model we found that SSA states with spiking characteristics, similar to the ones observed experimentally, can exist for regions of the parameter space of excitatory-inhibitory synaptic strengths in

which the inhibitory strength exceeds the excitatory one. In this regions of synaptic strengths the SSA states were transient with finite lifetimes and corresponded to large-scale network activity oscillations characterized by subsequent high and low global-activity phases flowed by abrupt unpredictable decay towards the resting state. Furthermore, we saw that regardless of the network architecture, in the absence or at very low inhibition as well as at very low excitatory synaptic strength, SSA states are not possible. By analyzing the dynamics of single neurons, as well as the phase space of the whole system, we could explain the importance of inhibition for sustaining the global oscillatory activity of the network. Our results strongly suggest that the sustained and irregular firing regimes in our simulations are transiently chaotic. The duration of the transients depends not only on the synaptic parameters but also on the network architecture. It was strongly influenced, separately, by the type of excitatory neurons, the type of inhibitory neurons, the modularity level and also by combinations of those characteristics. We found that networks comprising excitatory neurons of the regular spiking and chattering types have higher probability of supporting long-lived SSA than networks with excitatory neurons only of the regular spiking type. Fast spiking inhibitory neurons did not favor long-living SSA in comparison to low threshold spiking inhibitory neurons. Our study has also shown that modularity favors SSA. In general, independently of neuronal composition, the increase in the hierarchical level of the network (and hence in the number of modules) increases the lifetime expectancy of SSA in the network.

Summarizing, we can state not only that our initial expectations were justified, in the sense that in all investigated cases the interplay between topology and single-node dynamics took place, but also that we were able to detect in our systems new, hitherto unknown dynamical aspects.

Acknowledgments

First of all, I would like to express my sincere gratitude to my *Doktorvater* Michael Zaks, for his continuous guidance and support, for the countless motivating discussions and stimulating thoughts, for his help and inexhaustible patience.

I would like to thank Antonio Roque for the motivating research topics he proposed, for his support and scientific guidance during and after my stay in Brazil, and for making me feel welcome and comfortable in his group. I am grateful to the whole group of Antonio Roque for the friendly time spend together; in particular, to Rodrigo Pena for the great collaboration during our joint project.

I would like to thank Lutz Recke, Irina Kmit, Jörg Wolf, Oleksandr Burylko, Serhiy Yanchuk, Dmitry Puzyrev, Leonhard Lücken and Philip Pade as well as all my colleagues from the Graduiertenkolleg for the nice time spend together, for the fruitful discussions and help. I am also very grateful to David Hansmann from the Graduiertenkolleg for his administrative support.

I would also like to thank my friends Hans Ruiz and Andreas Pithis for the countless hours of inspiring discussions about physics, philosophy and basically any subject. I would like to thank my cousin Ralitza and my friends Valentin, Dilyana, Toma, Nora, Dejan, Stefan, Pavel, Maxim for always being there for me, for their constant support, bearing with me in times of frustration.

I would like to thank my parents and my sister for their love, support and encouragement throughout my entire life. Finally, I would like to thank my wife Kameliya for her love, patience, and understanding; for helping me get through all the years of my studies.

References

[1] Aguiar, M. A. and Dias, A. P. S. (2014). The lattice of synchrony subspaces of a coupled cell network: Characterization and computation algorithm. Journal of Nonlinear Science, 24(6), 949-996. 2.2

[2] Aldis, J. W. (2008). A polynomial time algorithm to determine maximal balanced equivalence relations. International Journal of Bifurcation and Chaos, 18(02), 407-427. 2.2

[3] Amit, D. J. and Brunel, N. (1997). Model of global spontaneous activity and local structured activity during delay periods in the cerebral cortex. Cerebral cortex, 7(3), 237-252. 12

[4] Antoneli, F., Dias, A. P. S., Golubitsky, M., and Wang, Y. (2005). Patterns of synchrony in lattice dynamical systems. Nonlinearity, 18(5), 2193. 2

[5] Antoneli, F. and Stewart, I. (2006). Symmetry and synchrony in coupled cell networks 1: Fixed-point spaces. International Journal of Bifurcation and Chaos, 16(03), 559-577. 2.2, 2.4

[6] Antoneli, F. and Stewart, I. (2007). Symmetry and synchrony in coupled cell networks 2: Group networks. International Journal of Bifurcation and Chaos, 17(03), 935-951. 2.2

[7] Antoneli, F. and Stewart, I. (2008). Symmetry and synchrony in coupled cell networks 3: exotic patterns. International Journal of Bifurcation and Chaos, 18(02), 363-373. 2.2

[8] Arenas, A., Díaz-Guilera, A., Kurths, J., Moreno, Y. and Zhou, C. (2008). Synchronization in complex networks. Physics Reports, 469(3), 93-153. (document), 12

[9] Arieli, A., Shoham, D., Hildesheim, R. and Grinvald, A. (1995). Coherent spatiotemporal patterns of ongoing activity revealed by real-time optical imaging coupled with single-unit recording in the cat visual cortex. Journal of Neurophysiology 73,2072–2093. 7

[10] Aronson, D. G., Golubitsky, M. and Mallet-Paret, J. (1991). Ponies on a merry-go-round in large arrays of Josephson junctions. Nonlinearity, 4(3), 903. 2.2, 2.4

[11] Ashwin, P., King, G. P. and Swift, J. W. (1990). Three identical oscillators with symmetric coupling. Nonlinearity, 3(3), 585. 2.2, 5, 12

[12] Ashwin, P., and Burylko, O. (2015). Weak chimeras in minimal networks of coupled phase oscillators. Chaos: An Interdisciplinary Journal of Nonlinear Science, 25(1), 013106. 2.4, 4.2, 12

[13] Aubin, D. and Dalmedico, A. D. (2002). Writing the history of dynamical systems and chaos: longue durée and revolution, disciplines and cultures. Historia mathematica, 29(3), 273-339. (document)

[14] Banerjee, A., Series, P. and Pouget, A. (2008). Dynamical constraints on using precise spike timing to compute in recurrent cortical networks. Neural Computation 20:974–993. 12

[15] Bastos, A. M., Usrey, W. M., Adams, R. A., Mangun, G. R., Fries, P. and Friston, K. J. (2012). Canonical microcircuits for predictive coding. Neuron 76,695-711. (document), 7

[16] Binzegger, T., Douglas, R. J. and Martin, K. A. C. (2004). A quantitative map of the circuit of cat primary visual cortex. Journal of Neuroscience 24,8441-8453. 7

[17] Birkhoff, George David (1966). Dynamical systems. Vol. 9. American Mathematical Soc. (document)

[18] Boccaletti, S., Latora, V., Moreno, Y., Chavez, M. and Hwang, D. U. (2006). Complex networks: Structure and dynamics. Physics reports, 424(4), 175-308. (document)

[19] Bringuier, V., Chavane, F., Glaeser, L. and Frégnac, Y. (1999). Horizontal propagation of visual activity in the synaptic integration field of area 17 neurons. Science 283,695–699. 7

[20] Brouwer, A. E. and Haemers, W. H. (2011). Spectra of graphs. Springer Science & Business Media. 2.1, 2.4

[21] Brunel, N. (2000). Dynamics of sparsely connected networks of excitatory and inhibitory spiking neurons. Journal of Computational Neuroscience 8,183–208. 7, 9.4, 12

[22] Buzsáki, G. and Draguhn, A. (2004). Neuronal oscillations in cortical networks. Science 304,1926–1929. 7

[23] Chung, F. R. (1997). Spectral graph theory (Vol. 92). American Mathematical Soc. 3.3

[24] Connors, B. W., Gutnick, M. J. and Prince, D. A. (1982). Electrophysiological properties of neocortical neurons in vitro. Journal of Neurophysiology 48,1302–1320. 7

[25] Contreras, D. (2004). Electrophysiological classes of neocortical neurons. Neural Networks 17,633–646. 7, 12

[26] Cronin, J. (1987). Mathematical aspects of Hodgkin-Huxley neural theory. Pan, 148, 678-683. II

[27] Crutchfield, J. P. and Kaneko, K. (1988). Are attractors relevant to turbulence? Physical Review Letters 60,2715–2718. 12

[28] Cvitanovic, P., Artuso, R., Mainieri, R., Tanner, G., Vattay, G., Whelan, N. and Wirzba, A. (2005). Chaos: classical and quantum. ChaosBook. org (Niels Bohr Institute, Copenhagen 2005). (document)

[29] Dayan, P. and Abbott, L. F. (2001). Theoretical Neuroscience: Computational and Mathematical Modeling of Neural Systems, MIT Press, Cambridge, MA. 8.1, 8.3

[30] Deco, G. Jirsa, V., McIntosh, A. R., Sporns, O. and Kötter, R. (2009). Key role of coupling, delay, and noise in resting brain fluctuations. Proceedings of the National Academy of Sciences (USA) 106,10302–10307. 7

[31] Deco, G., Jirsa, V. and McIntosh, A. R. (2010). Emerging concepts for the dynamical organization of resting state activity in the brain. Nature Reviews Neuroscience 12,43–56. 7

[32] Destexhe, A. Self-sustained asynchronous irregular states and Up-Down states in thalamic, cortical and thalamocortical networks of nonlinear integrate-and-fire neurons. Journal of Computational Neuroscience 27.3 (2009), 493–506. 7, 9.1, 12

[33] Destexhe, A. (2011). Intracellular and computational evidence for a dominant role of internal network activity in cortical computations. Current Opinion in Neurobiology 21,717–725. 7

[34] Diacu, F. and Holmes, P. (1996). Celestial encounters: the origins of chaos and stability. Princeton University Press. (document)

[35] Dias, A. P. S., and Stewart, I. (2004). Symmetry groupoids and admissible vector fields for coupled cell networks. Journal of the London Mathematical Society, 69(3), 707-736. 1, 1.2, 12

[36] Dias, A. P. S., and Stewart, I. (2005). Linear equivalence and ODE-equivalence for coupled cell networks. Nonlinearity, 18(3), 1003.

[37] Diestel, R. (1996). Graphentheorie (Vol. 2). Berlin, Heildelberg, New York, Springer. 5

[38] Douglas, R. J. and Martin, K. A. (2004). Neuronal circuits of the neocortex. Annual Review of Neuroscience 27,419–451. 7

[39] El Boustani, S. and Destexhe, A. (2009). A master equation formalism for macroscopic modeling of asynchronous irregular activity states. Neural Computation 21,46–100. 12

[40] Ermentrout, G. B., and Kopell, N. (1986). Parabolic bursting in an excitable system coupled with a slow oscillation. SIAM Journal on Applied Mathematics, 46(2), 233-253. II, II

[41] Ermentrout, B. (1996). Type I membranes, phase resetting curves, and synchrony. Neural computation, 8(5), 979-1001. II, II

[42] Fox, M. D. and Raichle, M. E. (2007). Spontaneous fluctuations in brain activity observed with functional magnetic resonance imaging. Nature Reviews Neuroscience 8,700–711. 7

[43] Gabbiani, F. and Koch, C. (1998). Principles of spike train analysis. In: Koch, C. and Segev, I. (Eds.), Methods in Neuronal Modeling: From Ions to Networks, 2nd edition, MIT Press, Cambridge, MA, 1998. pp. 313–360. 8.3, 8.3

[44] Garcia, G. C., Lesne, A., Hütt, M. and Hilgetag, C. C. (2012). Building blocks of self-sustained activity in a simple deterministic model of excitable neural networks. Frontiers in Computational Neuroscience 6,50. 7, 12

[45] Gervais, J. J. (1988). Bifurcations of subharmonic solutions in reversible systems. Journal of differential equations, 75(1), 28-42. 2.3

[46] Glendinning, P. (1994). Stability, instability and chaos: an introduction to the theory of nonlinear differential equations. Cambridge university press. 2.2, 5, 12

[47] Golubitsky, M., and Schaeffer, D. G. (1985) Singularities and Groups in Bifurcation Theory I. New York, Springer. 2.1, 2.2, 2.4

[48] Golubitsky, M., Schaeffer, D. G., and Stewart, I. (1988) Singularities and Groups in Bifurcation Theory II. New York, Springer. 2.1, 2.2, 2.4

[49] Golubitsky, M. and Stewart, I. (2003). The symmetry perspective: from equilibrium to chaos in phase space and physical space (Vol. 200). Springer Science & Business Media. 2.2, 2.2, 2.4, 2.4

[50] Golubitsky, M., Stewart, I. and Török, A. (2005). Patterns of synchrony in coupled cell networks with multiple arrows. SIAM Journal on Applied Dynamical Systems, 4(1), 78-100. 1, 1.2, 3, 3.2, 12

[51] Golubitsky, M. and Stewart, I. (2006). Nonlinear dynamics of networks: the groupoid formalism. Bulletin of the american mathematical society, 43(3), 305-364. 1, 1.2, 1.2, 12

[52] Gong, P. and van Leeuwen, C. (2009). Distributed dynamical computation in neural circuits with propagating coherent activity patterns. PLoS Computational Biology 5,e10000611. 7

[53] Guckenheimer, J. and Holmes, P. (1983). Nonlinear oscillations, dynamical systems, and bifurcations of vector fields (Vol. 42). Springer Science & Business Media. 2.1, 2.4

[54] Hahn, G., Petermann, T., Havenith, M. N., Shan, Y., Singer, W., Plenz, D. and Nikolić, D. (2010). Neuronal avalanches in spontaneous activities in vivo. Journal of Neurophysiology 104,3312–3322. (document), 7

[55] Haider, B., Häusser, M. and Carandini, M. (2013). Inhibition dominates sensory responses in the awake cortex. Nature 493,97–102. 9.1, 12

[56] Higgins, P. J. (1971). Categories and groupoids. Queen Mary College. 1.2

[57] Hilgetag, C. C., Burns, G. A. P. C., O'Neill, M. A., Scannell, J. W. and Young, M. P. (2000). Anatomical connectivity defines the organization of clusters of cortical areas in the macaque monkey and the cat. Philosophical Transactions of the Royal Society of London B, Biological Sciences 355,91–110. 7

[58] Hodgkin, A. L., and Huxley, A. F. (1952). A quantitative description of membrane current and its application to conduction and excitation in nerve. The Journal of physiology, 117(4), 500-544. II

[59] Hromádka, T., Deweese, M. R., and Zador, A. M. (2008). Sparse representation of sounds in the unanesthetized auditory cortex. PLoS Biology 6,e16. 9.1, 12

[60] Ionita, F., Labavić, D., Zaks, M. A. and Meyer-Ortmanns, H. (2013). Order-by-disorder in classical oscillator systems. The European Physical Journal B, 86(12), 1-13.

[61] Izhikevich, E. M. (2000). Neural excitability, spiking and bursting. International Journal of Bifurcation and Chaos, 10(06), 1171-1266. II, II

[62] Izhikevich, E. M. (2003). Simple model of spiking neurons. IEEE Transactions on Neural Networks, 14(6), 1569–1572. (document), II, II, 8.1, 8.1, 12

[63] Izhikevich, E. M. (2004). Which model to use for cortical spiking neurons? IEEE Transactions on Neural Networks 15,1063–1070 (document), II, 7

[64] Izhikevich, E. M. (2007). Dynamical systems in neuroscience. MIT press.. II, II, II

[65] Izhikevich, Eugene M., and Gerald M. Edelman. (2008). Large-scale model of mammalian thalamocortical systems. Proceedings of the National Academy of Sciences 105.9 , 3593–3598. 8.1, 12

[66] Kaiser, M. and Hilgetag, C. C. (2010). Optimal hierarchical modular topologies for producing limited sustained activation of neural networks. Frontiers in Neuroinformatics. 4,8. 7, 12

[67] Kamei, H. (2009). Construction of lattices of balanced equivalence relations for regular homogeneous networks using lattice generators and lattice indices. International Journal of Bifurcation and Chaos, 19(11), 3691-3705. 2.2

[68] Kamei, H. and Cock, P. J. (2013). Computation of balanced equivalence relations and their lattice for a coupled Cell network. SIAM Journal on Applied Dynamical Systems, 12(1), 352-382. 2.2

[69] Kumar, A., Schrader, S., Aertsen, A. and Rotter, S. (2008). The high-conductance state of cortical networks. Neural Computation 20,1–43. 7, 9.4, 12

[70] Kurrer, C. and Schulten, K. (1995). Noise-induced synchronous neuronal oscillations. Physical Review E, 51(6), 6213.

[71] Lai, Ying-Cheng, and Tél, Tamás. (2011). Transient Chaos: Complex Dynamics on Finite Time Scales. Applied Mathematical Sciences, Vol. 173. Springer. 9.2, 9.2, 11.2, 11.2, 12

[72] Lakatos, P., Karmos, G., Mehta, A. D., Ulbert, I. and Schroeder, C. E. (2008). Entrainment of neuronal oscillations as a mechanism of attentional selection. Science 320,110–113. 7

[73] Lewis, C. M., Baldassarre, A., Committeri, G., Romani, G. L. and Corbetta, M. (2009). Learning sculpts the spontaneous activity of the resting human brain. Proceedings of the National Academy of Sciences (USA) 106,17558–17563. 7

[74] Litwin-Kumar, A. and Doiron, B. (2012). Slow dynamics and high variability in balanced cortical networks with clustered connections. Nature Neuroscience 15,1498–1505. (document), 7, 12

[75] London, M., Roth, A., Beeren, L., Häusser, M. and Latham, P. E. (2010). Sensitivity to perturbations *in vivo* implies high noise and suggests rate coding in cortex. Nature 466,123–127. 12

[76] Luczak, A., Bartho, P. and Harris, K. D. (2009). Spontaneous events outline the realm of possible sensory responses in neocortical populations. Neuron 62,413–425. 7

[77] Maimon, G. and Assad, J. A. (2009). Beyond Poisson: increased spike-time regularity across primate parietal cortex. Neuron 62,426–440. 9.1, 12

[78] Marvel, S. A., Mirollo, R. E. and Strogatz, S. H. (2009). Identical phase oscillators with global sinusoidal coupling evolve by Möbius group action. Chaos, An Interdisciplinary Journal of Nonlinear Science, 19(4), 043104. (document), 2.4, 2.4, 3, 3.1, 5, 12

[79] McCormick, D. A., Connors, B. W., Lighthall, J. W. and Prince, D. A. (1985). Comparative electrophysiology of pyramidal and sparsely spiny stellate neurons of the neocortex. Journal of Neurophysiology 54,782–806. 7

[80] Meunier, D., Lambiotte, R. and Bullmore, E. T. (2010). Modular and hierarchically modular organization of brain networks. Frontiers in Neuroscience 4,200. (document), 7

[81] Newman, M. E. (2003). The structure and function of complex networks. SIAM review, 45(2), 167-256. (document)

[82] Nowak, L. G., Azouz, R., Sanchez-Vives, M. V., Gray, C. M. and McCormick, D. A. (2003). Electrophysiological classes of cat primary visual cortical neurons in vivo as revealed by quantitative analyses. Journal of Neurophysiology 89,1541–1566. 7, 12

[83] physics. (2015). In Encyclopædia Britannica. Retrieved from http://www.britannica.com/science/physics-science (document)

[84] Pikovsky, A., Rosenblum, M., and Kurths, J. (2003). Synchronization: a universal concept in nonlinear sciences. Cambridge university press. 1, 1.1

[85] Potjans, T. C. and Diesmann, M. (2014). The cell-type specific cortical microcircuit: relating structure and activity in a full-scale spiking network model. Cerebral Cortex 24,785–806. 7, 12

[86] Rabinovich, M. I. and Varona, P. (2012). Transient brain dynamics. In: Rabinovich, M. I., Friston, K. J. and Varona, P. (Eds.), Principles of Brain Dynamics: Global State Interactions, MIT Press, Cambridge, MA, 2012. pp. 71–92. 12

[87] Roopun, A. K., Kramer, M. A., Carracedo, L. M., Kaiser, M., Davies, C. H., Traub, R. D., Kopell, N. J. and Whittington, M. A. (2008). Temporal interactions between cortical rhythms. Frontiers in Neuroscience 2,145–154. 7

[88] Sadaghiani, S., Hesselmann, G., Friston, K. J. and Kleinschmidt, A. (2010). The relation of ongoing brain activity, evoked neural responses, and cognition. Frontiers in Systems Neuroscience 4,20. 7

[89] Sadovsky, A. J. and MacLean, J. N. (2013). Scaling of topologically similar functional modules defines mouse primary auditory and somatosensory microcircuitry. Journal of Neuroscience 33,14048–14060. 7

[90] Samu, D., Seth, A. K. and Nowotny, T. (2014). Influence of wiring cost on the large-scale architecture of human cortical connectivity. PLoS Computational Biology 10,e1003557. 12

[91] Shinomoto, S. and Kuramoto, Y. (1986). Phase transitions in active rotator systems. Progress of Theoretical Physics, 75(5), 1105-1110. (document), 2, 2.1, 3.3, II, 12

[92] Shmuel, A. and Leopold, D. A. (2008). Neuronal correlates of spontaneous fluctuations in fMRI signals in monkey visual cortex: implications for functional connectivity at rest. Human Brain Mapping 29,751–761. 7

[93] Skarda, C. A. and Freeman, W. J. (1987). How brains make chaos in order to make sense of the world. Behavioral and Brain Sciences 10,161–173. 12

[94] Smolin, L., and Harnad, J. (2008). The trouble with physics: the rise of string theory, the fall of a science, and what comes next. The Mathematical Intelligencer, 30(3), 66-69. (document)

[95] Softky, W. R. and Koch, C. (1993). The highly irregular firing of cortical cells is inconsistent with temporal integration of random EPSPs. Journal of Neuroscience 13,334–350. 9.1, 12

[96] Steinke, G. K. and Galán, R. F. (2011). Brain rhythms reveal a hierarchical network organization. PLoS Computational Biology 7,e1002207. 7

[97] Stewart, I., Golubitsky, M. and Pivato, M. (2003). Symmetry groupoids and patterns of synchrony in coupled cell networks. SIAM Journal on Applied Dynamical Systems, 2(4), 609-646. 1, 1.2, 3, 3.2, 12

[98] Stewart, I. (2007). The lattice of balanced equivalence relations of a coupled cell network. In Mathematical Proceedings of the Cambridge Philosophical Society (Vol. 143, No. 01, pp. 165-183). Cambridge University Press. 2.2

[99] Stratton, P. and Wiles, J. (2010). Self-sustained non-periodic activity in networks of spiking neurons: the contribution of local and long-range connections and dynamic synapses. NeuroImage 52,1070–1079. 7

[100] Strogatz, S. H. (2014). Nonlinear dynamics and chaos: with applications to physics, biology, chemistry, and engineering. Westview press. (document)

[101] Tessone, C. J., Mirasso, C. R., Toral, R. and Gunton, J. D. (2006). Diversity-induced resonance. Physical review letters, 97(19), 194101.

[102] Tomov, P. and Zaks, M. (2014). Phase dynamics on small hexagonal lattices with repulsive coupling. In Nonlinear Dynamics of Electronic Systems (pp. 246-253). Springer International Publishing.

[103] Tomov, P., Pena, R. F., Zaks, M. A. and Roque, A. C. (2014). Sustained oscillations, irregular firing, and chaotic dynamics in hierarchical modular networks with mixtures of electrophysiological cell types. Frontiers in computational neuroscience, 8. II

[104] Tsimring, L. S., Rulkov, N. F., Larsen, M. L. and Gabbay, M. (2005). Repulsive synchronization in an array of phase oscillators. Physical review letters, 95(1), 014101. (document), 12

[105] Tsodyks, M. V., Kenet, T., Grinvald, A. and Arieli, A. (1999). Linking spontaneous activity of single cortical neurons and the underlying functional architecture. Science 286,1943–1946. 7

[106] van Vreeswijk, C. and Sompolinsky, H. (1996). Chaos in neuronal networks with balanced excitatory and inhibitory activity. Science 274,1724–1726. 7, 12

[107] van Vreeswijk, C. and Sompolinsky, H. (1998). Chaotic balanced state in a model of cortical circuits. Neural Computation 10,1321–1371. 7, 12

[108] Vogels, T. P. and Abbott, L. F. (2005). Signal propagation and logic gating in networks of integrate-and-fire neurons. Journal of Neuroscience 25,10786–10795. (document), 7, 9.1

[109] Wang, Y. and Golubitsky, M. (2005). Two-colour patterns of synchrony in lattice dynamical systems. Nonlinearity, 18(2), 631.

[110] Wang, S. J., Hilgetag, C. C. and Zhou, C. (2011). Sustained activity in hierarchical modular neural networks: self-organized criticality and oscillations. Frontiers in Computational Neuroscience. 5,30. (document), 7, 8.2, 12, 12

[111] Watanabe, S. and Strogatz, S. H. (1993). Integrability of a globally coupled oscillator array. Physical review letters, 70(16), 2391. (document), 2.4, 2.4, 3, 3.1, 12

[112] Watanabe, S. and Strogatz, S. H. (1994). Constants of motion for superconducting Josephson arrays. Physica D: Nonlinear Phenomena, 74(3), 197-253. (document), 2.4, 2.4, 3, 3.1, 12

[113] Weinberg, S. (1995). The quantum theory of fields (Vol. 1). Cambridge university press.
Weinberg, S. (1996). The quantum theory of fields (Vol. 2). Cambridge university press.
Weinberg, S. (2000). The quantum theory of fields (Vol. 3). Cambridge university press. (document)

[114] Weinberg, S. (1998). Gravitation and Cosmology: Principles and applications of the general theory of relativity. Wiley. (document)

[115] West, D. B. (2001). Introduction to graph theory (Vol. 2). Upper Saddle River: Prentice hall. 4

[116] Yamauchi, S., Kim, H. and Shinomoto, S. (2011). Elemental spiking neuron model for reproducing diverse firing patterns and predicting precise firing times. Frontiers in Computational Neuroscience 5,42. II, 7

[117] Zaks, M. A., Neiman, A. B., Feistel, S. and Schimansky-Geier, L. (2003). Noise-controlled oscillations and their bifurcations in coupled phase oscillators. Physical Review E, 68(6), 066206.

[118] Zaks, M.A. and Tomov, P. (2015). Onset of time-dependence in ensembles of excitable elements with global repulsive coupling. *Submitted to* Physical Review Letters, October 2015.

[119] Zhou, C., Zemanová, L., Zamora, G., Hilgetag, C. C. and Kurths, J. (2006). Hierarchical organization unveiled by functional connectivity in complex brain networks. Physical Review Letters 97,238103.

(document), 7

Selbständigkeitserklärung

Ich erkläre, dass ich die vorliegende Arbeit selbständig und nur unter Verwendung der angegebenen Literatur und Hilfsmittel angefertigt habe.

Berlin, den 01.10.2015 Petar Georgiev Tomov